Chapter Five

Mechanical testing

This chapter describes the mechanical behaviour of the fabricated cantilevers. Section 5.1 describes tension testing experiments conducted to determine the Young's modulus, yield stress and ultimate tensile strength of electroplated nickel used to fabricate cantilevers. Section 5.2 introduces various models that describe the deflection behaviour of the fabricated cantilevers. Section 5.3 compares these analytical models with measured behaviour which is discussed in section 5.4. In section 5.5 finite element models are described and in section 5.6 yielding behaviour is discussed.

It was found that tension testing did not produce results consistent with the modelling. Although all cantilevers behaved in a linearly elastic manner, it was found that plane stress models only accurately represented longer cantilevers (cantilevers with a horizontal length of 300 μm and greater). It was concluded this was due to the simplification of the cantilever geometry made in the analytical model.

5.1 Tension testing samples

In order to understand the mechanical performance of the fabricated cantilevers it was desirable to compare models of mechanical behaviour with experimental data. It was therefore important to determine the Young's modulus and yield stress of the electroplated nickel from which the cantilevers were made.

In order to determine the mechanical properties, tension testing samples were prepared and pull tested. The following section describes the method of fabrication and the testing of these samples.

5.1.1 Fabrication of tension testing samples

The tension testing samples were fabricated as shown in Figure 5.1. The aim was to produce samples with dimensions such that they behaved as 1D fibres (rather than 2D plates) whilst producing measurable forces. Samples were fabricated with widths of 125, 250 or 500 μm, a length of 1.2 cm and as thick as practically possible (approximately 50 μm).

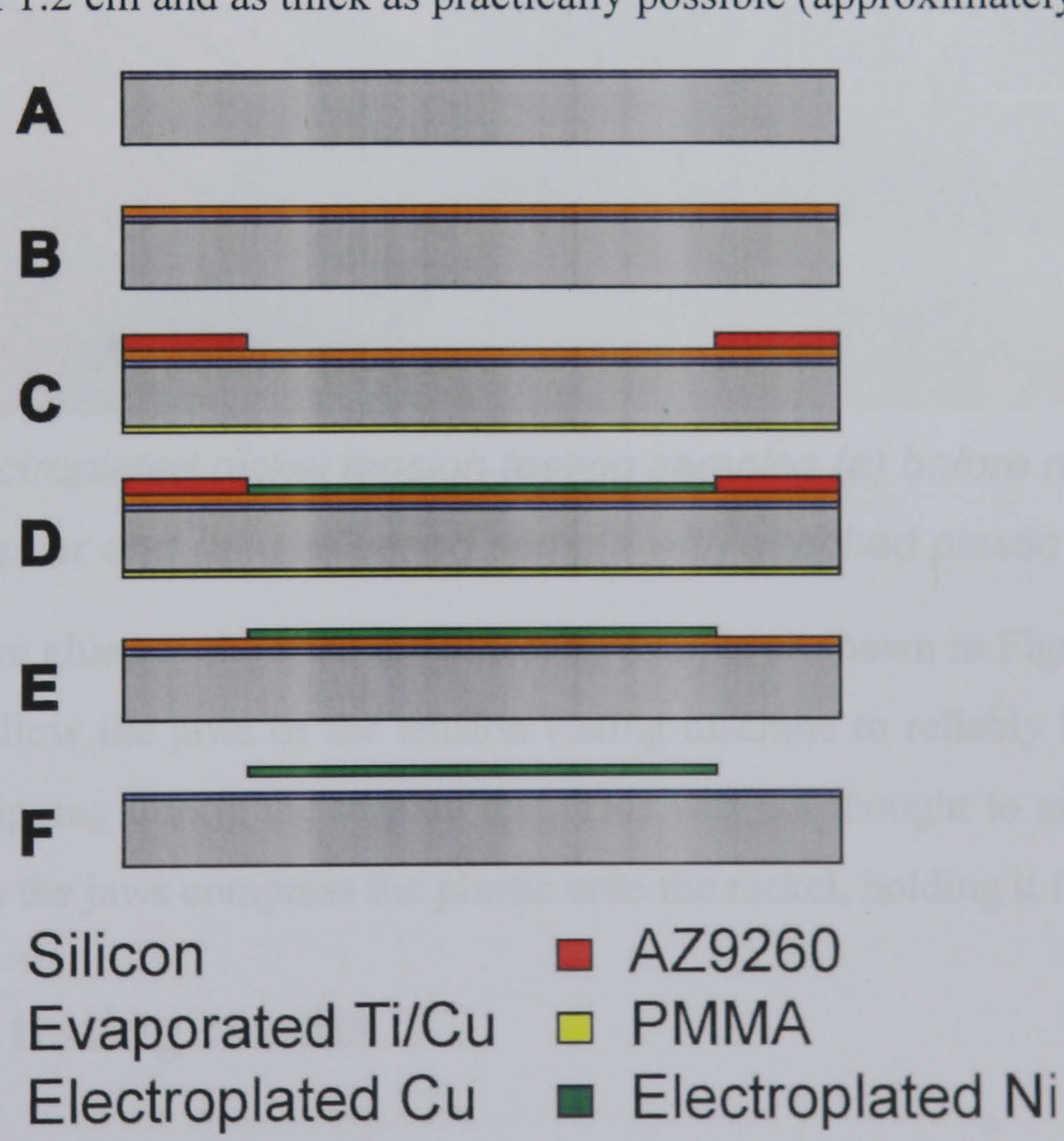

Figure 5.1 Fabrication sequence for tension testing samples

A: 30 nm seed layer of titanium and 150 nm of copper were evaporated onto a cleaned silicon wafer.

B: Copper was electroplated at 20 mA/cm^2 current density to a thickness of 7 μm. The bath used was of the same composition as that give in chapter 3.

C: A 55 μm layer of AZ9260 photoresist was spin coated and baked. This resist was patterned to form the electroplating moulds. PMMA dissolved in chlorobenzene (5% solids) was spin coated onto the back of the wafer. This prevented nickel electroplating onto the reverse of the wafer in subsequent steps. This was important to ensure that the current density at which the nickel was electroplated could be controlled.

D: The exposed copper surface was etched in 10:1 H_2O:HNO_3 for 30 s in order to ensure a clean surface for electroplating. Nickel was then electroplated at 12 mA/cm^2 for 5 hours to a target thickness 55 μm. The bath used was the smooth nickel formulation (see chapter 3) which was the same chemistry used to electroplate the cantilevers.

E: PMMA and AZ9260 were removed using acetone followed by washing in IPA and water.

F: The electroplated copper layer was dissolved in 1:1:1 H_2O:CH_3COOH:H_2O_2 releasing the nickel structures.

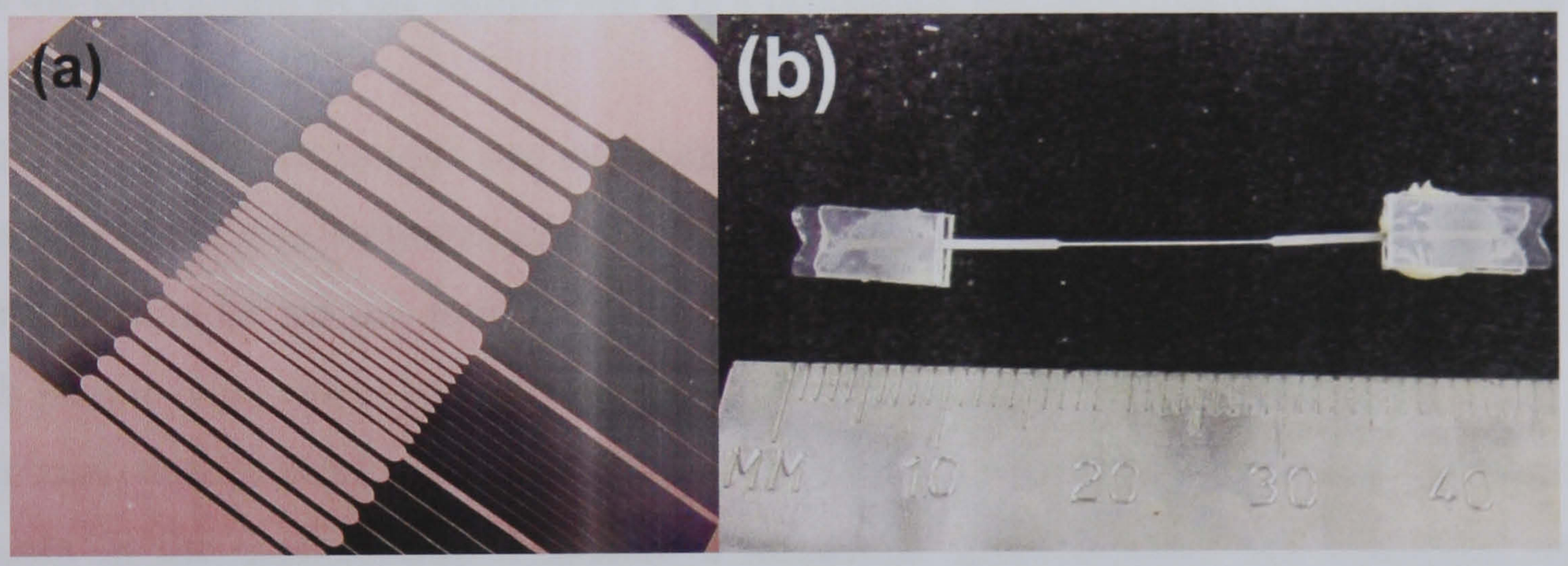

Figure 5.2 Electroplated nickel tension testing samples (a) before release from sacrificial copper and (b) a released sample with attached plastic mounting

Plastic sheets were glued to the ends of the testing sample as shown in Figure 5.2 (b). This was necessary to allow the jaws of the tension testing machine to reliably hold the sample and prevent any slipping during the tension test. This was not thought to affect the tension testing results since the jaws compress the plastic onto the nickel, holding it firmly.

5.1.2 Tension testing results

Tension testing was performed using an Instron 5565 universal testing machine. This can measure a maximum load of 5 kN and can apply a loading rate of between 0.001 and 1000 mm/min with an accuracy of ± 0.1%. The absolute positional accuracy is ± 0.02 mm or

0.05% of displacement (whichever is greater). The load is accurate to ± 0.4% in the range 5 kN to 50 N and ± 0.5% in the range 50 N to 20 N.

5.1.2.1 Young's modulus

The thickness of the nickel deposit varied from 42 μm to 140 μm across the wafer. This was a result of the non-uniform current distribution across the wafer, which itself was influenced by the seed layer properties and the position and quality of the connection between the wafer and the electroplating power supply. Because of this there was a variation in cross-section of the tension testing samples. This could be accounted for when calculating Young's modulus, *E*, as follows:

$$E = \frac{\sigma}{\varepsilon} = \frac{FL}{A\Delta} = \frac{F}{\Delta}\int_0^L \frac{1}{A}dx \qquad (5\text{-}1)$$

where *F* is the applied force, *Δ* is the extension of the sample, *A* is the cross-sectional area, *L* is the total length of the sample and *x* is a coordinate that describes the position along the length of the sample.

The length of each sample was calculated from the mask design. The thickness and width of each sample was measured using a Zygo NewView 100 Optical profilemeter by taking measurements before the samples were released (see Figure 5.1 and Figure 5.2 (a)). For each sample three values of thickness (t_1, t_2, t_3) were measured (see Figure 5.3).

An analytical evaluation of the integral in equation 5-1 was non-trivial since a function of *x* appears in the denominator. Therefore a numerical approximation was calculated using MatLab. For each sample three values of area were calculated and a second order polynomial was fitted through the reciprocal of them. This polynomial was used to interpolate an array of values which were then numerically integrated using the trapezoidal rule.

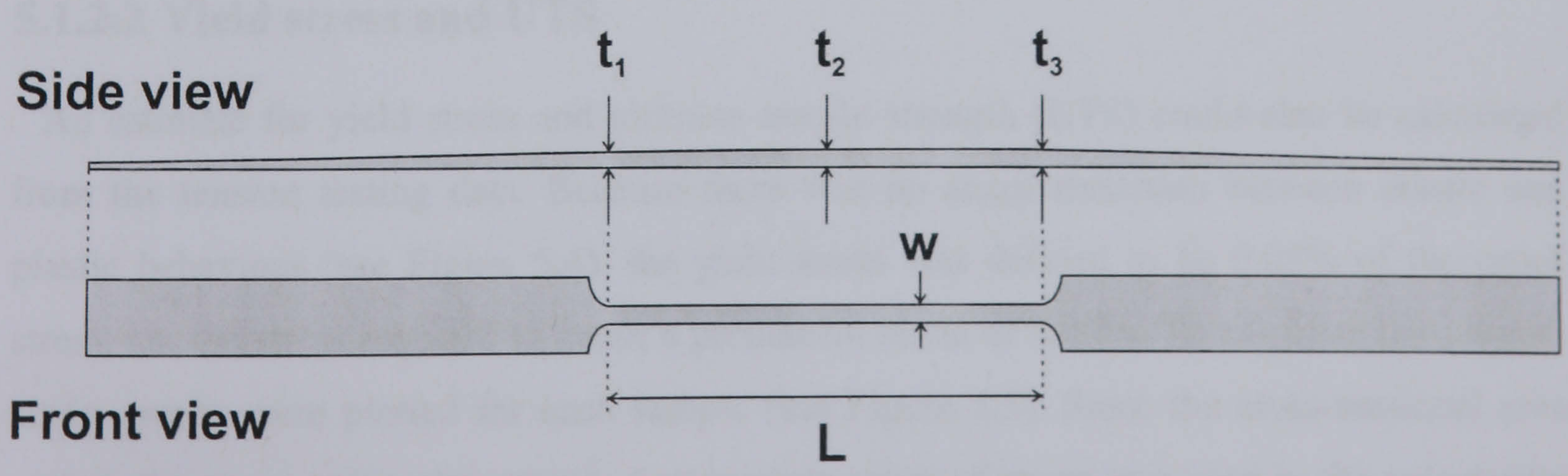

Figure 5.3 Tension testing sample

Five samples, all from one wafer, were tested to destruction. A summary of the results is shown in Table 5.1. *F/Δ* was calculated as the gradient of the load-displacement trace obtained from the testing. An example of a load-displacement curve obtained is shown in Figure 5.4.

sample	t_1 (μm)	t_2 (μm)	t_3 (μm)	w (μm)	$\int^1/_A$ (x10^5 m^{-1})	F/Δ (kN/m)	E (GPa)
1	42	64	54	509	4.198	166.3	69.80
2	61	78	52	522	3.330	201.7	67.15
3	58	100	62	520	2.822	246.0	69.43
4	68	140	120	527	1.959	288.4	56.50
5	106	92	70	509	2.640	265.8	70.19

Table 5.1 Calculated Young's modulus

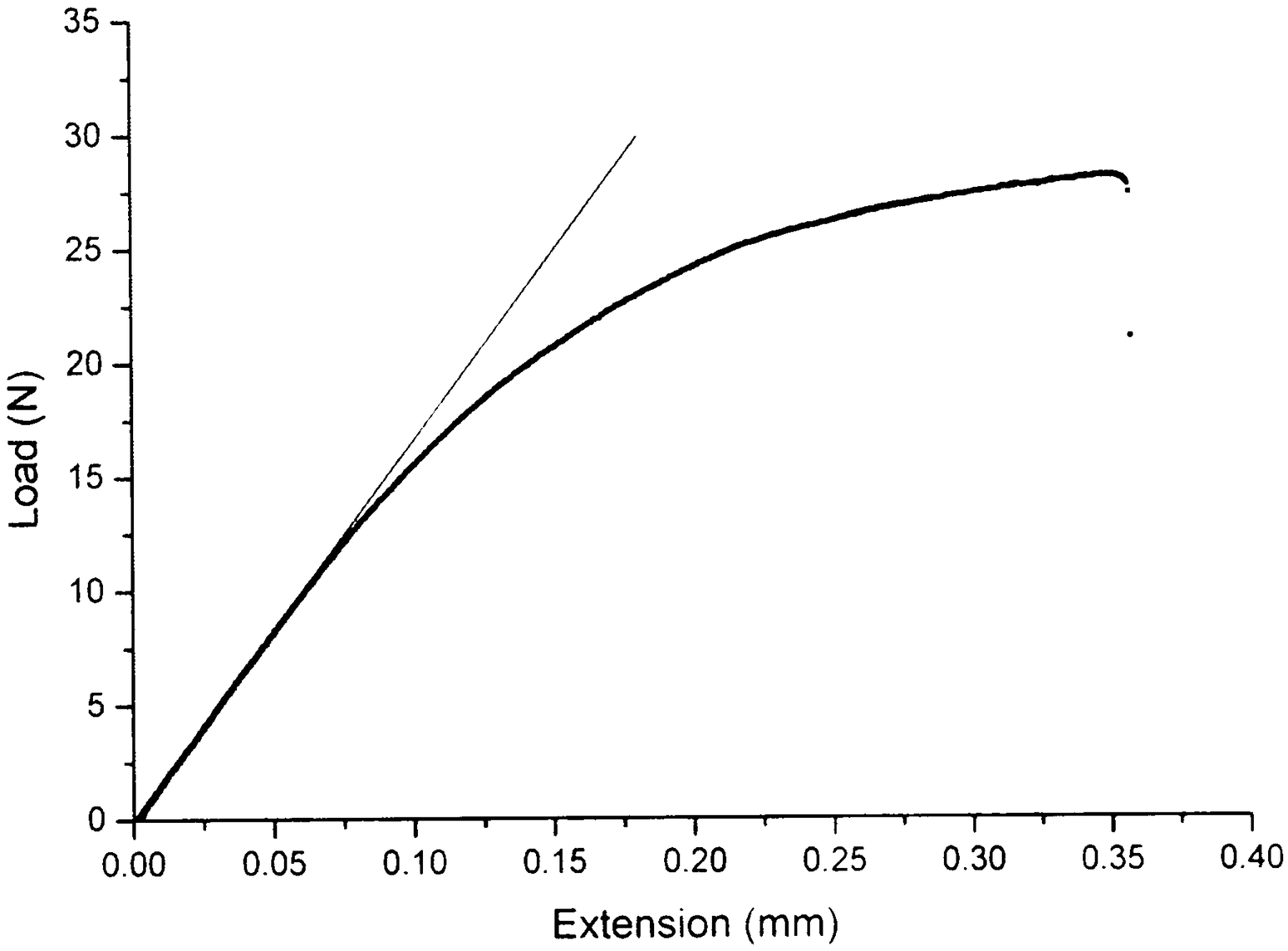

Figure 5.4 Results from tension testing sample 1

The average Young's modulus was 69.1 GPa and the sample standard deviation was 1.4 GPa.

5.1.2.2 Yield stress and UTS

An estimate for yield stress and ultimate tensile strength (UTS) could also be calculated from the tension testing data. Because there was no sharp transition between elastic and plastic behaviour (see Figure 5.4), the yield stress was defined to be 0.05% of the proof stress, i.e. the stress required to cause a permanent strain of 0.05%. To calculate this, stress-strain graphs were plotted for each sample (see Figure 5.5). Since the cross-sectional area varied, the stress value also varied. A maximum value of stress was used in the calculation of yield stress and UTS since the sample was assumed to fail when the area with the thinnest

cross-section surpassed the relevant threshold. The calculated yield stresses are shown in Table 5.2.

The UTS values could be calculated from the stress at the onset of necking and are shown in Table 5.3.

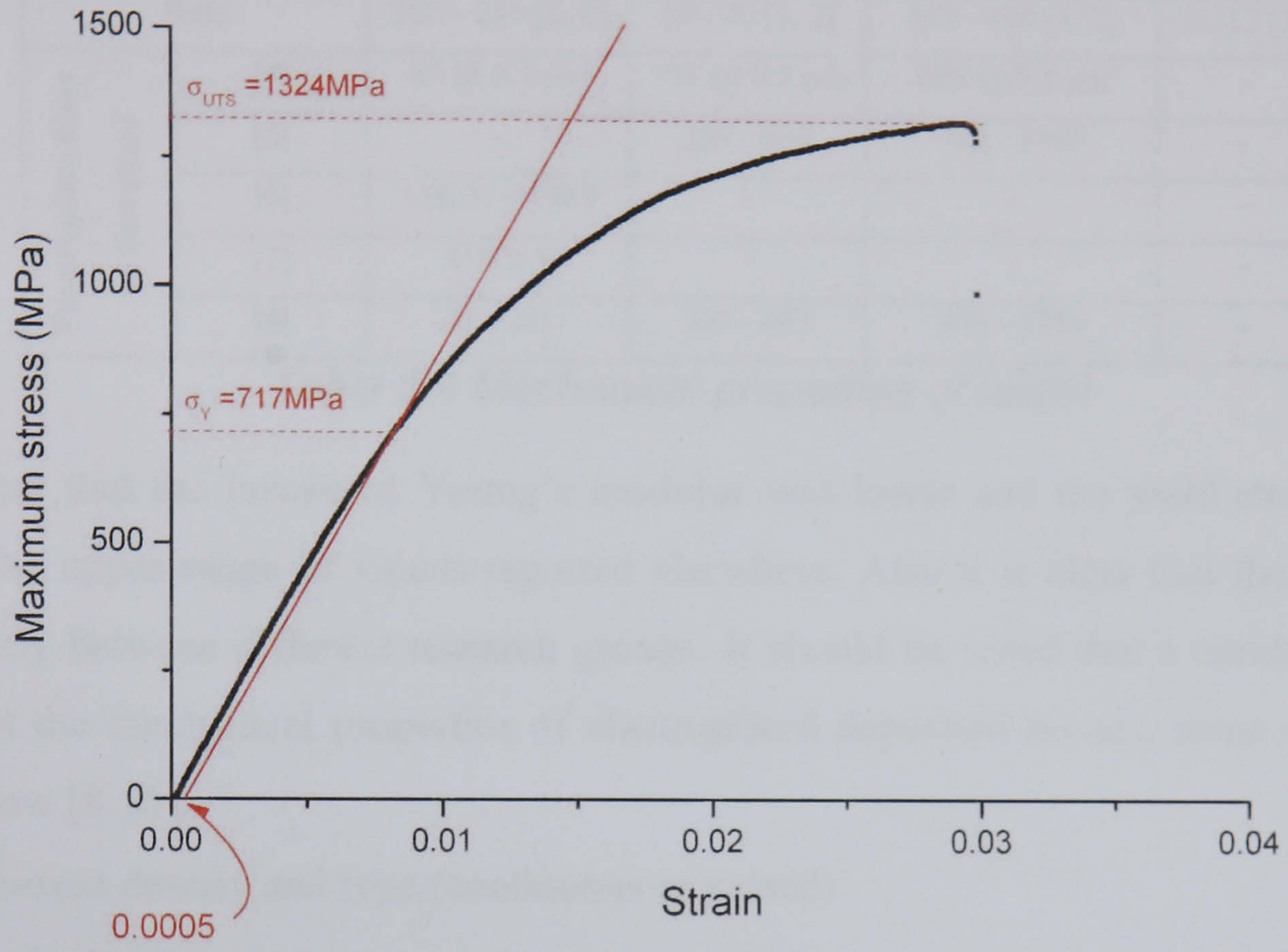

Figure 5.5 Calculation of yield stress from stress-strain data (Sample 1)

Sample	Yield stress MPa (0.05 %)
1	717
2	769
3	591
4	688
5	780

Table 5.2 Yield stresses of tension testing samples

Sample	UTS MPa
1	1324
2	1197
3	1109
4	1243
5	1169

Table 5.3 Ultimate tensile strengths of tension testing samples

The average yield stress was 709 MPa and the sample standard deviation was 75.9 MPa. The average ultimate tensile strength was 1208 MPa and the sample standard deviation was 89.8 MPa.

5.1.2.3 Comparison of Experimental results with literature

Table 5.4 compares the measured mechanical properties with those found in literature.

		E (GPa)	σ_Y (MPa)	σ_{UTS} (MPa)	υ
Measured		69.1 ± 4.1	709 ± 228	1208 ± 242	-
Bulk		207 – 214 [1, 2]	59 - 70 [1. 2]	317 - 400 [1. 2]	0.312 [3]
Electroplate films in literature	**[4]**	85 @ 9.5 µm	123 @ 9.5 µm	205 @ 9.5 µm	-
	[5]	-	339 - 667	705 - 1300	-
	[6]	148.04 - 159.9	-	-	-
	[7]	195 ± 5	-	-	-
	[8]	93 - 231	325 - 873	494 - 1750	-

Table 5.4 Mechanical properties of nickel

It is clear that the measured Young's modulus was lower and the yield stress and UTS were in the upper range of values reported elsewhere. Also it is clear that these properties vary widely between different research groups. It should be noted that a number of factors can affect the mechanical properties of electroplated deposited metals, some of which are listed below [8-10]:

- Current density and type (continuous or pulsed)
- Bath chemistry
- Bath temperature
- Bath pH
- Bath agitation
- Bath impurities and additives
- Deposited thickness of material
- Substrate material and structure. For example nickel grown on copper substrates is affected by the copper crystallographic texture [5].
- Anode material and surface properties
- Anode-substrate separation

For this reason the same current density, anode material, bath chemistry, substrate material, temperature and agitation were used for fabricating the cantilevers and the tension testing samples. However, in order to create samples with strengths great enough to test it was necessary to electroplate much thicker deposits for the tension testing samples than was used to fabrication the cantilevers. It is known that electroplated films exhibit certain textures which change with deposition thickness and can affect the mechanical properties [9].

It should also be noted that the extension values were taken directly from an internal sensor in the tension testing machine. It is known that measurements taken in this way can often be erroneous due to mechanical compliances within the machine leading to systematic errors.

The extremely low value of Young's modulus measured (almost a third that of the bulk value) is very difficult to explain purely on the grounds of microstructure and impurity inclusions. Although such physical and chemical factors could contribute to a low value of Young's modulus they cannot fully account for the discrepancy and so it may be assumed some degree of measurement error has occurred.

5.2 Cantilever deflection models

5.2.1 Bending of straight cantilevers

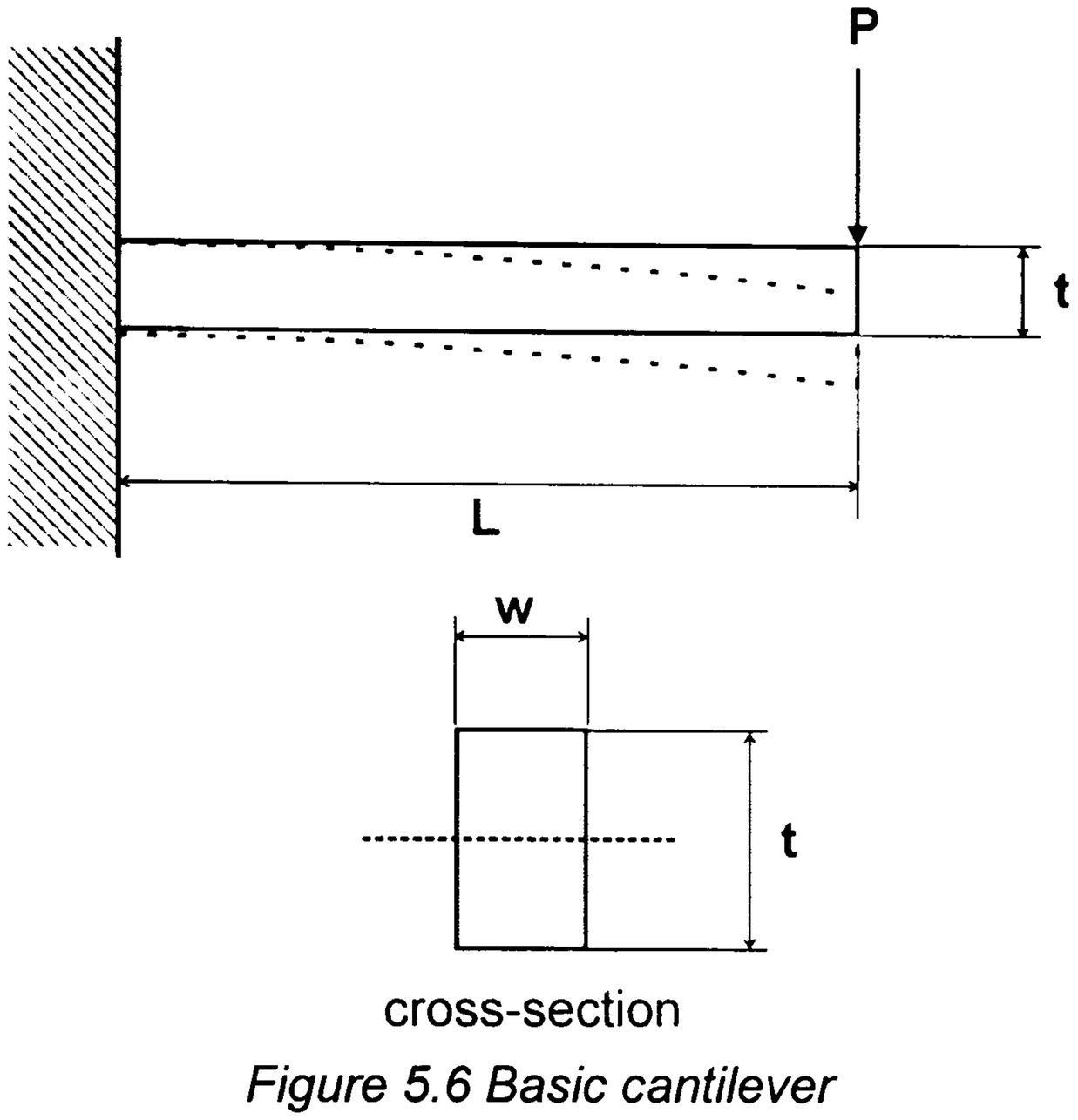

Figure 5.6 Basic cantilever

Consider the basic cantilever shown in Figure 5.6. The cantilever has a length L, width w and thickness t. It is subjected to a point load, P, at the free end. Making the assumptions listed in 5.2.2, it can be shown that the vertical deflection at the end of the cantilever, δ, is given by [11]:

$$\delta = \frac{PL^3}{3EI} \qquad (5\text{-}2)$$

where E is the Young's modulus of the cantilever and I is the second moment of area.

For a rectangular cross-section such as shown in Figure 5.6 it can be shown that the second moment of area can be calculated from [12]:

$$I = \int_A y^2 dA = \frac{wt^3}{12} \qquad (5\text{-}3)$$

where w is the width of the cross section and t is the thickness.

5.2.2 Assumptions for basic cantilever equation

Equation 5-2 is valid for the following assumptions [12]:

- The deflected cantilever remains elastic
- The deflection of the cantilever is small, such that the length of the cantilever in the longitudinal direction remains constant
- Longitudinal elements of the cantilever are subject only to simple compression or tension and there is no lateral stress, i.e. the system is represented as a plane stress problem
- The effect of shear force can be neglected
- The effect of self weight can be neglected
- Material properties are homogeneous and isotropic
- The cantilever does not buckle
- The radius of curvature of the deflected cantilever is greater than the thickness of the cantilever. This validates the assumption that transverse sections are perpendicular to circular arcs having a common centre of curvature as in Figure 5.7 (a). If this were not the case there would be a non-linear strain field as in Figure 5.7 (b)
- The effect of the contact stress distribution can be neglected

These approximations mean that equation 5-2 is practically useful for cantilevers where $\delta/L < 0.2$ [13] and $w/L < 0.1$ [14].

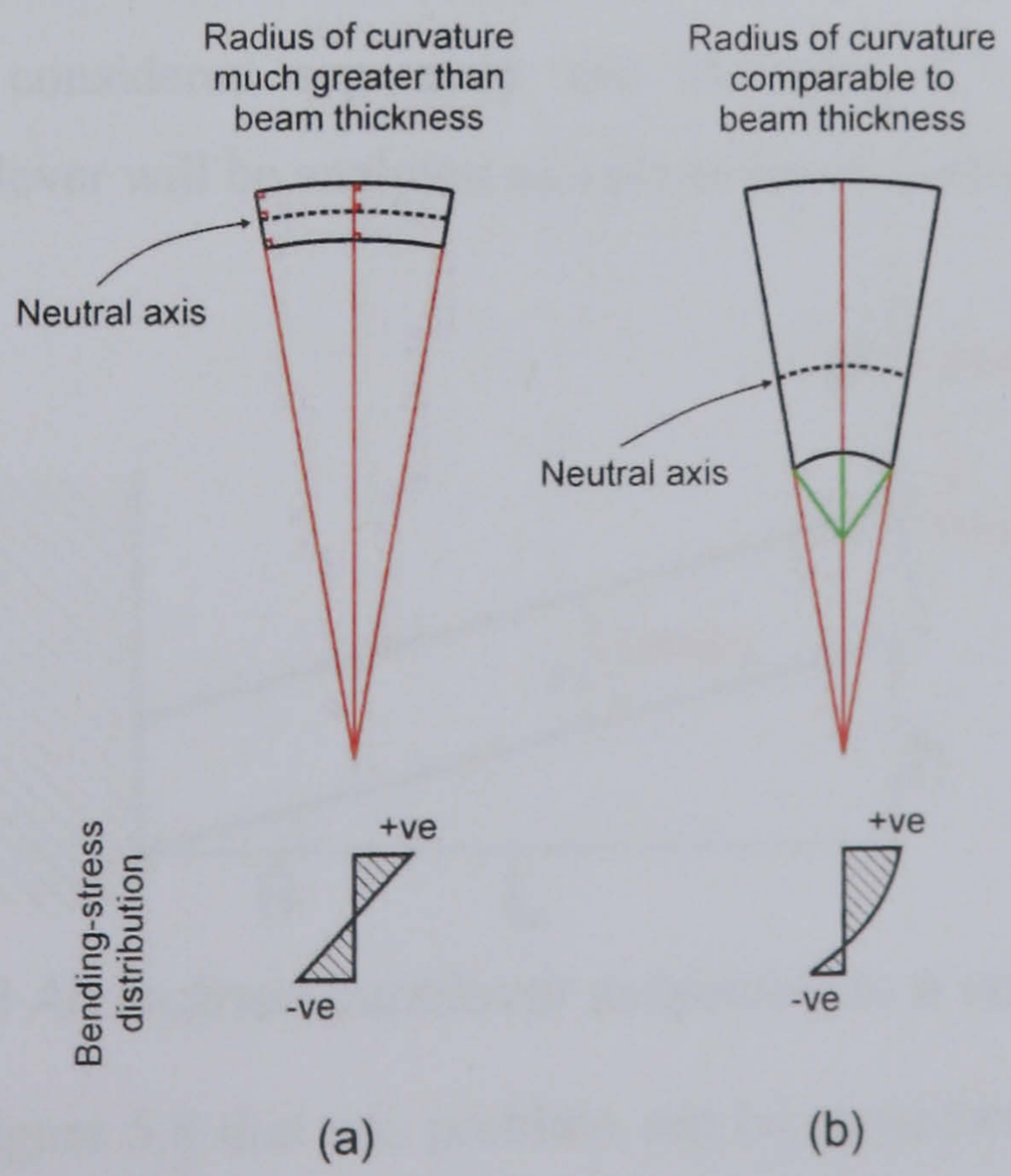

Figure 5.7 Effect of radius of curvature on bending-stress and neutral-axis

5.2.3 Deflection due to shear

Cantilevers can also be caused to deflect due to the effects of shearing. Shear effects are important to consider in a cantilever with a thickness much greater than its width or for a cantilever which has a small slenderness ratio (the slenderness ratio is the effective length to the radius of gyration of a beam, both with respect to the same axis of bending). Generally shearing is considered important for a slenderness ratio of less than 10 [15]. It can be shown that the vertical deflection δ of a cantilever, due to this shear stress caused by a point load applied at the end of the cantilever, can be given by [12]:

$$\delta = \frac{6PL}{5Gwt} \qquad (5\text{-}4)$$

where P is the applied load, L is the cantilever length, G is the shear modulus, w is the cantilever width and t is the cantilever thickness. Equation 5-4 does not account for the secondary effects of shearing distortions in a cantilever but instead assumes that sections remain plane during deflection.

It should be noted that shear modulus and Young's modulus are related (in isotropic materials) by the Poisson's ratio, υ, as shown in Equation 5-5 [12]:

$$E = 2G(1+\upsilon) \qquad (5\text{-}5)$$

5.2.4 Cantilever under bending moment, shear and axial load

To calculate the deflection of an inclined cantilever due to a vertical load, the normal and axial loading will be considered separately and the total deflection calculated using superposition. The cantilever will be analysed as a plane stress problem.

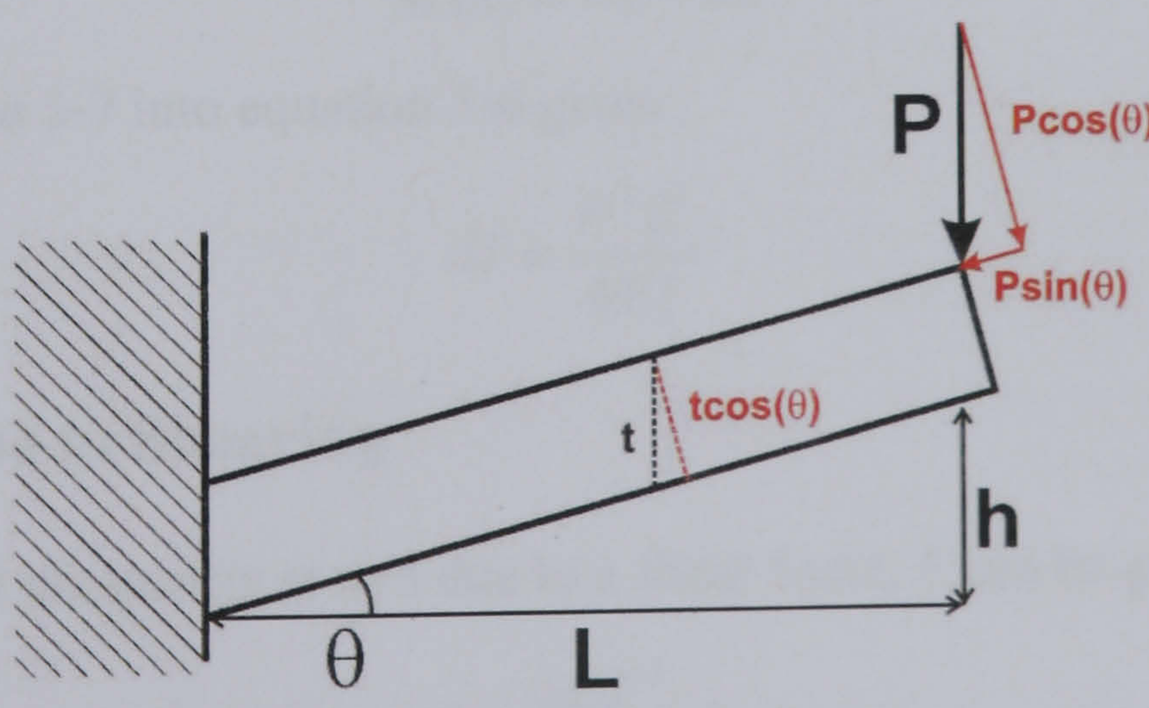

Figure 5.8 An inclined cantilever subjected to a vertical load

It can be seen from Figure 5.8 that this problem can be considered as a cantilever with a normal load of $P\cos(\theta)$ causing bending and shearing and an axial load of $P\sin(\theta)$ causing

axial compression. The cantilever has an effective length given by $\sqrt{L^2+h^2}$ and effective thickness of $t\cos(\theta)$.

Note that t has been defined as 'vertical' rather than 'true' thickness. This terminology was adopted since 'vertical' thickness could be directly measured by optical profiler before releasing the cantilevers (as shown in appendix 5-1).

5.2.4.1 Energy due to bending

It can be shown that the strain energy stored in a cantilever as a result of a moment, M, applied along its length can be given by [12]:

$$U = \int_0^L \frac{M^2}{2EI} dx \qquad (5\text{-}6)$$

where U is the energy stored, L is the length of the cantilever, E is the Young's modulus and I is the second moment of area.

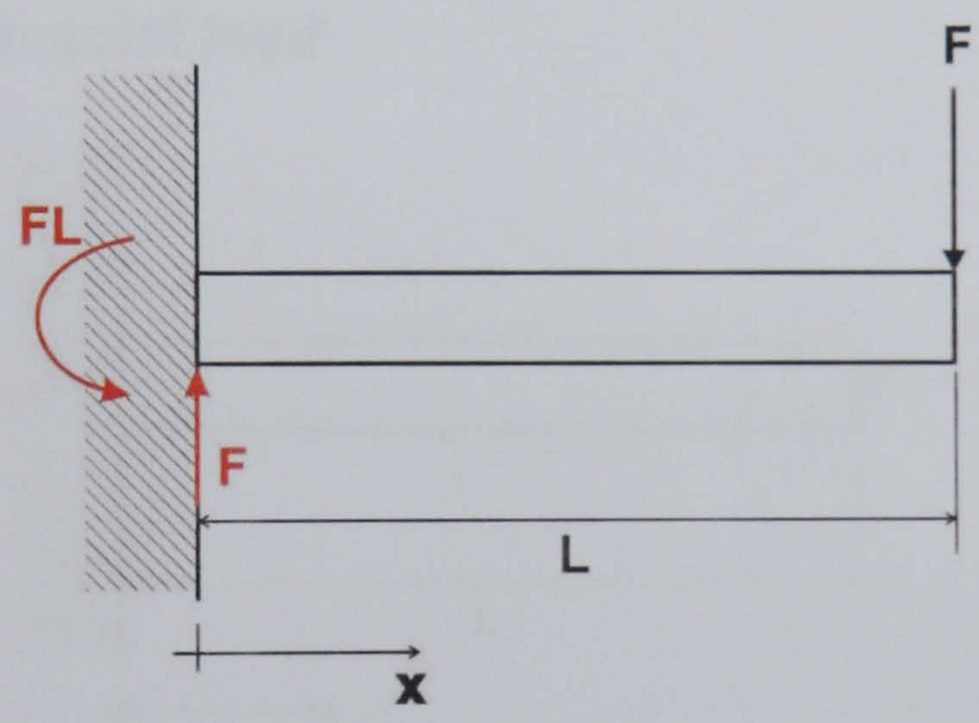

Figure 5.9 A cantilever with point end load

In Figure 5.9 the moment experienced at any point x along the cantilever is given by:

$$M(x) = FL - Fx \qquad (5\text{-}7)$$

substituting equation 5-7 into equation 5-6 gives:

$$U = \frac{F^2 L^3}{6EI} \qquad (5\text{-}8)$$

5.2.4.2 Energy due to Shearing

It can be shown that the energy stored due to a shear force, F can be given by [15, 16]:

$$U = \int_0^L \frac{CF^2}{2GA} dx \qquad (5\text{-}9)$$

where U is the energy stored, L is the length of the cantilever, G is the Shear modulus, A is the cross-sectional area and C is a constant that depends on the cross-sectional shape.

The shear stress correction factor, C, can be calculated from [16]:

$$C = \int_A \frac{S^2 A}{I^2 w^2} dA \qquad (5\text{-}10)$$

where S is the first moment of the area above the point where the shear stress is desired. This is taken about the principle axis which is perpendicular to the line of action of the force. A is the cross sectional area of the cantilever, I is the second moment of area and w is the width at the point where the shear stress is desired. For a rectangular cross-section $C = 1.2$ [15, 16].

Considering Figure 5.9 it can be seen that the shear stress in a cantilever with a point end load is equal to the end load. Hence for a rectangular cross section:

$$U = \frac{1.2F^2 L}{2AG} \qquad (5\text{-}11)$$

5.2.4.3 Energy due to axial load

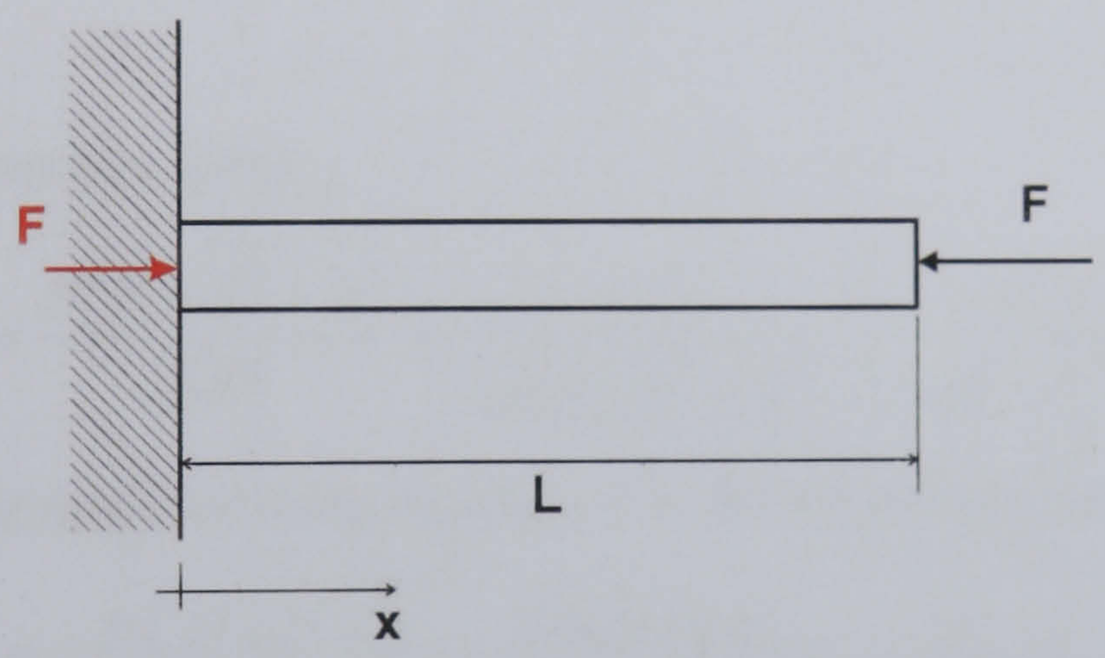

Figure 5.10 A cantilever subjected to an axial load

The energy stored per unit volume due to a normal stress is given by [12]:

$$U = \frac{\sigma^2}{2E} \qquad (5\text{-}12)$$

Therefore, the energy stored due to an axial load, F, can be given by:

$$U = \int_L \int_A \frac{F^2}{2EA^2} dA dx = \int_0^L \frac{F^2}{2AE} dx \qquad (5\text{-}13)$$

By considering Figure 5.10 it can be seen that the energy stored in a cantilever due to axial loading is given by [11]:

$$U = \frac{F^2 L}{2AE} \qquad (5\text{-}14)$$

where A is the cross sectional area, L is the length of the bar and E is the Young's modulus.

5.2.4.4 Deflection of inclined cantilever

Referring to Figure 5.8 and substituting appropriate values into equation 5-8, 5-11 and 5-14 it can be seen that the total energy stored, U_T, in the cantilever due to force P, is given by:

$$U_T = \frac{[P\cos(\theta)]^2\left[\sqrt{L^2+h^2}\right]^3}{6EI} + \frac{1.2[P\cos(\theta)]^2\sqrt{L^2+h^2}}{2AG} + \frac{[P\sin(\theta)]^2\sqrt{L^2+h^2}}{2AE} \quad (5\text{-}15)$$

substituting $\cos(\theta) = \frac{L}{\sqrt{L^2+h^2}}$ and $\sin(\theta) = \frac{h}{\sqrt{L^2+h^2}}$

$$U_T = \frac{P^2L^2\sqrt{L^2+h^2}}{6EI} + \frac{1.2P^2L^2}{2AG\sqrt{L^2+h^2}} + \frac{P^2h^2}{2AE\sqrt{L^2+h^2}} \quad (5\text{-}16)$$

If the force P show in Figure 5.8 causes a vertical deflection δ it can be shown this represents a total strain energy of [12]:

$$U = \frac{P\delta}{2} \quad (5\text{-}17)$$

equating the strain energies gives:

$$\frac{P\delta}{2} = \frac{P^2L^2\sqrt{L^2+h^2}}{6EI} + \frac{1.2P^2L^2}{2AG\sqrt{L^2+h^2}} + \frac{P^2h^2}{2AE\sqrt{L^2+h^2}} \quad (5\text{-}18)$$

Substituting for shear modulus using equation 5-5, the above equation simplifies to:

$$\delta = \frac{P}{E}\left(\frac{L^2\sqrt{L^2+h^2}}{3I} + \frac{2.4L^2(1+\upsilon)}{A\sqrt{L^2+h^2}} + \frac{h^2}{A\sqrt{L^2+h^2}}\right) \quad (5\text{-}19)$$

Assuming the cantilever has a rectangular cross-section, the above equation can be written in terms of thickness t' and width w.

t' is related to the measured (vertical) thickness t by $t' = t\cos(\theta)$ and therefore the cross-sectional area A, is given by:

$$A = wt' = wt\cos(\theta) = \frac{wtL}{\sqrt{L^2+h^2}} \quad (5\text{-}20)$$

Similarly the second moment of area can be found using equation 5-3 and is given by:

$$I = \frac{wt^3L^3}{12(L^2+h^2)^{3/2}} \quad (5\text{-}21)$$

substituting for I and A in equation 5-19 gives:

$$\delta = \frac{P}{E}\left(\frac{4\left(L^2+h^2\right)^2}{wt^3L}+\frac{2.4L^2(1+\upsilon)}{wtL}+\frac{h^2}{wtL}\right) \qquad (5\text{-}22)$$

where t is the cantilever vertical thickness, L is the horizontal length, w is the cantilever width, and h is the cantilever height at the tip (tip height).

5.2.5 Relative contribution of bending, axial load and shear in cantilever deflection

Equation 5-22 can be written over a common denominator such that

$$\delta = \frac{P}{E}\left(\frac{\left[4\left(L^2+h^2\right)^2\right]+\left\{2.4L^2t^2(1+\upsilon)\right\}+\left\langle h^2t^2\right\rangle}{wt^3L}\right) \qquad (5\text{-}23)$$

It is now possible to compare the relative importance of bending, axial-load and shear to deflection. The terms in the numerator in square brackets are proportional to the deflection due to bending, the terms in curly brackets are proportional to the deflection due to shear and the terms in triangular brackets are proportional to the deflection due to axial load.

Assuming a typical value for Poisson's ratio of $\upsilon = 0.312$ and by letting length, L, be defined relative to thickness, t, and tip height, h, such that:

$t = \frac{L}{a}$ and $h = \frac{L}{b}$ where a and b are >1

then the relative contributions of bending, axial load and shearing can be expressed as follows:

$$\partial_{bending} \propto \left[4L^4+8L^2h^2+4h^4\right] = \left[4+\frac{8}{b^2}+\frac{4}{b^4}\right]L^4$$

This coefficient is largest for a minimum value of b and is independent of a.

$$\delta_{shear} \propto \left\{2.4L^2t^2(1+\upsilon)\right\} = \left\{\frac{3.15}{a^2}\right\}L^4$$

This coefficient is largest for a minimum value of a and is independent of b.

$$\partial_{axial} \propto \left\langle h^2t^2\right\rangle = \left\langle\frac{1}{b^2a^2}\right\rangle L^4$$

This coefficient is largest for a minimum value of a and b.

For the cantilevers fabricated $a = 10 \ldots 70$ and $b = 1.7 \ldots 11.7$. Graphically the contributions of bending, axial load and shearing are shown in Figure 5.11. It can be seen that bending has the highest contribution to total deflection and axial load has the smallest.

The maximum contribution of shear and axial load to the cantilevers deflection, with respect to the contribution of bending, can be calculated as:

$$\left.\frac{\partial_{shear}}{\partial_{bending}}\right|_{a=\min,b=\max} = 0.00776 \quad \text{and} \quad \left.\frac{\partial_{axial-load}}{\partial_{bending}}\right|_{a=\min,b=\min} = 0.00048$$

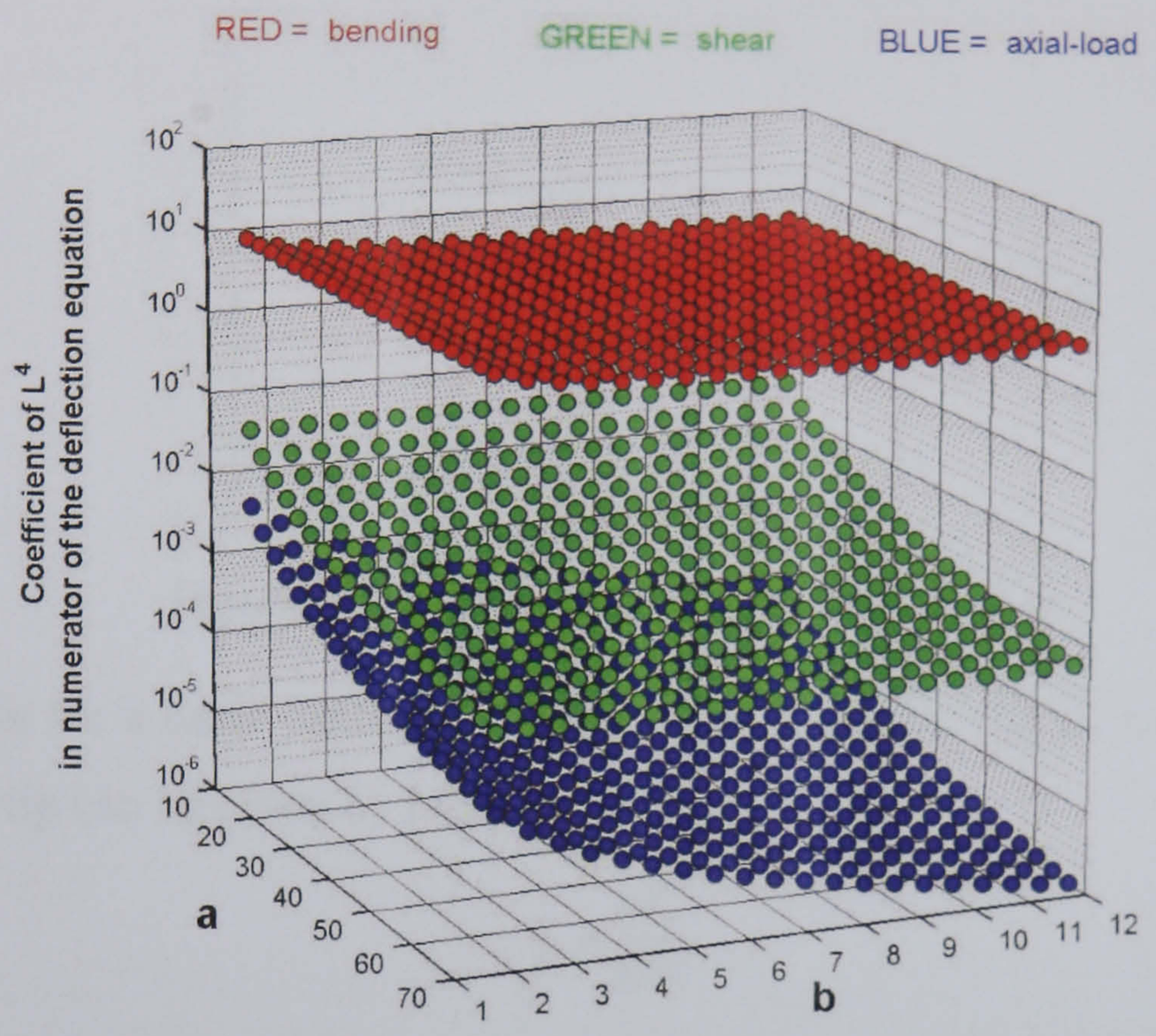

Figure 5.11 Relative contribution of bending, axial-load and shear to deflection of a cantilever

Since it is reasonable to neglect shear and axial-loading effects, equation 5-23 can be simplified to:

$$\delta = \frac{4P\left(L^2 + h^2\right)^2}{Ewt^3 L} \qquad (5\text{-}24)$$

5.2.6 Deflection of wide cantilevers

A cantilever is considered wide if its width is much greater than its thickness such that deflections are constrained by lateral stresses [17]. Wide cantilevers are treated as plane strain problems, that is to say lateral stresses exist during bending but the lateral strain is zero.

It can be shown that the vertical deflection, δ, due to pure bending of a cantilever such as that shown in Figure 5.6 is given by [17]:

$$\delta = \frac{PL^3(1-\upsilon^2)}{3EI} \qquad (5\text{-}25)$$

Therefore a wide cantilever behaves more stiffly than is predicted by the simple theory. The term $E/(1-\upsilon^2)$ is referred to as the plate modulus.

5.2.7 Cantilever deflection due to self weight

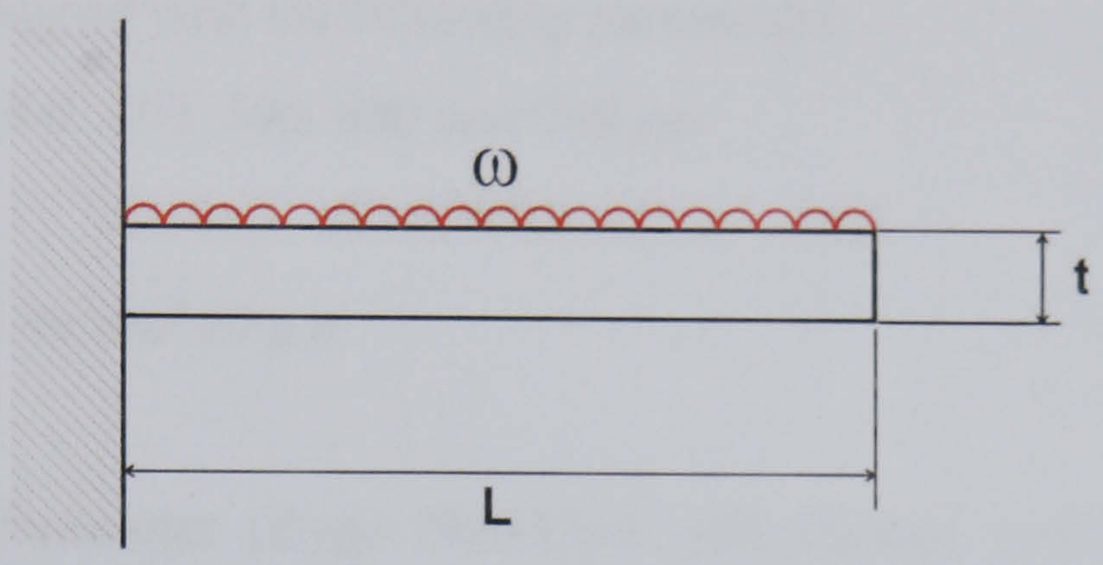

Figure 5.12 Cantilever with uniform load

It can be shown for a basic cantilever, such as that shown in Figure 5.12, that the vertical deflection at the tip can be given by [12]:

$$\delta = \frac{\omega L^4}{8EI} \qquad (5\text{-}26)$$

where ω is the uniform load in N/m, L is the cantilever length, E is the Young's modulus and I is the second moment of area. Assuming a rectangular cross section and substituting for I using equation 5-3 then:

$$\delta = \frac{3\omega L^4}{2EAt^2} \qquad (5\text{-}27)$$

If the cantilever is made from a material with density ρ, the mass of the cantilever can be calculated as:

$$m = \rho V = \rho AL \qquad (5\text{-}28)$$

Therefore the uniform force/unit length acting on the cantilever ω is given by:

$$\omega = \frac{mg}{L} = \rho Ag \qquad (5\text{-}29)$$

substituting this into equation 5-27 gives:

$$\delta = \frac{3\rho gL^4}{2Et^2} \qquad (5\text{-}30)$$

Consider a cantilever with length, $L = 700\ \mu m$ thickness $t = 10\ \mu m$ and made from nickel with a density $\rho = 8908\ kg/m^3$ and $E = 100\ GPa$ then the deflection at the tip, $\delta = 3.1\ nm$. Therefore the deflection due to self weight can be neglected in the cantilevers.

5.3 Results

5.3.1 Cantilever geometry used in models

Cantilevers were designed with the following parameters:

- $L = 100, 200, 300, 400, 500, 600$ and $700\ \mu m$
- $h = 60\ \mu m$
- $w = 10, 20, 30, 40$ and $50\ \mu m$
- $t = 10\ \mu m$.

A white light interferometer (Zygo NewView 100 Optical profilometer) was used to measure the dimensions of the fabricated cantilevers. Measurements were taken before the cantilevers were released since the presence of the sacrificial copper layer allowed the thickness of the cantilevers at any point to be measured. This can clearly be seen in Figure 5.13 and Figure 5.14.

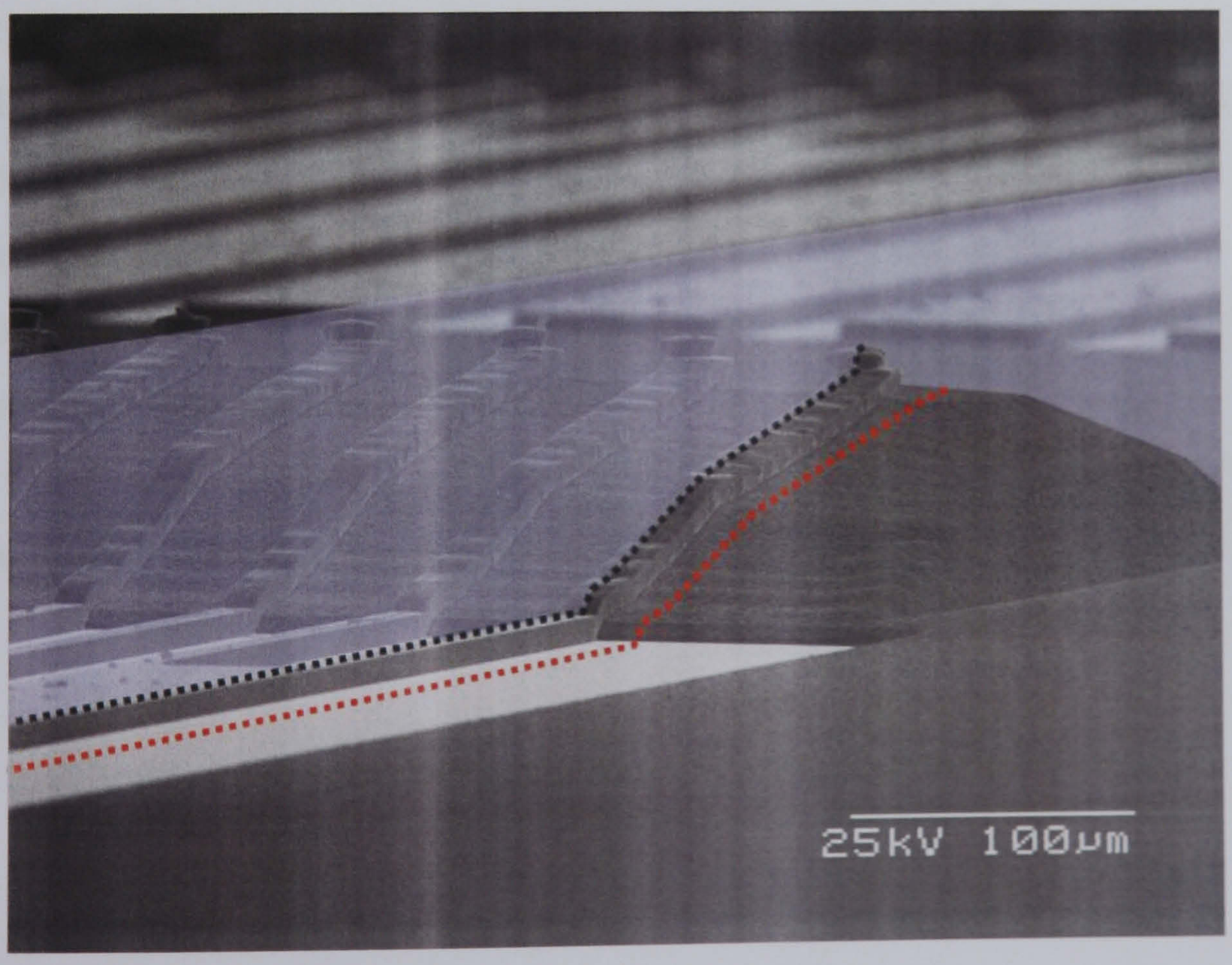

Figure 5.13 Micrograph showing unreleased cantilevers. The two dotted lines show where height data were taken

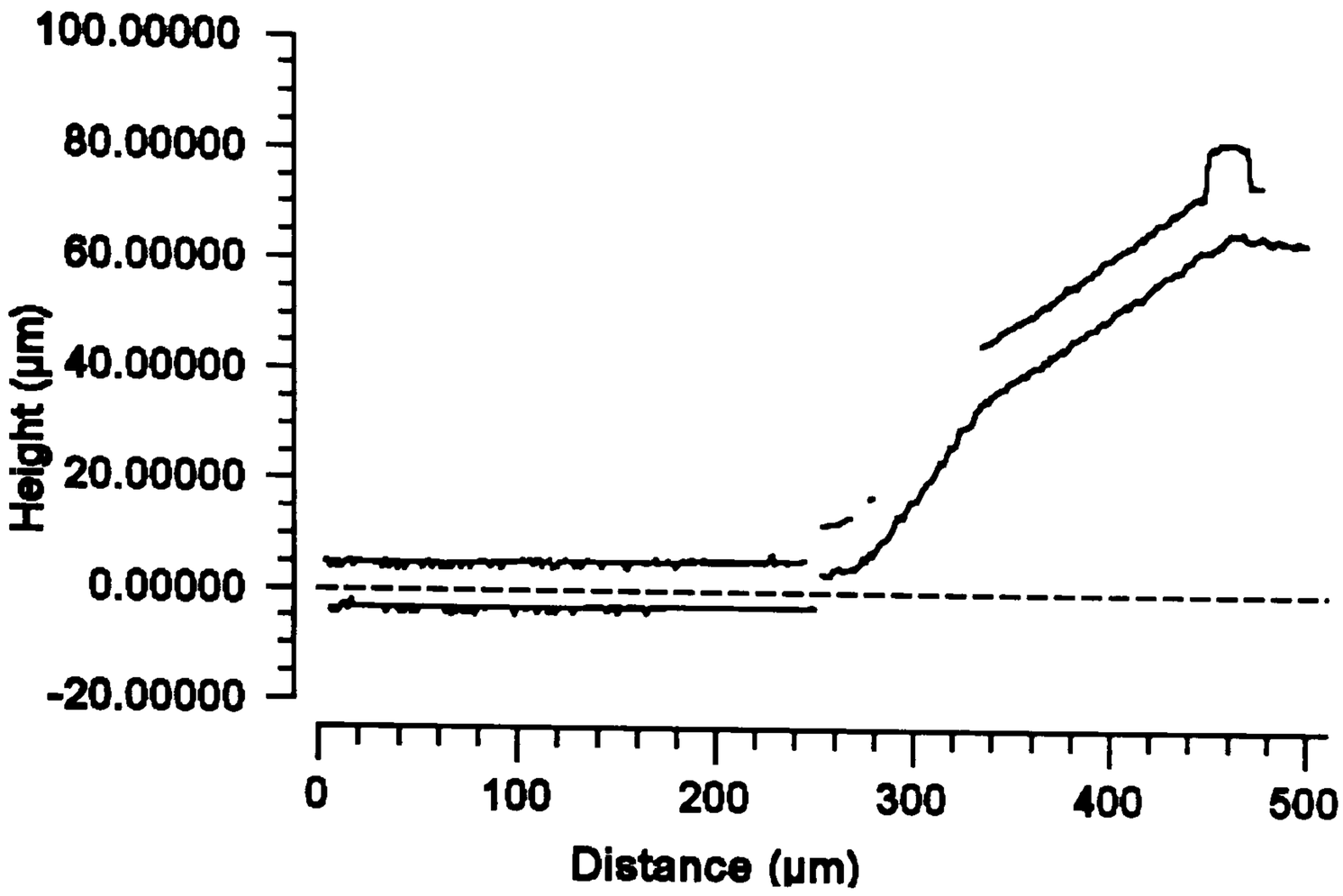

Figure 5.14 Profiles data measured using Zygo Optical profiler

Because measurements were taken before releasing the cantilevers it was important to consider any effects that might cause distortion when the cantilevers were released. One such consideration was the presence of stresses in the electrodeposited nickel.

The effect of any net residual stress in the electroplated nickel could be neglected since the change in geometry of the released cantilever would be negligible. For instance if there was an internal stress of 500 MPa in a 700 µm long cantilever, using the value for Young's modulus measured in section 5.1 this corresponds to a change of length of just 5.1 µm. However the effect of a residual stress gradient could be much greater causing the cantilever to curl up or down.

Therefore the cantilever tip heights were re-measured after the cantilevers had been released. By doing this, it was found that the electroplated nickel had a residual stress gradient that caused the cantilevers to curl down.

It can be shown for a horizontal cantilever of length L, where the tip deflects by an amount δ there was, prior to release, a linear strain gradient Γ given by [18, 19]:

$$\Gamma = \frac{2\delta}{L^2} \qquad (5\text{-}31)$$

Through simple trigonometry it can be shown that if the cantilever is inclined, with a horizontal length L and tip height h and undergoes a vertical tip deflects δ then the strain gradient can be calculated by modifying equation 5-31 such that:

$$\Gamma = \frac{2\delta}{L\sqrt{L^2 + h^2}} \qquad (5\text{-}32)$$

Using equation 5-32 the pre-release strain gradient was determined to be -6.8 x 10^{-5} (μm^{-1}). Using the value of Young's modulus calculated in section 5.1, this corresponds to a stress gradient of 4.7 MPa/μm. It should be noted that the cantilever curling relieves the residual stress, however this would not be true if the cantilever was made from more than one material [19]. More detailed calculations are in appendix 5-1.

In the following text, for simplicity cantilevers will be referred to using their "designed" dimensions rather than the measured dimensions. However where calculations are made the measured values will be used.

All relevant dimensions of the cantilevers are given in appendix 5-1.

5.3.2 Test results

Cantilevers were tested using the rig and procedures described in chapter 4. A force-deflection data set was collected as cantilevers were loaded (deflected) and unloaded. The first loading cycle of a cantilever will be referred to as "loading" whilst the first unloading will be referred to as "unloading". Subsequent loading cycles will be referred to as "reloading".

Each "loading" (or "reloading") was performed until the cantilever tip hit the substrate (approximately 60 μm from first contact between the test tip and cantilever tip). Loading was applied in 1 μm steps. 5 balance readings were taken in each step and a 3 s pause was used between steps to allow the readings of the instruments to stabilise. Typical load-deflection curves for three different geometries of cantilever are shown in Figure 5.15. Several cantilevers (at least 3) of the same geometry were tested in order to obtain more accurate results. Only "loading" results were used in calculations as these represent the cantilever behaviour before any plastic deformation had occurred. "Unloading" and "reloading" experiments were performed to experimentally verify that non-linear responses were due to plastic deformation and not higher order effects.

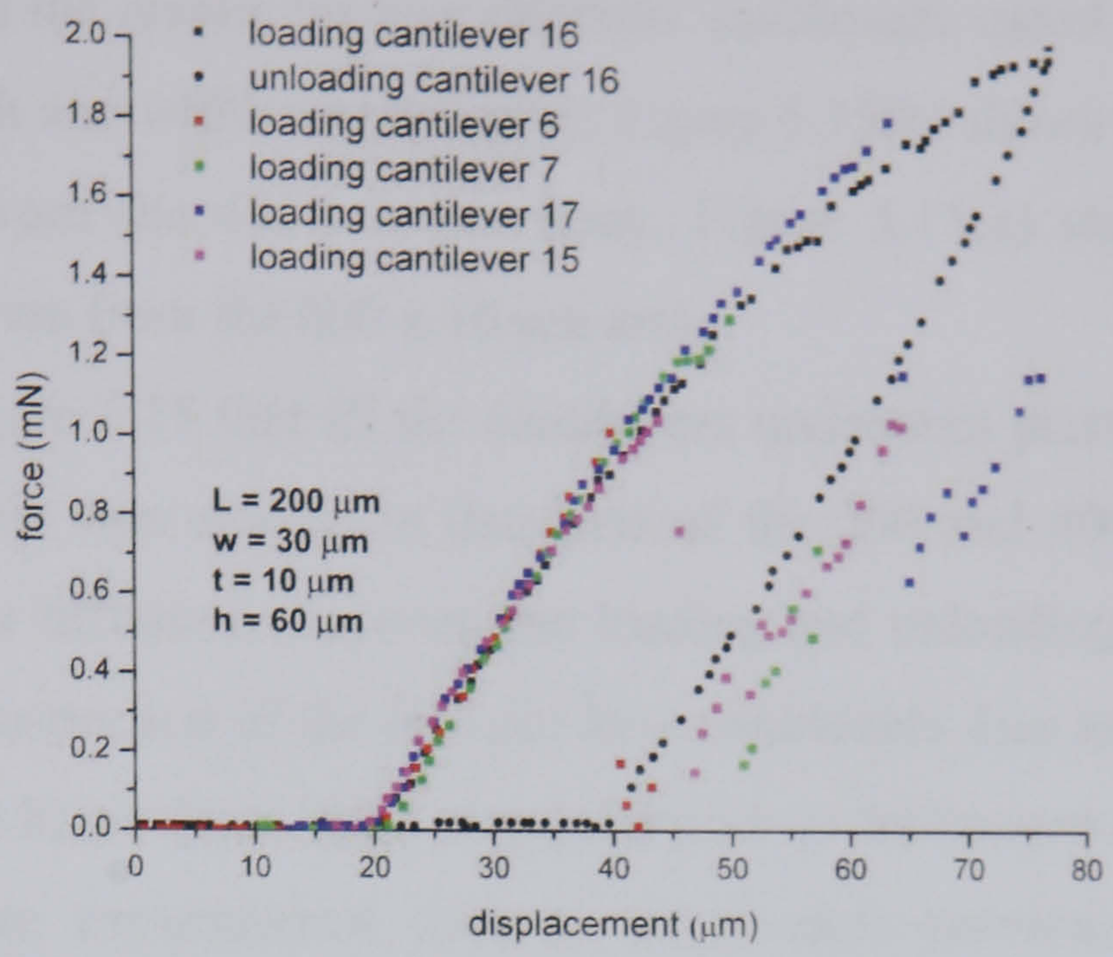

(a)

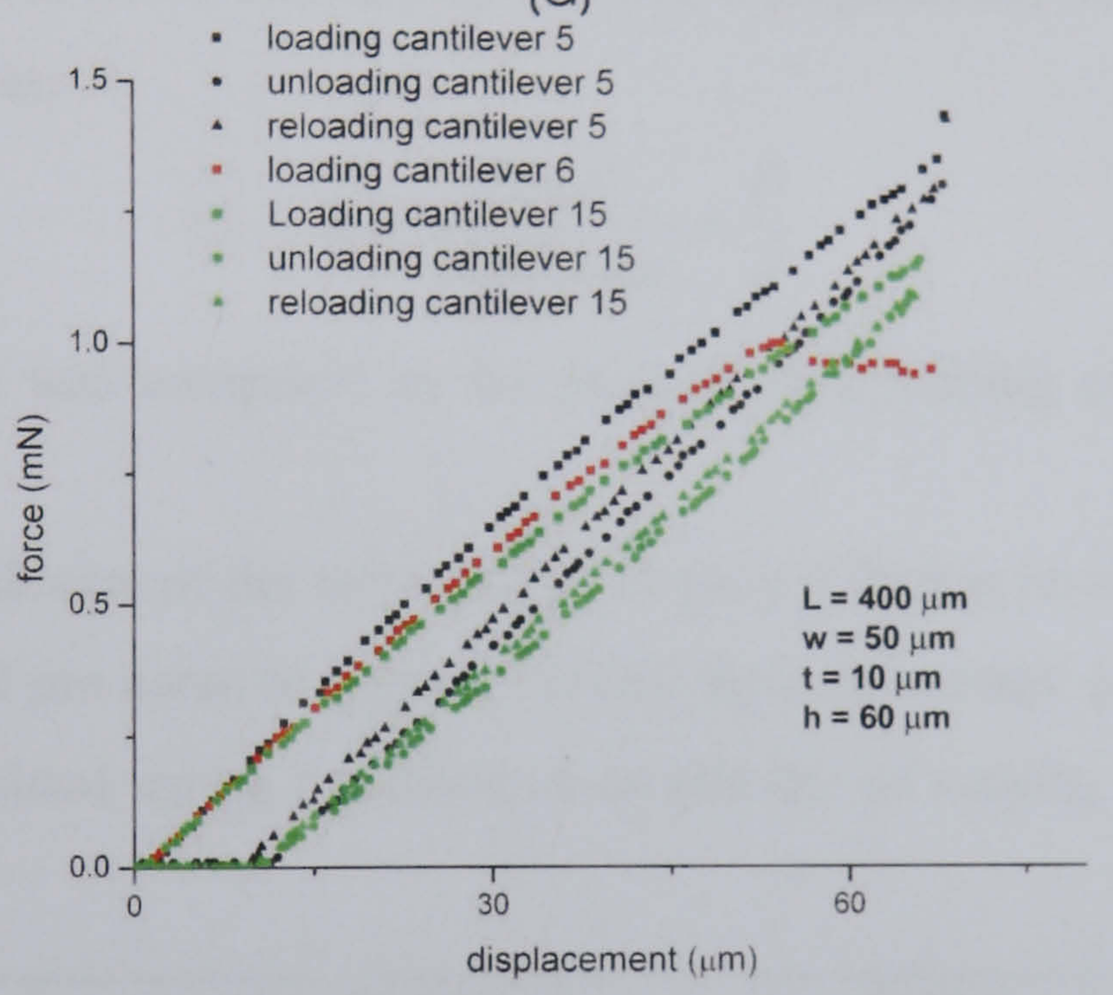

(b)

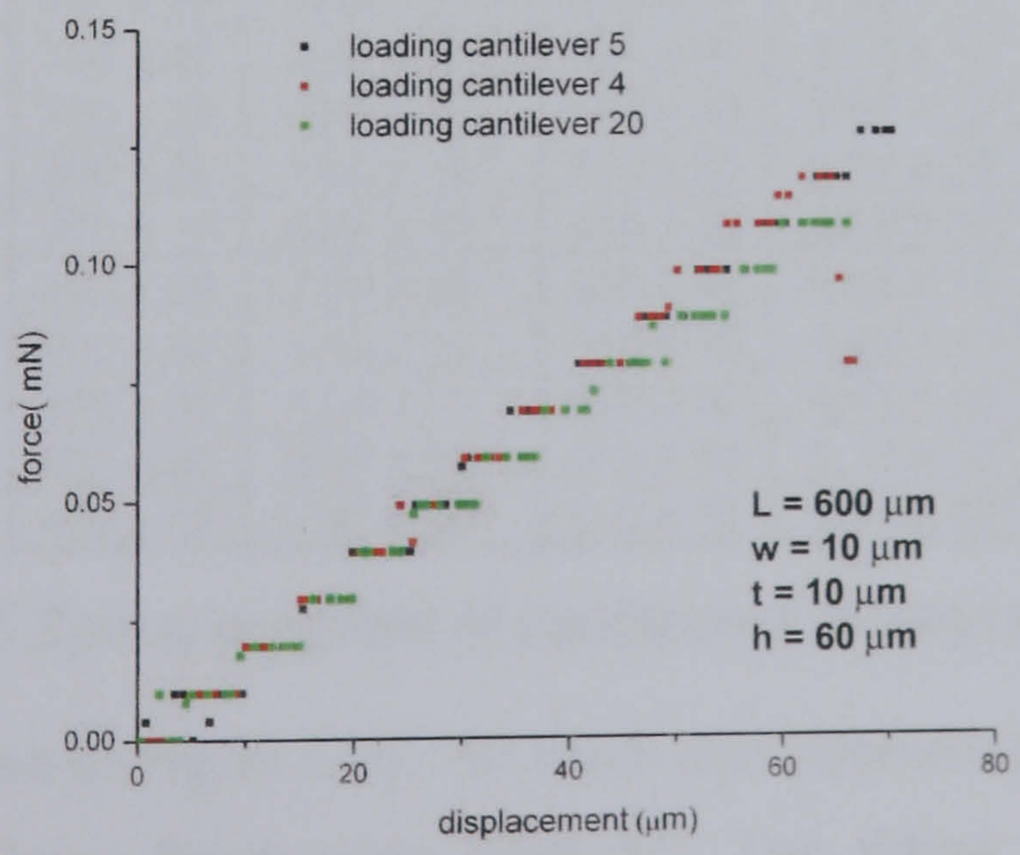

(C)

Figure 5.15 Typical load deflection behaviours

Figure 5.15(a) shows the results for four different cantilevers tested from the 200 x 30 μm array (horizontal length and width respectively). Figure 5.15(b) shows the behaviour of three different cantilevers from the 400 x 50 μm array. Figure 5.15(c) shows the behaviour of three different cantilevers from the 600 x 10 μm array.

It can be seen in Figure 5.15 that all the cantilevers underwent plastic deformation during the loading cycles. This was evident in data sets of the 200 and 400 μm long cantilevers since there was a clear difference between the loading and unloading (or reloading) traces. Additionally, careful inspection of the 600 μm long cantilevers data sets showed there was a slight deviation from a linear force-deflection behaviour at deflections above 50 μm.

In order to compare experimental data to the models previously developed, spring constants were calculated (from the loading data) for each geometry of cantilever. The spring constant, k, is defined as:

$$k = \frac{Load}{deflection} = \frac{P}{\delta} \qquad (5\text{-}33)$$

Experimentally, this was computed as the gradient of a loading curve during the initial linear region.

When different cantilevers of the same geometry gave differing results (as displayed in the results of the 400 x 50 μm array in Figure 5.15(b)) then an average gradient was used. The experimentally determined spring constants of cantilevers of varying geometries are shown in Table 5.5.

Probe	Spring constant (mN/μm)	Probe	Spring constant (mN/μm)	Probe	Spring constant (mN/μm)	Probe	Spring constant (mN/μm)
100 x 50	4.37×10^{-1}	300 x 50	4.49×10^{-2}	500 x 50	1.50×10^{-2}	700 x 50	5.02×10^{-3}
100 x 40	2.72×10^{-1}	300 x 40	3.46×10^{-2}	500 x 40	9.14×10^{-3}	700 x 40	3.90×10^{-3}
100 x 30	1.88×10^{-1}	300 x 30	2.39×10^{-2}	500 x 30	5.60×10^{-3}	700 x 30	2.77×10^{-3}
100 x 20	9.17×10^{-2}	300 x 20	1.60×10^{-2}	500 x 20	4.04×10^{-3}	700 x 20	2.26×10^{-3}
100 x 10	4.66×10^{-2}	300 x 10	9.28×10^{-3}	500 x 10	2.80×10^{-3}	700 x 10	1.34×10^{-3}
200 x 50	1.17×10^{-1}	400 x 50	2.21×10^{-2}	600 x 50	6.12×10^{-3}		
200 x 40	8.27×10^{-2}	400 x 40	1.48×10^{-2}	600 x 40	4.82×10^{-3}		
200 x 30	5.18×10^{-2}	400 x 30	1.04×10^{-2}	600 x 30	4.01×10^{-3}		
200 x 20	3.53×10^{-2}	400 x 20	6.94×10^{-3}	600 x 20	3.14×10^{-3}		
200 x 10	2.10×10^{-2}	400 x 10	4.60×10^{-3}	600 x 10	1.89×10^{-3}		

Table 5.5 Spring constant of cantilevers of varying geometry

These results are shown in Figure 5.16. The black dots represent the measured data through which a surface has been fitted using MatLab®. The fitting was achieved using the "griddata" command with a "v4" algorithm which is based on biharmonic spline interpolation.

As can be seen in Figure 5.16 the data forms a coherent set with no obviously erroneous results.

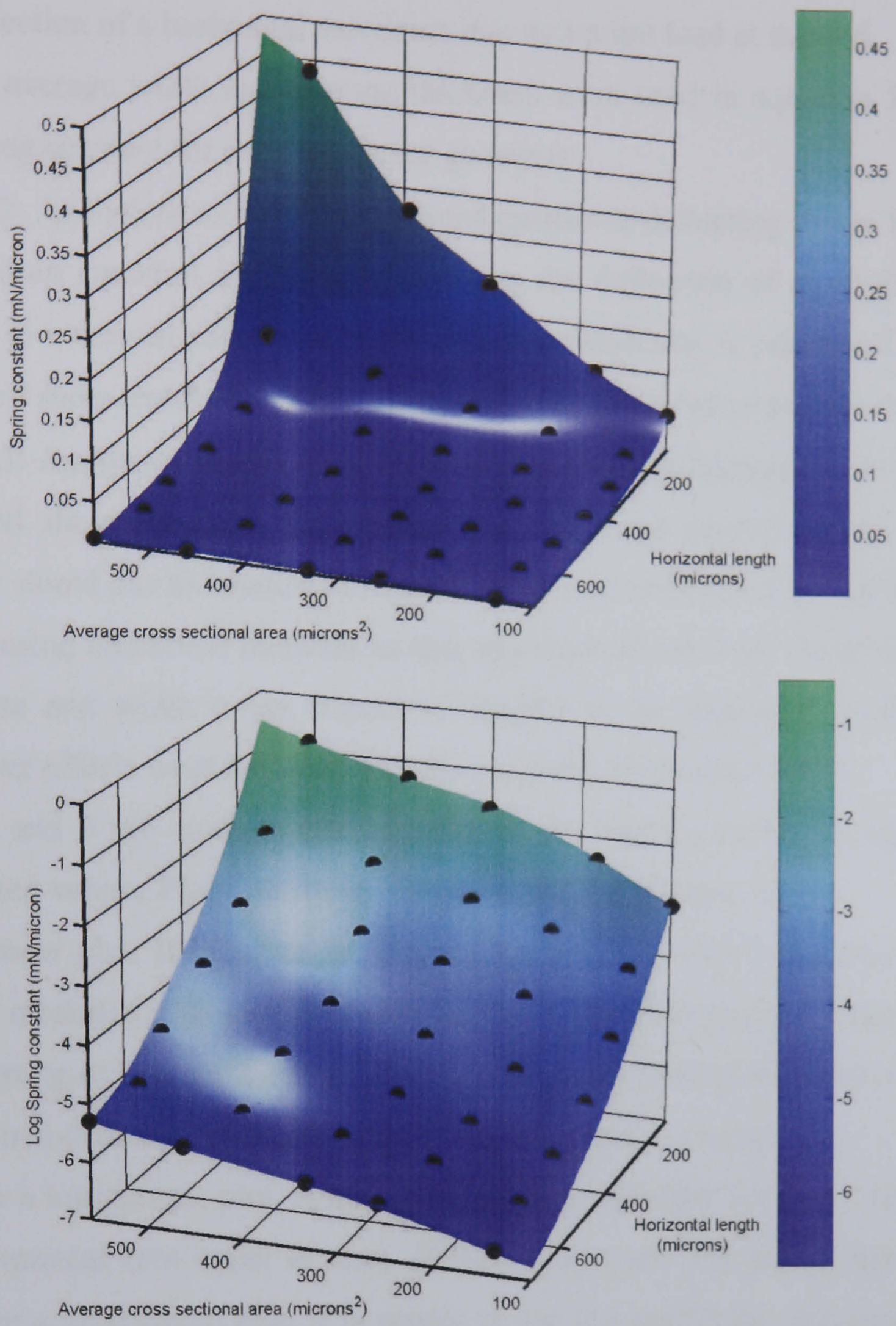

Figure 5.16 Measured spring constants of cantilevers as a function of geometry

5.3.3 Comparison of results and models

The experimental data set shown in Table 5.5 was compared to the various models developed in section 5.2. The models were used to calculate theoretical values of spring constants and these were compared with the measured values. Young's modulus was taken as 69.1 GPa which was obtained from the tension testing described in section 5.1. The Poisson's ratio was be taken as 0.312 which is the same as bulk nickel.

In the following sections three different models will be discussed:

- Model 1: Basic horizontal cantilever – This is based on equation 5-2 which describes the deflection of a horizontal cantilever due to a point load at the end. The horizontal length, average width and average thickness were used in equation 5-2 to estimate the spring constant for each cantilever geometry.
- Model 2: Analytical model of an inclined cantilever deflecting due to bending – This is based on equation 5-24 which describes the deflection of an inclined cantilever subject to a vertical point load at the end. The deflection is calculated neglecting the effects of shear and axial loading. The cantilever is treated as a plane stress problem.
- Model 3: Analytical model of an inclined cantilever deflecting due to bending, axial load and shear forces. – This model was based on equations 5-6, 5-9 and 5-13 (energy stored due to bending, shear and axial load respectively). The equations were solved using numerical methods as this approach allowed the variation in cantilever thickness and width (with respect to length) to be modelled. Additionally wide cantilever effects were included. Details are given in section 5.3.3.3.

Models 1, 2 and 3 are compared to experiment by plotting measured spring constants against calculated values. Plots are shown on linear and logarithmic scales.

Consider a linear plot. If the data set forms a linear trend with a gradient of 1 then this shows that the modelled and measured data agree. A different gradient suggests that either the model is wrong or that the value of Young's modulus used is not correct. A non-linear relationship or non-zero origin would suggest that the model is wrong.

Now consider a logarithmic plot. A non unity value for gradient implies a need to raise the model to an exponent (not equal to one). If this is the case, the model has to be wrong. Therefore, using a logarithmic plot, it is simple to see if a model fits that experimental data well. The effect of using an incorrect Young's modulus in the models would be to change the offset of the plot in the logarithmic domain.

5.3.3.1 Model 1 – horizontal cantilever

The comparison between calculated and measured values for model 1 is given in Figure 5.17.

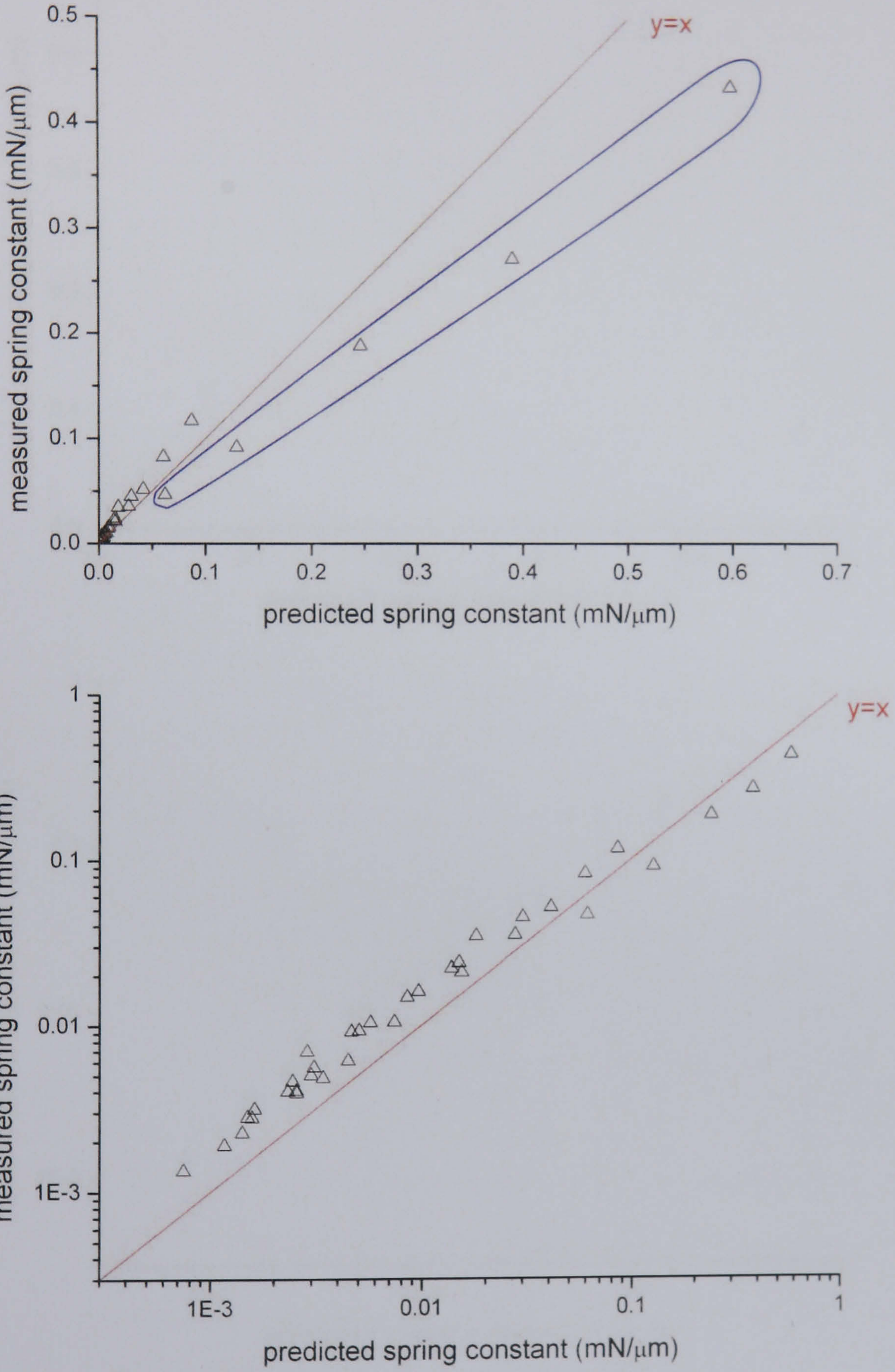

Figure 5.17 Measured spring constant vs. model 1

5.3.3.2 Model 2 – Inclined cantilever bending only

The comparison between calculated and measured values for model 2 is given in Figure 5.18.

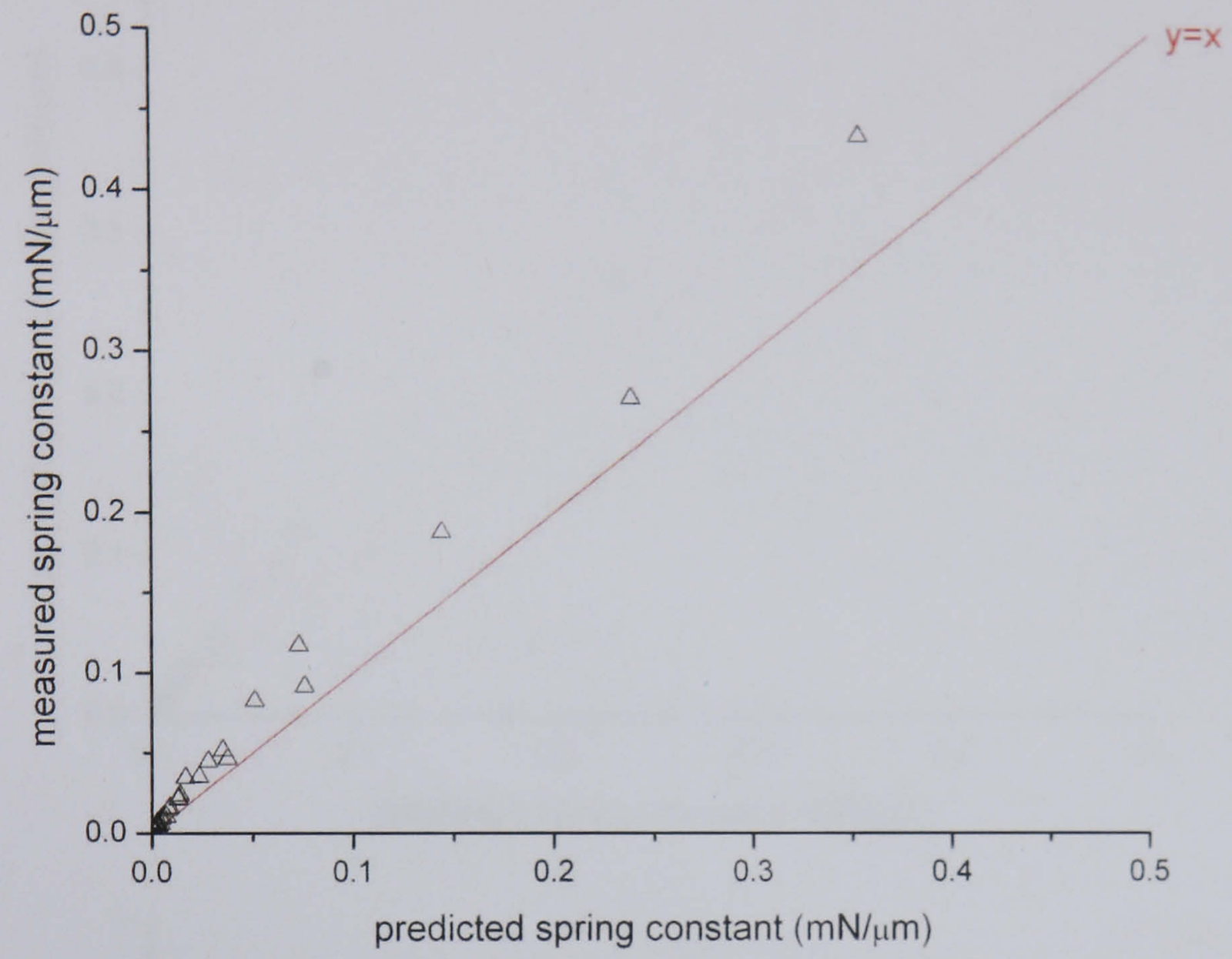

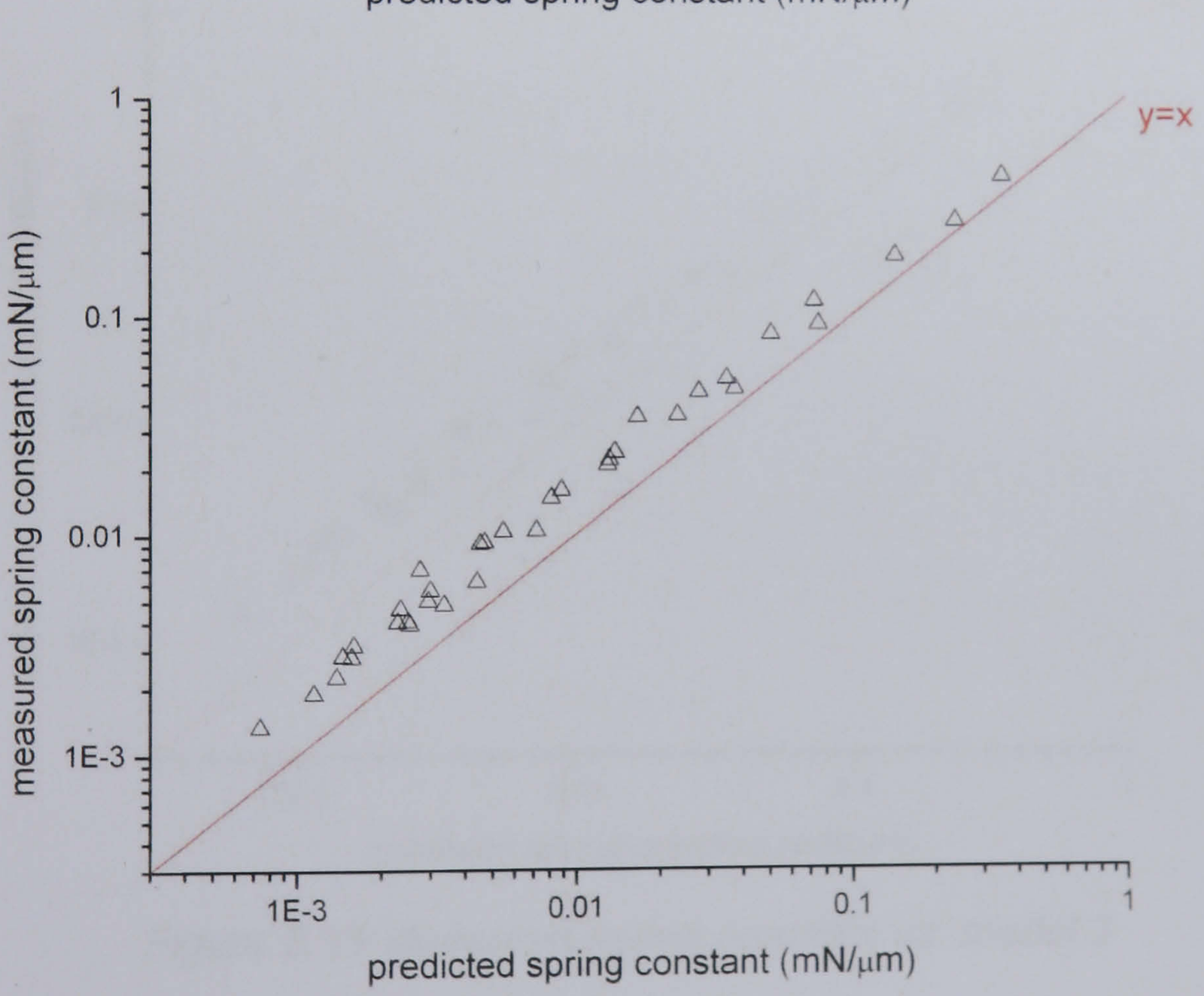

Figure 5.18 Measured spring constant vs. model 2

5.3.3.3 Model 3 – Full analytical model

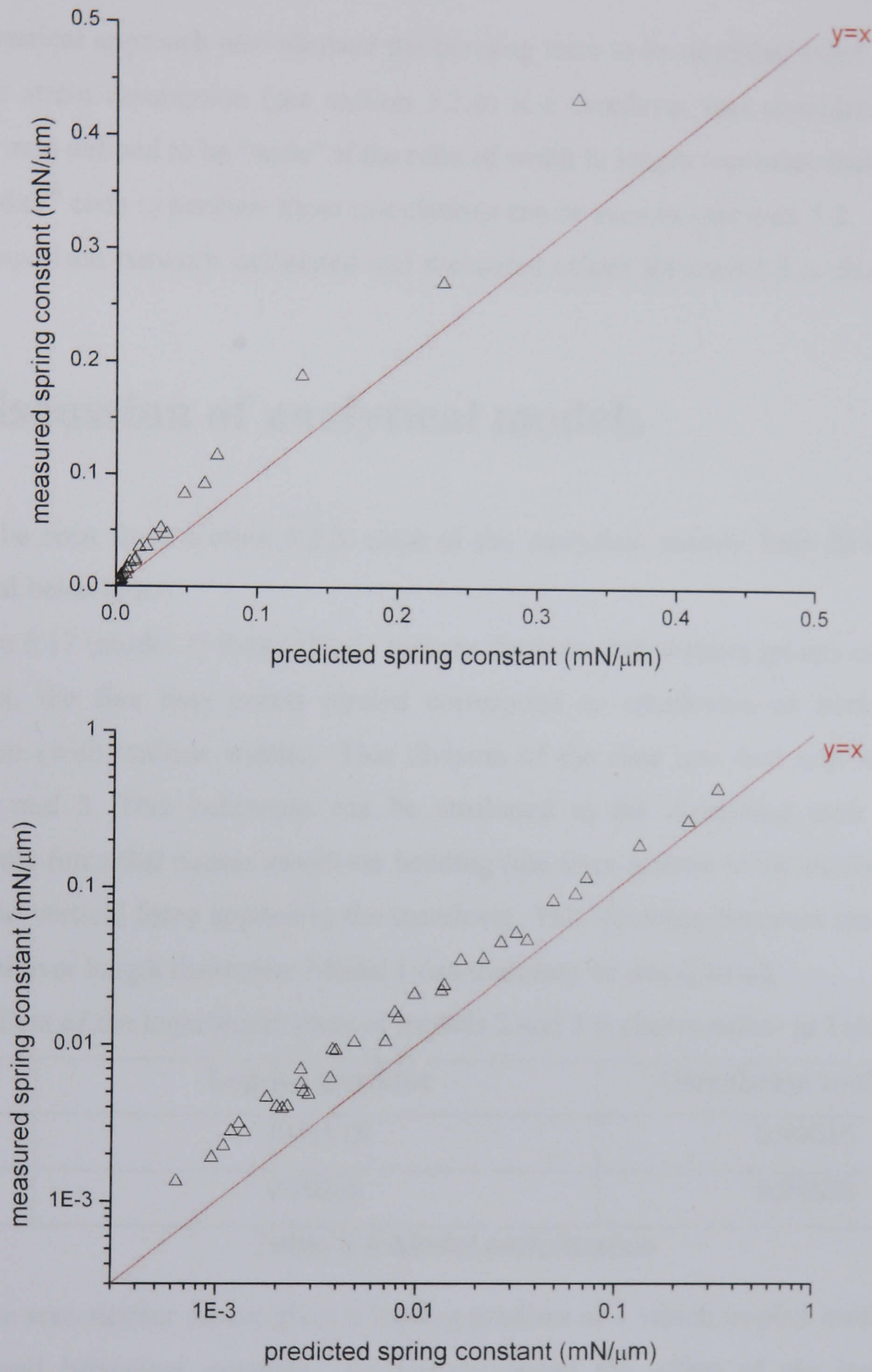

Figure 5.19 Measured spring constant vs. model 3

Functions were written in Matlab® that evaluated equations 5-6, 5-9 and 5-13 by using the trapezoidal method of numerical integration. The total strain energy of the system was calculated, from which a value for spring constant was determined.

Varying cantilever width and thickness were included in the model by representing them as functions of length inside the integral. Appropriate functions were achieved by fitting a first

order polynomial for thickness (using values measured at the root and end of the cantilever) and a second order polynomial for width (using values measured at the root, middle and end of the cantilever).

The numerical approach also allowed the bending term to be modified from a plane stress to a plane strain assumption (see section 5.2.6) if a cantilever was considered "wide". A cantilever was defined to be "wide" if the ratio of width to length was more than 10%.

The Matlab® code to perform these calculations can be seen in appendix 5-2.

The comparison between calculated and measured values for model 3 is shown in Figure 5.19.

5.4 Discussion of analytical models

As can be seen from section 5.3.3, none of the analytical models fully fit the measured mechanical behaviour.

In Figure 5.17 (model 1) it can clearly be seen there are two distinct groups of data. On the linear plot, the five data points circled correspond to cantilevers of horizontal length L = 100 μm (with various widths). This division of the data into two sets is not seen in models 2 and 3. This behaviour can be attributed to the increasing error incurred by assuming the force that causes cantilever bending (the force normal to the cantilever) was the same as the vertical force applied to the cantilever. This assertion becomes more inaccurate as the cantilever length decreases. Model 1 can therefore be disregarded.

The gradient of the logarithmic plots of models 2 and 3 is shown below in Table 5.6.

Model	Log-log gradient	Correlation coefficient
2	0.93118	0.99615
3	0.90881	0.99623

Table 5.6 Model performance

As can be seen neither model gives a log-log gradient of 1 which implies neither model fit the measured behaviour correctly. As already stated the offset of the log-log plot is dependent on the value of Young's modulus chosen in the model. Therefore it is reasonable to translate the data vertically to get a stronger correlation between experimental and modelled data (y = x) since this equates to using a different estimate of Young's modulus. If this translation were performed, and since both log-log gradients are less than unity, it can be

seen this implies that the models (relatively) over-predict stiffness for short wide cantilevers and (relatively) under-predict stiffness for long thin cantilevers.

In the linear domain it can be seen that the experimental data show a gradient greater than unity for both model 2 and 3. This indicates that the value of Young's modulus used in the models might be different from the actual properties of the nickel used to fabricate the cantilevers. Since the exact value of Young's modulus used is uncertain it is possible that both models 2 and 3 correctly predict the behaviour of long thin cantilevers and greatly over predict the stiffness of short cantilevers (by substituting a higher Young's modulus into the models and changing the offset of the data in the linear domain, see introduction to section 5.3.3). By comparison with Finite element models, it will be shown in the next section that models 2 and 3 work well for the long thin cantilevers (if the right value for Young's modulus is chosen). However, they over-predict the stiffness of shorter cantilevers.

5.5 Finite element modelling

5.5.1 Comparison between FE and analytical models

Model 3 described in section 5.3.3.3 was compared to results from Finite element analysis (FEA) simulated using FEMLAB 3.1. The solver used was based on the equilibrium of global stresses and was linear. Large deflection effects were not modelled and the material was assumed to be isotropic. Three dimensional models were created to represent inclined cantilevers (such as that shown in Figure 5.20) and were meshed in an unstructured way using tetrahedral elements.

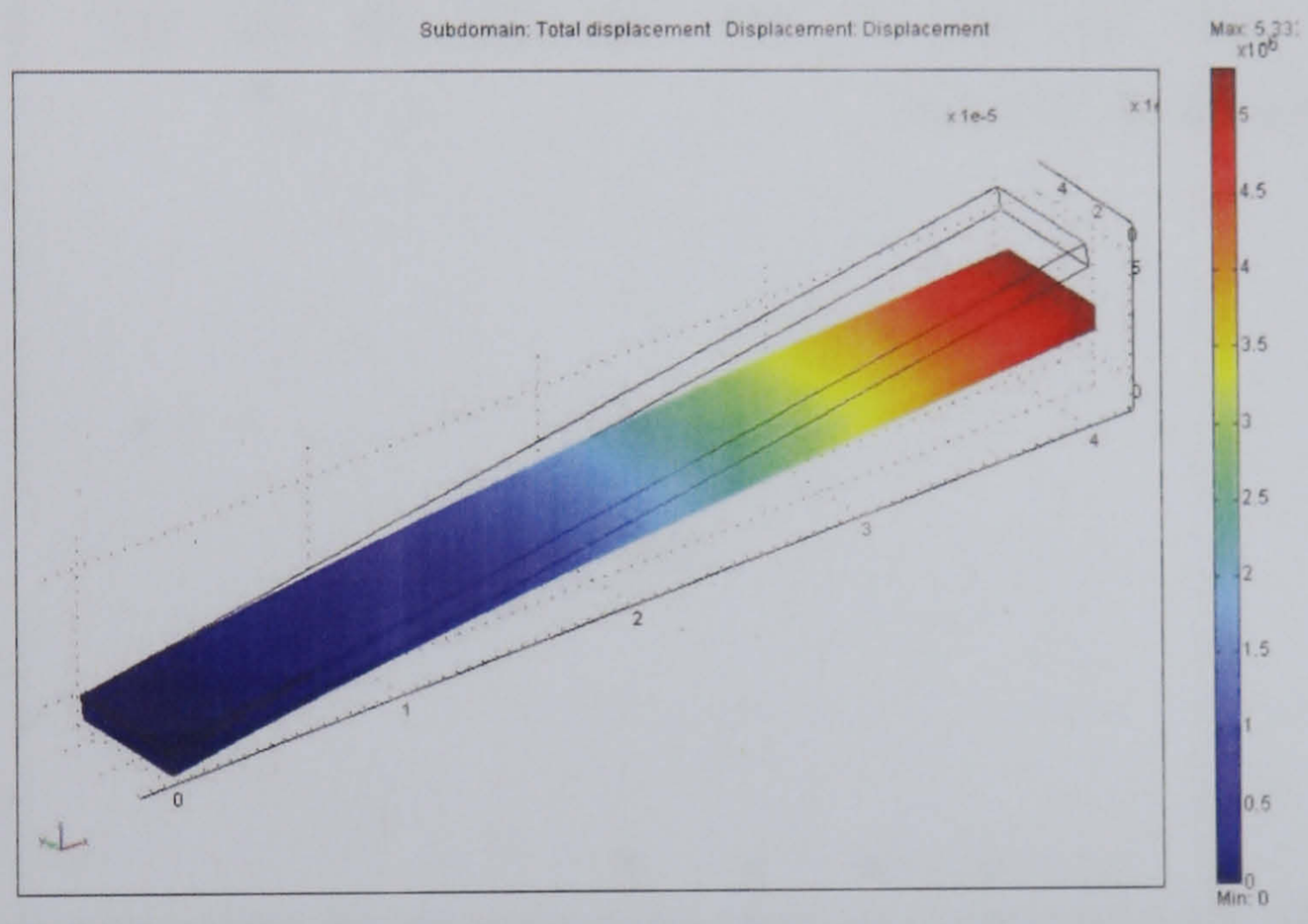

Figure 5.20 FEA model of simple inclined cantilever

Using FEMLAB, a force was applied to the end of the cantilever (defined as a force per length along an appropriate edge) and corresponding displacements simulated. From this, a spring constant was calculated and compared to results calculated using model 3

The following geometric values were used in both the FEA models and analytical calculations:

$L = 100, 200 \ldots 1000\ \mu m$

$w = 50\ \mu m$

$t = 10\ \mu m$

$h = 60\ \mu m$

$E = 100\ GPa$

$\upsilon = 0.312.$

Two versions of model 3 were used. One was the model as described in section 5.3.3.3, the other was the same except it did not include wide effects (i.e. the model was fixed as a plane stress model regardless of width to length ratio). These two versions of model 3 will be referred to as model 3a and model 3b respectively to avoid confusion with earlier nomenclature.

The comparison of analytical and FEA results can be seen in Figure 5.21.

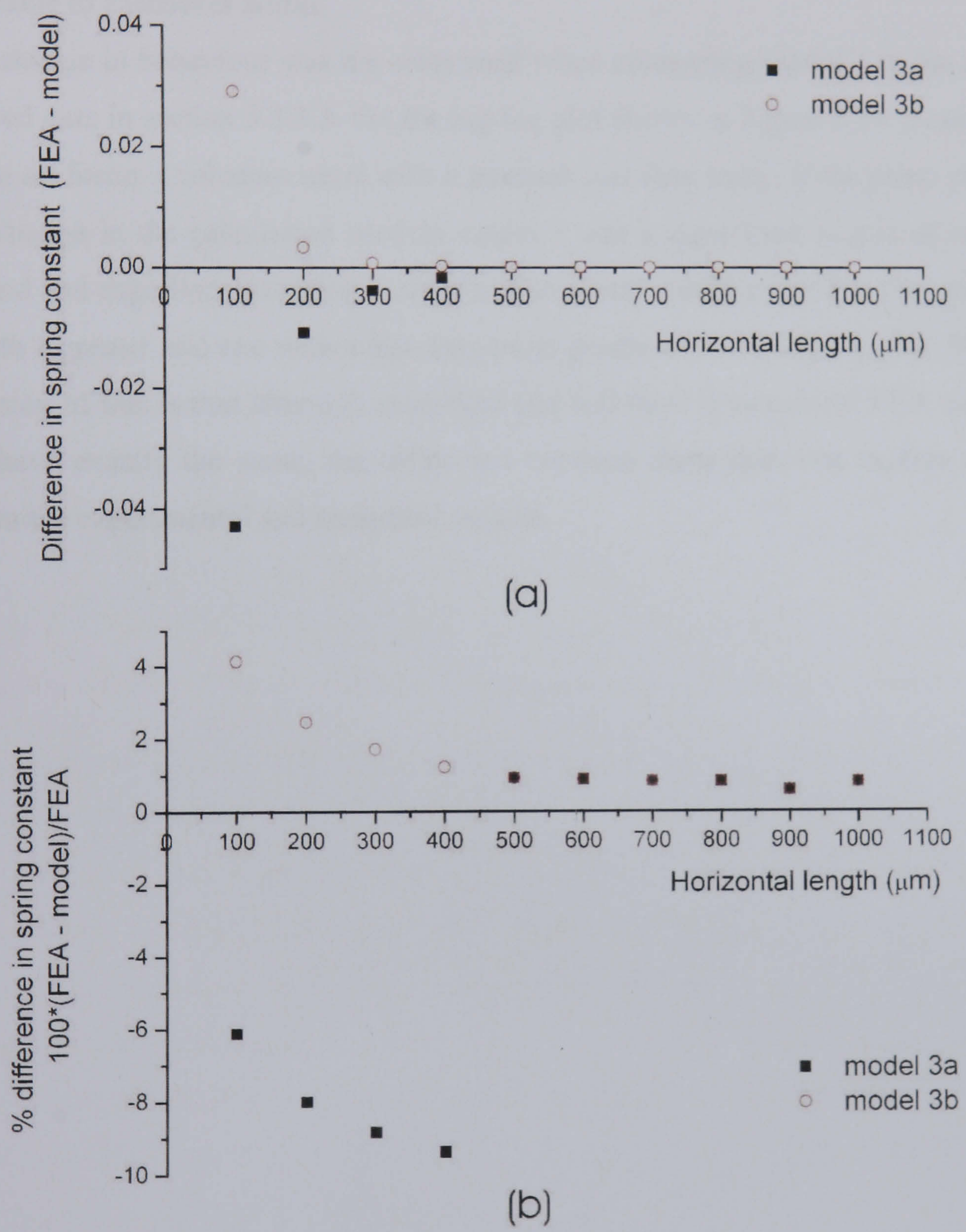

Figure 5.21 Comparison between spring constants predicted by FEA and analytical model simulation (a) Absolute difference (b) Percentage difference relative to FEA results

Figure 5.21 shows that model 3a and 3b are in reasonable agreement with FEA results for the long cantilevers; however neither model correctly predicts the behaviour of the shorter cantilevers.

Figure 5.21 shows model 3b (plane stress, no wide effects) underestimates and model 3a (plane strain, wide effects) overestimates the stiffness of cantilevers when compared to FEA. The effect is most pronounced for shorter cantilevers where horizontal length becomes comparable to cantilever width.

This change in behaviour was not witnessed when comparing model 3 to the experimental measured data in section 5.3.3.3. On the log-log plot shown in Figure 5.19 it can be seen that the data set forms a coherent trend with a gradient less than unity. If the plane stress to plane strain change in the calculation used in model 3 was a significant source of error between modelled and experimental spring constants, this would manifest itself as two groups of data, one with a greater and one with a less than unity gradient on the log-log plot. The important conclusion of this is that although analytical and full three dimensional FEA simulations do not behave exactly the same, the difference between them does not explain the variation between the experimental and analytical models.

5.5.2 Geometrically exact FEA

It has been shown that the simplification of the physical situation to a plane stress or strain approximation cannot explain the difference between experimental and analytically modelled behaviour. Therefore it is reasonable to investigate if the simplification of the geometry to an inclined cantilever (such as that shown in Figure 5.20) could be the source of the error. In order to see if this was the case, geometrically exact models of w = 50 μm cantilevers were constructed and analysed using FEA.

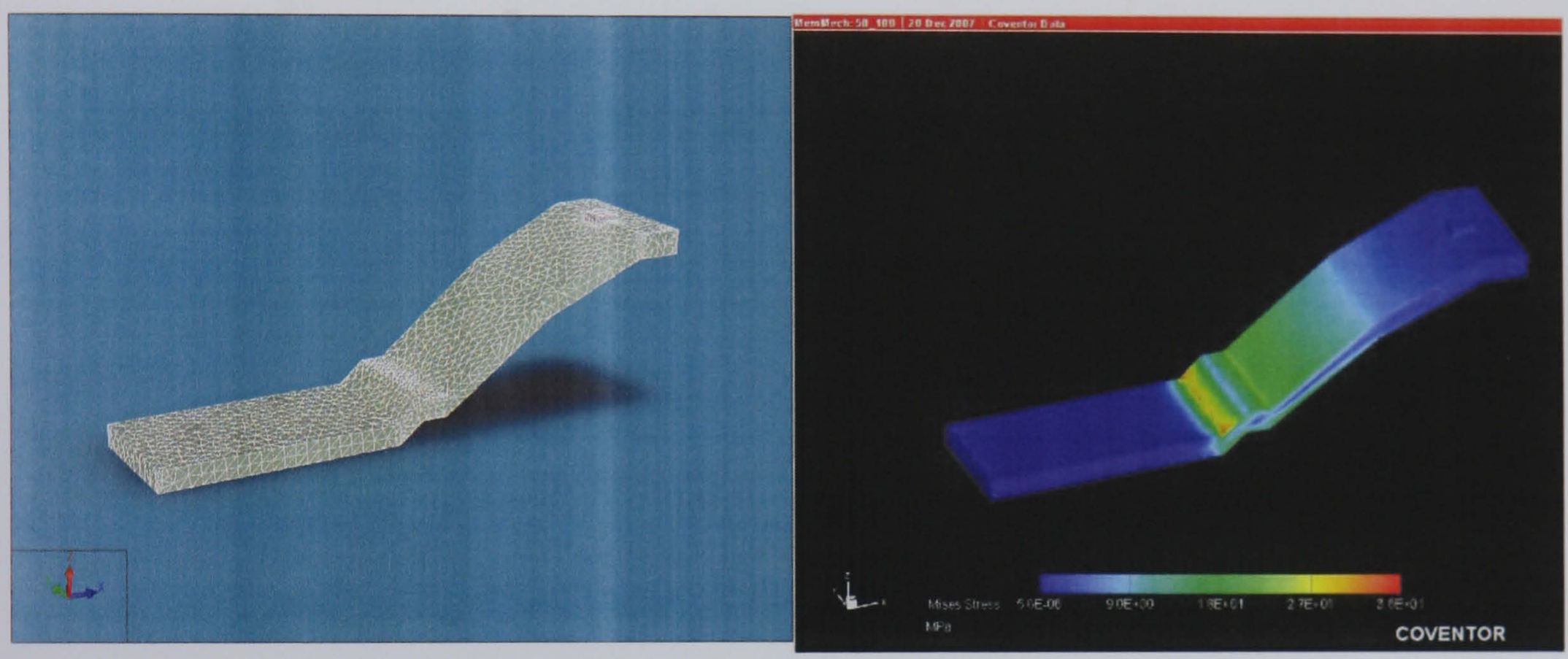

Figure 5.22 Example of full model for 50 x 100 μm cantilever

An example of a meshed model and resultant plot are shown in Figure 5.22. The meshing and FEA simulation were conducted using CoventorWare, although the models were defined using AutoCad and imported since non-planar models could not be created in CoventorWare. A non-linear solver was used which included large deflection effects. Meshing was based on unstructured tetrahedral elements. Materials were defined as homogenous and isotropic.

During the calculation of spring constants only small loads were simulated. This ensured that the simulation would accurately represent the linear behaviour region of the deflection. It was important to consider this region of mechanical behaviour since the experimental results were extracted from the linear region of force-deflection data.

Figure 5.23 shows a comparison between simulated and measured spring constants using E = 69.1 GPa (as obtained from tension testing in section 5.1) and $\upsilon = 0.312$. The gradient of the logarithmic plot is 1.00622 (with correlation coefficient of 0.99949) which indicates that the model fits the behaviour well despite the linear plot showing that the model material constants are not correct.

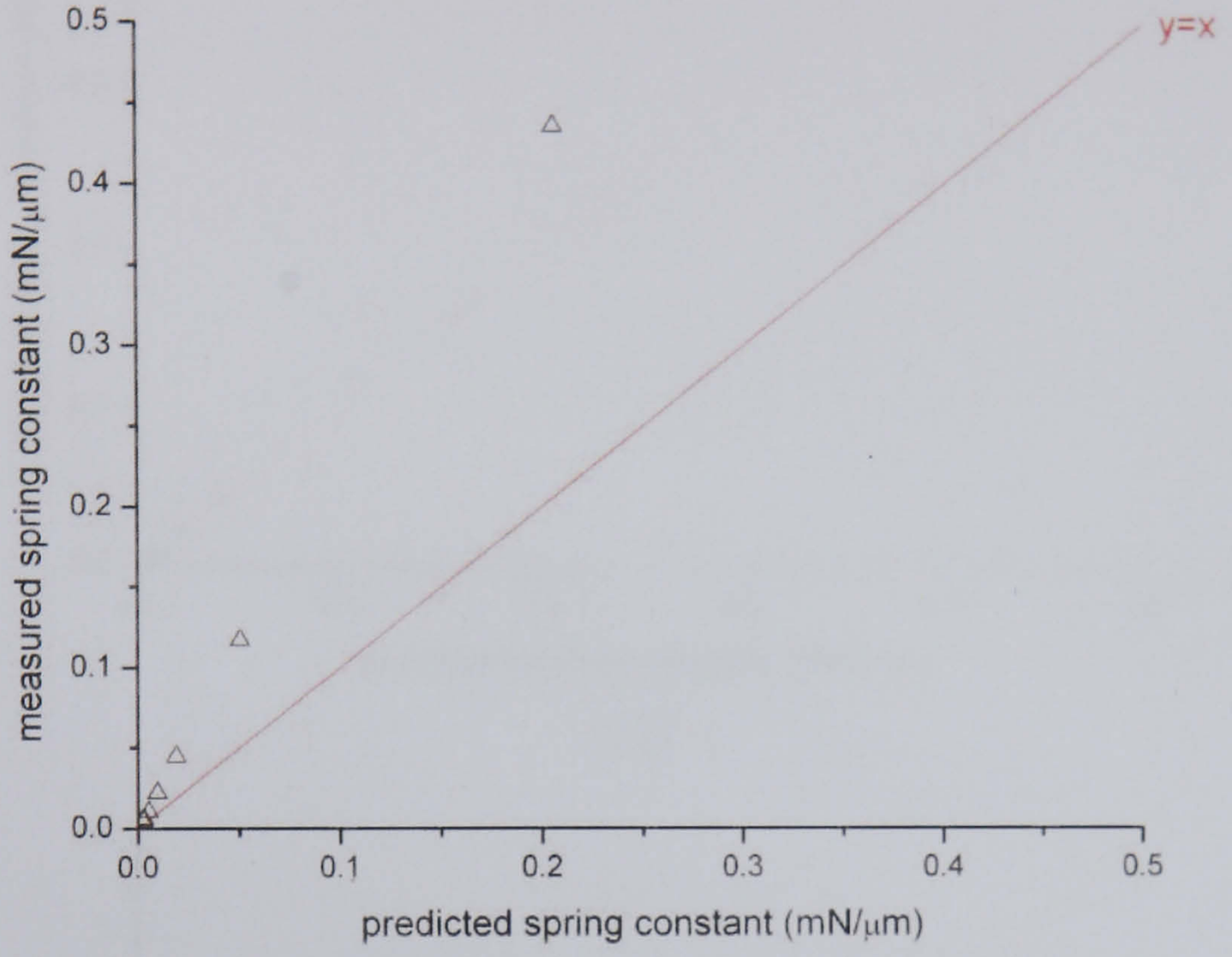

(a)

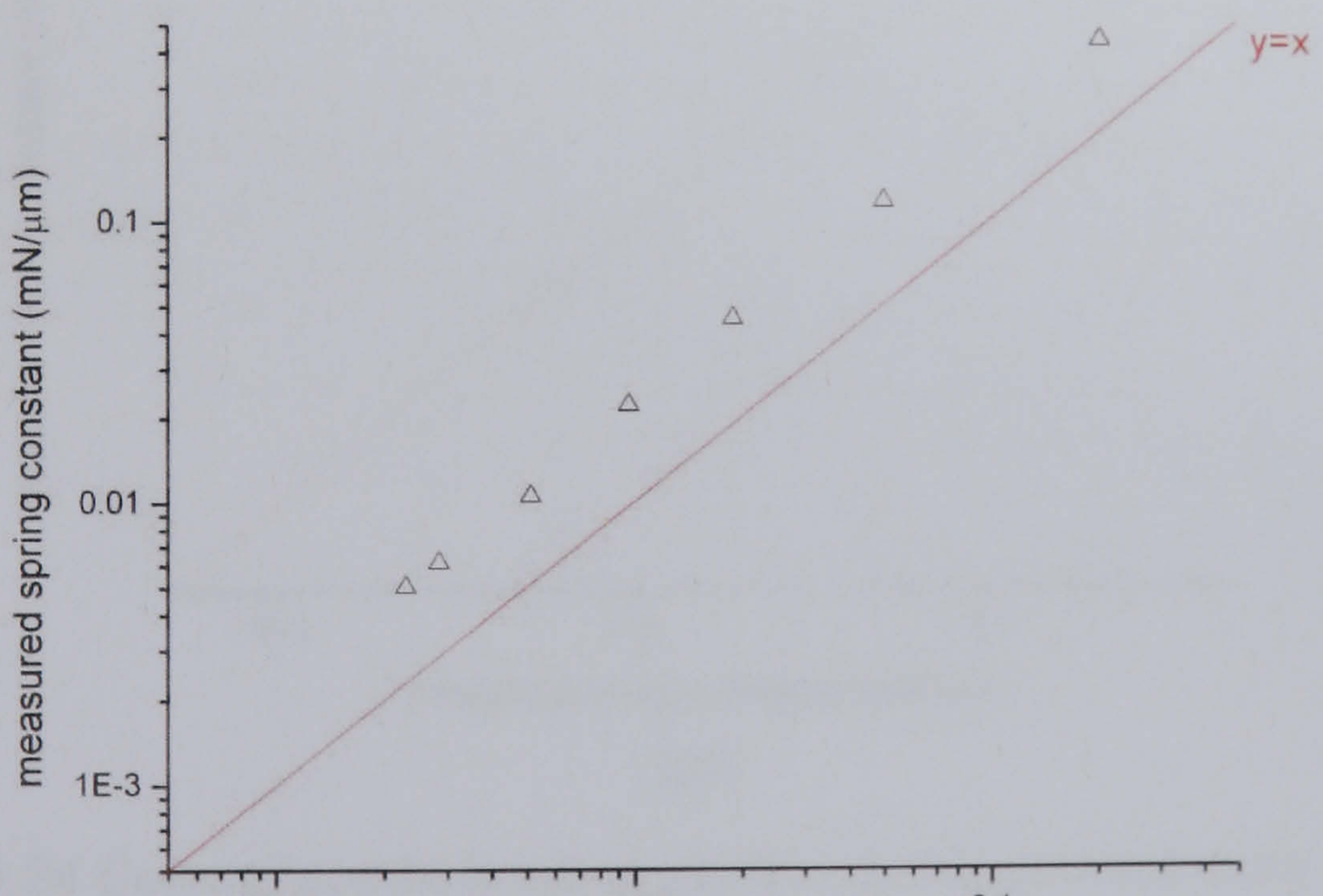

(b)

Figure 5.23 Comparison between experiment and geometrically exact FEA (E = 69.1 GPa) on (a) linear and (b) logarithmic plots

By adjusting the Young's modulus to a value of E = 146.22 GPa the FEA simulations were made to fit the experimental data accurately. This can be seen in Figure 5.24.

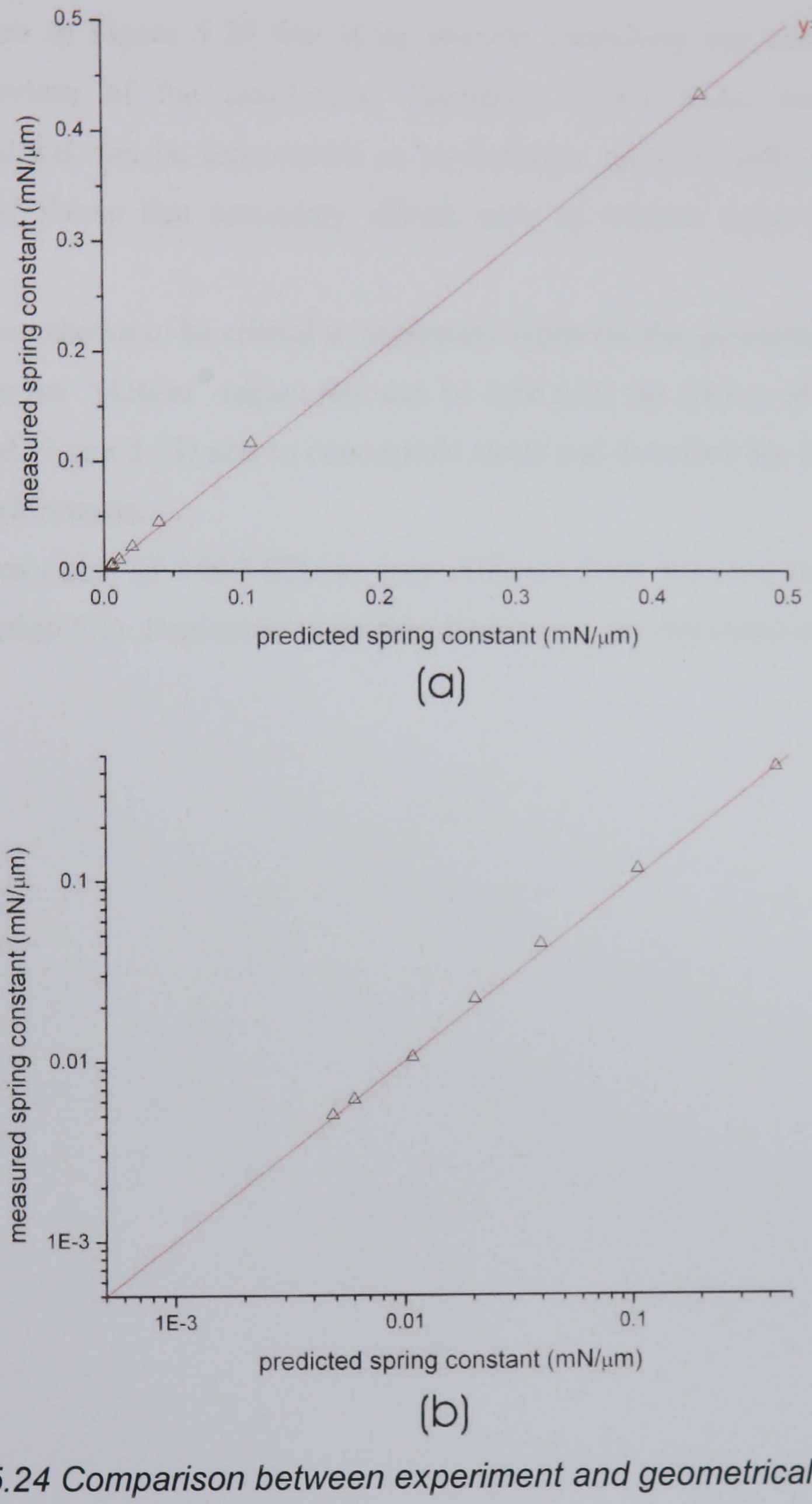

Figure 5.24 Comparison between experiment and geometrically exact FEA (E = 146.2 GPa) on (a) linear and (b) logarithmic plots

5.5.3 Discussion of finite element models

It can be seen in Figure 5.24 that finite element modelling can accurately predict the observed behaviour of the cantilevers. Therefore, in the linear response region the electroplated nickel can be represented as an isotropic material with E = 146.2 GPa and $\upsilon = 0.312$. This shows that secondary effects such as contact stress at the tip are not significant.

It has also been shown to be critical to accurately represent the geometry of the cantilevers. This is because the "plateau" region that can be seen near the anchor of the cantilever (see Figure 5.22 and Figure 5.13) acts to concentrate stress and therefore has a large effect on the mechanical performance.

A Young's modulus of 146.2 GPa is very different from the one measured by tension testing (see section 5.1). Explanations for this discrepancy are discussed section 5.7.

5.6 Cantilever yield

5.6.1 Finite element models

The models discussed in section 5.5.3 (geometrically exact models) were used to simulate cantilever behaviour for the range of loads applied during the experiments. A non-linear solver including large deflection effects was used in the simulation. Therefore it was possible to see if any non-linear effects could be expected in the measured behaviour as a result of non-linear strain fields. An example of both simulation and measured results is shown in Figure 5.25. In the FEA the value of Young's modulus used was 146.2 GPa and $\upsilon = 0.312$.

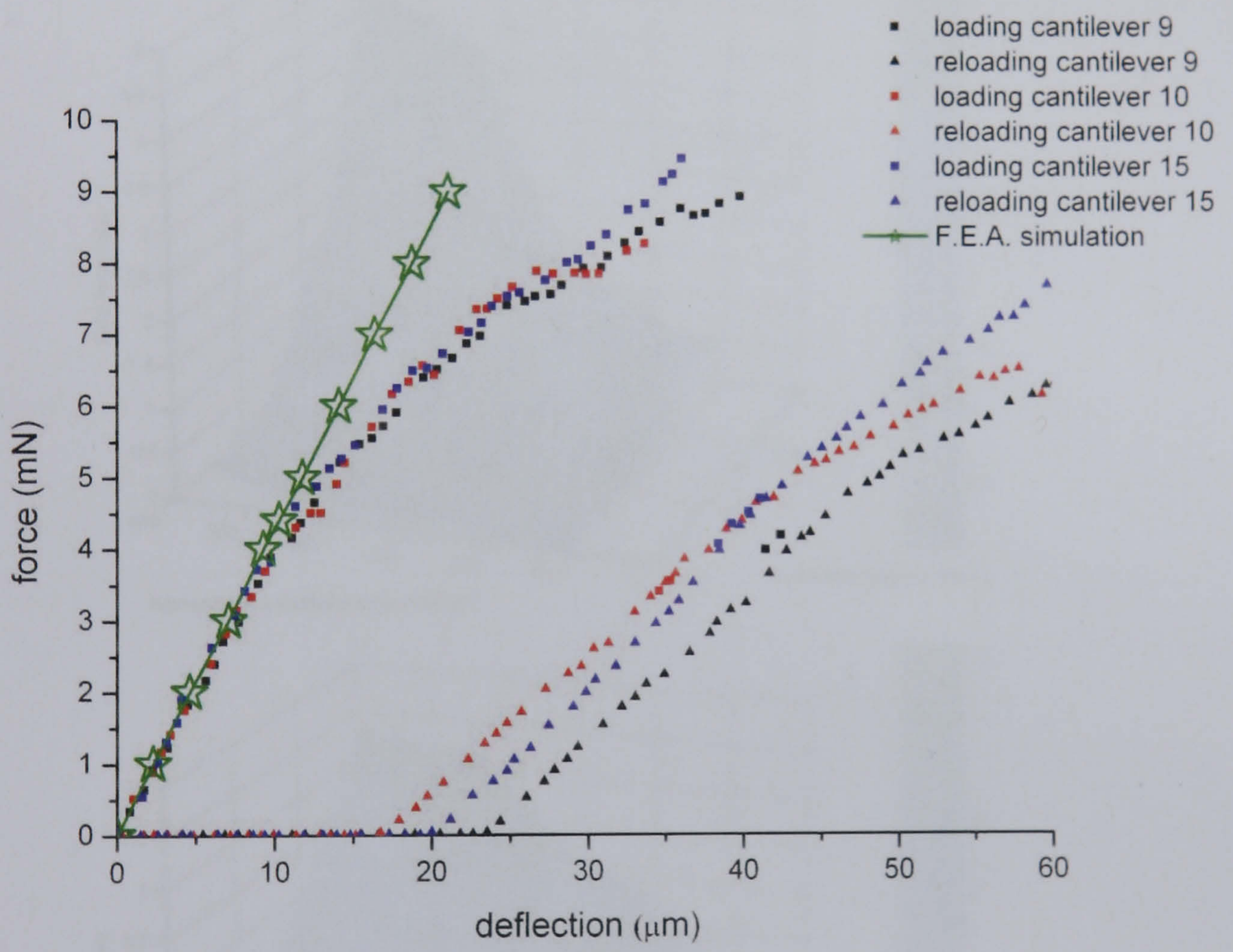

Figure 5.25 Measured and simulated behaviour for the deflection of 100 x 50 μm cantilevers

It is obvious from Figure 5.25 that the simulated behaviour is linear over the range of forces shown. This was true for all the 50 μm wide cantilever models. Therefore, it can be concluded that any non-linearity seen in the experimental force-deflection behaviour is due to the cantilever undergoing yield.

5.6.2 Yield behaviour results

Yield stress is usually determined as the stress required to create a defined small permanent strain (as described in section 5.1.2.2). However for the cantilevers force-deflection and not stress-strain data was readily available. For simplicity therefore the yield point was defined as the point at which deviation from the linear region could be seen. The forces and cantilever deflections at this point were recorded and will be referred to as yield force and yield deflection respectively. The results for yield force are shown below in Figure 5.26. Note that no results are shown for the 700 μm long cantilever as they did not yield when the tip was fully deflected.

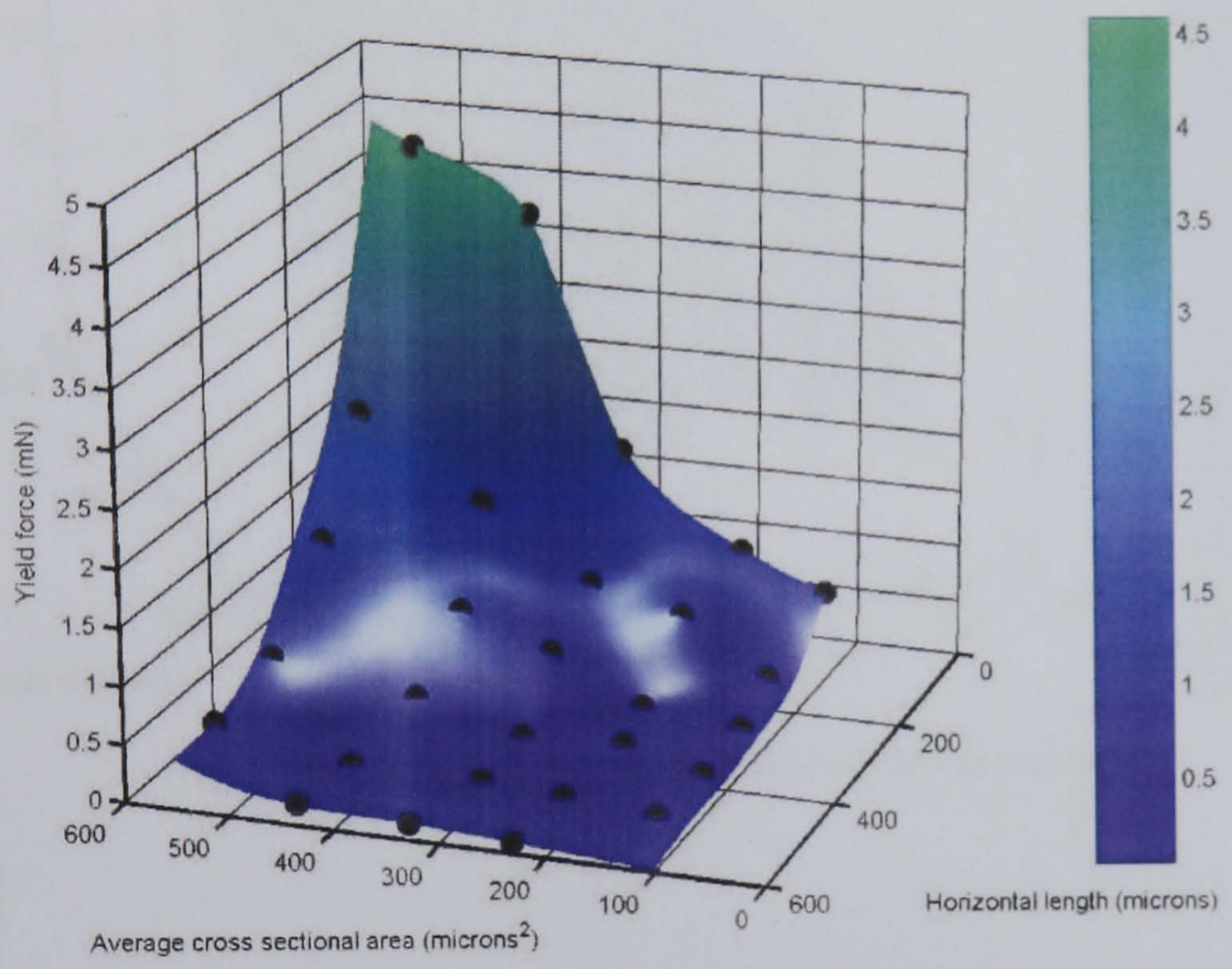

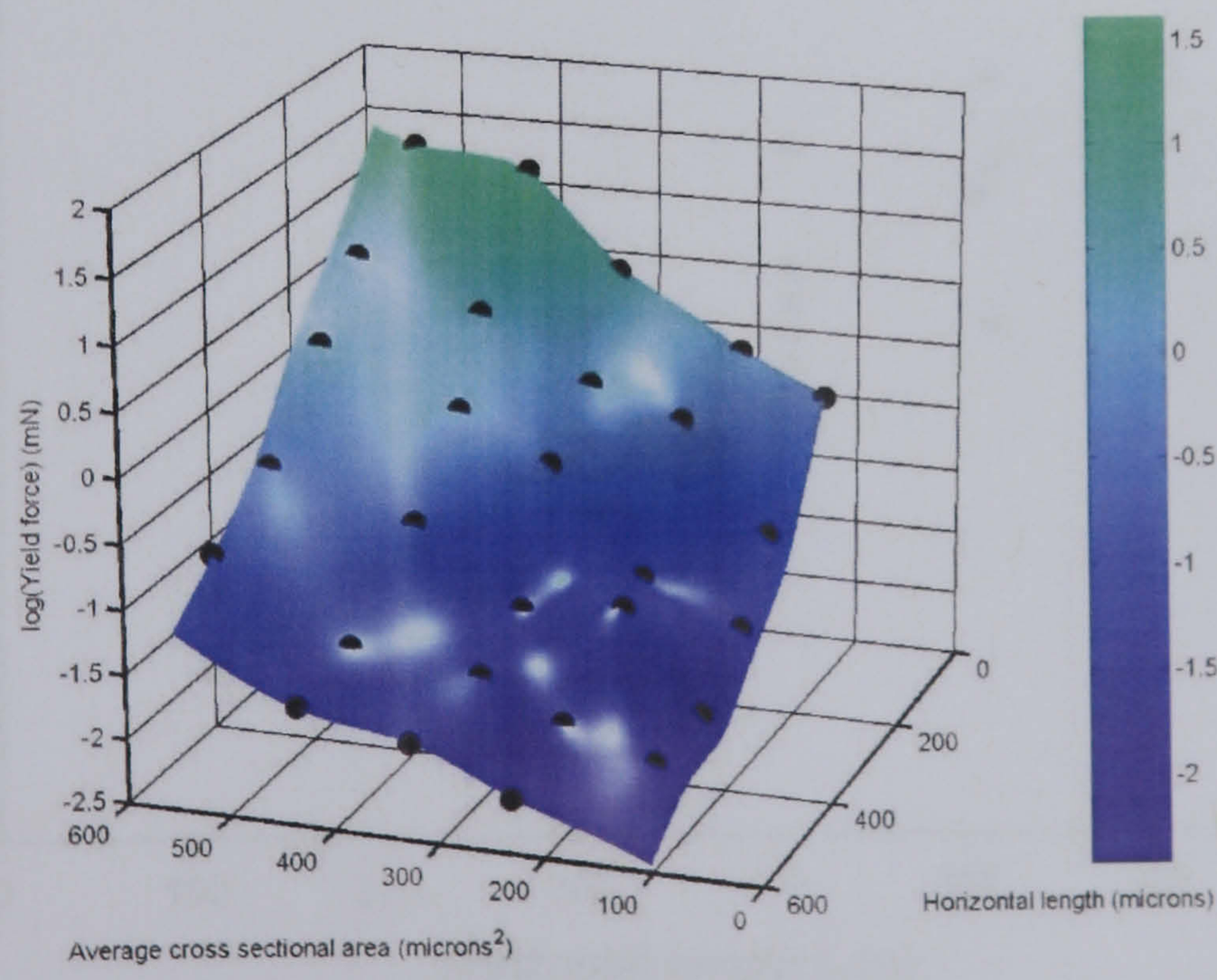

Figure 5.26 Yield Force of cantilevers as a function of geometry

The black dots represent the measured data points through which a surface has been fitted using MatLab and the "v4" algorithm mentioned in section 5.3.2.

The yield displacement is shown below in Figure 5.27. In the top plot, the black dots represent the measured data and the fitting algorithm used was "nearest". This algorithm was used because the data does not form a sensible surface and so it would be misleading to fit a smooth function through it. The bottom plot shows the yield displacement versus horizontal cantilever length.

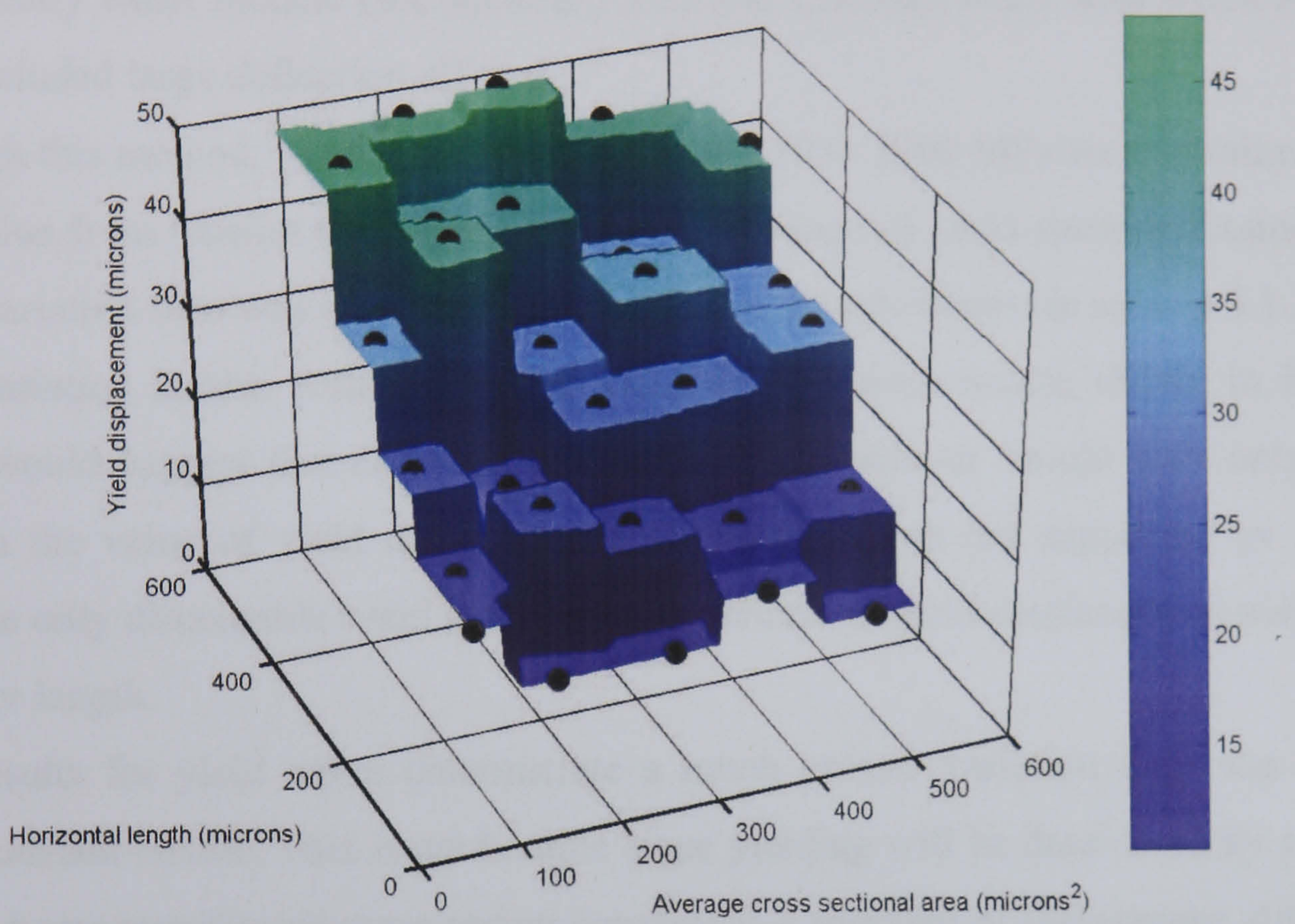

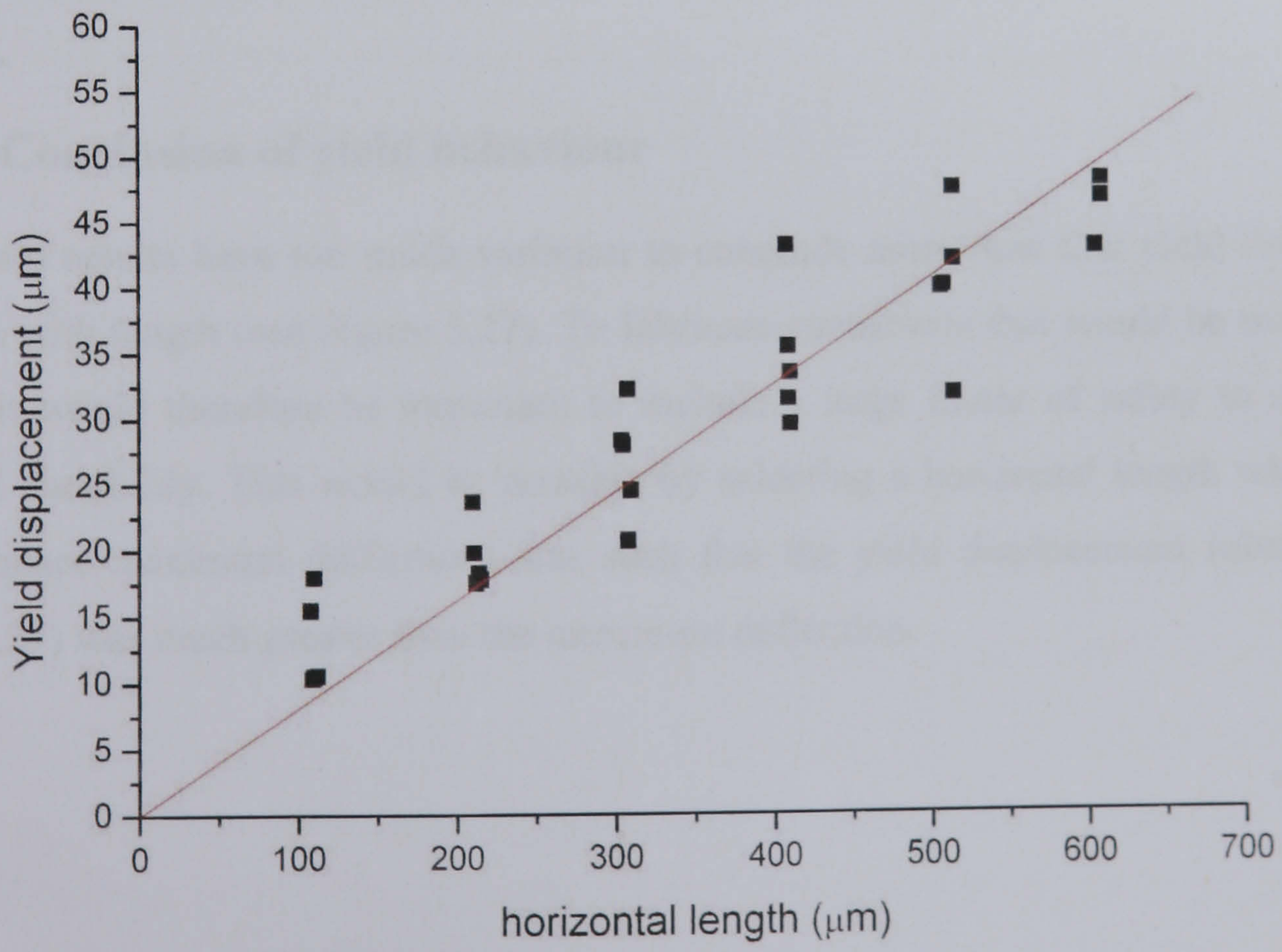

Figure 5.27 Yield displacement of cantilevers as a function of geometry

5.6.3 Discussion of yield behaviour

FEA was required to calculate the yield stress. This could be achieved by simulating the cantilevers with a load equal to their yield force and examining the calculated Tresca or Von Mises stress distribution. The Tresca yield criteria is based the maximum shear stress whilst Von Mises yield criteria is based on elastic strain energy density [12].

To calculate the stress distribution, appropriate simulations were conducted using the geometrically exact models (see section 5.5.2) and CoventorWare with a non-linear solver which included large deflection effects.

Through this method, yield stresses in the range 550 to 1300 MPa were obtained compared to the value from tension testing of 709 MPa. The range of yield stresses obtained indicates greater variation than was seen in the tension testing results shown in section 5.1.2.2.

This variation is also reflected in the yield displacement results shown in Figure 5.27. Theory would suggest that changing the width of a cantilever should have only a minimal effect on the value of yield displacement. However this is not supported by Figure 5.27 where the only discernable trend is an average increase in yield displacement with increasing cantilever length.

The results for yield stress demonstrate a much greater variation than was seen in the spring constant results. This is predictable since yielding will be dominated by point defects and non-homogeneities whereas spring constant is a measure of the average stiffness of the structure.

5.6.3.1 Conclusion of yield behaviour

The yield results have too much variation to conclude more than that yield displacement increases with length (see Figure 5.27). To fabricate cantilevers that would be mechanically durable it would therefore be important to include a large factor of safety to counter the observed variability. This would be possible by selecting a horizontal length where the tip height (hence maximum deflection) was such that the yield displacement (obtained from Figure 5.27) was much greater than the maximum deflection.

5.7 Conclusion

Tension testing results gave a poor estimation of the material properties of the electroplated nickel from which the cantilevers we fabricated. It should be noted that all the tension testing samples were fabricated on one wafer whist all the cantilevers were fabricated on another. There are three likely causes for the discrepancy in mechanical properties between the cantilevers and tension testing samples.

The first and most likely explanation is systematic errors in the measurement of extension data. Such errors are known to result from mechanical compliances within tension testing machines and can only be eliminated by the use of external, noncontact measurements of displacement.

A second contributing factor could be a change in the nickel microstructures with increasing deposit thickness. As noted earlier the tension testing samples were electroplated to a much greater thickness than was used to fabricate the cantilevers.

Lastly there could be an uncontrolled variation (such as impurity concentration) between different nickel depositions despite using the same deposition parameters being used.

It has been shown that geometrically simplified analytical models based on plane stress assumptions accurately modelled the displacement of long cantilevers. It was also shown that axial load and shear effects could be neglected without introducing significant error. Further, it was shown that, as the cantilevers became shorter, plain stress assumptions under predicted cantilever stiffness, whilst plain strain assumptions over predicted cantilever stiffness.

For shorter cantilevers it was found that the mechanical behaviour became dominated by stress concentration caused by the "plateau" section near the anchor of the cantilever. Therefore, since the geometric simplifications were a cause of error, to accurately predict the mechanical behaviour of these cantilevers it was necessary to use FEA and geometrically exact models.

Non-linear FEA showed that for the geometries of cantilevers fabricated, over the range of deflections tested, the elastic behaviour remained linear. Therefore, it was concluded that any non-linearity in the force-deflection behaviour could be attributed to yielding.

Although the plastic behaviour was not studied in the same amount of details as the elastic behaviour it was noted that there was greater variation in the yield stress than was found in

the elastic behaviour. This was attributed to the defect dominated nature of yield compared to the averaging nature of elastic behaviour. It should also be noted that fatigue, where failure occurs due to a cyclical loading below the yield stress, was not investigated. The observed variability in yield stress and the likelihood of fatigue mean that to fabricate mechanically robust cantilevers it would be necessary to design them with as large a safety factor as possible.

5.7.1 Results and specifications

In chapter 2 is was specified that the probes should be able to be deflected between 30 and 40 μm without damage. The testing described in this chapter showed that only cantilevers with horizontal lengths of 600 μm or more fulfilled this specification. The cantilever stiffness was shown to increase with decreasing length and increasing width. The stiffest 600 μm long cantilever tested had a spring constant of 6.12 μN/μm which corresponds to a contact force of 245 μN at 40 μm deflection. Therefore, the probes tested will only have satisfied the original specification if a low resistance contact can be achieved at forces of, or below, 245 μN.

References

1. Ashby, M.F. and D.R.H. Jones, *Engineering materials 1 - An introduction to their properties and applications*. 1996, Butterworth Heinemann.
2. *Matweb website*: http://www.matweb.com.
3. *Goodfellow website*: http://www.goodfellow.com/csp/active/static/A/Nickel.HTML.
4. Dini, J.W., *Electrodeposition: The Materials Science of Coatings and Substrates*. 1993, William Andrew Inc.
5. Ebrahimi, F. and Z. Ahmed, *The effect of substrate on the microstructure and tensile properties of electrodeposited nanocrystalline nickel.* Materials Characterization, 2002. **49**(5): p. 373-379.
6. Kim, S.H., *Determination of mechanical properties of electroplated Ni thin film using the resonance method.* Materials Letters, 2007. **61**(17): p. 3589-3592.
7. Majjad, H., et al., *Dynamic determination of Young's modulus of electroplated nickel used in LIGA technique.* Sensors and Actuators A - Physical, 1999. **74**(1-3): p. 148-151.
8. Connolley, T., P.E. McHugh, and M. Bruzzi, *A review of deformation and fatigue of metals at small size scales.* Fatigue & Fracture of Engineering Materials & Structures, 2005. **28**(12): p. 1119-1152.

9. Watanabe, T., *Nano-plating: Microstructure control theory of plated film and data base of plated film microstructure*. 2004, Elsevier.
10. Schlesinger, M. and M. Paunovic, *Modern Electroplating*. 2000, Wiley: New York.
11. Case, J. and A.H. Chilver, *Strength of Materials*. 1959, Edward Arnold.
12. Benham, P.P., R.J. Crawford, and C.G. Armstrong, *Mechanics of Engineering Materials*. 1996, Pearson Education Limited.
13. Belendez, T., C. Neipp, and A. Belendez, *Large and small deflections of a cantilever beam.* European Journal of Physics, 2002. **23**(3): p. 371-379.
14. Xiang, Y. and D.A. LaVan, *Analysis of soft cantilevers as force transducers.* Applied Physics Letters, 2007. **90**(13).
15. Salisbury, S.P. and R. Ben Mrad, *Analytical stiffness estimation for short flexures.* Mechatronics, 2006. **16**(7): p. 399-403.
16. Orosz, I., *Simplified method for calculating shear deflections of beams*. U.S.D.A.F. service, Editor. 1970. p. 11.
17. Hearn, E.J., *Mechanics of Materials 2 - An introduction to Mechanics of Elastic and Plastic Deformation of Solids and Structural Materials*. 1997, Butterworth Heinemann.
18. Madou, M.J., *Fundamentals of Microfabrication*. 1997. CRC press.
19. Senturia, S.D., *Microsystem Design*. 2003, Kluwer academic publishers.

Chapter Six

Electrical testing

This chapter describe the results of electrical testing of the fabricated probes. Contact resistance as a function of applied load and contact material was examined in detail. It was found that the presence of surface films prevented reliable electrical contacts being formed and therefore contact forces higher than 3.5 mN are required. The leakage current between adjacent cantilever probes was also measured to be less than 10 pA.

6.1 Introduction

This chapter introduces basic concepts of electrical contact resistance theory before electrical testing results are given and discussed. The chapter begins by introducing two models for the contact area as a function of applied load. Common expressions for the constriction resistance of single and of multiple contact spots are then given. The effects of bulk resistivity and surface films are discussed before analytical estimates for contact resistance as a function of applied load are derived. A brief consideration of thermal effects in electrical contacts is then presented before a discussion of micro electrical contacts.

Next the results of contact resistance testing are given. The contact resistance is examined as a function of material type and applied load. The results are discussed with reference to the aforementioned theoretical background and conclusions are drawn. The results of electrical isolation between adjacent probes is also presented.

6.2 Contact resistance theory

Electrical contact resistance is the resistance associated with the interface between two conductors. To estimate this resistance it is necessary to know about physical (applied force, Young's modulus, hardness, surface film thickness, surface roughness, etc.) and electrical (bulk resistivity, surface films resistivity, surface film dielectric constant, contact work function etc.) properties of the contacting surfaces. A physical analysis must be used to determine the true area of contact between the two bodies for a given contact force, and then electrical analysis is used to determine the current paths and hence the total effective resistance. Additionally, Joule heating from the current passed through the contact can cause the growth of surface oxide layers or the inter-diffusion of metals affecting the contact resistance stability. A summary of some of the important results for the analysis of electrical contacts are now given to provide a basis for interpretation of the results presented later.

6.2.1 Contact mechanics

In order to estimate the contact resistance between surfaces it is critical to know the area of contact. A review of relevant literature indicates that the two most frequently used estimates for contact area come from Hertzian elastic analysis or semi-empirical relationships based on plastic deformation [1-7]. First we will discuss the elastic analysis of a contact.

Expressions for the maximum compressive stress at the interface between two curved bodies were derived by Hertz in 1881 [8]. His analysis assumed that the bodies deformed in a linear-elastic manner, that the bodies could be treated as semi-infinite half planes, that the bodies possessed isotropic and homogeneous properties and that there was no frictional or adhesive forces between them. A Hertzian analysis is therefore only strictly applicable to contact between two large smooth bodies where the area of contact is small compared to the size of the bodies and the deformation of the bodies is very small.

The most commonly used Hertzian relationship in electrical contact analysis is that for two contacting spheres (as shown in Figure 6.1) and is given by equation 6-1 [9].

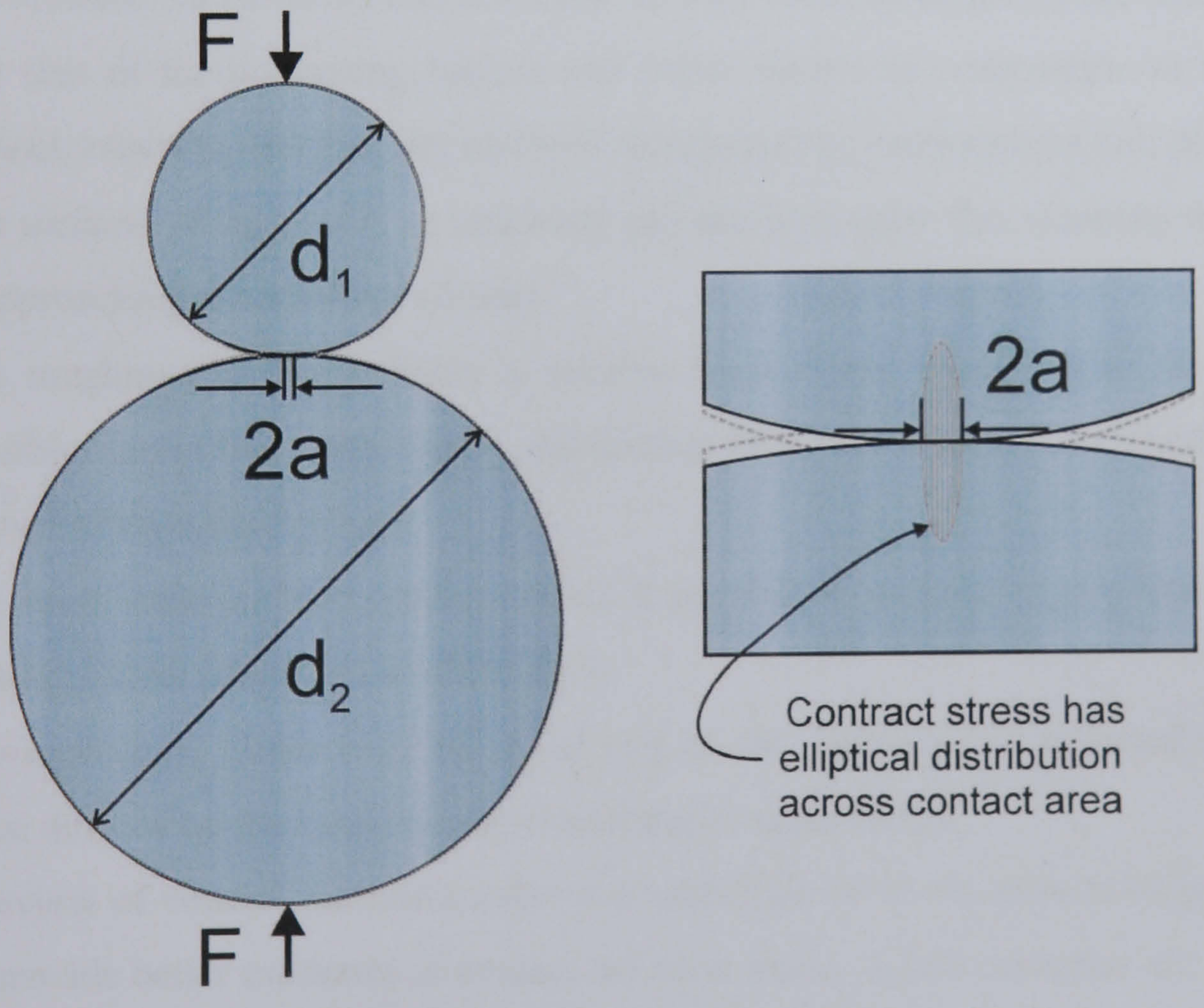

Figure 6.1 Hertzian contact between two spheres

$$a = K_a \sqrt[3]{F} \qquad (6\text{-}1)$$

where a is the radius of the circular area of contact, F is the applied load and K_a is a constant defined in equation 6-2.

$$K_a = \left[\frac{3}{8} \cdot \left\{ \frac{\left(\frac{(1-\nu_1^{\,2})}{E_1} \right) + \left(\frac{(1-\nu_2^{\,2})}{E_2} \right)}{\left(\frac{1}{d_1} \right) + \left(\frac{1}{d_2} \right)} \right\} \right]^{\frac{1}{3}} \qquad (6\text{-}2)$$

where υ_1 and υ_2 represent the Poisson's ratios, E_1 and E_2 represent Young's moduli and d_1 and d_2 diameters of spheres *1* and *2* respectively (see Figure 6.1)

For the contact between a sphere and a flat plane we set $d_2 = \infty$ and K_a can be simplified, as shown in equation 6-3.

$$K_a = \left[\frac{3d_1}{8} \cdot \left(\frac{(1-\nu_1^{\,2})}{E_1} + \frac{(1-\nu_2^{\,2})}{E_2} \right) \right]^{\frac{1}{3}} \qquad (6\text{-}3)$$

A Hertzian analysis (equation 6-1) would suggest that contact area increases in proportion to applied force raised to the power of two thirds. The contact area also increases as the diameter of the spheres increases and as the Young's modulus of the materials decrease.

Unfortunately, many of the assumptions required to use Hertzian models make their use for the contact between the probe tip and bond pad invalid; these assumptions are listed below:

- The size of the contacting bodies will (most likely) be comparable to the area of contact, meaning that they are not well represented by semi-infinite half planes.
- The surfaces of the probe tip and bond pad are both quite flat, meaning the situation is approaching a conformal contact.
- The roughness of the surfaces is relative large (when compared to the maximum possible size of the contact area) and there is likely to be significant frictional forces acting between the surfaces.
- The small nature of the contact makes it possible to achieve high contact pressures making plastic deformation likely [10].
- The contact tip slides over the bond pad as the cantilever is deflected (due to the locus defined by the cantilever tip) resulting in shear forces.

A brief review of contact mechanics shows a multitude of works have built upon Hertz's models to provide better estimates of contact area and stress. A few examples are:

- The analysis of elastic contact between rough surfaces by considering a single asperity contact as Hertzian and then using a statistical model to predict the behaviour of multiple asperities [11].

- The contact between two spherical bodies including both elastic deformation and adhesive forces [12].
- The contact between two spherical bodies including both elastic deformation. adhesive and Van der Waals forces [13].

Since it has been reasoned the contact is not likely to be wholly elastic in nature it is not worth describing these more detailed models here. Therefore, having considered the basic case of an elastic contact, we will now consider the simplest plastic analysis.

The most common estimates for the contact area when plastic deformation dominates the behaviour come from indentation testing. At its simplest, the hardness of a material is a measure of a materials resistance to plastic deformation and is generally defined as the load required to produced an indentation of a certain area [14]. For most metals the hardness is dependent only on the yield strength and work hardening properties of the material [15]. However in very hard metals, polymers, rubbers and glasses the hardness is also influenced by elastic properties. This is attributed to the compression of the material beneath the plastic region which imposes different constraints on plastic material flow [15].

Different hardness scales use different indenter shapes (for example Brinell and Mayer use spherical indenters, Vickers uses a square based pyramid whilst the Knoop a rhombic based pyramid) and measure different areas (Brinell, Vickers and Knoop uses the surface area of the indentation whilst Mayer use the projected area) [15]. Some hardness testing methods vary more with test conditions (load, indentation time etc.) than others. Generally spherical indenters produce a greater variation in hardness values as the testing conditions change [14].

Regardless of the particular hardness scale used, an estimate of contact area, A (mm^2) can be obtained from the basic definition of hardness as shown in equation 6-4.

$$A = \frac{P}{H} \qquad (6\text{-}4)$$

where H is the hardness of the material (kgf/mm^2) and P is the load (kgf).

The hardness value used to estimate the area of contact between two different materials should be the softer of the two [1]. In electrical contacts, to estimate contact area, either Vickers [3] or Mayer's [16] hardness values are typically used.

Using hardness values to predict area of contact (for a given load) implies that the area of contact is directly proportional to the applied force and independent of the geometry of the contact (including its apparent area). This seems contradictory to the previously stated fact that changing test conditions (such as indenter size) when measuring hardness using a

spherical indenter affects the measured value. However this variation in hardness values is due to a change in the *geometric nature* of the contact as indentation depth increases [14]. For instance, consider an indenter pressed into a surface far enough that the indentation is a complete hemisphere. Pushing the indenter further into the material will result in indentation shapes very different in nature from those obtained at lower loads. This is why the Vickers test uses a square based pyramid indenter which does not produce this geometric variation [14].

In the case of electrical contacts, the amount of plastic deformation (hence depth of indentation) should be very small and so regardless of the contacting areas' shapes such geometric effects do not occur. Therefore the relationship between area and force can be assumed to be linear.

A caveat to this is that the surfaces of the contacting bodies possess uniform surface roughness. This is important since contact between 'real surfaces' occurs only at asperities. If the surface has a non-uniform roughness then the density of asperities on the surface will not be independent of the selected area and the linearity implied in equation 6-4 is invalid [10].

Using equation 6-4 to estimate electrical contact area assumes the contact area is dominated by plastic deformation. Typically, in wafer level probing it is the bond pad that is plastically deformed (not the probe) and this is a reasonable assumption. Using equation 6-4 to estimate contact area also implies that the true contact area and area of the indentation are the same. This is unlikely to be the case as real contact only occurs at asperities (see Figure 6.2).

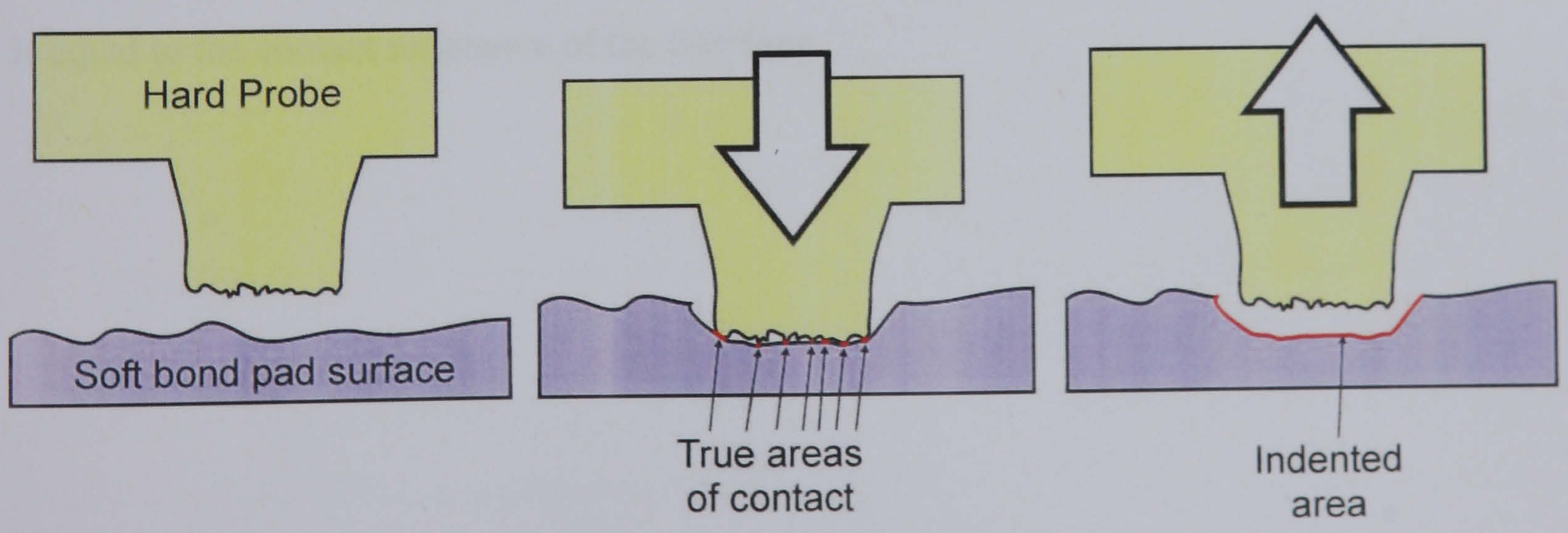

Figure 6.2 Comparison between indentation area and true area of contact

Therefore it is necessary to include a scaling factor, η (of less than 1) to estimate true contact area; this is shown in equation 6-5. The value of η depends on the surface roughness of the contacts.

$$A = \frac{\eta P}{H} \qquad (6\text{-}5)$$

where A is the true contact area (mm^2), H is the hardness of the (softer) material (kgf/mm^2) and P is the load (kgf).

6.2.2 Electrical contact analysis

When two metallic bodies are brought into contact there exists between them an electrical resistance associated with the interface. The origin of this resistance is both the limited area of contact, resulting from the surface roughness, and the resistance caused by the presence of electrically insulating layers on the surfaces.

6.2.2.1 Constriction resistance

The true areas of electrical contact between two surfaces are known as *'a-spots'* and are typically only a fraction of the apparent area. Moreover, due to insulating surface films the 'a-spots' will also only be a fraction of the total number of actual mechanical contacts. These points of contact restrict the current flow, dividing it into narrow paths creating electrical resistance. This leads to what is termed a *constriction* resistance. An illustration of this can be seen in Figure 6.3 which shows equipotential surfaces (grey) and current flows (green lines) through contacting asperities at the interface between two conducting bodies. If the surface of the contacts are free from any contaminating films then the constriction resistance is equal to the contact resistance of the interface.

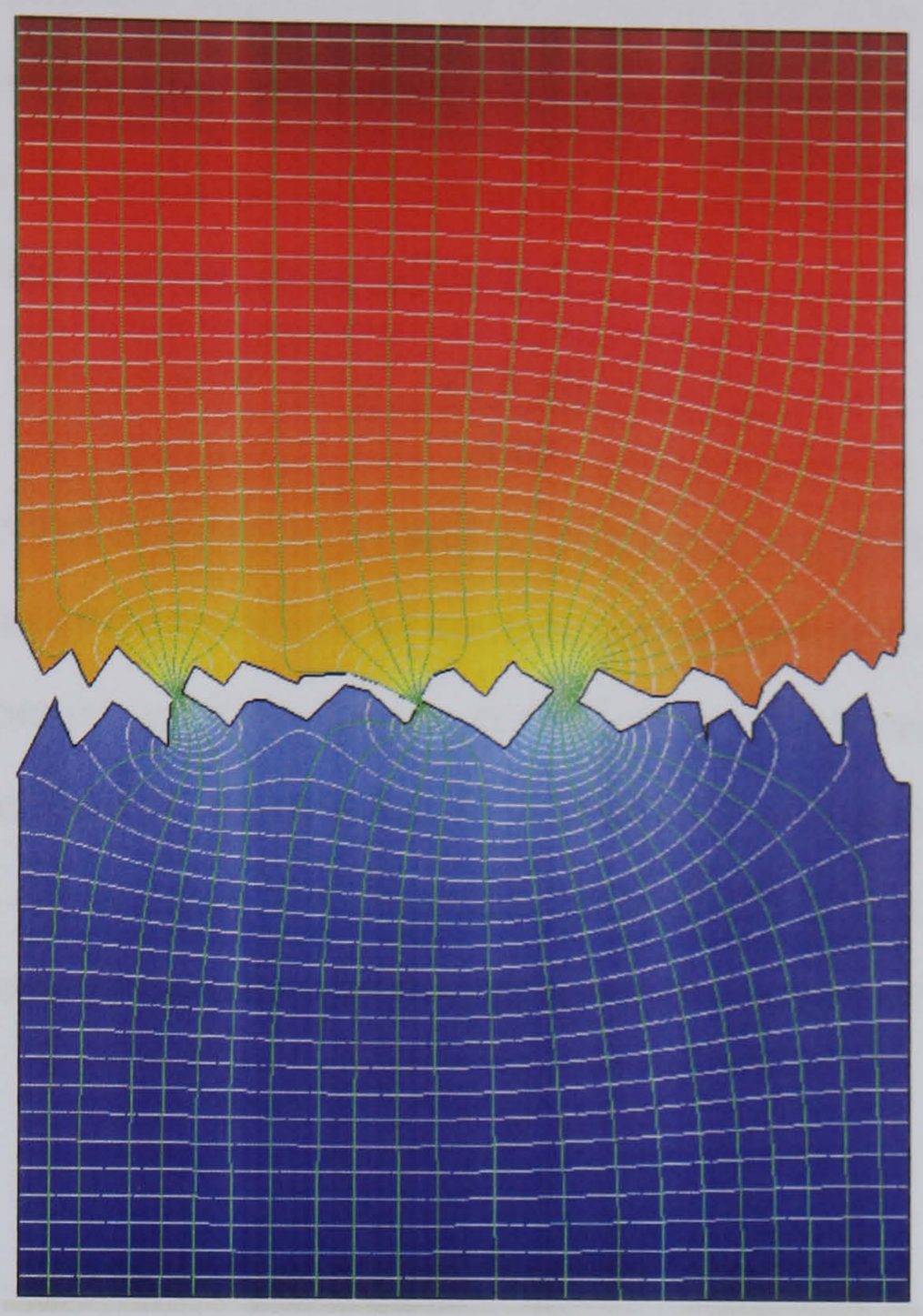

Figure 6.3 The microstructure of an electrical interface

Holm [16] adapted Maxwell's 1873 solution for the spreading resistance of a long circular conductor in contact with a massive electrode [17], to derive an expression for the resistance between two bodies caused by a single (circular) area of contact. Holm's expression for the constriction resistance of a singular circular contact is given in equation 6-6 [10].

$$R = \frac{\rho_1 + \rho_2}{4a} \qquad (6\text{-}6)$$

where R is the constriction resistance, ρ_1 and ρ_2 represent the resistivities of the contacting materials and a is the radius of the circular contact area.

It should be noted that Holm also derived expressions for elliptical contact regions but these results are not given (they can be found in [10, 16]). Holm showed that if elliptical and circular spots of the same area were compared, then the circular spot represented the highest constriction resistance. Increasing the elongation of the ellipse was found to decrease the constriction resistance (relative to a circle of the same area). This effect must be considered if the contacting surfaces possess non-uniform roughness such that contacting areas are not circular. Such a situation arises when considering machine cut surfaces [16].

Holm's incorporation of Maxwell's solution implicitly assumes the equipotential surfaces in the bodies either side of the contact followed elliptical forms. This is only true if the bodies are semi-infinite and there is only one point of contact between them. However,

Holm also gave an approximate expression for n circular contacts. His expression assumed the contacts were far enough apart not to significantly interfere with each other and so the total constriction resistance could be approximated to n independent resistances in parallel. Holms resulting expression is given in equation 6-7.

$$R = \frac{\rho_1 + \rho_2}{4na} \qquad (6\text{-}7)$$

where R is the constriction resistance, ρ_1 and ρ_2 represent the resistivities of the contacting materials, a represents the average radius of contact and n represents the number of contacts.

Holm also derived a special solution for the constriction resistance R of n circular contacts of radius a which are uniformly distributed in a circle of radius α (often called the Holm radius). In this solution, the current flow through each of the constrictions was not assumed to be independent. The expression for the constriction resistance of this special case is give by equation 6-8.

$$R = \rho\left(\frac{1}{2na} + \frac{1}{2\alpha}\right) \qquad (6\text{-}8)$$

where ρ is the resistivity of the metals in contact (assumed to be the same).

Greenwood [18], expanded on Holm's work deriving an expression for the constriction resistance of a variety of different patterns of (circular) contacts. Greenwood introduced an extra term that represented the interaction between individual contacts based on their spatial separation. Greenwood's approximation for the constriction resistance of n circular contacts between two bodies (of the same resistivity, ρ) is given by equation 6-9.

$$R \approx \rho\left[\left(\frac{1}{\pi n^2}\sum\sum_{i \neq j}\frac{1}{r_{ij}}\right) + \left(\frac{1}{2\sum a_i}\right)\right] \qquad (6\text{-}9)$$

where a_i is the radius of the i^{th} contact and r_{ij} is the distance between i^{th} and j^{th} contact and n is the number of contacts. The interaction term is represented by the contents of the first circular bracket set. This expression is valid as long as there is no correlation between the size of a given spot and its position [19].

From equation 6-9 it can be seen that the constriction resistance decreases if the resistivity decreases, the real areas of contact increase or the distance between contacts increase. Recent work by Boyer [19] generalised Greenwood's results for the calculation of constriction resistance for various 'a-spot' shapes however the basic form of the solutions is similar to Greenwood's.

So far it has been assumed that the bodies in contact are infinitely large. A expression for the constriction resistance between finite bodies can be found by solving the Laplace equation with suitable boundary conditions [10]. A solution for the constriction resistance, R, due to a singular point of contact of radius a between two cylindrical contacts of radius r and resistivity ρ is given by equation 6-10 [10].

$$R = \frac{\rho}{2a}\left[1 - 1.41581\left(\frac{a}{r}\right) + 0.06322\left(\frac{a}{r}\right)^2 + 0.15261\left(\frac{a}{r}\right)^3 + 0.19998\left(\frac{a}{R}\right)^4\right] \quad (6\text{-}10)$$

The variation in constriction resistance (normalised) as a function of the ratio between the contact radius a, and conductor radius r, is shown in Figure 6.4. From Figure 6.4 it can be seen that that equations 6-6 to 6-9 represent maximum possible values of constriction resistances.

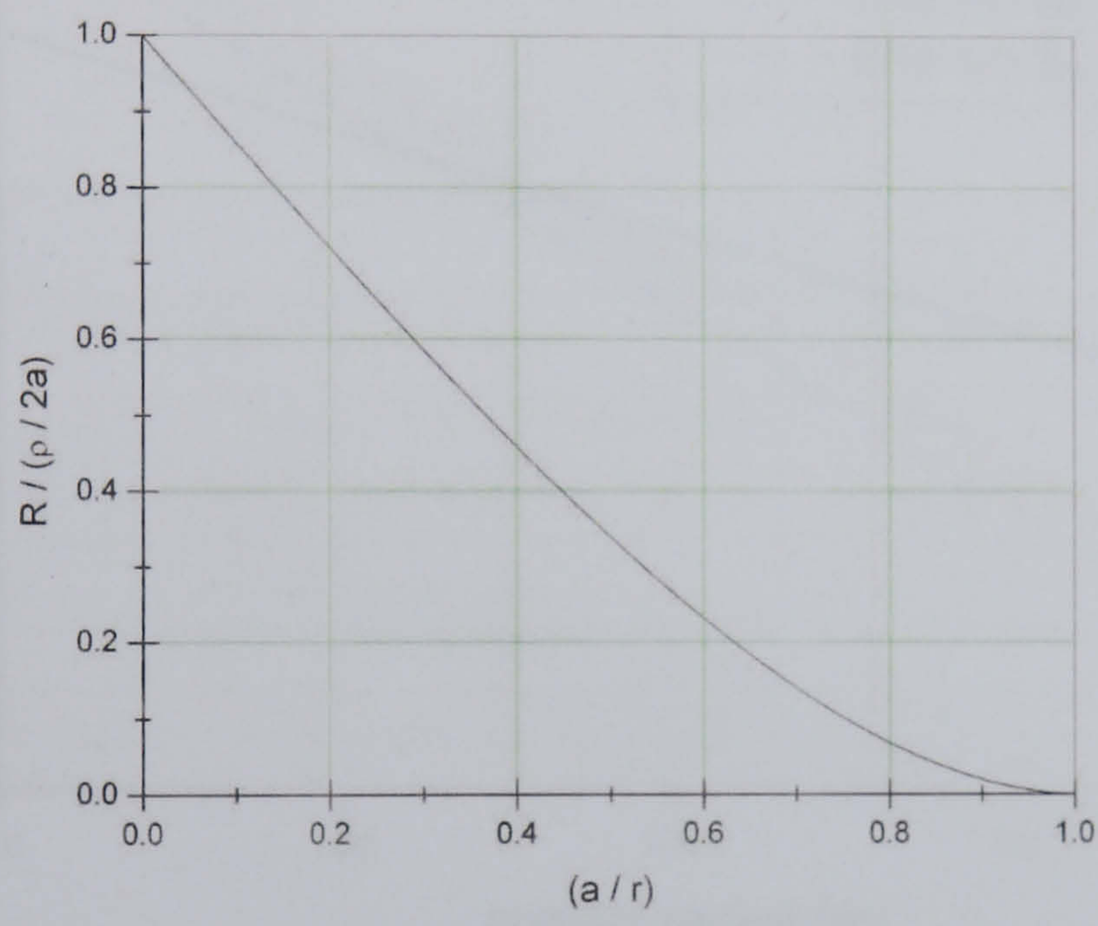

Figure 6.4 Variation in constriction resistance (normalised) as a function of the ratio of contact radius to conductor radius

Solutions based on the Maxwell spreading resistance are only valid for contacts where electrons move in a diffusive way. This is only true if the radius of contact is much greater than the electron mean free path length [20] (typically 10 to 40 nm at room temperature [21, 22]). For a contact radius much smaller than the electron mean free path the constriction resistance has been described by Sharvin [20]. Here the conduction mechanism is ballistic and electrons are only scattered at the boundary of the contact. Sharvin's expression for constriction resistance is give by equation 6-11.

$$R = \frac{4\rho l_e}{3\pi a^2} \quad (6\text{-}11)$$

where R is the constriction resistance, ρ is the resistivity, l_e is the mean free path of the electron and a is the radius of contact.

If the contact radius is comparable to the electron mean free path then the resistance is found by interpolating between Maxwell's and Sharvin's solutions. Such calculations can be found in the work of Wexler [23] or Nikolic [20].

In most practical situations, it is acceptable to use Maxwellian based solution for constriction resistance of a contact of greater than 200 nm diameter without incurring much error. This can be seen in Figure 6.5 where constriction resistances have been calculated using equations 6-6 and 6-11 by letting $\rho = 6.93 \times 10^{-8}$ Ωm (which is the resistivity of nickel at room temperature) and various arbitrary electron mean free path lengths, l_e.

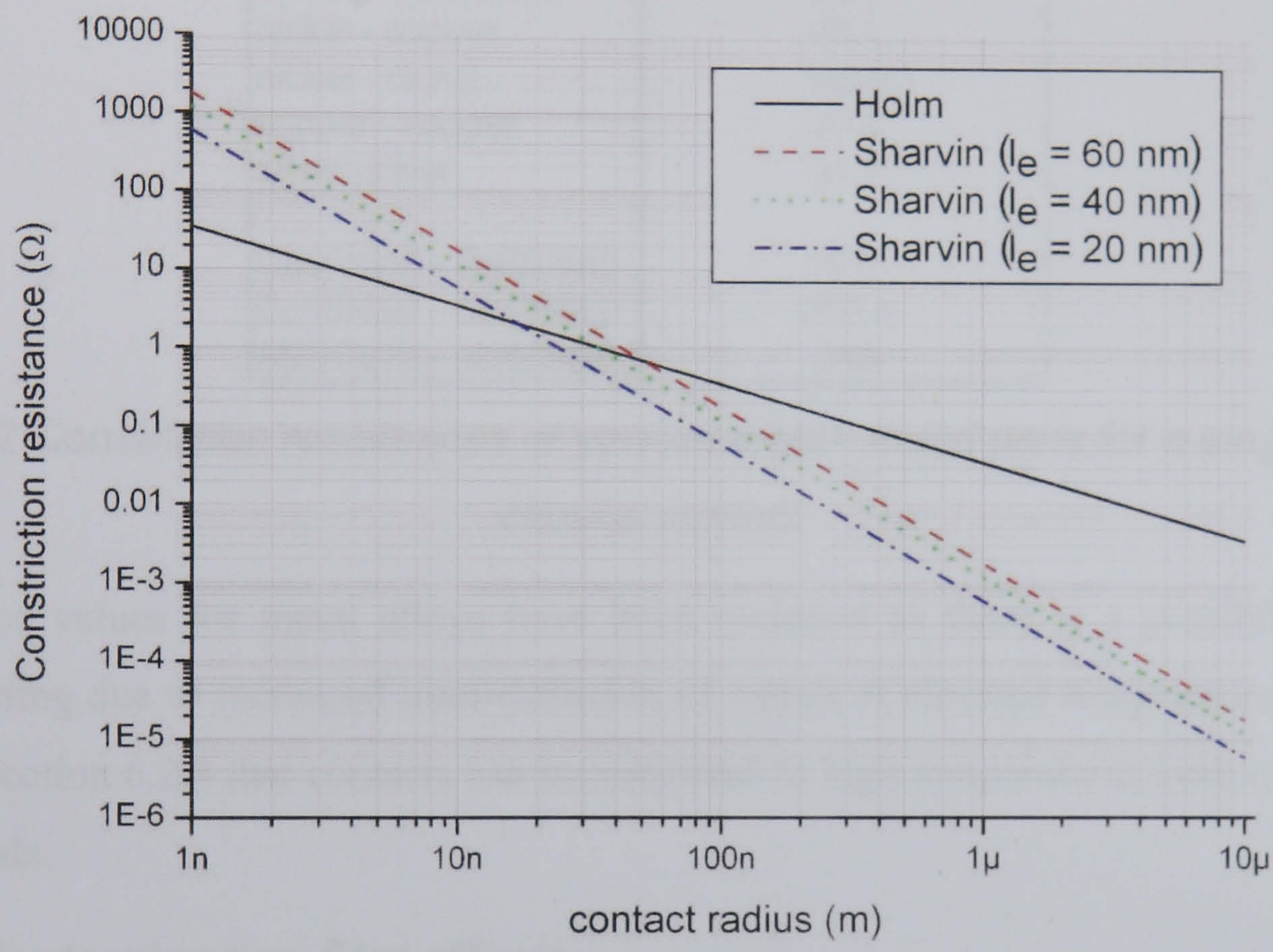

Figure 6.5 Comparison of constriction resistance as calculated by Holm and Sharvin equations

6.2.2.2 Calculated constriction resistances

Consider a nickel-aluminium contact. The resistivity (at 293 K) of aluminium is 2.65×10^{-8} Ωm and nickel is 6.93×10^{-8} Ωm. Using equation 6-6 it is possible to calculate the constriction resistance due to a single circular contact of varying radius a. This is shown in Table 6-1.

a (µm)	R (Ω)
0.1	0.2395
0.2	0.1198
0.25	0.0958
1	0.02395
10	0.002395

Table 6-1 Constriction resistance

As can be seen for a 0.5 μm diameter contact, the constriction resistance of the pure metal-metal interface is less than 0.1 Ω. A selection of constriction resistances for a series of metal-metal pairs (with a single circular contact of 0.5 μm diameter) is shown in Table 6-2. Notice that the higher resistivity of metal alloys leads to significantly higher constriction resistance values.

contact pair	R (mΩ) for a = 250 nm
gold - gold	44.3
gold - nickel	91.4
gold - aluminium	48.6
gold - copper	38.9
nickel - aluminium	95.8
nickel - copper	86.1
nickel - nickel	138.6
copper - copper	33.6
silver -silver	31.7
Cu50Ni50 - Cu50Ni50	1010
Cu10Ni90 - Cu10Ni90	356.4
Al25Cu75 - Al25Cu75	246

Table 6-2 Constriction resistances of various metal- metal pairs for a single 0.5 μm circular contact

Resistance values for metal alloys have been included as there is a possibility of such alloys forming due to increased inter-diffusion of metals at elevated temperatures. It will be shown in section 6.2.4 that contacts can be subjected to high temperatures even under typical current loads.

6.2.2.3 Contaminating film effects

Films present on the surface of the contacts can affect contact resistance in a number of ways. Mechanically, the hardness of a coating film will affect the area of contact. If the film is relatively thick then all the deformation will occur within the film and the area of the contact will be entirely dependent on its mechanical properties. If the film is very thin, such as a native oxide layer, then the area of contact will be determined by both the film and the bulk mechanical properties. This is especially true for low contact forces [10].

Depending on the nature of the film, the effect on the electrical behaviour of the contact varies. Contaminating films can be conducting (such as alloys formed by inter-diffusion of metals) or insulating (such as metal oxides or absorbed hydrocarbon layers). Figure 6.6 illustrates the effect of conducting contaminating films (of comparable thickness to the radius of contact) on the current paths within the contact.

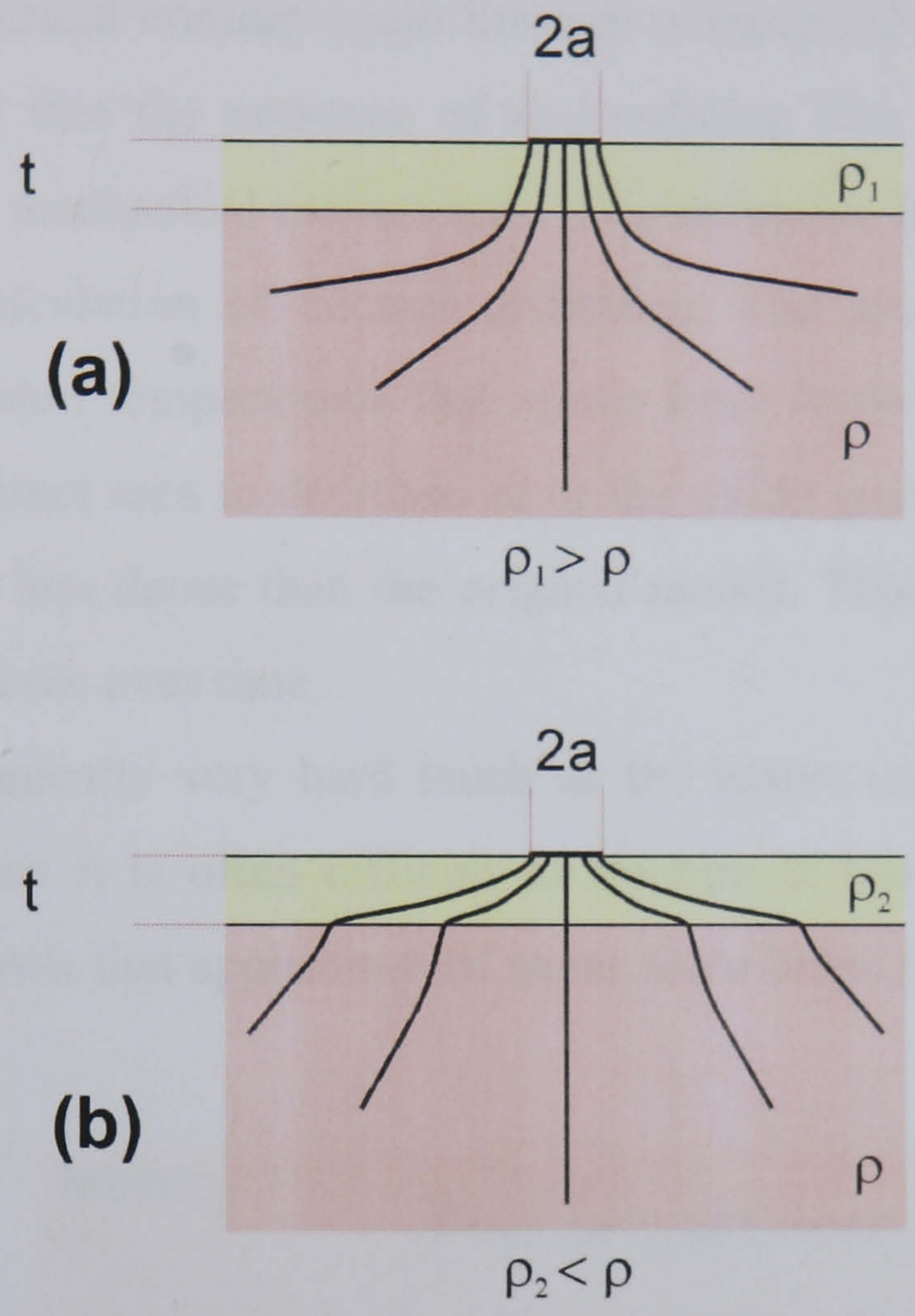

Figure 6.6 Effect of films of different resistivity on spreading resistance (a) film resistivity higher than bulk (b) film resistivity lower than bulk

If the resistivity of the film is much higher than the bulk (Figure 6.6 (a)) then very little current spreading occurs within the film [10]. In this case the constriction resistance (associated with one side of the contact) can be approximated as shown in equation 6-12.

$$R = \frac{\rho_{film} t}{\pi a^2} + \frac{\rho_{bulk}}{4a} \qquad (6\text{-}12)$$

where R is the contact resistance, a is the radius of contact, ρ_{film} is the resistivity of the film, t is the thickness of the film and ρ_{bulk} is the resistivity of the conductor. This expression assumes the current follows a cylindrical path through the film before the current spreads out in the contact bulk.

If the resistivity of the film is much lower than the bulk (Figure 6.6 (b)) then the majority of the spreading occurs in the film. In the case where the film is thick compared to the radius

of contact ($t >> a$) then the contact resistance can approximated by equation 6-6 using the film resistivity in place of the bulk.

If the contaminating film is insulating then electrical contact can only occur by some form of tunnelling (if the film is very thin). In thicker films conduction can occur by electrical breakdown under high electric fields (fritting) or by mechanically fracturing the film [10]. An illustration of electrical contact made through a fractured insulating film is shown in Figure 6.7. It is likely that the presence of an insulating film would reduce the electrical contact area below the mechanical contact area. This reduction in the radius of contact has to be included in the calculation of contact resistance. The growth of oxide films can be promoted by the elevated temperatures that result from Joule heating (see section 6.2.4). This can cause the contact area to decrease since the oxide growth forces the contacts apart (as the metal oxide is less dense than the original metal). This can led to an increasing or unstable contact resistance over time.

If the film is mechanically very hard (such as the native oxides formed on aluminium, nickel or tungsten) then it is often difficult to fracture at low forces. In the case of low contact forces it is known that application of shear force helps fracture a contaminating film [24, 25].

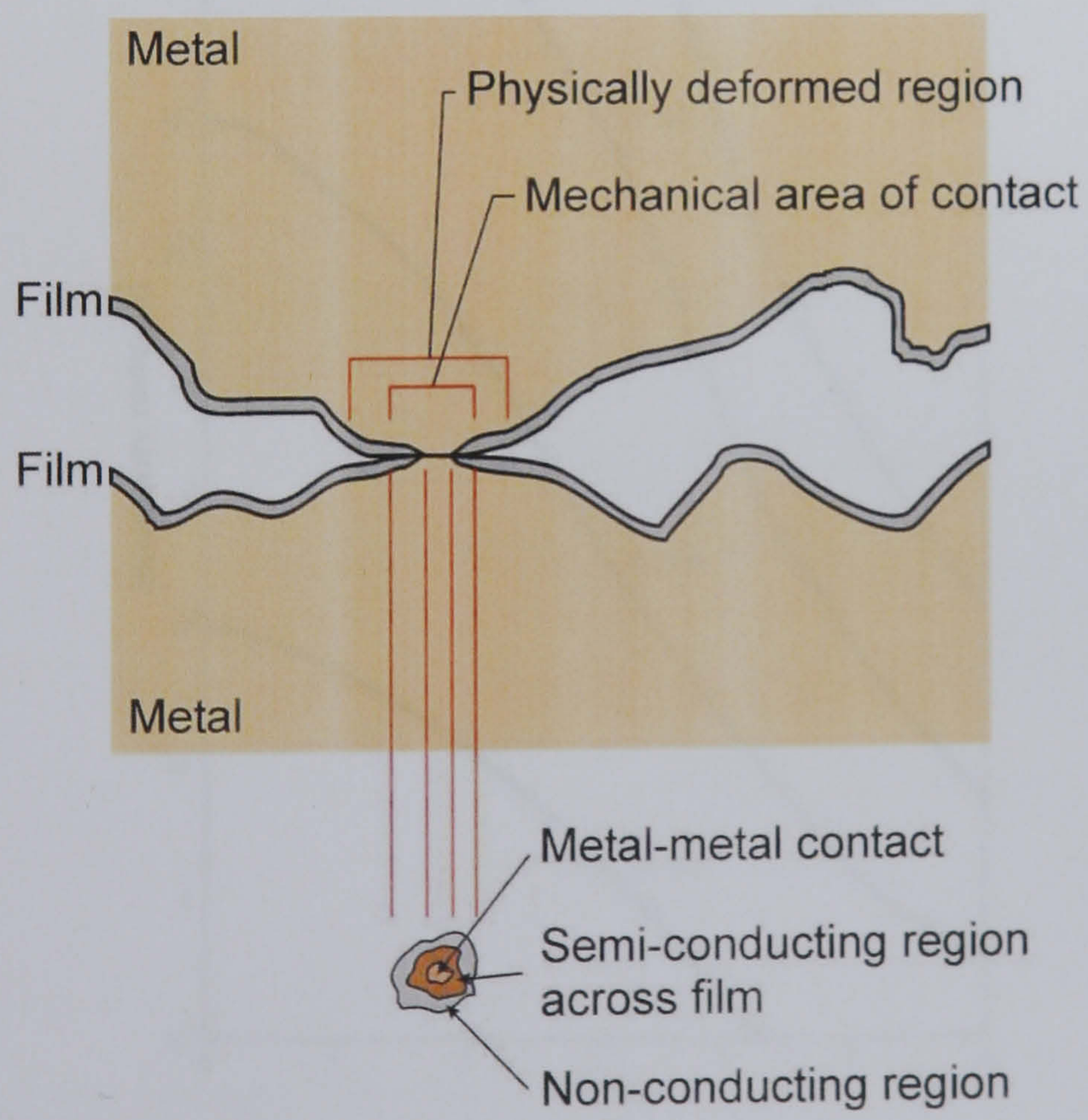

Figure 6.7 Effect of insulating films on the 'a-spot'

Insulating films can be very thin (such as layers of absorbed oxygen, water or hydrocarbons or native metal oxides [26]) or much thicker (such as metal oxides, nitrides

and sulphides formed at high temperatures or in corrosive environments [10]). The typical thickness of an absorbed film on a metal surface is 2 - 20 Å whilst native oxides (aluminium and tungsten) range from 50 - 60 Å at room temperature [26]. Absorbed films are typically thin enough to permit electrical conduction through tunnelling (although these films are also easily mechanically fractured) whilst native oxides represent much greater tunnelling resistances [26].

The contribution of tunnelling current to electrical contact resistance was addressed by Holm [27] and later Simmons [28]. The tunnel resistivity, σ_{film} (Ωm^2) of a film depends on the applied voltage V (V), the film thickness s (Å), dielectric constant ε_r, and barrier height φ (eV) (barrier height depends on the work functions of the metals in contact and the band structure of the insulating film). A detailed discussion of tunnelling is beyond the scope of this work, however relevant data for tunnel resistivity extracted from *"Generalized Formula for the electric tunnel effect between similar electrodes separated by a thin insulating film"* [28] is shown in Figure 6.8 and Figure 6.9.

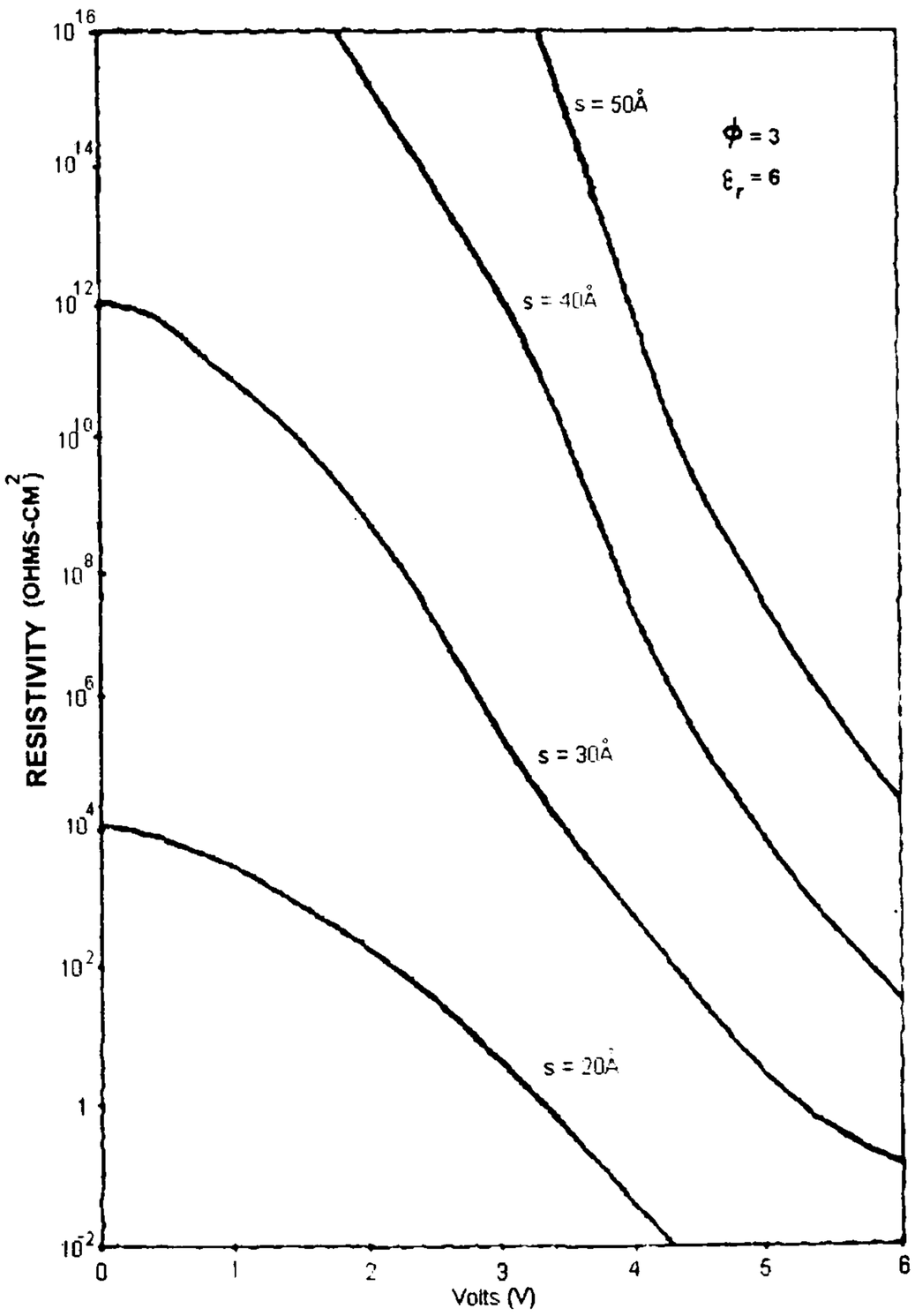

Figure 6.8 Variation in tunnelling resistivity as a function of voltage across the film [28]

Figure 6.8 shows how tunnel resistivity varies as a function of the applied voltage for films of different thickness with a dielectric constant of 6 and a barrier height of 3 eV. At low

voltages, the tunnel resistivity becomes Ohmic, this region is shown in Figure 6.9. Here the tunnel resistivity (for different dielectric constants and barrier heights) is shown as a function of film thickness. It has been reported that oxide films of 2 - 20 Å typically represent a tunnelling resistivity of 10^{-5} - 10^{-10} Ωcm^2 [26, 29-31].

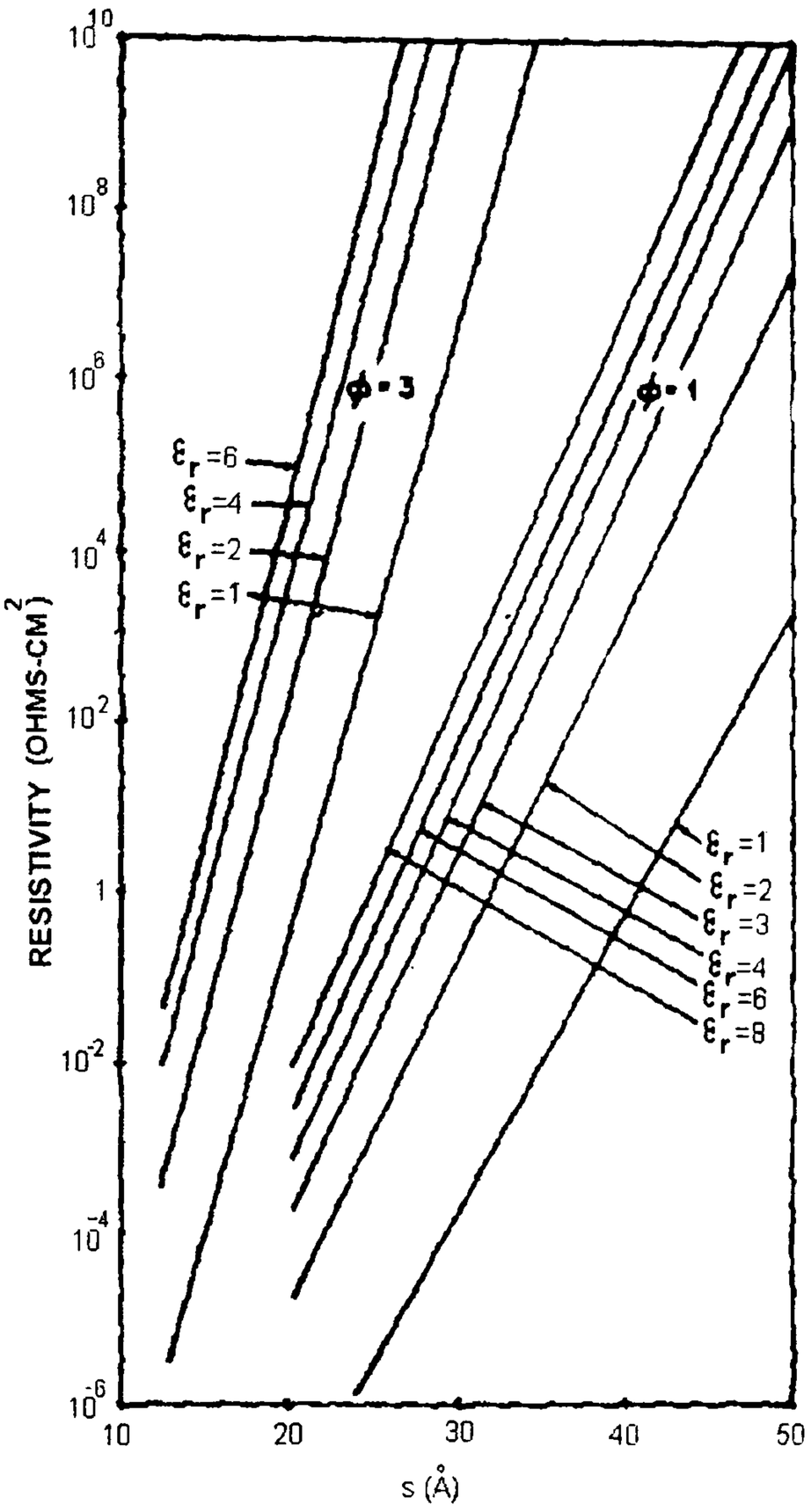

Figure 6.9 Variation in tunnelling resistivity at low voltages as a function of film thickness and dielectric constant [28]

In the Ohmic region (low voltage) the tunnelling resistance can then be calculated using equation 6-13.

$$R_{tunneling} = \frac{\sigma_{film}}{\pi a^2} \qquad (6\text{-}13)$$

where a is the radius of the (circular) contact, and σ_{film} is the film tunnelling resistivity.

From Figure 6.9 it can be seen that tunnelling resistance rapidly increases with increasing film thickness. For films thicker than 10 nm it can be assumed (for practical purposes) that no tunnelling occurs.

6.2.2.4 Material transfer

In static contacts, material can be transferred from one body to another through cold or thermal micro welding. Cold micro welding (or press welding) is a process that occurs in pure metal to metal contacts and is due to covalent bonding in hard metals (e.g. tungsten) and metallic bonding in soft metals (e.g. aluminium and copper) [26].

Thermal micro welding is due to the elevated temperature of the junction caused by Joule heating (see section 6.2.4). Adhesion starts to occur when the junction reaches "softening temperature" [26]. This process can cause a contact to degrade over multiple touchdowns. As material is removed (say from an aluminium bond pad) onto a probe, the exposed metal surface will readily oxidise. This means oxidised metal builds up on the probe, gradually increasing the contact resistance [26].

6.2.3 Estimation of contact resistance

In section 6.2.1 two estimates were given for contact area as a function of load. One relationship was based on a Hertzian analysis (elastic) and one on a semi-empirical relationship based on indentation testing (plastic). It was argued that in the case of contact between a cantilever tip and a bond pad that the assumptions required for a Hertzian analysis were invalid. Therefore the elastic analysis will be discounted and only the plastic case will be considered.

Real surfaces are not smooth and therefore mechanical contact only occurs at asperities on the surfaces. This fact means even at low loads it is reasonable to propose that plastic deformation will occur. Therefore it is valid to use hardness and force to estimate the area over which mechanical contact is established [10].

It has been discussed previously that contact occurs through multiple 'a-spots' across the apparent area of contact. Unfortunately it is not easy to estimate the size or distribution of these 'a-spots' and so instead we shall assume that all mechanical load is transmitted through a single circular contact of radius a. This simplification incurs little error since it has been shown by Greenwood [18] that the resistance of a single circular contact is very similar to multiple small contacts contained within an area of the same size.

Using equation 6-5 it is possible to estimate the contact radius a (m) in terms of contact force F (N), hardness (of the softer of the two contact materials), H (kgf/mm^2), and η a scaling factor dependent on surface roughness. An expression for contact radius a (m) is given in equation 6-15.

$$\pi a^2 = \frac{\eta F}{9.81H} \times 10^{-6} \qquad (6\text{-}14)$$

hence

$$a = 1.8 \times 10^{-4} \sqrt{\frac{\eta F}{H}} \qquad (6\text{-}15)$$

The calculated radius of contact (assuming η = 1) as a function of load is shown in Figure 6.10 for various representative hardness values.

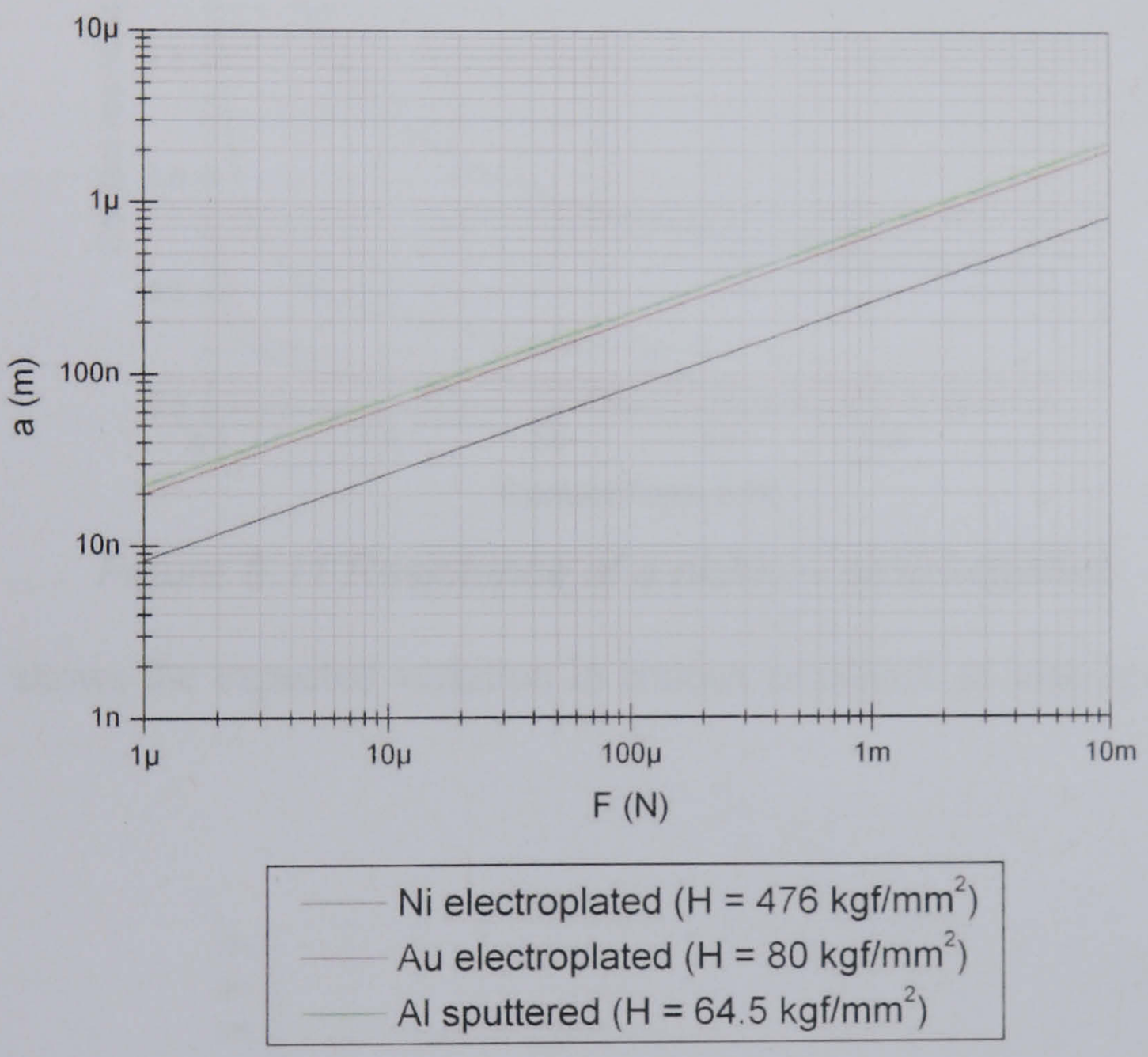

Figure 6.10 Radius of contact vs. load for different hardness values

Since it has been assumed that contact occurs through a single circular contact, in the absence of any surface films, using equation 6-6 it is possible to write an expression for contact resistance as shown in equation 6-16.

$$R_c = \frac{\rho_1 + \rho_2}{7.21 \times 10^{-4}} \sqrt{\frac{H}{\eta F}} \qquad (6\text{-}16)$$

where R_c is the contact resistance (Ω), ρ_1 and ρ_2 are the metal resistivities (Ωm), H is the hardness of the softer metal (kgf/mm^2), F is the contact force (N) and η is a scaling factor

dependent on the surface roughness. Expression of this form are widely used in contact resistance calculations [3, 10, 16, 31-33].

The resistance of a nickel-nickel contact as a function of force can be calculated using equation 6-17 for different values of η (assuming $\rho = 6.93 \times 10^{-8}$ Ωm and $H = 476$ kgf/mm^2); this is shown in Figure 6.11. It can be seen that theory would suggest for a nickel to nickel contact (free of contaminating films) only a low contact force (less than 2 mN) is required to achieve a low resistance contact (less than 1 Ω).

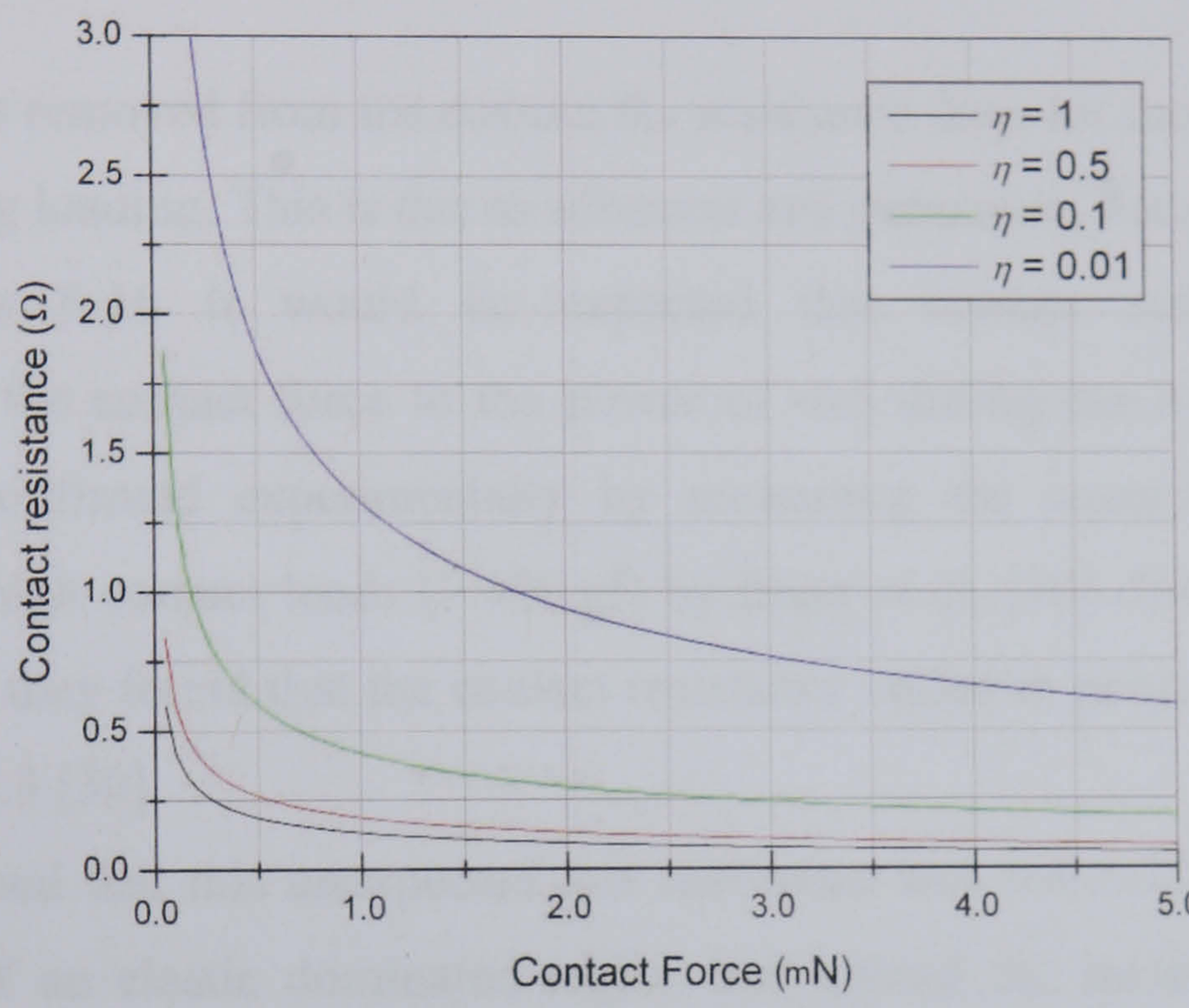

Figure 6.11 Resistance of a nickel – nickel contact

Figure 6.12 shows the expected variation in contact resistance as load is applied and then removed.

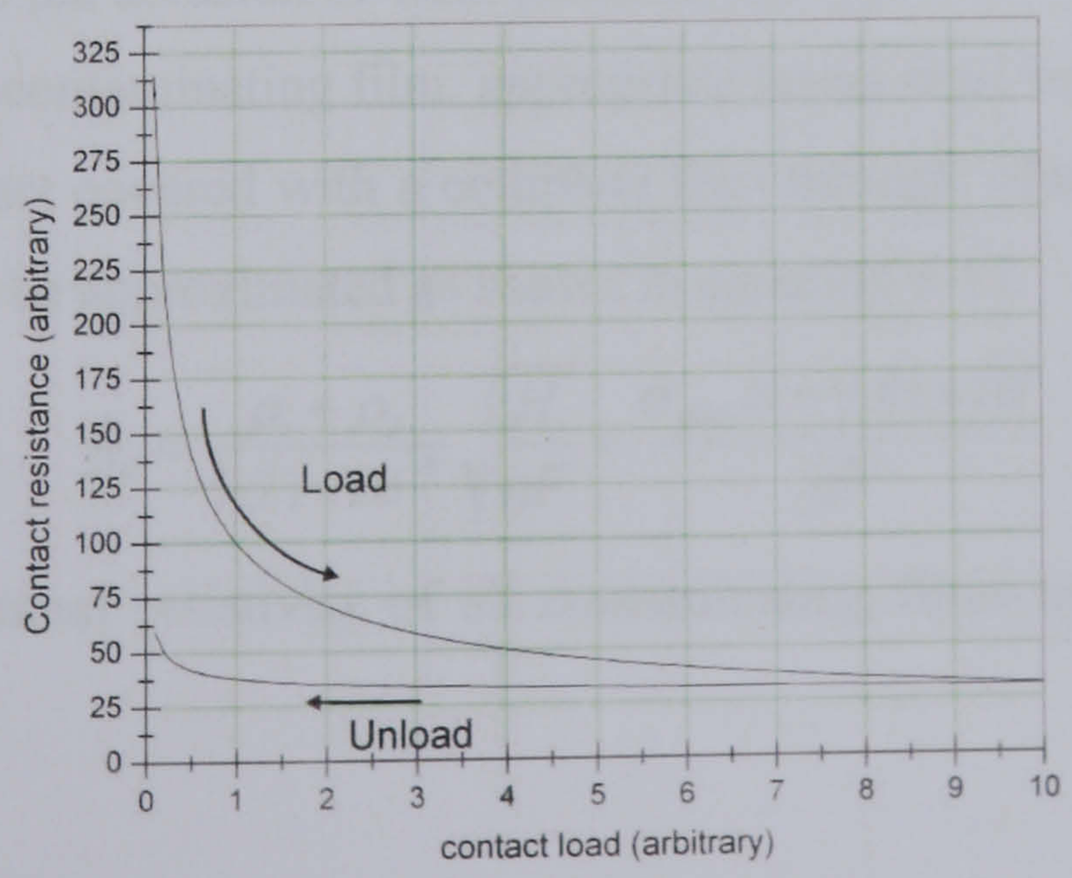

Figure 6.12 Change in contact resistance with load

The physical origin of this behaviour can be explained as follows. Initially at very low loads only very few asperities are in contact and therefore the contact resistance is very high. As the load increases these asperities are plastically deformed both increasing their area of contact (decreasing resistance) and bringing many more asperities into contact. It is this that causes the rapid decrease in contact resistance with increasing load. Gradually, as the asperities become increasingly deformed they become work hardened reducing the rate at which new asperities are brought into contact. This causes the contact resistance to approach a constant value.

When the load is removed from the contact the resistance does not increase at the same rate it decreased during loading. This is due to adhesion and permanent flattening of asperities.

From equations 6-16 it would be expected that contact resistance would vary proportionally to the contact force to the power of -0.5 during the loading of the contact. This has been confirmed experimentally by measuring the contact resistance between crossed wires at high contact loads (> 100 gf) by Ittner et al. [30]. However at lower loads (100 gf to 0.1 gf) they found that the contact resistance varied in proportion to contact force to the power of -0.3 [30].

Ittner et al. argued that this unexpected low resistance was not evidence, as many people had suggested, of an elastic dominated region but instead the result of many secondary factors including vibration smearing 'a-spots' into elliptical contacts and some asperities fortuitously interlocking in a tessellating manner. It should be noted at low contact forces that processes such as vibration affect a contact over time and can lead to unstable (dropping) contact resistance even at fixed loads. Generally, vibration causes contacts to fail in the long term due to the abrasion of wear particles etc. [3].

In the presence of a contaminating film, appropriate terms must be added to equation 6-16. For an electrical contact covered with a complete film through which tunnelling occurs, the contact resistance can be approximated as shown in equation 6-17.

$$R_c = \frac{\rho_1 + \rho_2}{7.21\times10^{-4}}\sqrt{\frac{H}{\eta F}} + \frac{\sigma_{film} H \times 9.81\times10^{6}}{\eta F} \qquad (6\text{-}17)$$

where σ_{film} is the tunnel resistivity of all contaminating films between the two contacts (Ωm^2).

Figure 6.13 shows the resistance represented by the tunnelling term in equation 6-17 (assuming the contact is dominated by the mechanical properties of nickel so $H = 476\text{kgf/mm}^2$ and that $\eta = 1$) as a function of force. If this is compared to Figure 6.11 it is clear that the tunnelling resistance will dominate spreading resistance if the tunnel resistivity is greater than $10^{-8}\ \Omega\text{cm}^2$ and the reverse is true if the tunnel resistivity is less than $10^{-9}\ \Omega\text{cm}^2$.

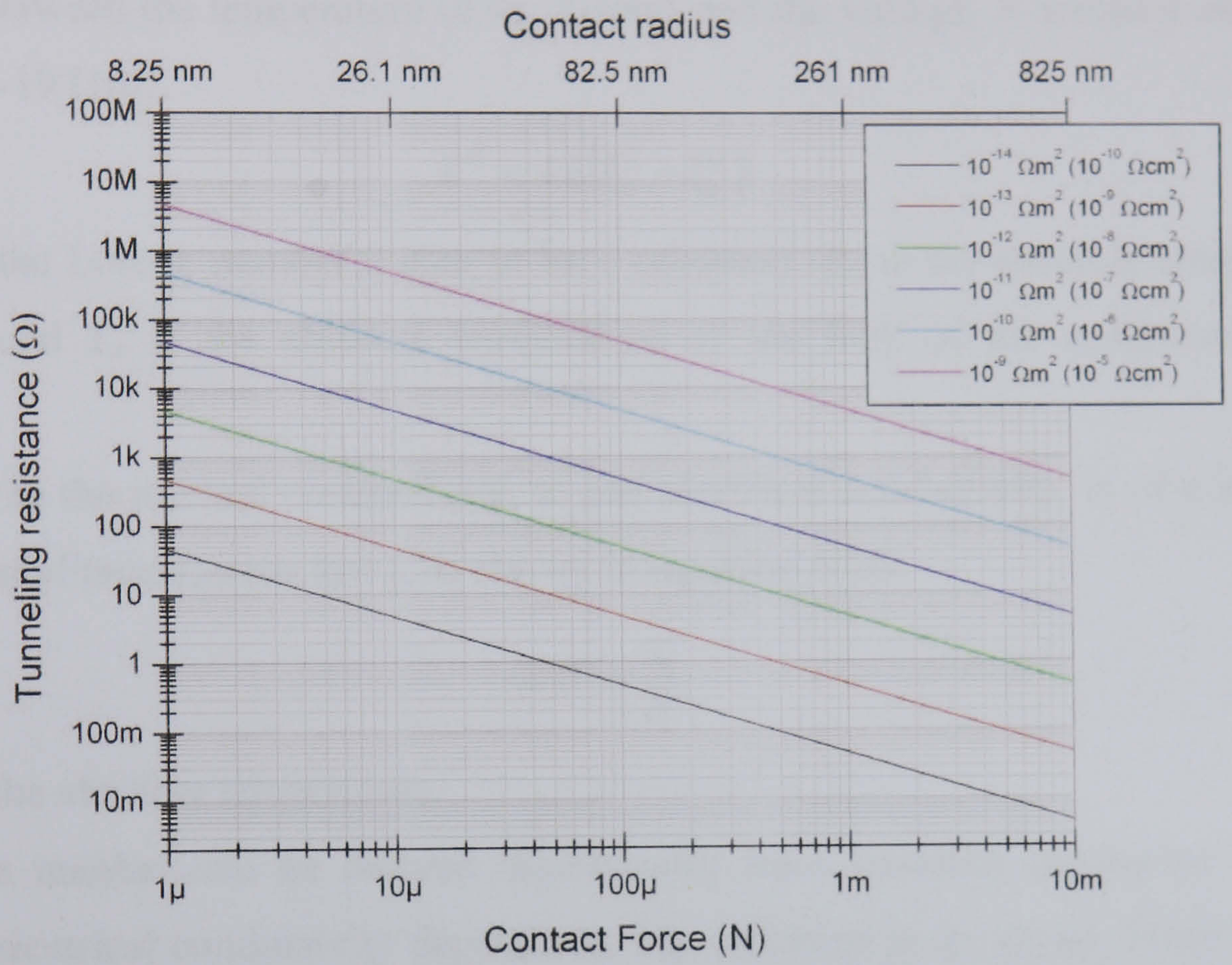

Figure 6.13 Resistance due to tunnelling

Alternatively if the contaminating films on the contact surfaces are conductive then equation 6-16 is modified as shown in equation 6-18 which is only valid if the given conditions are met.

$$R_c = \frac{\rho_1 + \rho_2}{7.21\times10^{-4}}\sqrt{\frac{H}{\eta F}} + \sum_i \frac{\left(\rho_{film}\right)_i t_i \cdot H \times 9.81\times10^6}{\eta F} \qquad (6\text{-}18)$$

$$\text{where } \sum_i t_i \approx 1.8\times10^{-4}\sqrt{\frac{\eta F}{H}} \text{ and } \left(\rho_{film}\right)_i >> \rho_1, \rho_2 \text{ for all } i$$

where $(\rho_{film})_i$ is the resistivity of the i^{th} film (Ωm) and t_i is the thickness of the i^{th} film (m) between the two contacting bodies.

6.2.4 Thermal considerations

When a current passes through an 'a-spot' it is heated by Joule heating. Since the contact spots are small there is little loss to the air and instead most heat is dissipated through the conductors, quickly causing the temperature to rise until it reaches equilibrium. The relationship between the temperature of an 'a-spot' and the voltage, V across it and is given by equation 6-19 [10].

$$V^2 = 4L\left(T_m^2 - T_o^2\right) \qquad (6\text{-}19)$$

where L is the Lorenz number (taken to be a constant), T_m is the absolute temperature of the 'a-spot' and T_o is the absolute temperature of the bulk of the conductor (ambient temperature).

L is related to the thermal conductivity, κ, and electrical conductivity, σ, of a material by the Wiedemann-Franz-Lorenz law [34] shown in equation 6-20.

$$L \cdot T = \frac{\kappa}{\sigma} \qquad (6\text{-}20)$$

where T is the absolute temperature.

The Lorenz number can be derived theoretically from quantum mechanics since both thermal and electrical conductivity depends on free electrons in the metal. From theory, the Lorenz number is defined as 2.45×10^{-8} V^2/K^2, however experimentally it varies slightly with both material and temperature as shown in Table 6-3.

Metal	L (V^2/K^2) @ 273 K ($x10^8$)	L (V^2/K^2) @ 373 K ($x10^8$)
Ag	2.31	2.37
Au	2.35	2.4
Cu	2.23	2.33
Ir	2.49	2.49
Mo	2.61	2.79
Pt	2.51	2.6
Sn	2.52	2.49
W	3.04	3.2
Zn	2.31	2.33

Table 6-3 Lorenz constants for various metals [35]

Using $L = 2.45 \times 10^{-8}\ V^2/K^2$ the temperature of the contact, as a function of voltage drop and ambient (bulk) temperature, is shown in Figure 6.14. Note that even for a small voltage drop the temperature of the contact quickly increases. The voltage drop across the contact can be calculated from the current flowing thought the contact and the contact resistance. At a current of 150 mA, a contact resistance of 1 Ω causes the contact temperature to reach 290 °C (assuming the bulk conductor is at room temperature).

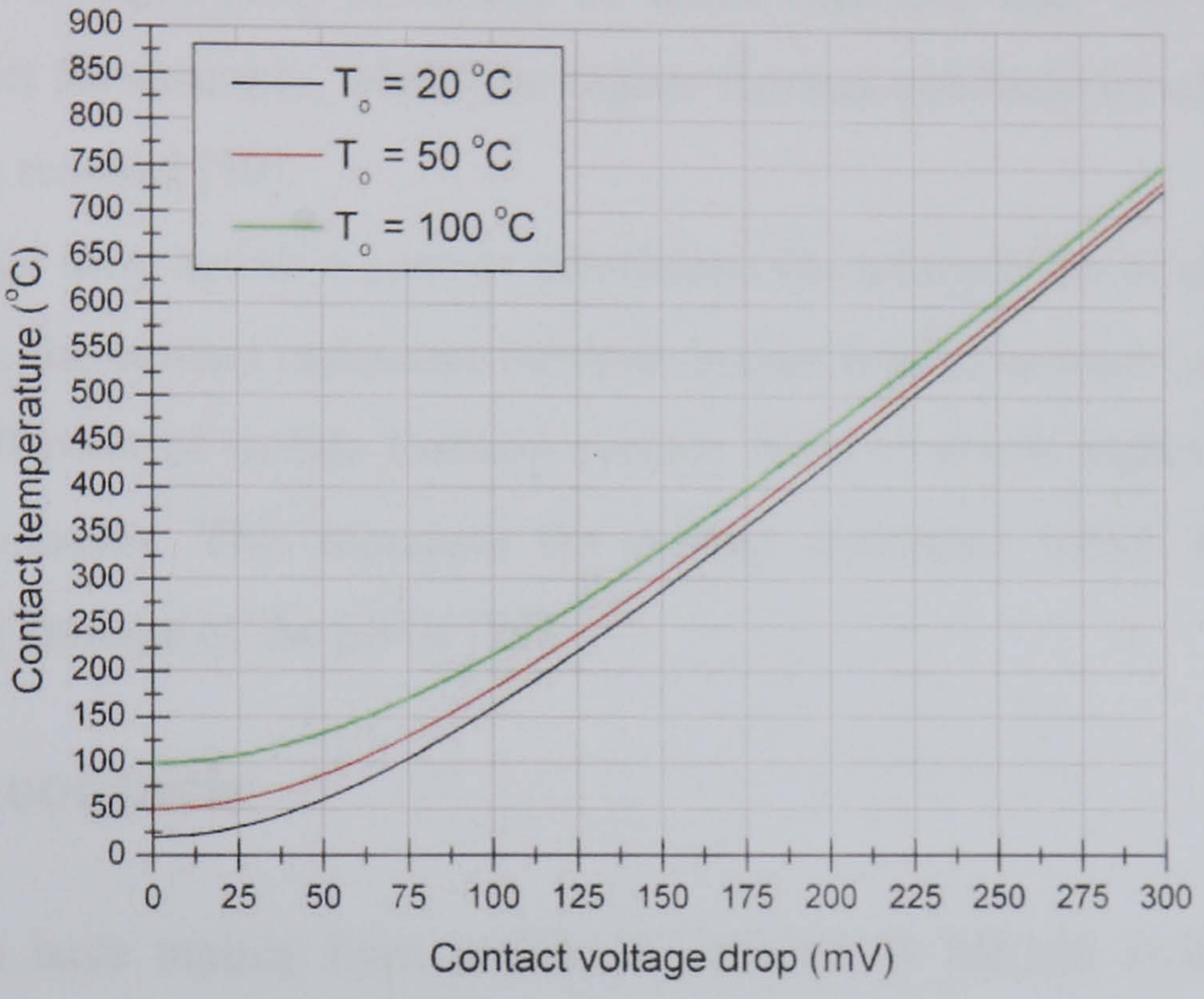

Figure 6.14 Contact temperature as a function of voltage drop

Values for melting and softening voltages (both theoretical and measured) are shown in Table 6-4. The melting point temperatures were taken from [36] whilst the softening temperatures and measured melting and softening voltages are taken from [10] and [26]. Theoretical values for melting and softening voltages were calculated from equation 6-19 assuming $T_o = 20$ °C. The softening temperature is that at which work hardened asperities in the contact are annealed [37].

Material	T_{melt} (°C)	T_{soft} (°C)	V_{melt} (V) calculated	V_{melt} (V) measured	V_{soft} (V) calculated	V_{soft} (V) measured
Iron	1538	500	0.57	0.6 *	0.26	0.19 - 0.35
Nickel	1455	520	0.55	0.65**	0.26	0.16
Copper	1085	190	0.43	0.43	0.17	0.1 - 0.12
Zinc	420	170	0.24	0.17	0.17	0.1
Molybdenum	2623	900	0.91	0.75	0.38	0.25
Aluminium	660	150	0.31	0.3	0.16	0.1
Tungsten	3422	1000	1.16	1.1	0.41	0.4 - 0.6
Silver	962	180	0.40	0.37	0.17	0.09 - 0.24
Gold	1064	100	0.43	0.43	0.15	0.06 - 0.08
Tin	232	100	0.18	0.13	0.15	0.07

T_o assumed to be 20 °C

* Valid for short periods of current only since contact doesn't reach equlibrium. Thermal runaway above $V_{melt} = 0.19$ V

** Valid for short periods of current only since contact doesn't reach equlibrium. Thermal runaway above $V_{melt} = 0.16$ V

Table 6-4 Melting and softening voltages for various metal contacts

Underlying equation 6-19 was the assumption that thermal equilibrium can be reached. This is only true if heat produced by the Joule heating (caused by the constriction resistance) can be dissipated by thermal conduction through the metal [10]. Iron and nickel are special cases where the change in resistivity and thermal conductivity is such that above a critical temperature, the thermal conductivity of the contact is incapable of removing all the heat generated and equilibrium is not reached. This leads to thermal runaway of the contact (for a constant applied voltage) [10]. It should be noted that this does not apply to a nickel-aluminium contact for example, where the higher thermal conductivity of aluminium allows equilibrium to be reached [10].

Since the voltage drop across a contact determines the temperature of an 'a-spot' it is very important to keep the contact resistance between bodies low. If contacts become hot this will promote inter-diffusion of metals forming surface films of much higher resistivities or the growth of oxide layers. This increases the contact resistance which enforces a positive feedback, risking damage of the probe [38].

6.2.5 Micro contacts

Micro contacts have mainly been studied in relation to MEMS switches. Due to their extremely small nature, these surfaces must be treated as rough and are often modelled using fractal geometry techniques (where the contact spot distribution follows the power law proposed by Mandelbrot) [39]. At forces less than 200 mN such modelling has shown the contact radius of an average 'a-spot' (between two sputtered gold beams) is less than 50 nm [39]. This means that the contact size is comparable to the mean free path of the electrons in the metal and resistance should be calculated using a combination of the equations derived by Holm and Sharvin. In ballistic conduction, scattering only occurs at the boundary of the contact. Whilst this leads to an increase in the constriction resistance it does not lead to additional heating of the contact since it does not occur within the bulk [39]. This effect means that equation 6-19 (the contact temperature in terms of voltage drop) overestimates the temperature of the contact.

At even smaller force ranges (100 μN and below) the contact resistance can be much greater than expected. This is due to absorbed films which can contribute to the support of contact loading [40] reducing the metal-metal contact areas.

Lastly the degradation of micro contacts can be much more rapid than larger contacts. This is since most failure mechanisms are surface effects (e.g. the growth of oxide films) and at low forces the surface properties of the contact will dominate its behaviour.

6.3 Test results – contact resistance

6.3.1 Introduction

Chapter 4 describes the equipment used to determine the contact resistance as a function of load. Briefly, a test tip made from electroplated nickel was brought simultaneously into contact with two cantilever probes. The probes were connected in pairs such that on contact to the test tip they formed a complete circuit. On electrical contact, current could flow down one side of the test tip, through the cantilever probes and return along the other side of the test tip.

The total path resistance was composed of the resistance of the test tip, the cantilever probes and two contacts (interfaces). To obtain the contact resistance of one interface the cantilever and test tip resistance had to be subtracted from measured resistance after which the value was halved. The resistance of the wires between the test tip and ohmmeter was eliminated by the use of a four wire arrangement. The measured value of contact force was also halved to obtain the force associated with one probe and hence contact.

All results discussed in this section have been processed in this way and therefore show the contact resistance and force of a single probe-test tip interface.

Testing was performed between gold coated test tips and gold coated cantilever tips, between gold coated test tips and uncoated nickel cantilever tips, between uncoated nickel test tips and uncoated nickel cantilever tips and between aluminium coated test tips and uncoated nickel cantilever tips. In the following sections the results for each is discussed.

6.3.2 Gold coated cantilever tips versus gold coated test tip

Three different behaviours in contact resistance with contact load were observed and representative examples are shown in Figures 6.15 (a), (b) and (c). Each cantilever tested had tips electroplated from the smooth nickel formulation.

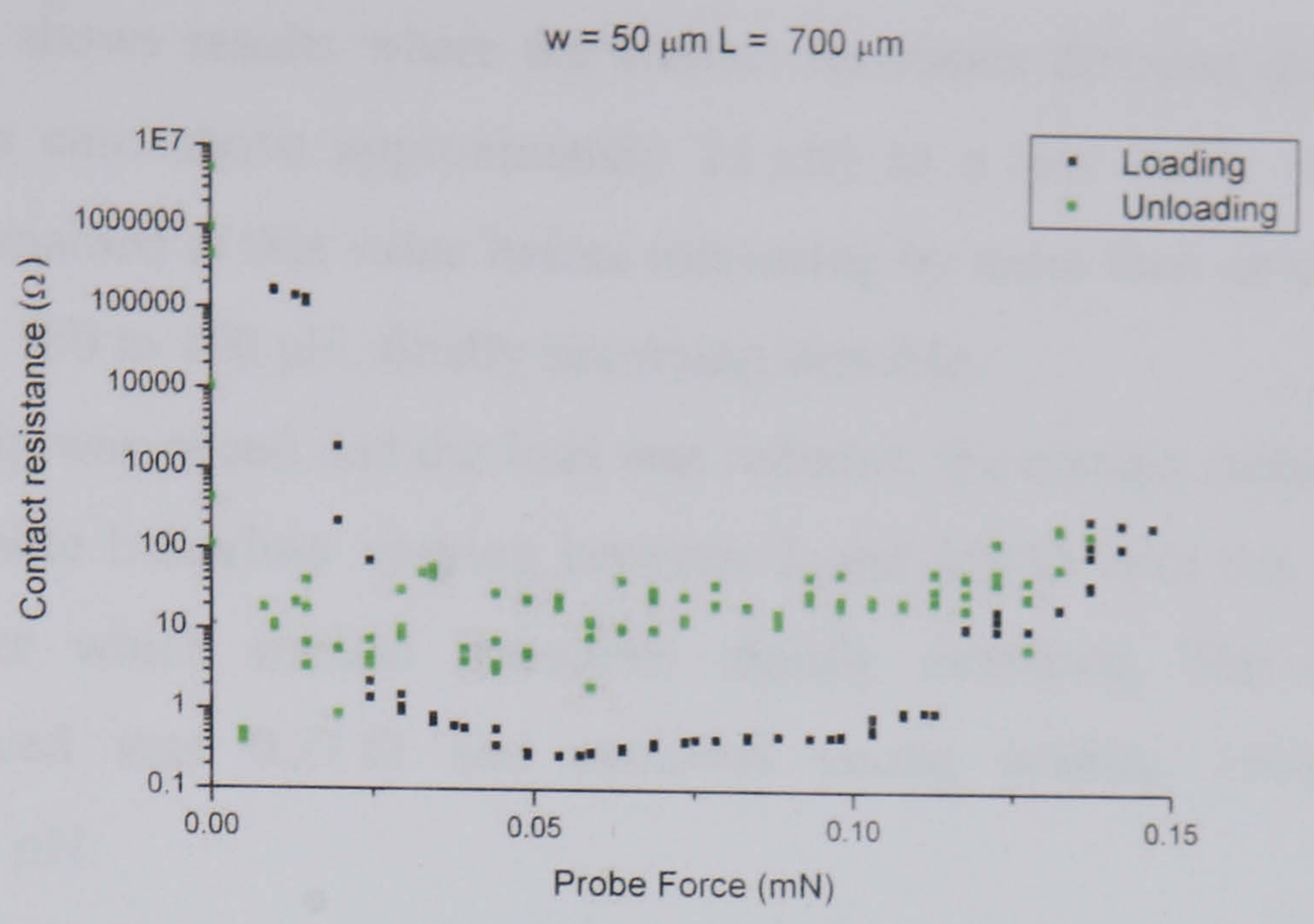

(a)

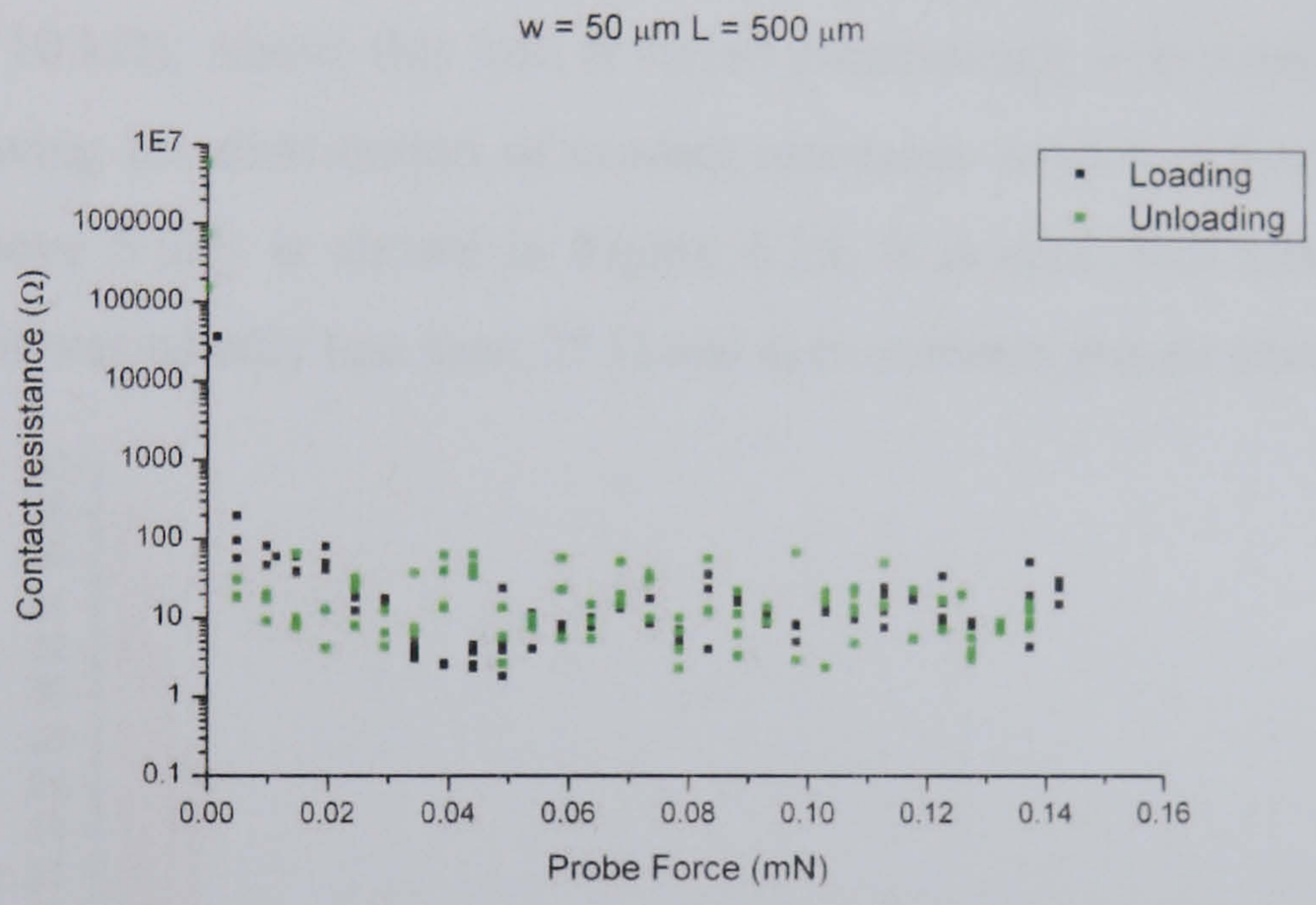

(b)

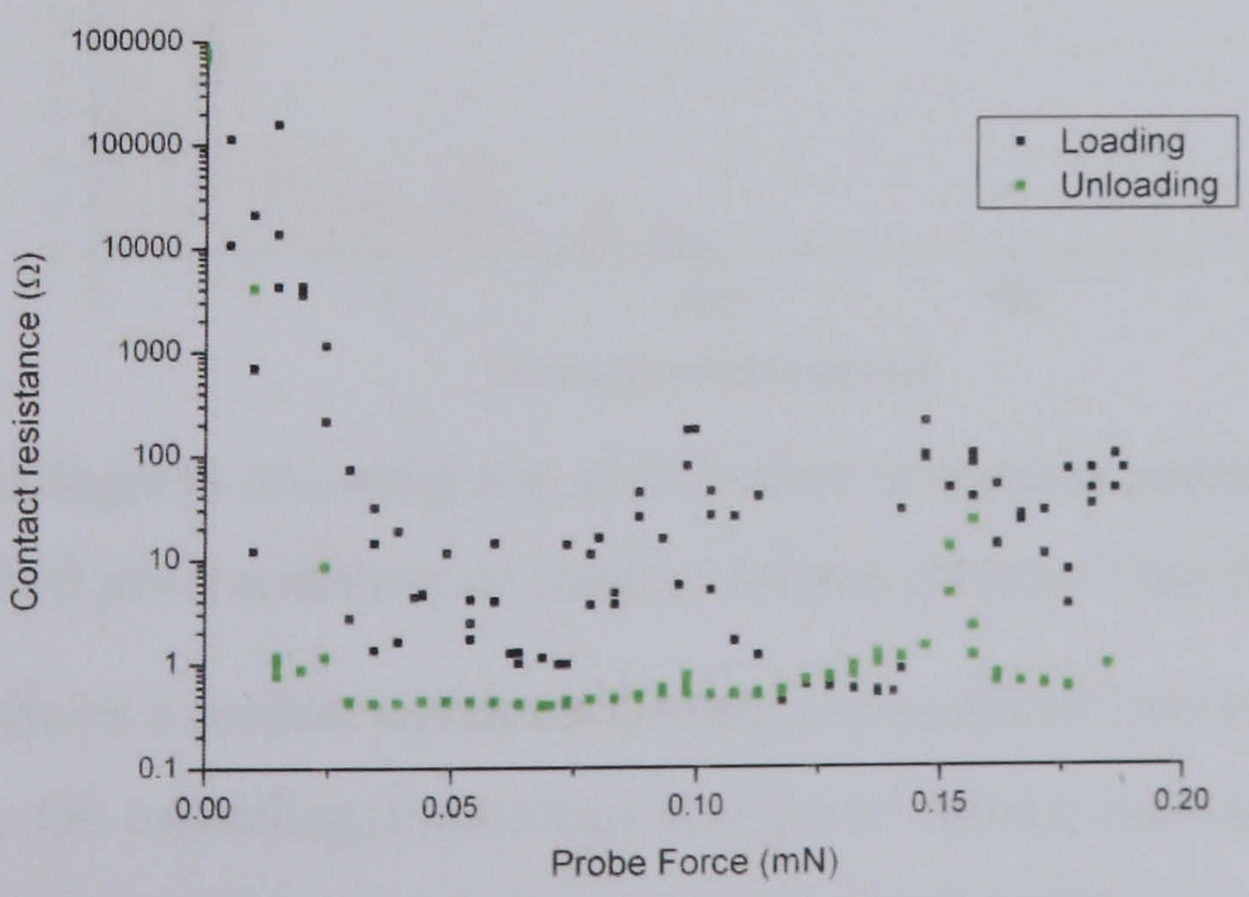

(c)

Figure 6.15 Contact resistance versus probe force for gold on gold contacts

Figure 6.15 (a) shows results where the contact resistance dropped quickly as load was increased (in this case above approximately 25 μN) to a low stable value. The contact resistance then remained at this value before increasing by more than an order of magnitude in the force range 100 to 150 μN, finally becoming unstable.

When the test tip was raised and the load was reduced, the contact resistance continued to display this unstable behaviour varying between 2 and 250 Ω until the contact force was below 5 μN after which contact resistance rapidly increased. The minimum contact resistance observed was 0.27 Ω and occurred during loading cycle at a force of approximately 55 μN.

Figure 6.15 (b) shows a contact that failed to become stable over the entire loading and unloading range of the cantilever. Below a contact load of 5 μN the resistance value was very high (above 10 kΩ). Above this load it varied continuously over a range of 2 to 200 Ω. A histogram showing the distribution of contact resistance extracted from this data set (at contact forces above 5 μN) is shown in Figure 6.16. It is clear that although the contact resistance varied it was usually less than 25 Ω and almost never greater than 100 Ω.

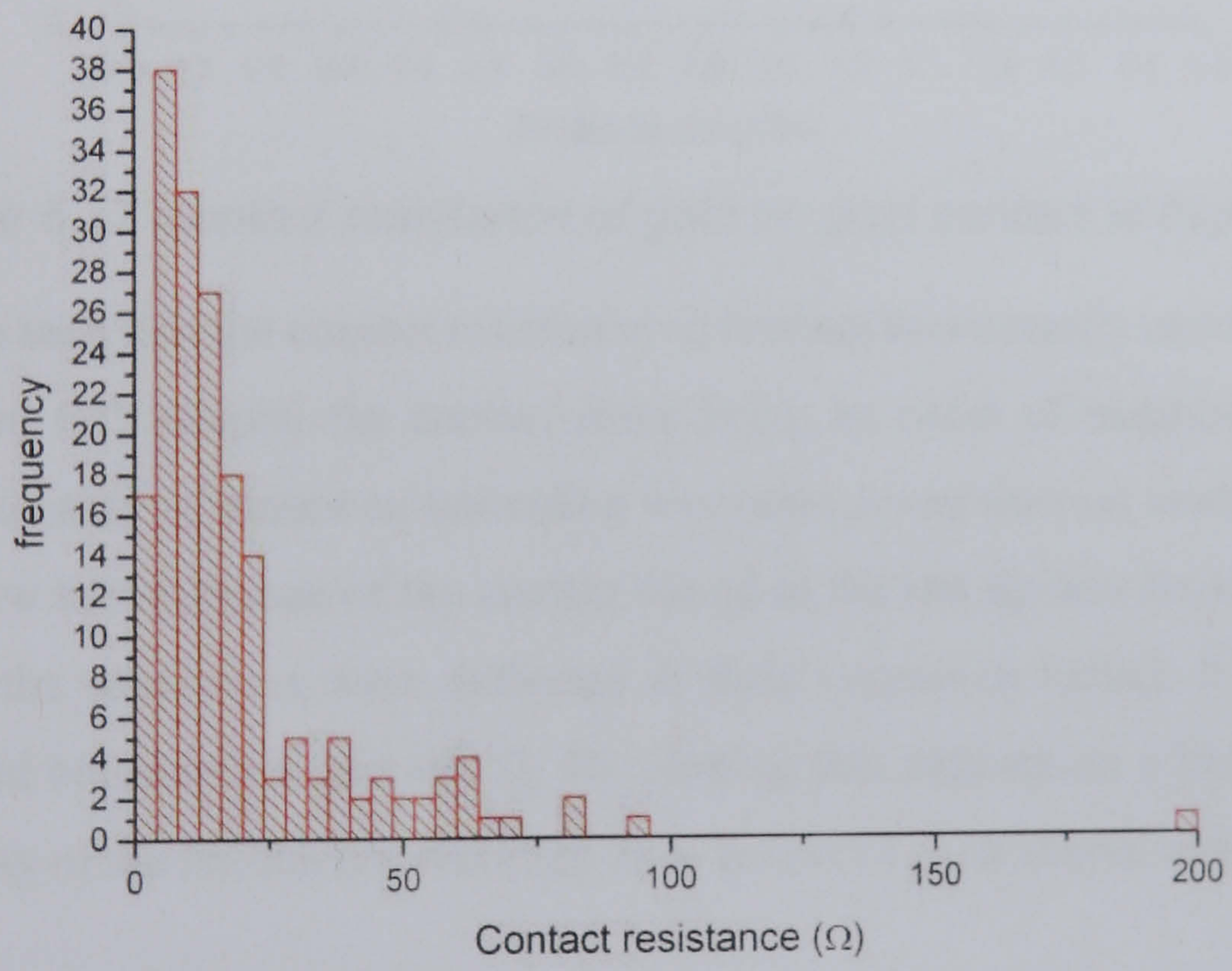

Figure 6.16 Histogram showing the distribution of contact resistance for a 50 by 500 μm cantilever at contact forces greater than 5 μN

Figure 6.15 (c) shows a contact which on loading intermittently cycles between an unstable and stable contact. On unloading, the contact resistance initially increased before decreasing to a low stable resistance. The contact resistance remained at this low value through most of the unloading, decreasing slightly as the contact load decreased. The minimum contact resistance measured was 0.39 Ω (at a load of 70 μN) during the unloading cycle.

The data sets shown in Figure 6.15 all relate to experiments where the contact forces were relatively low (maximum 200 μN). The theory developed in section 6.2 suggests that lower stable contacts could be achieved by the application of higher contact forces. An example of such an experiment is shown in Figure 6.17 where a shorter cantilever has been tested resulting in a maximum contact force of approximately 1400 μN.

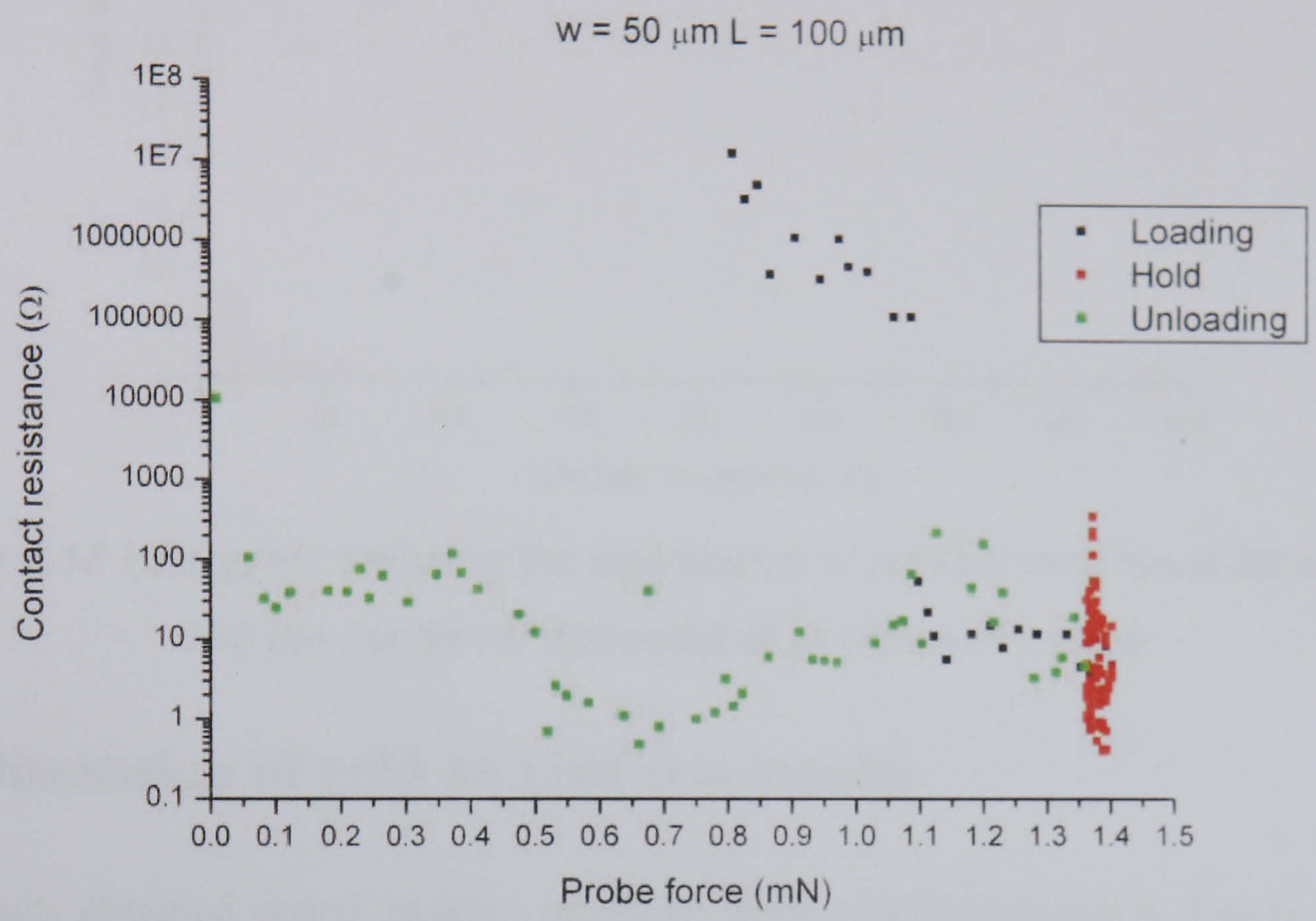

Figure 6.17 Contact resistance of gold on gold contact at high force

Here it can be seen that the contact resistance on loading was actually much higher that any shown in Figure 6.15 despite the contact force being an order of magnitude higher. Also notice that the contact resistance on unloading was much lower than on loading. The red data set indicates how the resistance of the contact varied as the test tip was fixed at its maximum travel (so that the cantilevers were deflected at their maximum value). It can be seen the resistance varied between 0.4 and 400 Ω. By plotting this data set on a histogram it can be seen the majority of the resistances recorded were below 25 Ω as shown in Figure 6.18.

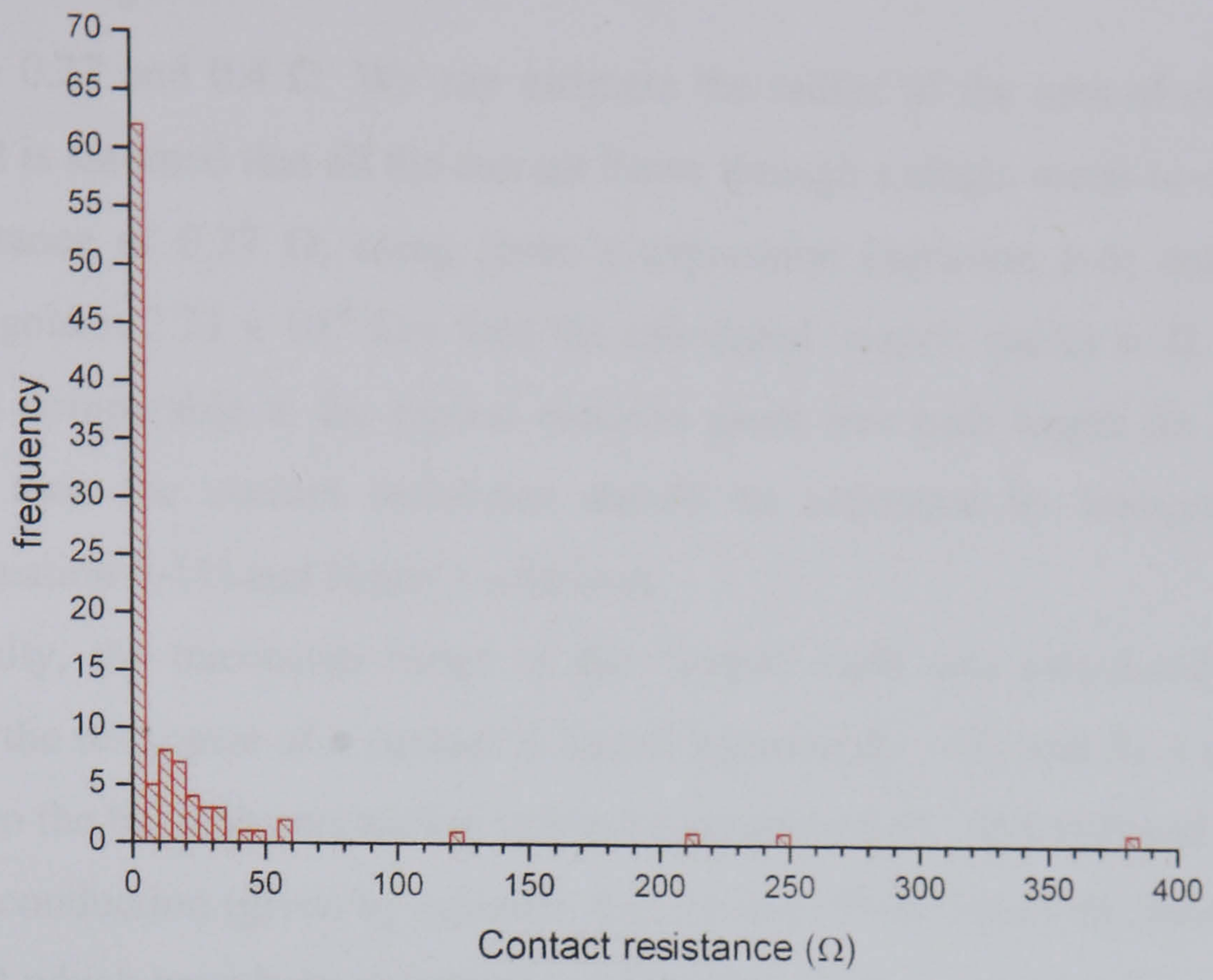

Figure 6.18 Histogram showing the distribution of contact resistance for a 50 by 100 μm cantilever deflected at its maximum value

6.3.3 Discussion of gold on gold test results

The results obtained varied greatly - however, some conclusions can be drawn. A total of 19 cantilever pairs were tested of which 52% produced a low resistance stable contact (such as the loading results shown in Figure 6.15 (a)), 16% showed an intermittently stable contact (such as the loading results shown in Figure 6.15 (c)) and 32% never formed a stable contact (such as the results shown in Figure 6.15 (b)).

Generally (with the single exception of the result shown in Figure 6.15 (a)), for the same force, the unloading resistances were lower than the loading resistances. This can be attributed to plastic deformation of surface asperities. In the case of Figure 6.15 (a) it is believed that the gold film on either the test tip or cantilever tip delaminated during unloading resulting in an unstable, higher resistance.

It was clear, that in general, the contact force did not dominate the contact resistance behaviour. For instance, the minimum contact resistance was never observed at the maximum applied force. In contrast, resistance was often seen to increase with increasing load. The most plausible explanation for such behaviour was the presence of surface contamination as will be discussed in section 6.3.3.2.

If we only consider only the tests where a stable contact was formed, the minimum measured contact resistance (recorded in either the loading or unloading cycle) was found to

vary between 0.27 and 0.4 Ω. We can estimate the radius of the area of contact from the resistance if it is assumed that all the current flows through a single metal-to-metal contact.

For a resistance of 0.27 Ω, using Holm's expression (equation 6-6) and assuming the resistivity of gold is 2.21 x 10^{-8} Ωm then the calculated 'a-spot' radius is 41 nm. Since this spot radius is comparable to the typical electron mean free path length (in metals at room temperature) then the contact resistance should be estimated by interpolating between Sharvin's (equation 6-11) and Holm's solutions.

For simplicity, the maximum range of the 'a-spot' radii was calculated. According to Wexler [23], the resistance of a contact is bound between $R_S + R_H$ and $R_S + 0.694R_H$, where R_S is related to the ballistic conduction (given by equation 6-11, Sharvin) and R_H is related to the diffusive conduction (given by equation 6-6, Holm). These limits are shown in equations 6-21 and 6-22 which have been rearranged as functions of the 'a-spot' radii, a.

Upper limit:
$$R = \frac{4\rho l_e}{3\pi a^2} + \frac{\rho}{2a} \quad \Rightarrow Ra^2 - \frac{\rho}{2}a - \frac{4\rho l_e}{3\pi} = 0 \qquad (6\text{-}21)$$

Lower limit:
$$R = \frac{4\rho l_e}{3\pi a^2} + \frac{0.694\rho}{2a} \quad \Rightarrow Ra^2 - \frac{0.694\rho}{2}a - \frac{4\rho l_e}{3\pi} = 0 \qquad (6\text{-}22)$$

Solving the quadratic expressions shown in equations 6-21 and 6-22 (assuming l_e = 40 nm and ρ = 2.21 x 10^{-8} Ωm) it can be shown that resistance of 0.27 Ω has an 'a-spot' radius between 54 nm and 63 nm.

Table 6-5 shows the minimum measured values of contact resistance and the forces at which they occurred for all the tests that formed stable contacts. Since these are the minimum values of resistance, the 'a-spot' radii relate to the largest possible area of electrical contact experienced during each experiment.

Contact Force (μN)	Resistance (Ω)	Tip type	Estimated radius of contact (nm) *
54	0.27	Smooth	54 – 63
69	0.39	Smooth	42 – 48
119	0.31	Smooth	49 – 57
275	0.31	Smooth	49 - 57
1388	0.40	Smooth	42 - 47

Table 6-5 Minimum contact resistance and contact force for gold on gold contacts

* Calculated using equations 6-21 and 6-22 (assuming l_e = 40 nm and ρ = 2.21 x 10^{-8} Ωm).

As can be seen the 'a-spot' radii vary between 42 and 63 nm. Conversely the damage to the gold film on the cantilever tip after testing (Figure 6.19 (b)) was observed to be several microns in diameter. Therefore it would seem the mechanical area of contact was greater than the electrical and hence it can be concluded there was surface contamination. Possible contaminating films are discussed in section 6.3.3.1.

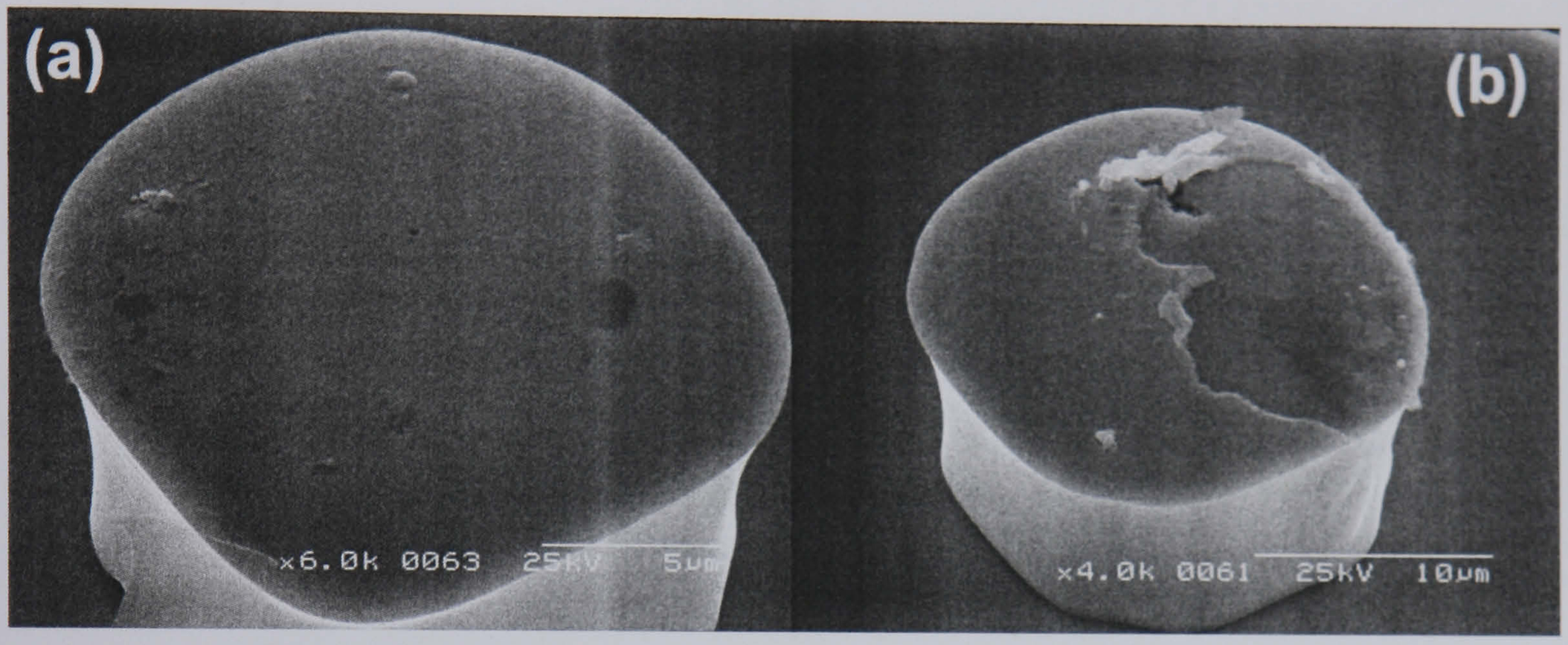

Figure 6.19 (a) Gold coated smooth nickel tip before contact (b) Gold coated smooth nickel tip after contact

6.3.3.1 Contaminating films

If poorly conducting or insulating films were present on the surface of either the test tip or cantilever tip it would imply that the actual contact area was larger than previously calculated. This could mean the contact consisted of multiple poorly conducting paths or some conducting and some non-conducting contacts. Such a film would most likely result from the formation of an alloy (for instance between the electroplated nickel and evaporated gold) or absorbed contaminating layers such as hydrocarbons and water. Contaminating films are unlikely to be stable oxides or other ceramic type compounds since gold is largely inert.

The diffusion coefficient for nickel in gold at 200 °C is reported as 1.2×10^{-19} cm^2/s [41]. If a standard one dimensional solution (see "Laboratory techniques in Electro-analytical chemistry" [42]) for the concentration (resulting from an initial concentration profile described by a step function), as a function of time and space, is solved it can be shown that after 1 year at 200 °C, the material 100 nm from the original gold-nickel interface still consists of 99.99% gold. This is shown graphically in Figure 6.20.

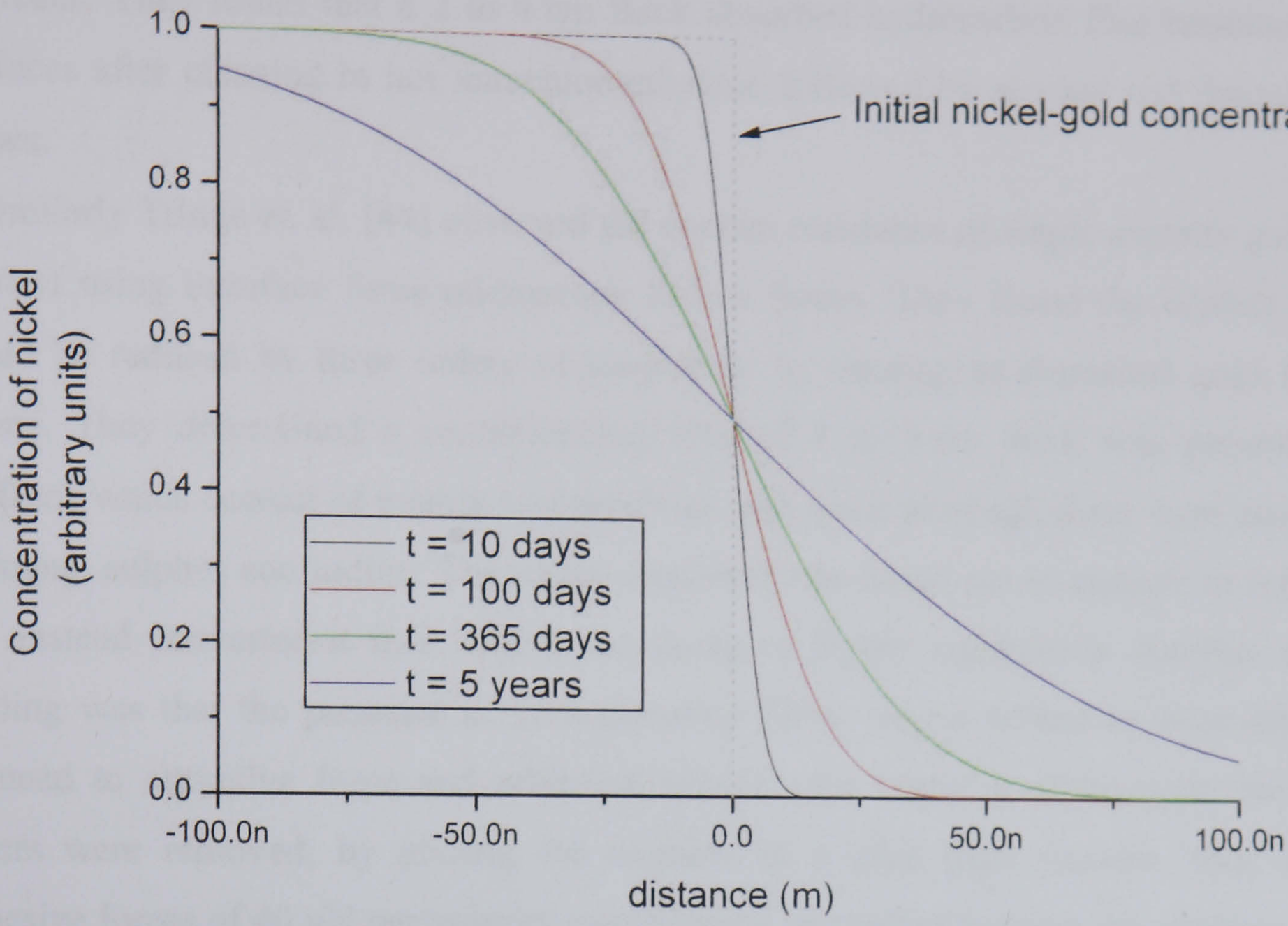

Figure 6.20 Nickel concentration as a result of diffusion into gold at 200 °C

The thickness of the gold film evaporated on the test tip was 200 nm (with a 15 nm chromium adhesion layer) whilst the gold film on the cantilever tips was 150 nm thick (with a 10 nm titanium adhesion layer). The cantilever probes were not exposed to high temperatures during processing and were stored at room temperature.

It is possible that Joule heating during the electrical testing could cause the temperature to rise significantly (see section 6.2.4). However the low value at which the current was limited (1.5 mA maximum) and short duration of any testing mean it was unlikely that Joule heating would have driven significant solid state diffusion. Therefore, assuming that the diffusion of chromium or titanium into gold behaves similarly to nickel, it is unlikely that any significant alloy formation has occurred.

Now we will consider the case for absorbed contaminating films.

Ma et. al. [43] studied reliability of RF MEMS switches as a function of contact cleaning methods, storage and packaging technologies. They observed significant organic contamination resulting from the ambient environment consisting mainly of carbon and sulphur. Contamination of 'clean' gold surfaces was found to be initially very rapid when exposed to a cleanroom environment. Further, contamination was found to slowly rise even in a hermetically sealed container.

Hyman et. al. [40] studied the contact resistance and surface damage in gold RF MEMS switches. They found that a 2 to 4 nm thick absorbed hydrocarbon film remained on gold surfaces after cleaning in hot tetrachloroethylene followed by alcohol and deionised water rinses.

Similarly Tringe et. al. [44] observed the contact resistance of single asperity gold on gold contact using interface force microscopy at low forces. They found the contact resistance could be reduced by three orders of magnitude by treating as deposited gold films with ozone. They determined a contaminating film of 4 to 6 nm thick was present on their surfaces which consist of mainly hydrocarbons and water although there were also traces of nitrogen, sulphur and iodine. The ozone treatment was found not to remove or thin the film but instead converted it from highly insulating to highly conductive. Another interesting finding was that the presence of contaminating films, ozone treated or otherwise, greatly reduced to attractive force and adhesion between the surfaces. If however the absorbed layers were removed, by placing the contacts in a ultra high vacuum, then significant adhesive forces of 40 μN per asperity were formed on contact between the surfaces.

Although no chemical surface analysis of the contacts was conducted, it was thought that this type of hydrocarbon and water contamination was the most likely cause of contamination to the gold surfaces; especially as the test tips were stored for several months.

6.3.3.2 Proposed gold contact behaviour

Two forms of behaviour need to be explained: These are the total failure to form a stable contact and the cyclical formation of a stable contact followed by increasing contact resistance and eventual loss of stability.

SEM observation of the used test tips and cantilever tips showed areas where gold has been ripped from the surface of the contacts as can be seen in Figure 6.21. This means that adhesion must be occurring, causing the gold to be removed when the contacts were separated. This is likely to result from either cold pressing or from micro welding as a result of the applied testing voltage.

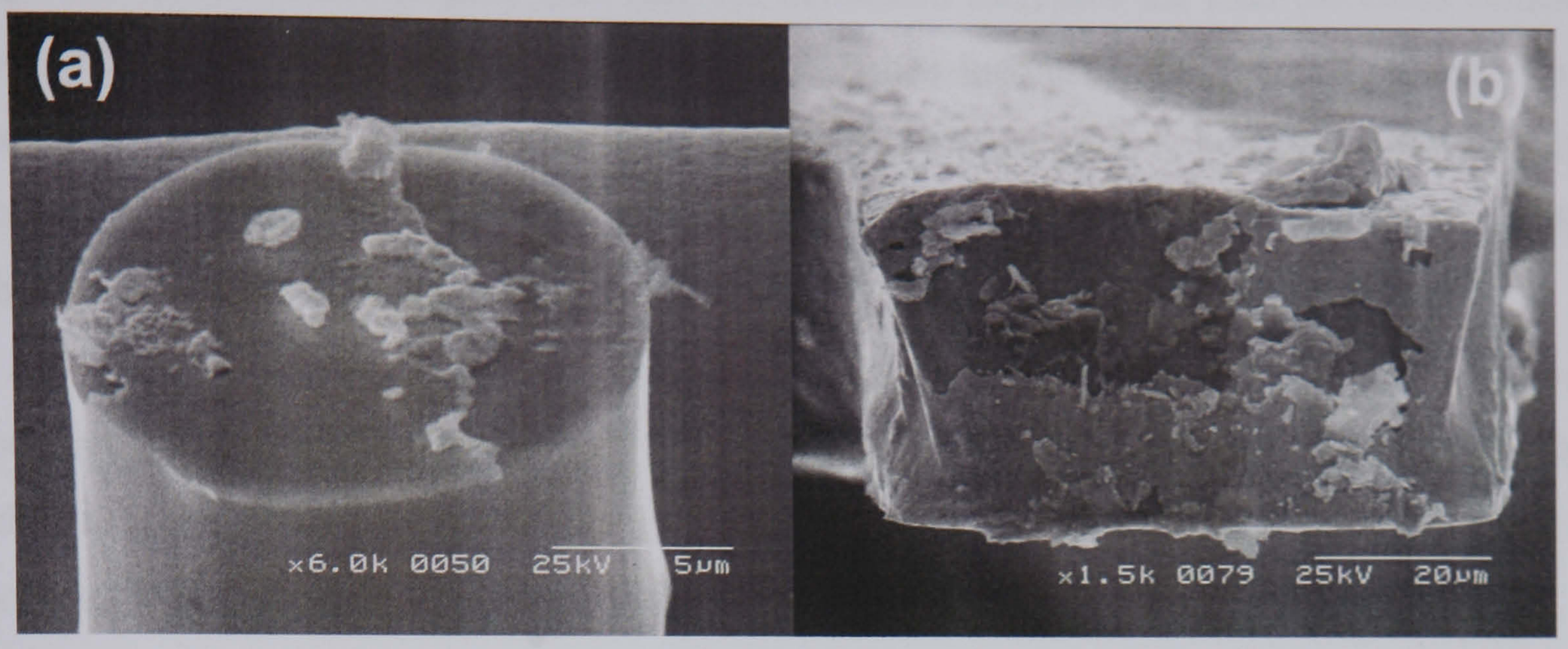

Figure 6.21 SEM images showing (a) a cantilever tip missing gold coating after testing was performed (b) a test tip missing gold coating after testing was performed

The following is a proposal for how the contacts formed intermittently stable periods. The process is shown diagrammatically in Figure 6.22.

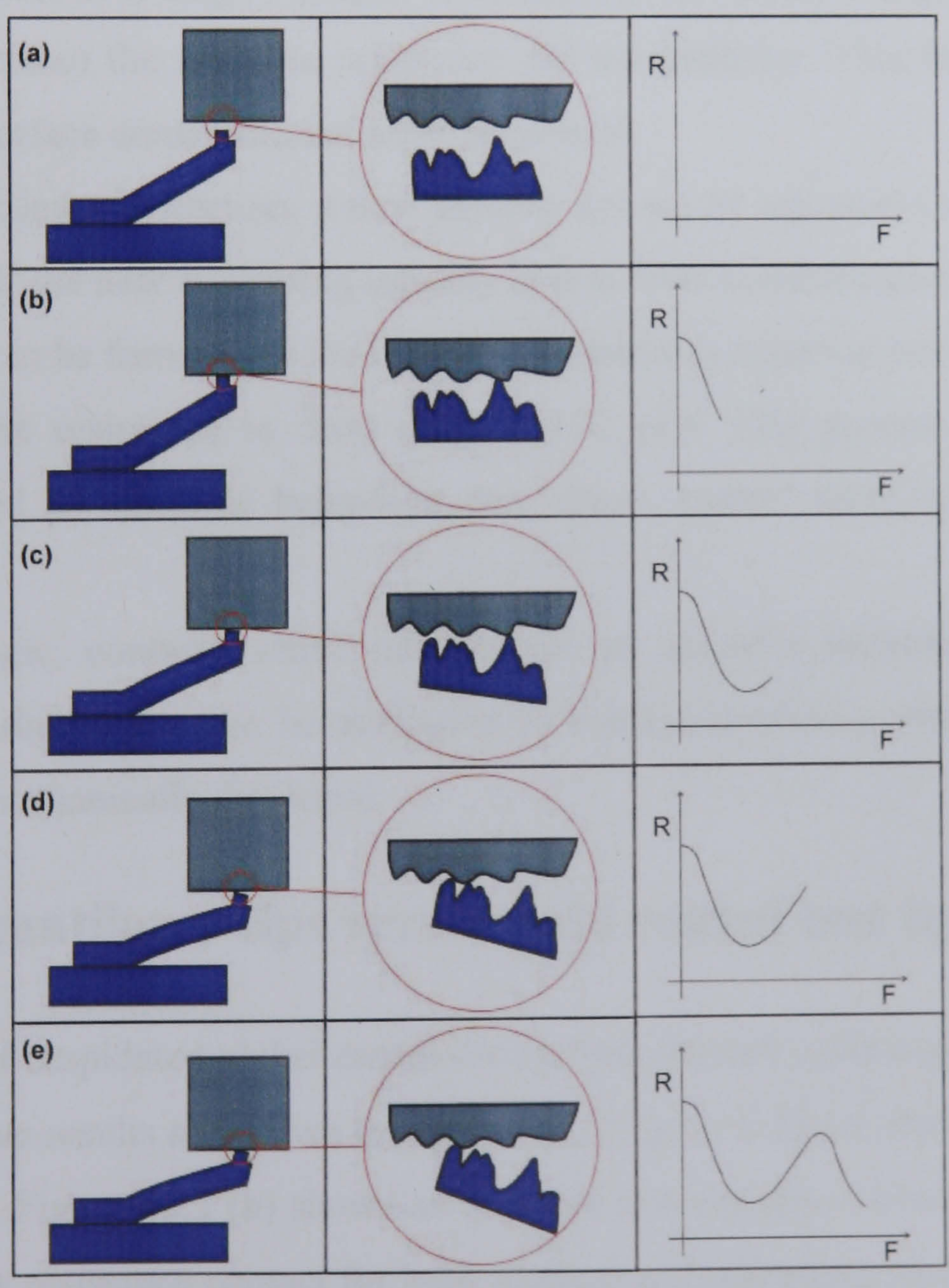

Figure 6.22 Change in contact area with increasing cantilever deflection

When the cantilever and test tip first make contact it will be through a single asperity. At this moment the force applied is low and hence the area of contact is small resulting in a

high contact resistance (Figure 6.22 (a)). As deflection increases the load increases causing the deformation of the contacting asperity and hence increasing the area of contact. This causes the contact resistance to decrease (Figure 6.22 (b)). If gold is present on either of the contacting surfaces then adhesion between the contacting points is highly likely in the absence of surface contamination.

As the cantilever continues to deflect, the cantilever probe tip tries to rotate and skid over the surface of the test tip (Figure 6.22 (c)). This begins to apply shear force across the adhered gold bridge and resistance begins to increase and eventually the gold contact is broken.

The unstable contact regions are believed to occur when the cantilever tip passes over an area of significant local contamination. Here current can only flow through tunnelling and the contact is very sensitive to mechanical vibration as this alters the distance between the two conducting surfaces.

It was found that even if large voltages were applied (in order to cause fritting i.e. local melting of the surface) the unstable resistance did not stabilise. This further supports the theory that some surface contamination must be present.

At a critical cantilever deflection, a new asperity (or set of asperities) comes into contact (Figure 6.22 (d)). If the new contacting asperity is free from contamination then this allows a new stable contact to be formed. As the load is increased this again causes the area of contact to increase and the resistance to drop (Figure 6.22 (e)). This process of stable contact formation followed by unstable behaviour can repeat several times as the cantilever is deflected.

By the same logic, contacts which demonstrate an unstable resistance throughout the loading and unloading cycle can be attributed to blanket insulating surface contamination which cannot be mechanically displaced.

6.3.4 Nickel cantilever tips versus gold coated test tip

Both smooth and cuspidated nickel cantilever tips were tested against gold coated test tips. Some representative results are shown in Figure 6.23. Figure 6.23 (a) shows an unstable high resistance contact, Figure 6.23 (b) shows an unstable low resistance contact, Figure 6.23 (c) shows a stable low resistance contact for both loading and unloading whilst Figures 6.23 (d) and (e) show contacts that were intermittently stable during loading and stable during unloading.

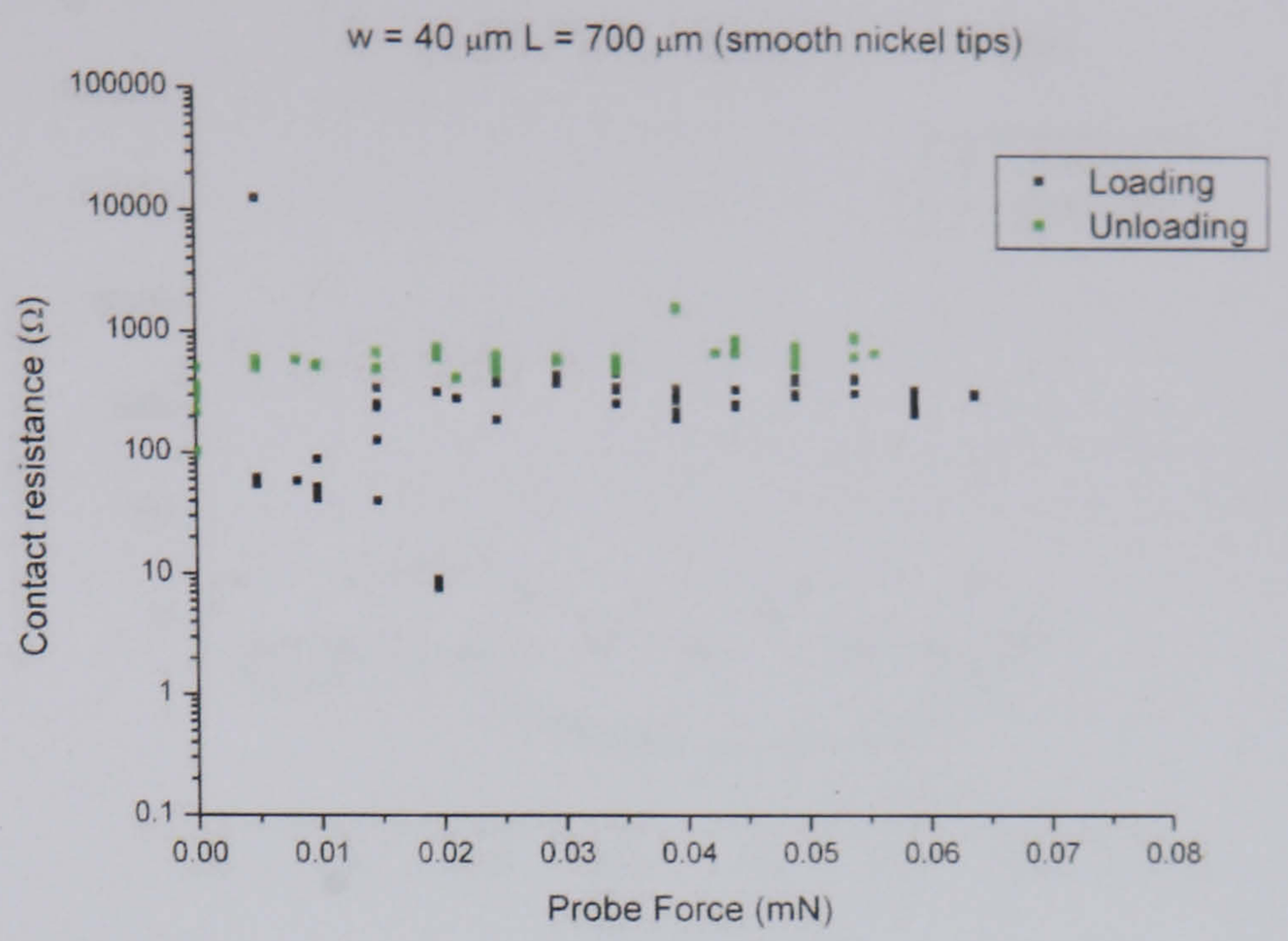
w = 40 μm L = 700 μm (smooth nickel tips)
Contact resistance (Ω)
100000
10000
1000
100
10
1
0.1
0.00
0.01
0.02
0.03
0.04
0.05
0.06
0.07
0.08
Probe Force (mN)
Loading
Unloading

(a)

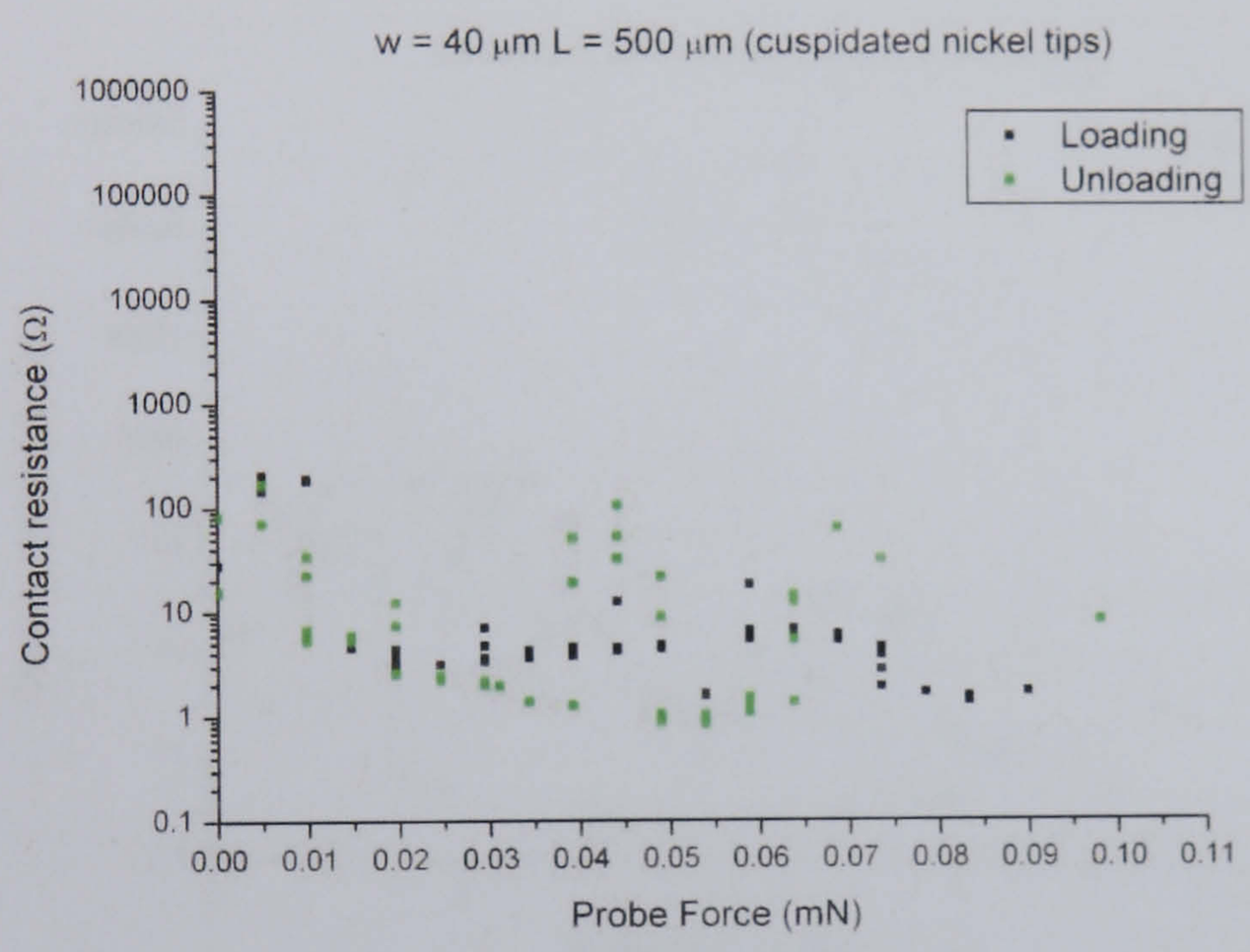
w = 40 μm L = 500 μm (cuspidated nickel tips)
Contact resistance (Ω)
1000000
100000
10000
1000
100
10
1
0.1
0.00
0.01
0.02
0.03
0.04
0.05
0.06
0.07
0.08
0.09
0.10
0.11
Probe Force (mN)
Loading
Unloading

(b)

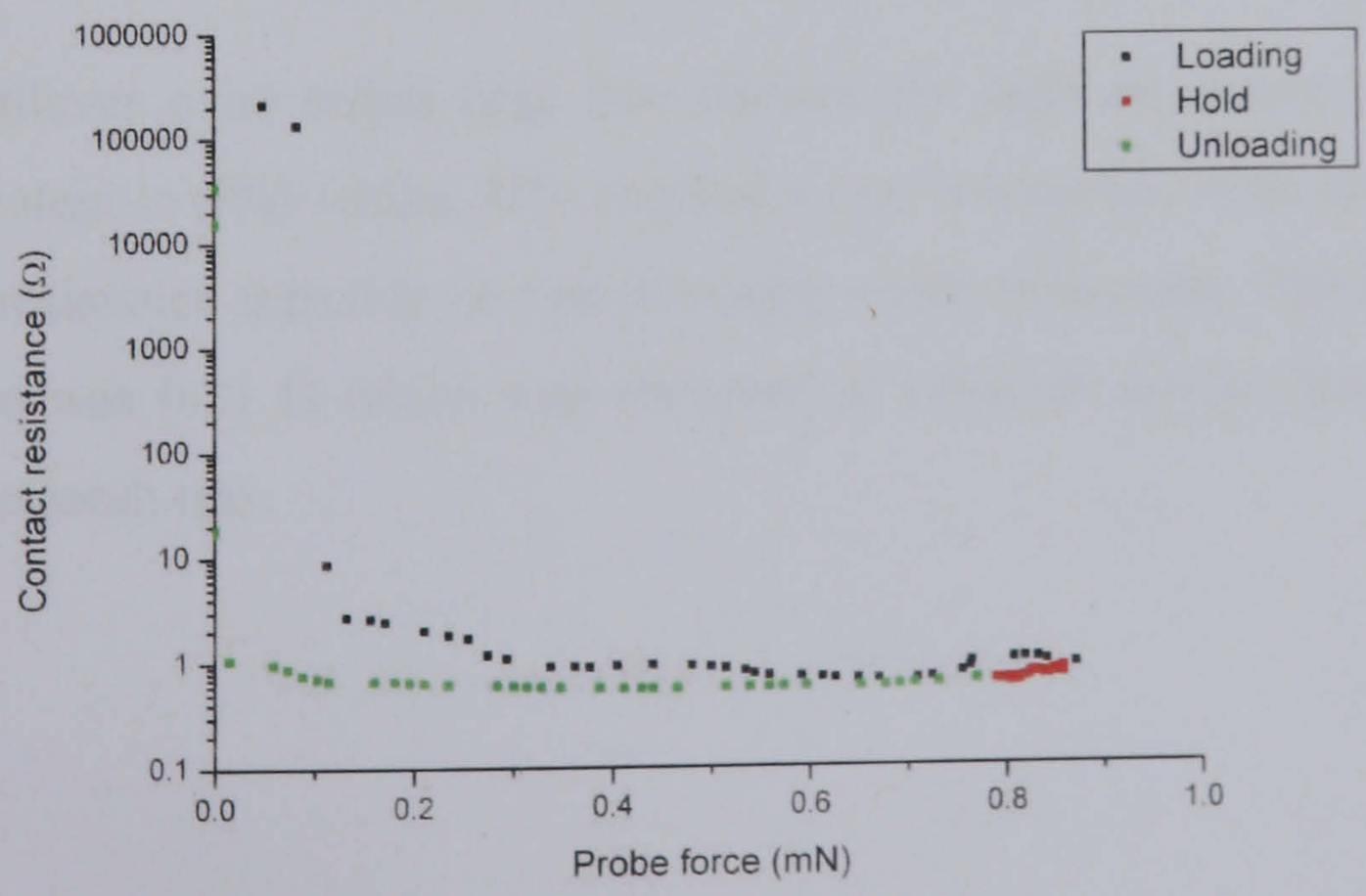
w = 20 μm L = 100 μm (cuspidated Ni tips)
Contact resistance (Ω)
1000000
100000
10000
1000
100
10
1
0.1
0.0
0.2
0.4
0.6
0.8
1.0
Probe force (mN)
Loading
Hold
Unloading

(c)

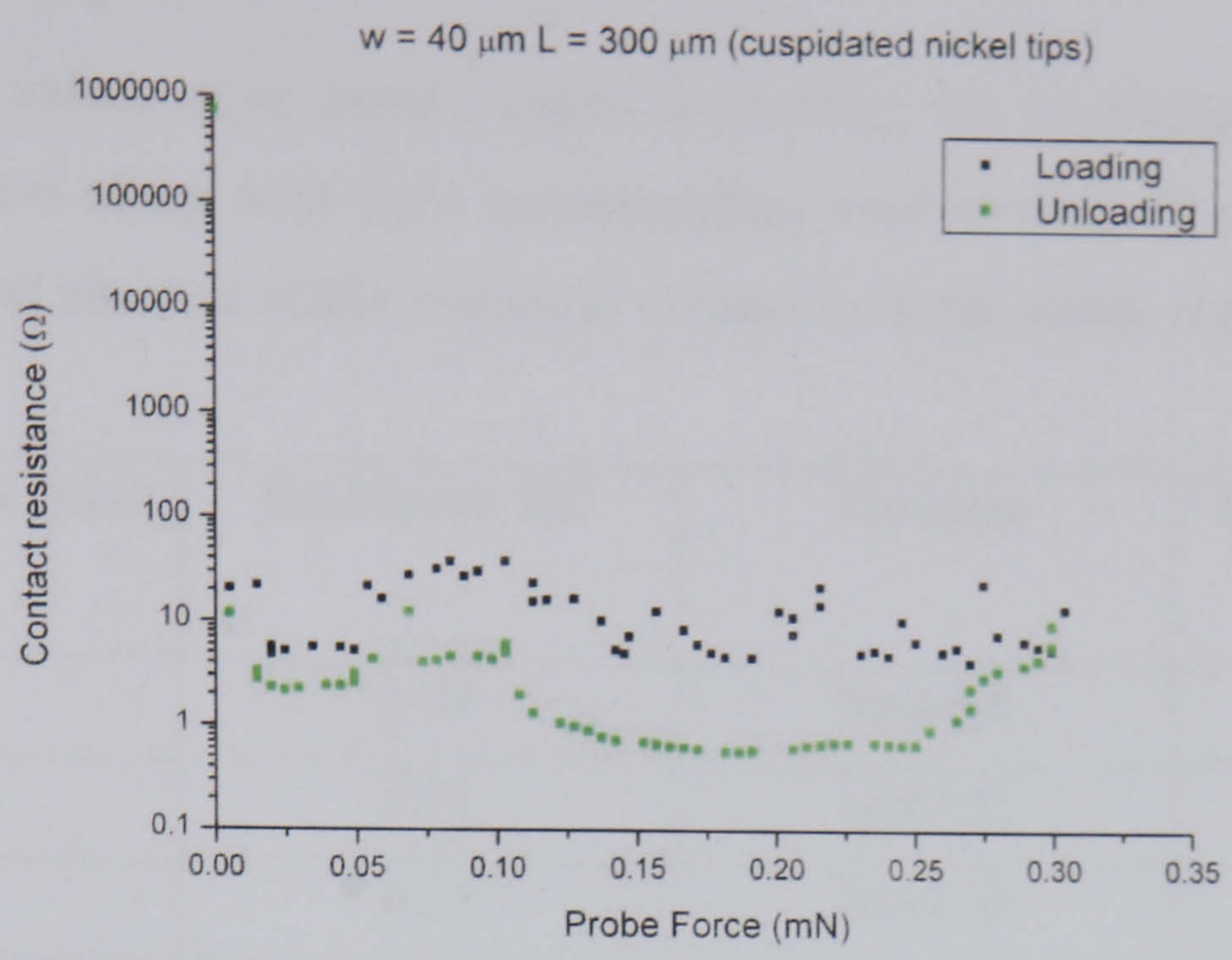

(d)

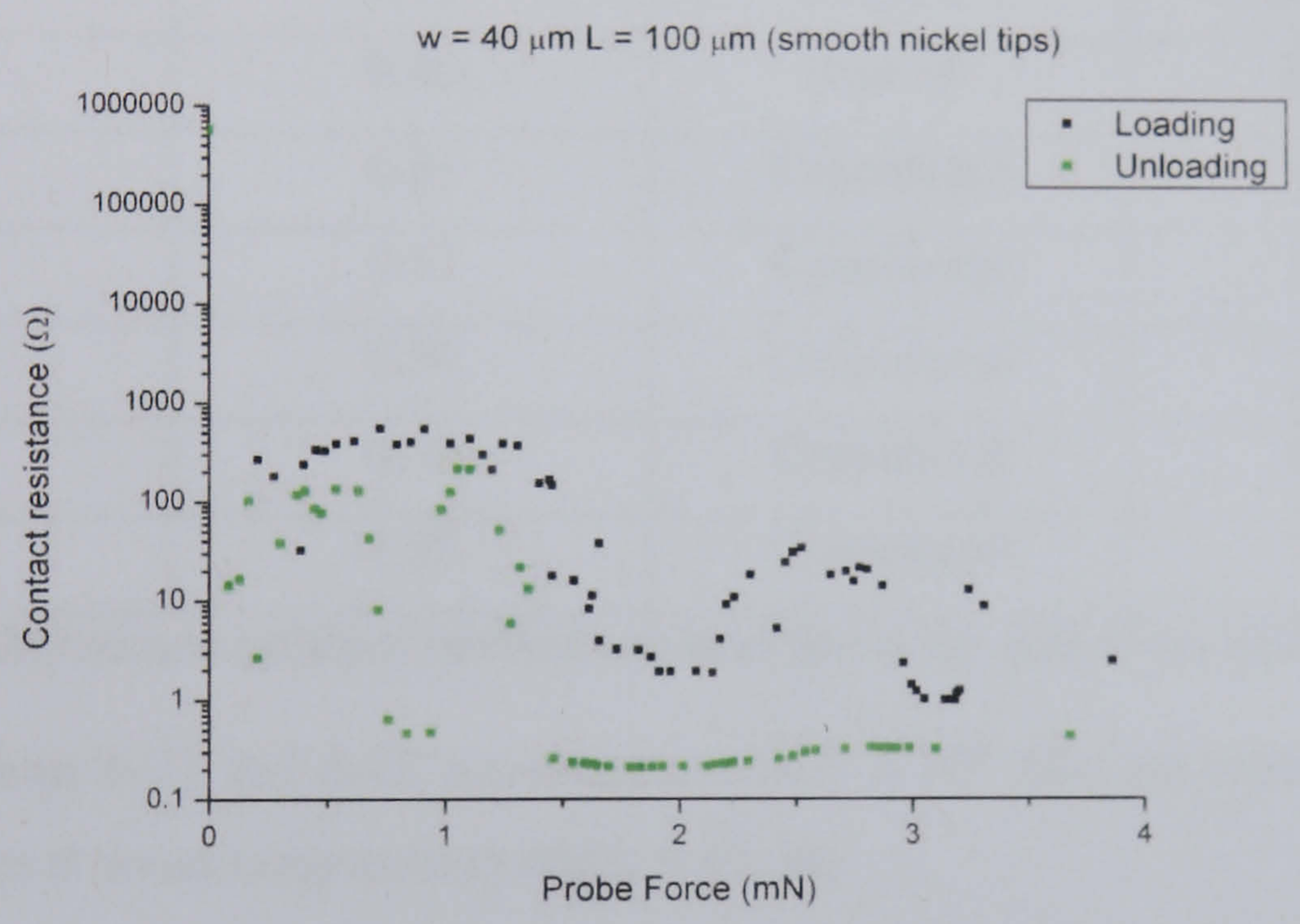

(e)

Figure 6.23 Contact resistance versus probe force for nickel on gold contacts

Of the 21 cantilever pairs tested only one showed the high resistance unstable contact behaviour (equivalent to 5%) whilst 33% showed a low resistance stable contact behaviour and 62% a low resistance unstable or intermittently stable behaviour. The lowest recorded contact resistance was 0.21 Ω which was observed at 1834 μN contact force when testing cantilevers with smooth tips.

The minimum values of resistance, taken from either the loading or unloading data, are listed in Table 6-6 along with their corresponding contact load. These values were taken from contacts that showed stable electrical contact or from stable regions in intermittently stable contacts.

Contact Force (μN)	Resistance (Ω)	Tip type	Estimated contact radius (nm) *
54	1.04	Smooth	36 – 40
128	0.71	Smooth	46 – 53
52	0.35	Smooth	75 - 90
118	0.6	Smooth	52 - 60
1834	0.21	Smooth	109 – 136
1300	0.40	Smooth	68 - 81
54	0.83	Cuspidated	42 - 47
186	0.57	Cuspidated	53 - 62
441	0.54	Cuspidated	55 - 65
731	0.48	Cuspidated	60 - 71
78	1.55	Cuspidated	28 - 31

Table 6-6 Minimum contact resistance and force for nickel on gold contacts

* Using equations 6-21 and 6-22 assuming $\rho = 4.57 \times 10^{-8}$ Ωm (an average of gold and nickel resistivities at room temperature) and $l_e = 40$ nm.

The resistances shown in Table 6-6 were plotted against the contact load as shown in Figure 6.24. From this it can be seen that there is no significant difference between the cuspidated and smooth nickel tips. Additionally, it can be seen that the resistance values broadly follow the relationship predicted by equation 6-16 (i.e. the contact resistance is proportional to contact force raised to the power of -0.5). Also, it can be seen that the resistance values of the gold on gold contacts are lower (for the same force) than the nickel on gold contacts. This is most likely due to the higher resistivity of nickel compared to gold. It is unlikely to be the result of significantly insulating oxides on the nickel as will be argued in section 6.3.4.1. However the trend is not conclusive enough to conclude whether the minimum values of resistance are determined by plastic, elastic or mixed contact deformation.

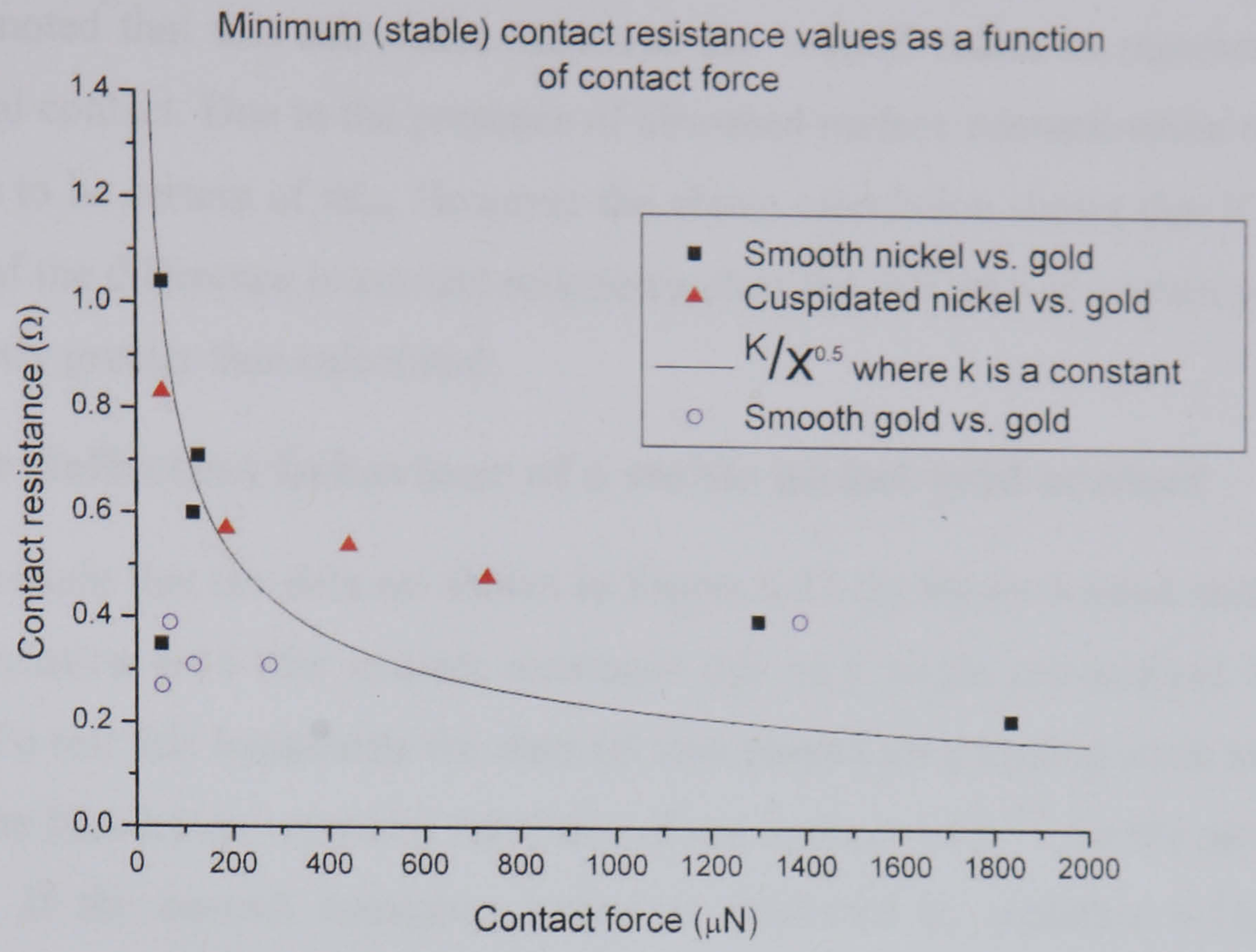

Figure 6.24 Minimum stable contact resistance values from nickel on gold and gold on gold testing as a function of contact force

6.3.4.1 Nickel surface oxide

Suppose that the entire surface of the nickel tip is covered with a nickel oxide layer such that, for current to flow, the electrons have to tunnel across the oxide. In order to calculate the resulting tunnelling resistance, the area of contact and tunnelling resistivity must be known.

It can be assumed that the area of contact (for any given force) between a smooth nickel cantilever tip and a gold coated test tip should be comparable to the area of contact between a gold coated smooth nickel cantilever tip and a gold coated test tip since the surfaces are geometrically similar. From Table 6-5 it can be seen the 'a-spot' radii associated with the minimum observed contact resistances were all less than 63 nm (over a force range of 54 to 1388 μN). Assuming a value of tunnel resistivity $\sigma = 10^{-8}$ Ωcm^2 and using a radius of contact of 63 nm it is possible to calculate the tunnelling resistance from equation 6-13 to be 80.2 Ω. Since the total contact resistance is the summation of both tunnelling resistance and constriction resistance, the minimum resistance for a contact of this area should be larger than 80 Ω.

All the resistance values shown in Table 6-6 (which relates to electrically stable regions) are lower than 1.55 Ω so it can be assumed that any oxide layer present on the nickel tip surfaces must have been fractured during testing, allowing direct metal to metal contact (else be extremely thin).

It should be noted that this calculation assumed the 'a-spot' radius to represent the true area of electrical contact. Due to the presence of absorbed surface contamination on the gold it is impossible to be certain of this. However the above calculation shows that if tunnelling was the cause of the difference in contact resistance, then the true area of contact would have to be significantly greater than calculated.

6.3.4.2 Force-deflection behaviour of a stable nickel-gold contact

It might be thought that the data set shown in Figure 6.23 (c) shows a trend similar to that predicted by equation 6-16 (the contact resistance due to a single constriction and plastic deformation). To test this hypothesis the data set was plotted on a log-log scale as shown in Figure 6.25. The blue traces represent functions of the form $y = k\,x^{-0.5}$, i.e the same form as equation 6-16. If the contact resistance varied as predicted by equation 6-16, then the experimental data should form a line of the same gradient. This is clearly not the case (although small sections of data approximately follow the trend). Attempts were also made to fit the data using equations of the forms of 6-17 (constriction and tunnelling resistance) and 6-18 (constriction and film resistance). This was also found not to be possible.

Therefore it is concluded that the actual change in contact resistance was much more rapid (with increasing load) than predicted by theory give in section 6.2. This is thought to be evidence for the softening of gold (due to the test voltage) since this would mean that contact area increases much more rapidly with increasing load than the theory predicts.

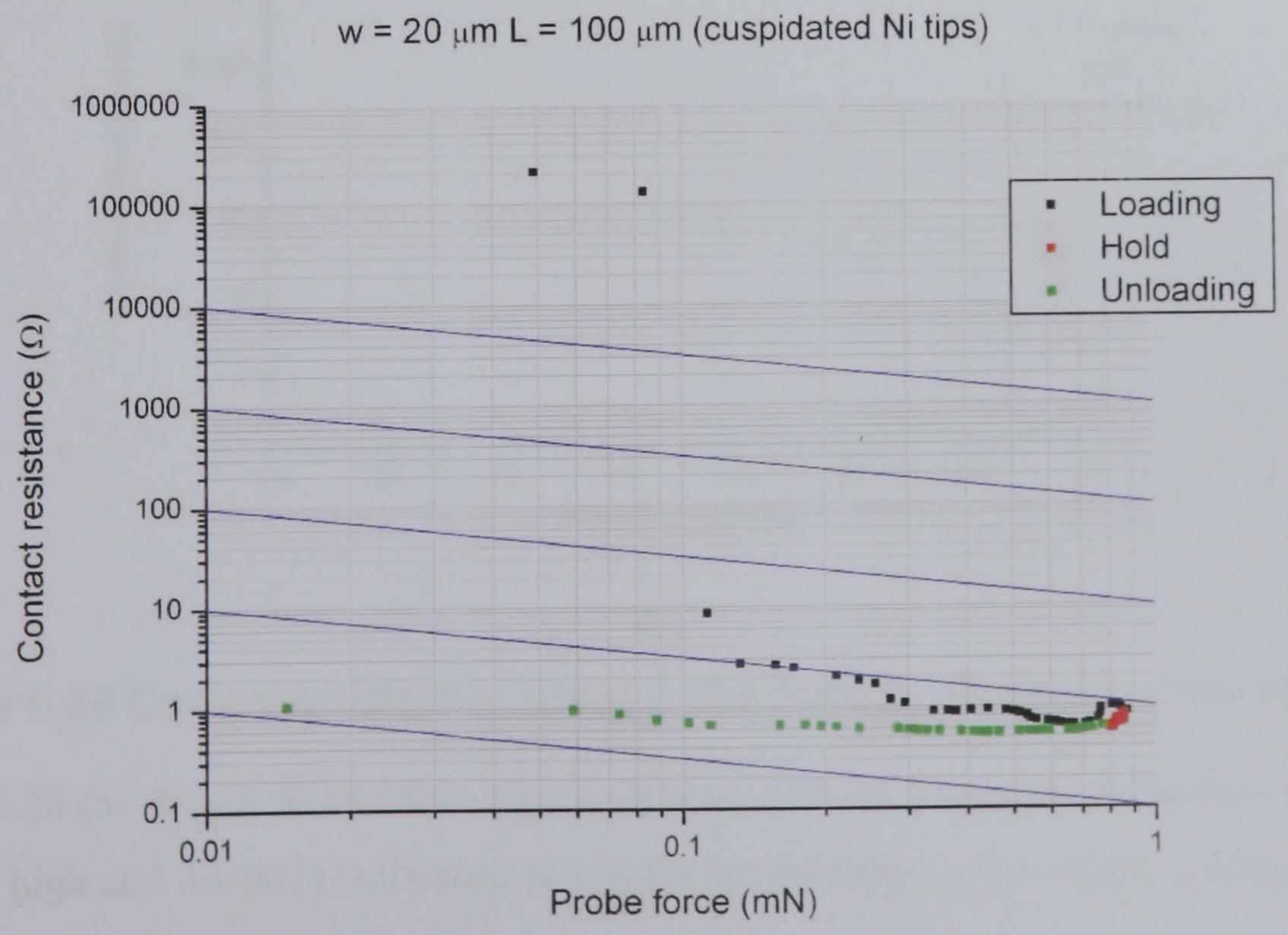

Figure 6.25 Nickel on gold stable contact plotted on log-log scale

6.3.5 Nickel cantilever tips versus nickel test tip

Both smooth and cuspidated nickel cantilever tips were tested against uncoated nickel test tips. Some representative results are shown in Figure 6.26.

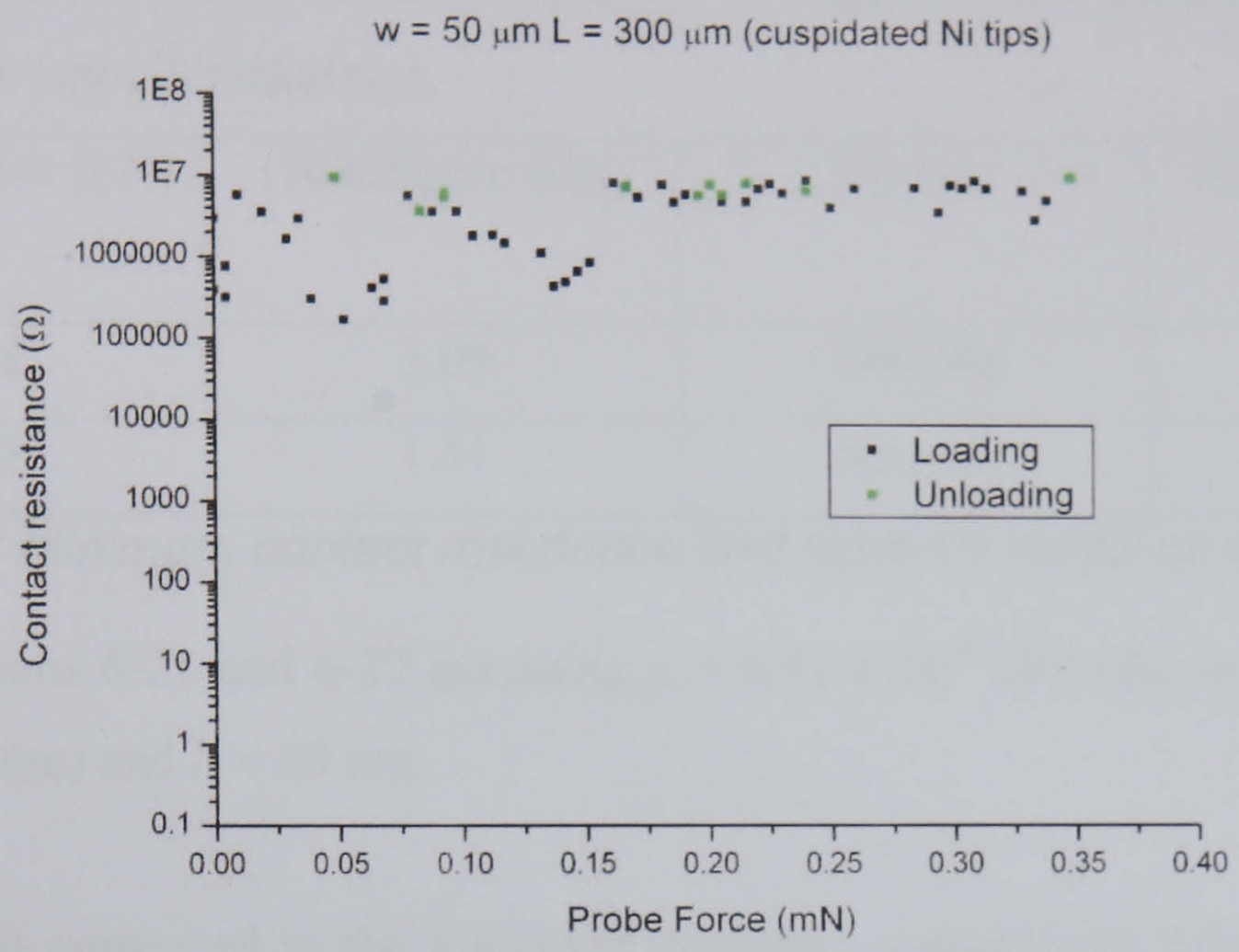

(a)

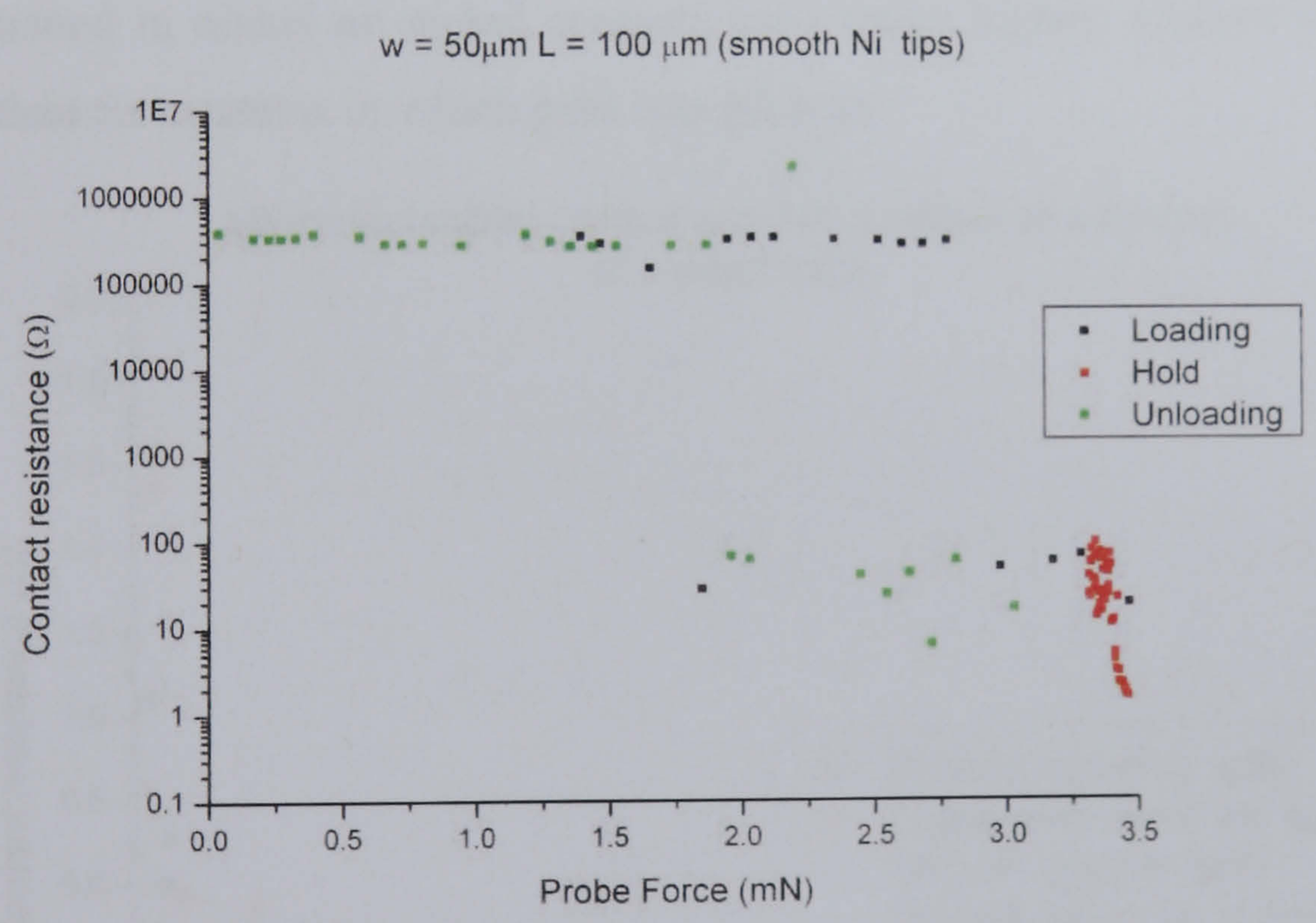

(b)

Figure 6.26 Contact resistance versus probe force for nickel on nickel contacts

Figure 6.26 (a) shows an unstable high resistance contact. Figure 6.26 (b) shows a contact that has a high and unstable resistance at low forces but forms a low stable resistance at high forces.

Only 11 cantilever pairs were tested. Of these, 55% produced unstable contacts where the resistance remained greater than 100 kΩ over the entire loading-unloading cycle whilst the other 45% formed contacts with resistance below 500 Ω. These were also often unstable. Only in two experiments were low resistance stable contacts observed. These are listed in Table 6-7. Both of these contacts occurred at high contact forces and when testing cantilevers with smooth nickel tips.

Contact Force (μN)	Resistance (Ω)	Tip type	Estimated contact radius (nm) *
1628	1.09	Smooth	46 - 52
3463	1.51	Smooth	37 - 42

Table 6-7 Minimum contact resistance and force for nickel on nickel contacts

* Using equations 6-21 and 6-22 assuming $\rho = 6.93 \times 10^{-8}$ Ωm (the resistivity of nickel at room temperature) and $l_e = 40$ nm.

This data was compared to the minimum resistance values from stable gold on gold and gold on nickel contacts (see Figure 6.27). From Figure 6.27 it can be seen that the resistances obtained in nickel on nickel contacts were much higher, relative to the applied contact force, than for contacts in which gold was present.

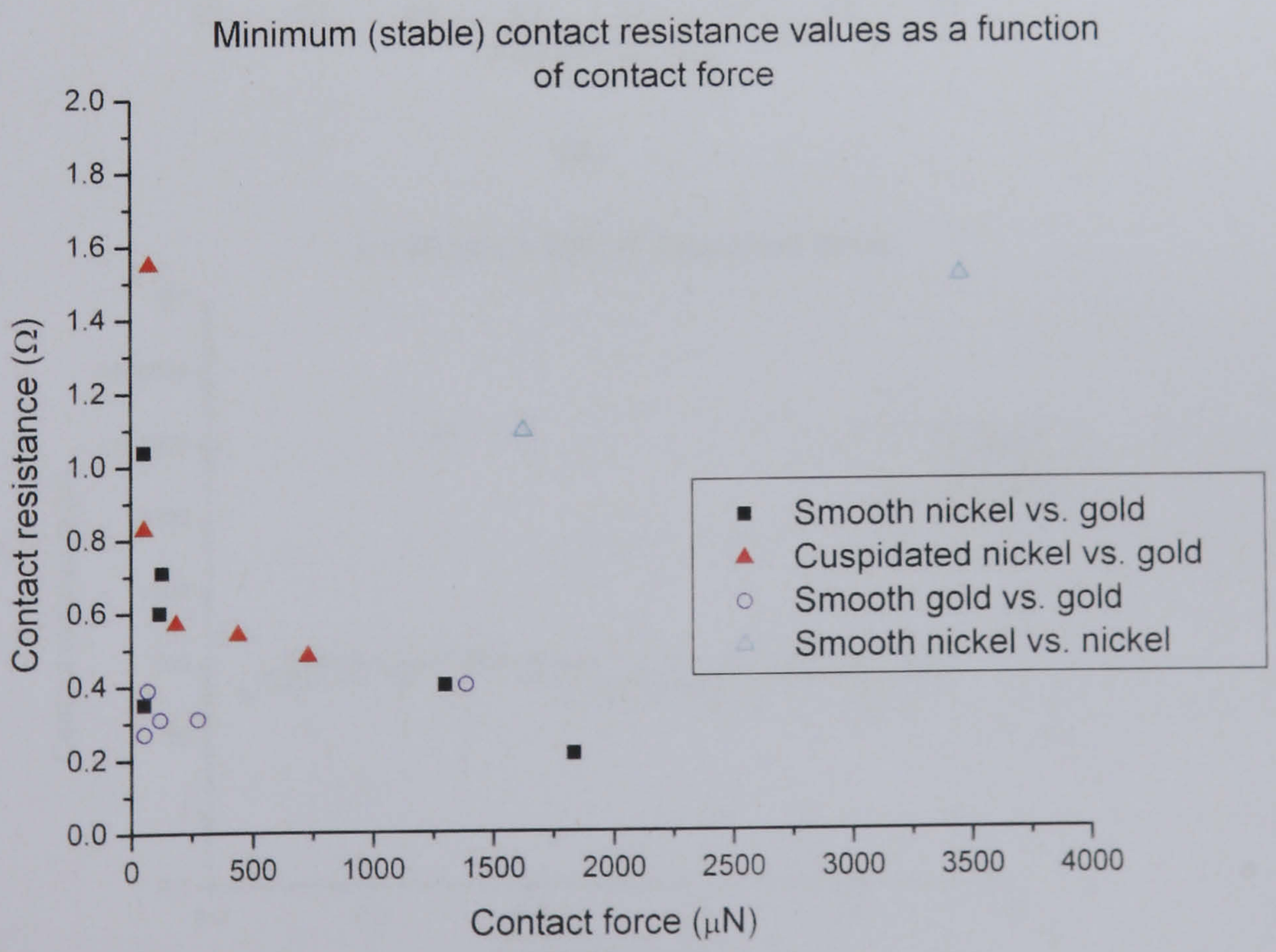

Figure 6.27 Minimum stable contact resistance values from nickel on nickel, nickel on gold and gold on gold testing as a function of contact force

The likely explanation for this is the greater hardness of nickel compared to gold since the higher the hardness, the higher the contact force required to produce the same contact area. As with the nickel on gold results, the minimum resistance values are sufficiently low to make the dominance of insulating oxides (tunnelling) unlikely. Therefore it can be assumed that any native oxide films have been broken or are very thin in the case of stable contacts.

6.3.6 Nickel cantilever tips versus aluminium coated test tip

Both smooth and cuspidated nickel cantilever tips were tested against aluminium coated test tips. Some representative results are shown in Figure 6.28.

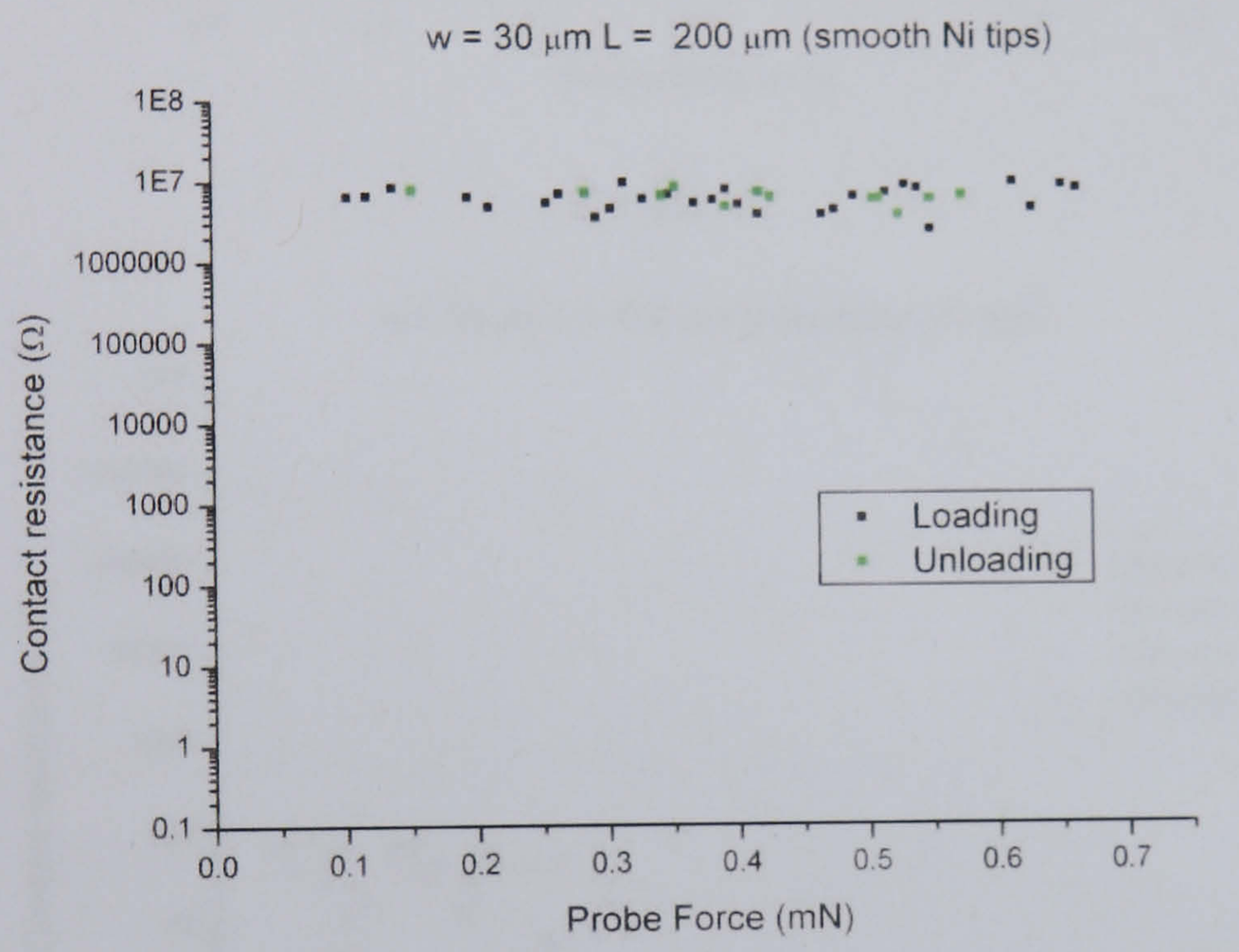

(a)

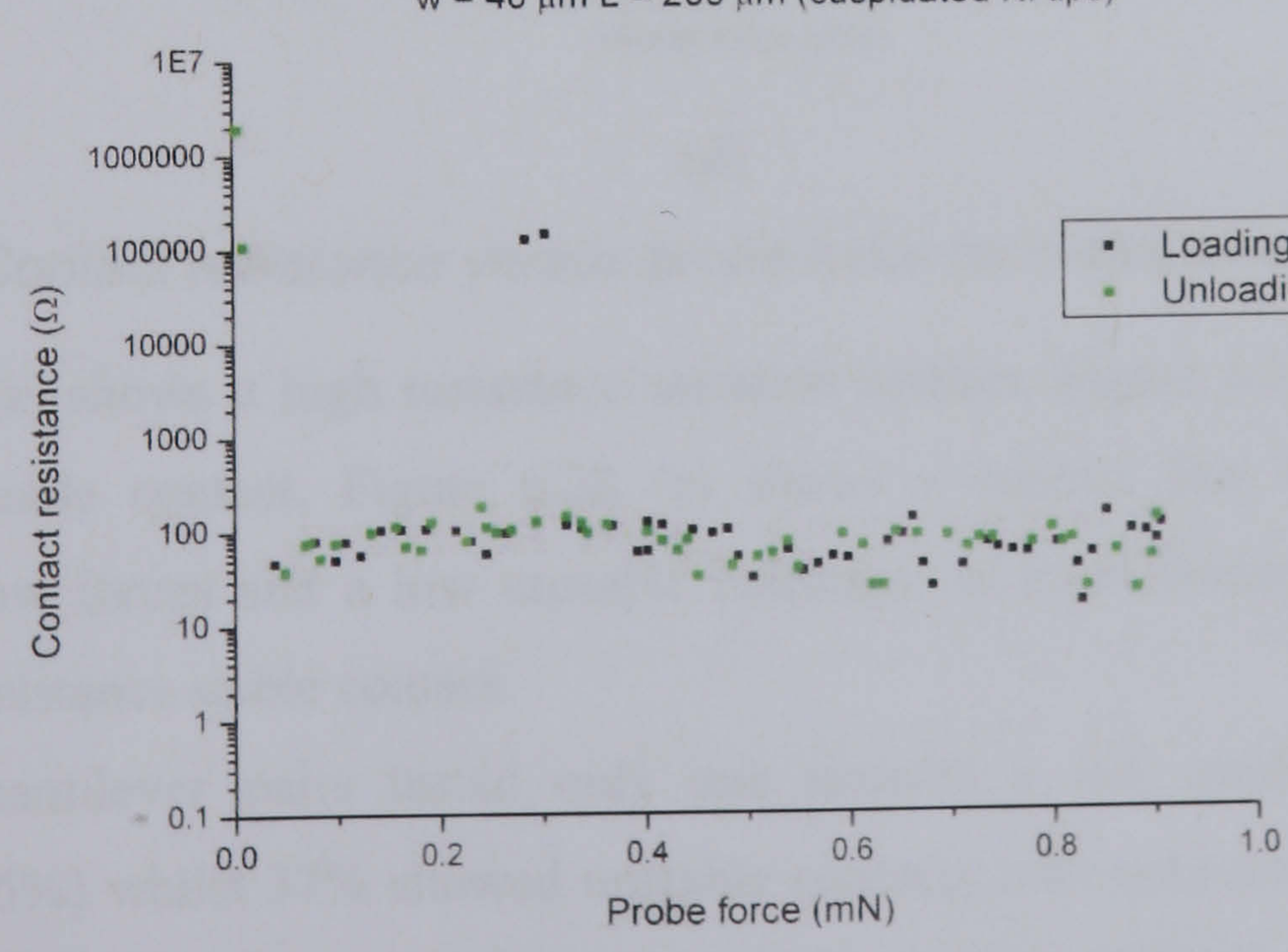

(b)

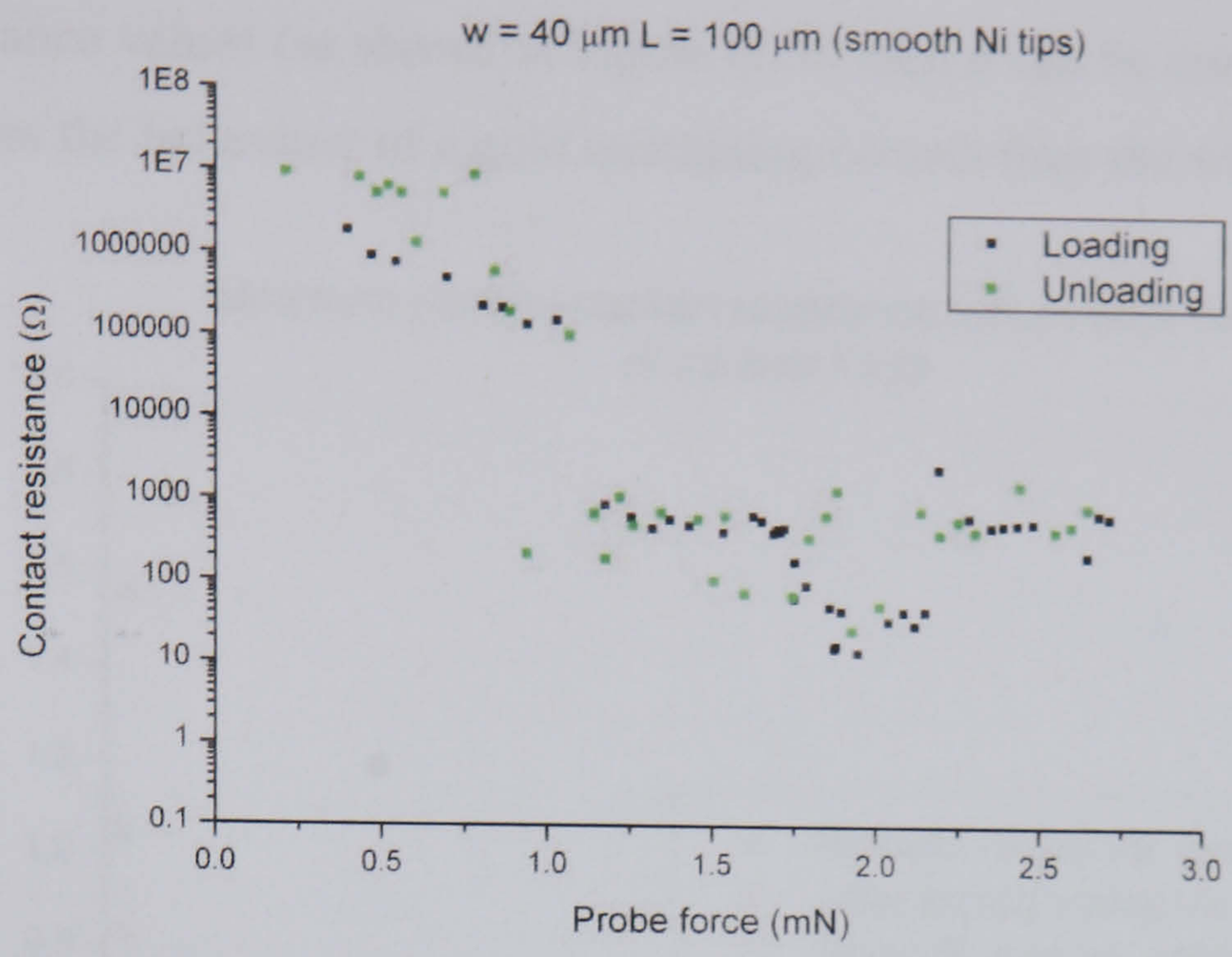

(c)

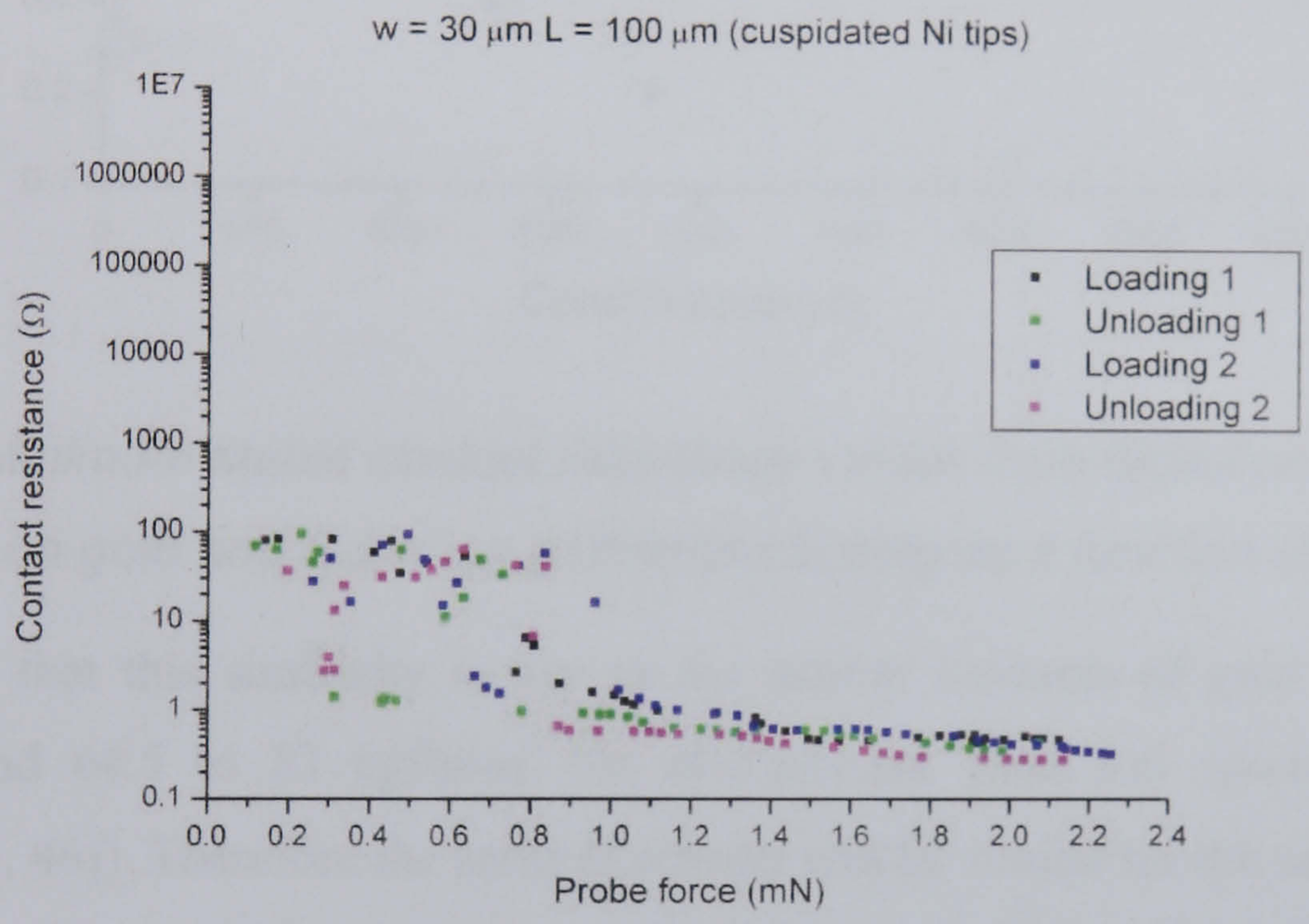

(d)

Figure 6.28 Contact resistance versus probe force for nickel on aluminium contacts

Figure 6.28 (a) shows a high resistance unstable contact, Figure 6.28 (b) shows a lower resistance unstable contact, Figure 6.28 (c) shows a contact that had a high unstable resistance at low forces and a low unstable resistance at high forces and Figure 6.28 (d) shows a low resistance stable contact.

Of the 19 cantilever pairs tested only one showed a low resistance stable contact (equivalent to 5%) whilst 37% showed unstable contacts with resistances below 500 Ω and 58% showed resistive unstable contacts with resistances above 100 kΩ.

Only one test demonstrated a low stable resistance, the minimum contact resistance achieved was 0.26 Ω which occurred at a contact force of 2135 μN. The cantilevers which

were used in this test had cuspidated nickel tips. If this value is plotted alongside other minimum resistance values (as shown in Figure 6.29) then it can be seen that the value more closely resembles the behaviour of a gold containing contact than the wholly nickel contacts.

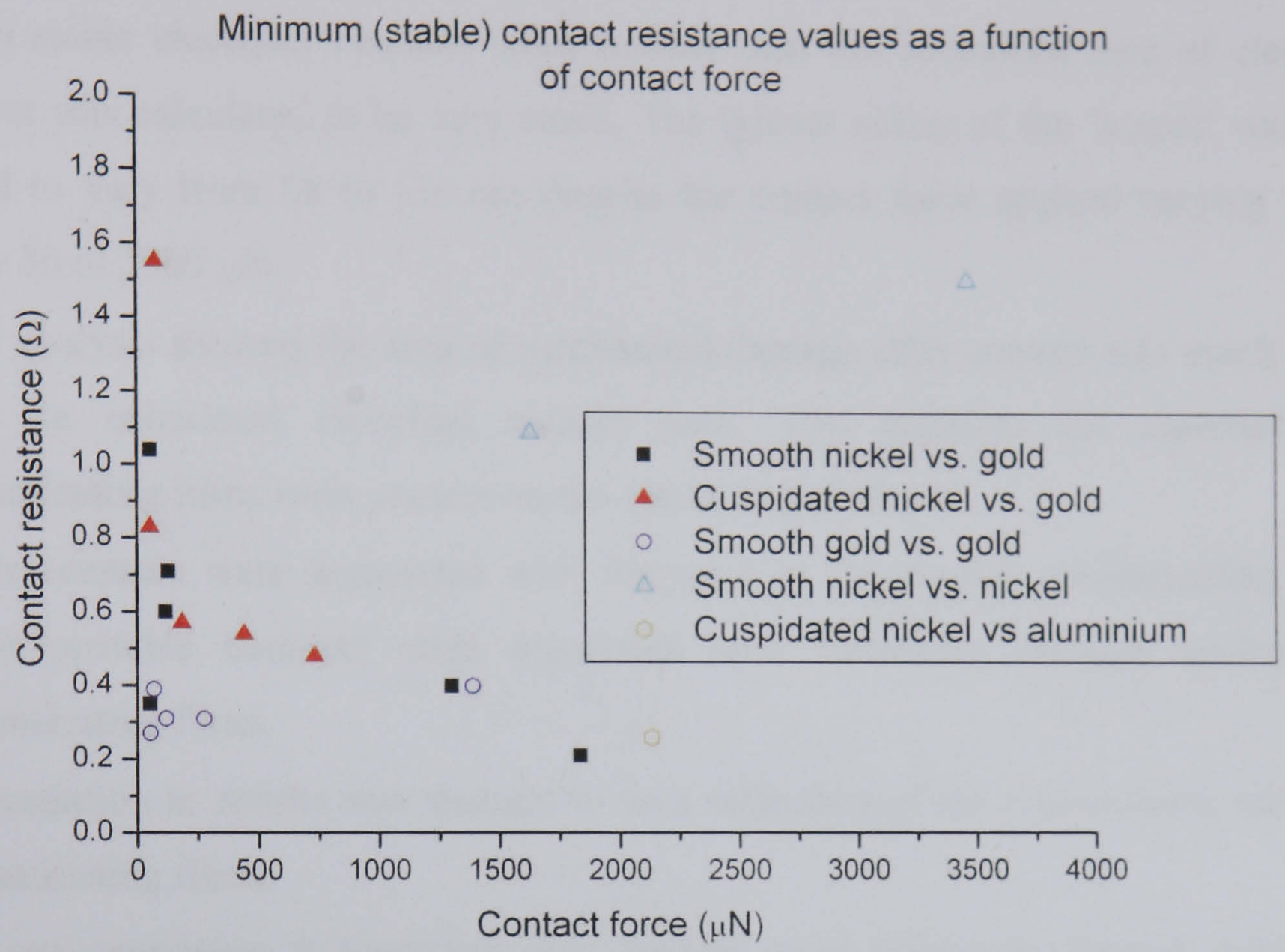

Figure 6.29 Minimum stable contact resistance values from nickel on nickel, nickel on gold, gold on gold and nickel on aluminium testing as a function of contact force

It is believed that this similarity is due to the similar hardness of gold and aluminium (80 kgf/mm^2 and 64.5 to 83 kgf/mm^2 for electroplated gold and sputtered aluminium respectively [45, 46]). Therefore the areas of contact will be similar for the same force.

Most of the cantilevers tested never formed a stable electrical connection. This is attributed to the presence of an un-fractured oxide film on the aluminium surface.

6.3.7 Conclusions

The results showed a large variation. However some conclusions can be made:

- Generally it was found that the resistance, for the same force, in the unloading cycle was lower than during the loading cycle. This was attributed to mechanical deformation of surface asperities.
- If the unloading cycle demonstrated higher resistances than the loading cycle then this was attributed to contamination of the contacting surfaces during the loading

cycle. The most likely causes being the removal of an evaporated metal (e.g. gold) exposing a more resistive metal (e.g.) nickel beneath or the accumulation of debris onto the cantilever tip acquired during the skid action.

- When stable electrical contacts were formed then the calculated area of electrical contact was calculated to be very small. The typical radius of the 'a-spot' was only found to vary from 28 to 136 nm despite the contact force applied varying in the range 50 to 3500 μN.
- SEM analysis showed the area of mechanical damage after contact was much larger than the calculated electrical contact area. This supports the assertion that contaminating films were present on the contacting surfaces.
- Stable contacts were associated with fractured or incomplete contaminating films whilst unstable contacts were associated with tunnelling through un-fractured contaminating films.
- The variation in results was thought to be a reflection of the non-uniform nature of contaminating films.
- Contacts containing at least one gold surface more frequently formed stable low resistance contacts. This was attributed to the absence of native oxides, the softness of gold and its extremely low softening voltage. It is believed that the gold surfaces were softened by the testing voltage applied across them and this helped the interfaces to adhere.
- The cyclical decrease and increase of contact resistance over a probe's loading is attributed to the formation and subsequent breaking of contact points as the cantilever tip rotated and skidded over the test tip surface.
- The adhesion and then transfer of gold across contacts was observed. This precludes the practical use of evaporated gold covered cantilever tips.
- There was no significant difference in the performance of cuspidated and smooth nickel tips.
- Softer metals such as gold or aluminium required lower contact forces to form stable electrical contacts than harder metals such as nickel (assuming that the native oxide or contaminating layers were fractured).

6.4 Test results – leakage current

The leakage current between adjacent probes was measured using a HP4145B parameter analyser. Connections were made to two adjacent, but electrically isolated probes. One probe was grounded whilst a voltage was applied to the other. The voltage was swept from -100 to +100 V in 1 V steps. The current passing between the probes was measured and is shown in Figure 6.30. For clarity, this data has been smoothed using a 5 point moving average to reduce the signal noise. The dimensions of the cantilevers that were tested are shown in the legend. Also shown, is the open circuit response of the parameter analyser.

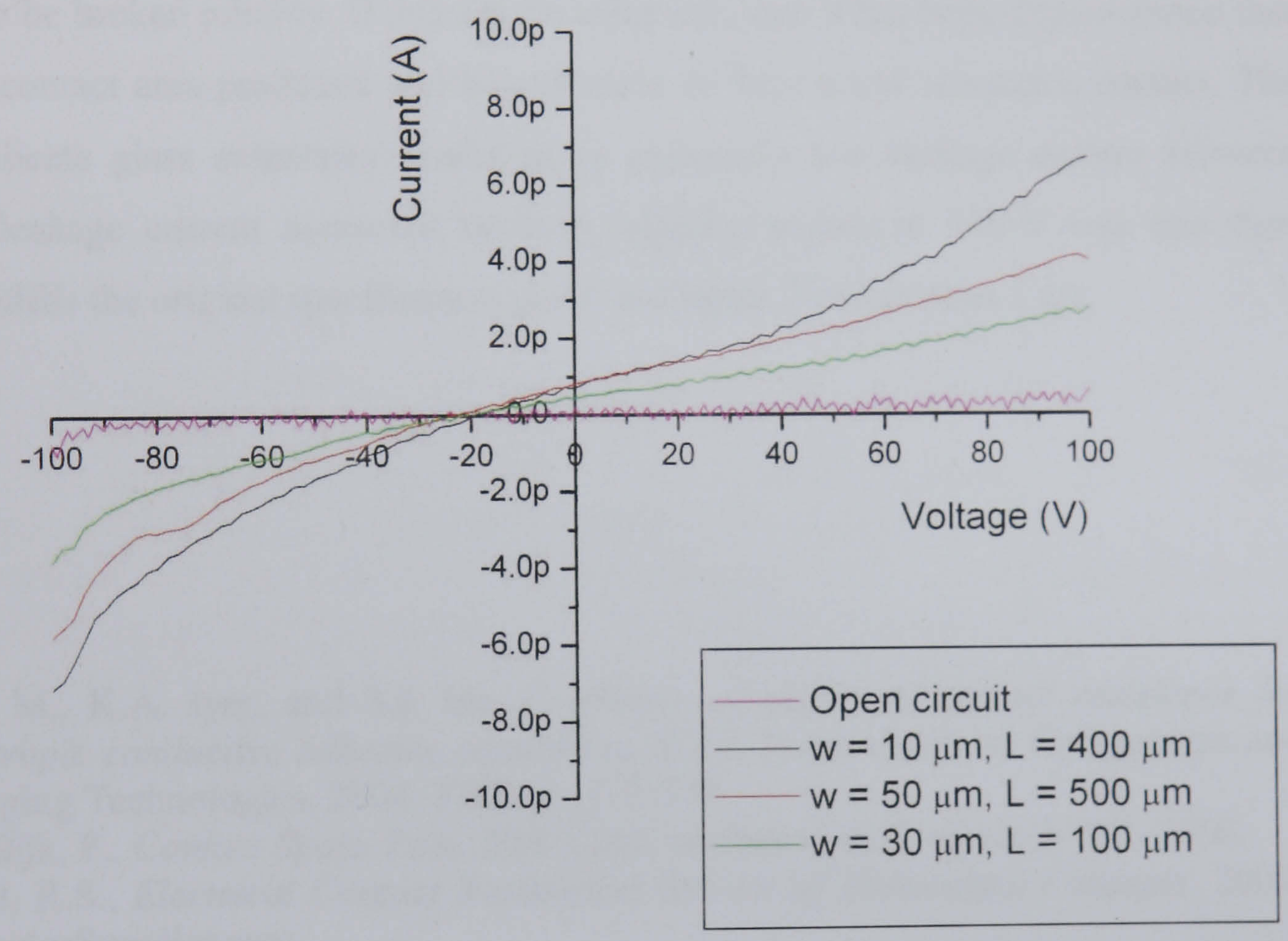

Figure 6.30 Leakage current as a function of voltage

From this data it can be seen that the leakage current between adjacent probes was less than 10 pA over the entire voltage range (calculated from the unsmoothed data). This equates to an isolation resistance better than 10 TΩ.

6.5 Summary

It is obvious that, to be practically useful, a probe card must not be a source of uncertainty during device testing. Therefore any instability in electrical contact resistance must be eliminated. Testing of the fabricated cantilever showed contact behaviour was very unreliable. The devices presented so far are therefore not sufficiently robust to act as electrical probes and hence do not meet the specification given in chapter 2 of providing a low and stable resistance contact of less than 2 Ω (to gold).

It is believed that there is a need to apply higher forces to permit contaminating films on the surfaces to be broken reliably. If this can be achieved, then it has been demonstrated that the electrical contact area produced will be sufficient to form a low resistance contact. The use of borosilicate glass substrates results in an extremely low leakage current between probes. The leakage current measured between adjacent probes at 100 V was less than 10 pA. This fulfils the original specification given in chapter 2 of less than 1 nA.

References

1. Chin, M., K.A. Iyer, and S.J. Hu, *Prediction of electrical contact resistance for anisotropic conductive adhesive assemblies.* IEEE Transactions on Components and Packaging Technologies, 2004. **27**(2): p. 317-326.
2. Van-Dijk, P., *Contact Spots.* Proc. 20th Conf. on Electrical Contacts, ICEC, 2000.
3. Timsit, R.S., *Electrical Contact Resistance: Review of Elementary Concepts.* 2007: ConnectorSupplier.com.
4. Kataoka, K., T. Itoh, and T. Suga, *Characterization of fritting phenomena on Al electrode for low contact force probe card.* IEEE transactions on components and packaging technologies, 2003. **26**(2): p. 382-387.
5. Beiley, M., J. Leung, and S.S. Wong, *A micromachined array probe card-characterization.* IEEE Transactions on components, packaging, and manufacturing technology, Part B, 1995. **18**(1): p. 184-191.
6. Pruitt, B.L., W.T. Park, and T.W. Kenny, *Measurement system for low force and small displacement contacts.* Journal of Microelectromechanical Systems, 2004. **13**(2): p. 220-229.
7. Lee, H., et al., *Nanoindentation technique for characterizing cantilever beam style RF microelectromechanical systems(MEMS) switches.* Journal of Micromechanics and Microengineering, 2005. **15**(6): p. 1230-1235.
8. Hertz, H., *On the contact of elastic solids.* J. Reine Angew. Math, 1881. **92**: p. 156-171.

9. Johnson, K.L., *Contact Mechanics*. 1985: Cambridge University press.
10. Slade, P.G., *Electrical Contacts Principles and Applications*. 1st ed. 1999: CRC.
11. Greenwood, J.A. and J.B.P. Williamson, *Contact of Nominally Flat Surfaces.* Proceedings of the Royal Society of London. Series A, Mathematical and Physical Sciences, 1966. **295**(1442): p. 300-319.
12. Johnson, K.L., K. Kendall, and A.D. Roberts, *Surface Energy and the Contact of Elastic Solids.* Proceedings of the Royal Society of London. Series A. Mathematical and Physical Sciences, 1971. **324**(1558): p. 301-313.
13. Derjaguin, B.V., V.M. Muller, and Y.P. Toporov, *Effect of contact deformation on the adhesion of elastic solids.* J. Colloidal Interface Sci, 1975. **53**: p. 314–326.
14. Benham, P.P., R.J. Crawford, and C.G. Armstrong, *Mechanics of Engineering Materials*. 1996, Pearson Education Limited.
15. Tabor, D., *The hardness of solids.* Reviews of Physics in Technology. 1970. **1**(3): p. 145-179.
16. Holm, R. and E. Holm, *Electrical Contacts Theory and Applications*. 4th ed. 1967, Berlin/Heidelberg/New York: Springer-Verlag.
17. Maxwell, J.C., *A Treatise on Electricity and Magnetism*. 3rd ed. 1891, New York: Dover.
18. Greenwood, J.A., *Constriction resistance and the real area of contact.* British Journal of Applied Physics, 1966. **17**: p. 1621-1632.
19. Boyer, L., *Contact resistance calculations: generalizations of Greenwood's formula including interface films.* IEEE transactions on Components and Packaging, 2001. **24**(1): p. 50-58.
20. Nikolic, B. and P.B. Allen, *Electron transport through a circular constriction.* Physical Review B, 1999. **60**(6): p. 3963-3969.
21. Zhang, W., et al., *Influence of the electron mean free path on the resistivity of thin metal films.* Microelectronic Engineering, 2004. **76**(1-4): p. 146-152.
22. Braunovic, M., N.K. Myshkin, and V.V. Konchits, *Electrical Contacts: Fundamentals, Applications and Technology*. 2006, CRC Press. p. 134.
23. Wexler, G., *The size effect and the non-local Boltzmann transport equation in orifice and disk geometry.* Proceedings of the Physical Society, 1966. **89**(4): p. 927-941.
24. Dickrell, D.J. and M.T. Dugger, *Electrical Contact Resistance Degradation of a Hot-Switched Simulated Metal MEMS Contact.* IEEE Transactions on Components and Packaging Technologies, 2007. **30**(1): p. 75-80.
25. Braunovic, M., N.K. Myshkin, and V.V. Konchits, *Electrical Contacts: Fundamentals, Applications and Technology*. 2006: CRC Press.
26. Kister, J., *Introduction to physics of contact resistance*, in *SouthWest Test workshop*. 1998: San Diego.
27. Holm, R., *The Electric Tunnel Effect across Thin Insulator Films in Contacts.* Journal of Applied Physics, 1951. **22**(5): p. 569-574.
28. Simmons, J.G., *Generalized Formula for the electric tunnel effect between similar electrodes separated by a thin insulating film.* Journal of applied physics, 1963. **34**(6): p. 1793-1803.
29. Rahman, M.R.A., *Antenna-coupled tunnel diodes for dual-band millimetre-wave / infrared focal-plane arrays*. 2004, University of Central Florida Orlando. Florida.
30. Ittner III, W.B. and P.J. Magill, *A Survey of Contact Resistance Theory for Nominally Clean Surfaces.* IBM Journal of Research and Development, 1957. **1**(1): p. 44-48.
31. Martens, R.I. and S. Mitchell, *Electrical and Mechanical characterization of BladeRunner(TM) Tips on Reflowed Eutectic Bumps*, in *Southwest Test Workshop*. 2002: Long Beach, CA.

32. Humphrey, G. and R. Gaggl, *Extending Cantilevered Probe Card Life: An "Abrasive" Approach*, in *SouthWest Test Workshop*. 2004: San Diego.
33. Martens, R.I. and L. Levy, *Optimization of MicroSpring Contact Design Parameters for Low Pressure Probing*, in *SouthWest Test Workshop*. 2004: San Diego.
34. Lorenz, L., *Bestimmung der Wärmegrade in absolutem Maasse.* Annalen der Physik. 1872. **223**(11): p. 429-452.
35. Kittel, C., *Introduction to Solid State Physics*. 5th ed. 1976, New York: Wiley.
36. Lide, D.R., *Handbook of chemistry and physics*. 83rd ed. 2003. New York: CRC Press.
37. Angus, H.C., *Adhesion between precious metals.* Journal of Physics D Applied Physics, 1969. **2**(6): p. 831-837.
38. Sun, M., et al., *Lifetime resistance model of bare metal electrical contacts.* , IEEE Transactions on Advanced Packaging Part B, 1999. **22**(1): p. 60-67.
39. Jensen, B.D., et al., *Effect of Nanoscale Heating on Electrical Transport in RF MEMS Switch Contacts.* Journal of Microelectromechanical Systems. 2005. **14**(5): p. 935-946.
40. Hyman, D. and M. Mehregany, *Contact physics of gold microcontacts for MEMS switches.* IEEE Components and Packaging Technologies Part A, 1999. **22**(3): p. 357-364.
41. Abdul-Lettif, A.M., *Determination of diffusion coefficients in Au/Ni thin films by Auger electron spectroscopy.* Physica Status Solidi(a), 2004. **201**(9): p. 2063-2066.
42. Kissinger, P.T. and W.R. Heineman, *Laboratory Techniques in Electroanalytical Chemistry*. 1996: Marcel Dekker Inc.
43. Ma, Q., et al., *Metal contact reliability of RF MEMS switches*, in *Reliability, Packaging, Testing, and Characterization of MEMS/MOEMS VI* 2007: San Jose, CA, USA p. 05.
44. Tringe, J.W., et al., *A single asperity study of Au/Au electrical contacts.* Journal of Applied Physics, 2003. **93**: p. 4661.
45. Nath, P., et al., *Microhardness and Electrical-Resistivity of Au-TiC Multilayer Structures Prepared by RF Sputtering.* Journal of Physics D - Applied Physics, 1979. **12**(9): p. 1597-1600.
46. Randall, N., *Quality Control Of Integrated Circuit (IC) Bonding Pads With The Nano Hardness Tester (NHT) From CSM Instruments*, in *CSM instruments advanced mechanical surface testing issue 2*. 1996.

Chapter Seven

PDMS device

This chapter describes the fabrication and testing of a new probe structure. The new structure overcame many of the fabrication and performance limitations of the previous design. The new design was very similar to the previous structure except that an elastomer was incorporated beneath the cantilever probes. Mechanical and electrical testing of this new device showed that the elastomer layer allowed contact force to be increased to a level where stable electrical contacts could be formed. Contact forces of over 100 mN could be applied by the new structures without probe damage.

7.1 Introduction

The original objectives stated in chapter 2 were to produce a probe card that:

- had a pitch less than 25 μm.
- had a leakage current less than 1 nA.
- had a stable contact resistance of less than 2 Ω (to gold).
- could be produced at low cost and quickly (batch fabricated).
- applied the minimal contact force.
- could be fabricated on different substrate materials.
- had an inclined cantilever structure.
- could accommodate 30 to 40 μm of overdrive without damage.

An additional objective was to test the effect of different tip textures on the force-contact resistance behaviour. The success, or otherwise, of securing these objectives is now discussed in the following two section.

7.1.1 Fabrication

The fabrication process, described in chapter 3, could produce inclined nickel cantilevers with a minimum pitch was 23 μm. The fabrication was such that it did not depend on the substrate material and was entirely based on batch techniques. Therefore this method of fabrication satisfied three of the design objectives.

However, the fabrication process was fundamentally limited by the stability of the sacrificial thick photoresist layer. Although greyscale lithography provided a convenient method of controlling the 3D layer, the poor thermal resilience of the resist caused a loss of control of the cantilever profile and, on occasion, catastrophic failure due to delamination between layers. Additionally, the internal stress gradient of the nickel caused the released cantilever tip heights to deviate from their desired positions. This caused a reduction in the tip co-planarity.

7.1.2 Electrical and mechanical properties

In chapter 6 it was shown that at 100 V the measured leakage current between probes was less than 10 pA, which is well within the required specification. However, low resistance electrical contacts generally could not be obtained.

The contact resistance behaviour suggested that contaminating films often remained un-fractured on the contacting surface. Additionally, these films were non-uniform which lead to the large variation in contact resistance results. It was found that changing the tip texture from smooth to cuspidated had no significant effect on the contact resistance behaviour. The use of evaporated gold on tips was found to increase the probability of a good electrical contact. However, it was found that adhesion and transfer of gold occurred during contact, rendering its use impractical.

As shown in chapter 6 the stiffest cantilevers fabricated (horizontal length 100 μm and width 50 μm) could not provide sufficient contact force when fully deflected to provide stable electrical contact. It was thought that increasing the probe force was the only practical method of obtaining a reliable and stable electrical contact. Fritting contacts were rejected since they require double the number of probes per-pad hence would significantly reduce the ultimate probe pitch. To increase probe force, the cantilevers would have to be made thicker, the length decreased or the width increased, each of which is problematic as explained below.

The widths of the cantilevers could not be increased since this would have affected the minimum possible pitch. The thickness of the cantilevers could not be increased beyond 18 μm without risking over-plating (see chapter 3). Even if this fabrication problem could have been solved, the thickness of the cantilever was still limited since, if it surpassed the width, the structure would become unstable (see Kim et. al. [1]).

It was not possible to decrease the length of the cantilever since shorter cantilevers result in higher stresses for the same deflection. In chapter 5 it was shown that a 10 μm thick cantilever required a horizontal length greater than 500 μm to prevent yielding occurring when the tip was displaced by 40 μm.

It was not possible to change the cantilever geometry to increase contact force (whilst still meeting minimum pitch requirements) so an alternative method of increasing contact force was sought. One method considered was to use a structural metal with much higher Young's modulus and yield stress. This was rejected since such a structure would still be very fragile

and so easily damaged by excessive overdrive or shear forces. Therefore a third solution was investigated, which is described in section 7.2.

7.2 New probe design

It was believed that a modification of the fabrication process could be used to increase the probe contact force whilst leaving other aspects of the design unaltered. The proposal was to replace the sacrificial resist layer with a permanent elastomer layer. Polydimethylsiloxane (PDMS) was chosen as the elastomer since it has high dielectric strength as well as high compressibility [2]. The fabrication of this new design is described in section 7.3 whilst mechanical and electrical testing is given in sections 7.4 and 7.5 respectively.

The new design used the PDMS layer to provide the required mechanical stiffness whilst the metal cantilever acted as the electrical path. Nickel was chosen as the material to form both the cantilevers and tips. Nickel was a logical choice for the cantilever tip since it is hard wearing and has high yield strength. Both of these properties are required for the tip to prevent damage during the probing action. Nickel was also used for the cantilevers since it had already been thoroughly characterised. However, in future gold could be considered as an alternative due to its lower resistivity.

7.2.1 Device geometry

Two different sets of devices were fabricated by the same process. The first devices, *type A,* were produced using the same mask set that was used to fabricate the suspended structures described in chapter 3. This mask set included cantilevers of length 100 to 700 μm (horizontal) and width 10 to 50 μm at pitches between 23 and 50 μm. This allowed direct comparison between the previous fabrication method and the new. In particular it was possible to check that the new process could produce fine pitch probes.

The probes in the second set of devices, *type B*, had greater widths, lengths and pitches than those of *type A*. This made both the fabrication and testing of the devices simpler and quicker. The geometry of type *B* probes is shown in Figure 7.1.

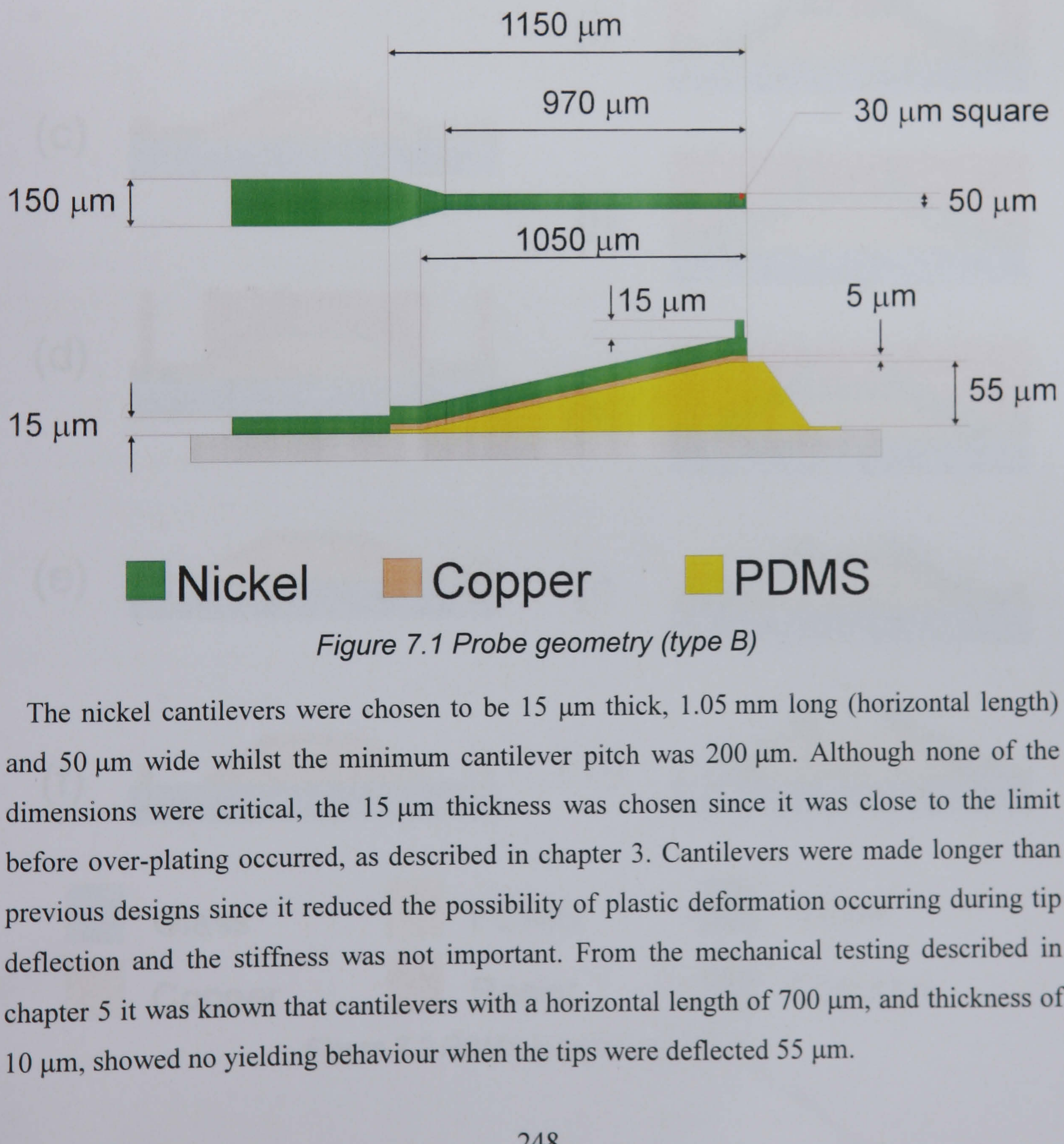

Figure 7.1 Probe geometry (type B)

The nickel cantilevers were chosen to be 15 μm thick, 1.05 mm long (horizontal length) and 50 μm wide whilst the minimum cantilever pitch was 200 μm. Although none of the dimensions were critical, the 15 μm thickness was chosen since it was close to the limit before over-plating occurred, as described in chapter 3. Cantilevers were made longer than previous designs since it reduced the possibility of plastic deformation occurring during tip deflection and the stiffness was not important. From the mechanical testing described in chapter 5 it was known that cantilevers with a horizontal length of 700 μm, and thickness of 10 μm, showed no yielding behaviour when the tips were deflected 55 μm.

7.3 Fabrication

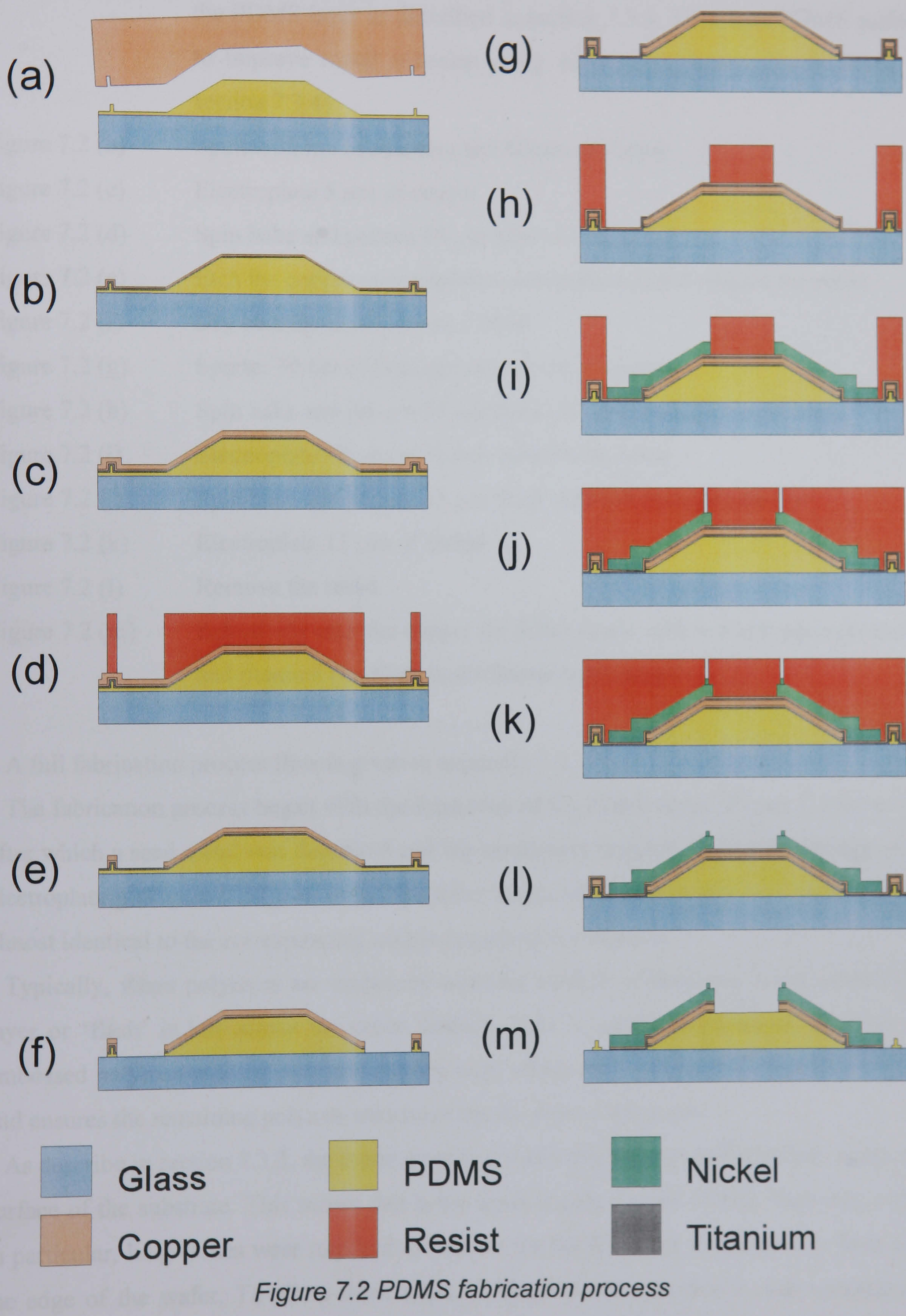

Figure 7.2 PDMS fabrication process

The following fabrication steps refer to Figure 7.2.

Fabrication step	*Description*
Figure 7.2 (a)	Clean borosilicate wafer and then mould and cure and de-mould to form the PDMS layer as described in section 7.3.3. Then treat PDMS surface to improve metal adhesion using an oxygen plasma (as described in section 7.3.4)
Figure 7.2 (b)	Sputter 30 nm of titanium and 60 nm of copper
Figure 7.2 (c)	Electroplate 5 μm of copper
Figure 7.2 (d)	Spin bake and pattern 55 μm thick AZ9260
Figure 7.2 (e)	Etch the copper (electroplated and sputtered) and remove the resist
Figure 7.2 (f)	Dry etch the titanium and PDMS
Figure 7.2 (g)	Sputter 30 nm of titanium and 60 nm of copper
Figure 7.2 (h)	Spin bake and pattern 55 μm thick AZ9260 to define cantilevers
Figure 7.2 (i)	Electroplate 15 μm of nickel, remove the resist
Figure 7.2 (j)	Spin bake and pattern 55 μm thick AZ9260 to define the tips
Figure 7.2 (k)	Electroplate 15 μm of nickel
Figure 7.2 (l)	Remove the resist
Figure 7.2 (m)	Selectively etch the copper (in dilute acetic acid and hydrogen peroxide) and titanium (in dilute hydrofluoric acid) layers

A full fabrication process flow is given in appendix 7-1.

The fabrication process began with the formation of the PDMS layer (Figure 7.2 (a) to (f)) after which a seed metal was deposited and the cantilevers and tips formed by through resist electroplating (Figure 7.2 (g) to (m)). The latter stages of cantilever and tip formation were almost identical to the corresponding stages discussed in chapter 3.

Typically, when polymers are embossed onto the surface of substrate, an unwanted thin layer or 'flash' is left across the entire surface. This is usually resolved by thinning the embossed polymer with an isotropic etching step, which removes the flash from the surface and ensures the remaining polymer structures are the correct thickness.

As describe in section 7.3.3, the crude moulding method left a non-uniform flash across the surface of the substrate. This meant that some areas required more etching than others and, in particular, long etches were required to remove the thicker areas that tended to form near the edge of the wafer. To allow thick areas of 'flash' to be removed it was necessary to protect the desired PDMS features during the etching stage. This was achieved by depositing

and patterning a thick copper mask (Figure 7.2 (b) to (e)). Electroplated copper was used as a mask since it contained no pinhole defects.

7.3.1 Fabrication results

Images of fabricated *type B* probes, just prior to complete electrical isolation (the final copper and titanium etches), are shown in Figure 7.3.

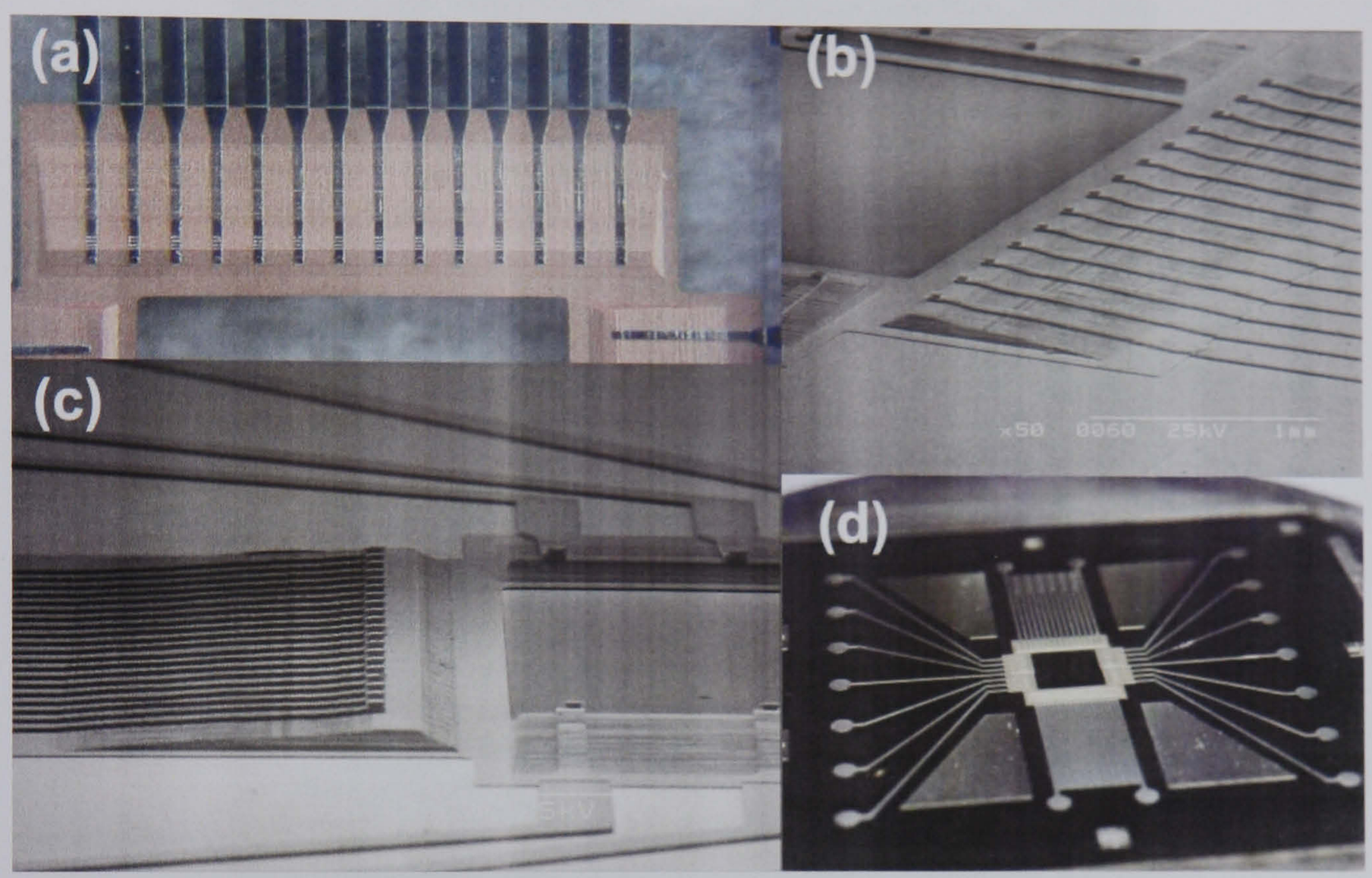

Figure 7.3 PDMS probe devices just prior to completion

To electrically isolate the probes, the sputtered copper and titanium seed layers and electroplated copper mask layer had to be removed (Figure 7.2 (m)). This was achieved by etching the electroplated copper for a limited time so that it was removed between cantilevers but remained beneath the nickel. SEM images of a probe, prior to and after such etching are shown in Figure 7.4.

Figure 7.4 Nickel cantilever and tip (a) before and (b) after electrical isolation

Completed probe arrays are shown in Figure 7.5. Figure 7.5 (a) is of *type B* whilst Figure 7.5 (b) is of *type A* probes.

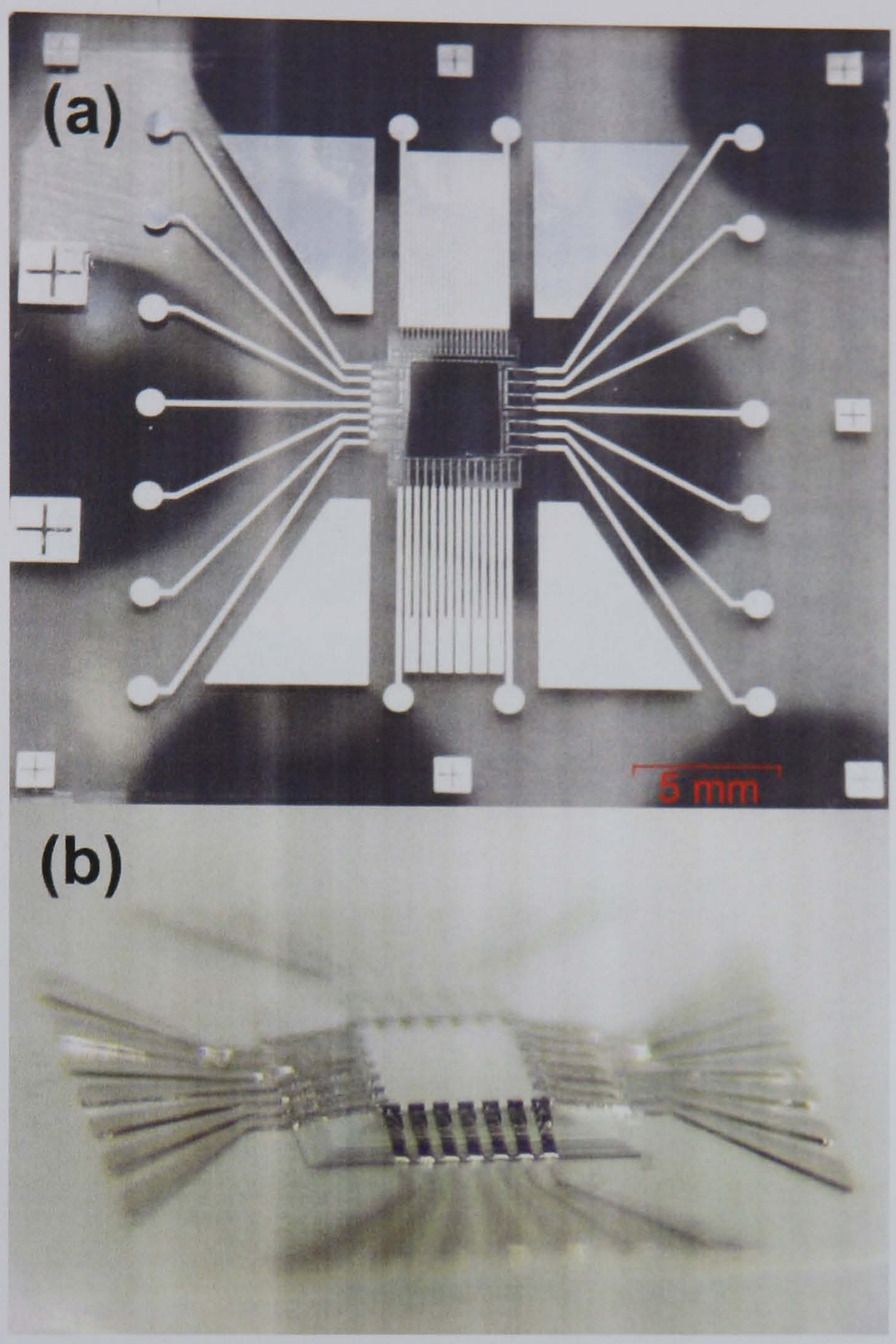

Figure 7.5 Completed PDMS probe devices

Although the moulding of the PDMS layer was inherently more complex than forming a 3D photoresist layer, it was found to be much more stable against subsequent processing. Unlike the thick AZ9260 no deformation occurred during baking processes and there was no trapped solvent to cause ruptures.

Measured 3D profiles of a masked and etched PDMS layer before and after cantilever deposition are shown in Figure 7.6 (a) and (b) respectively. The measurements were taken using a Stil Micromeasure system.

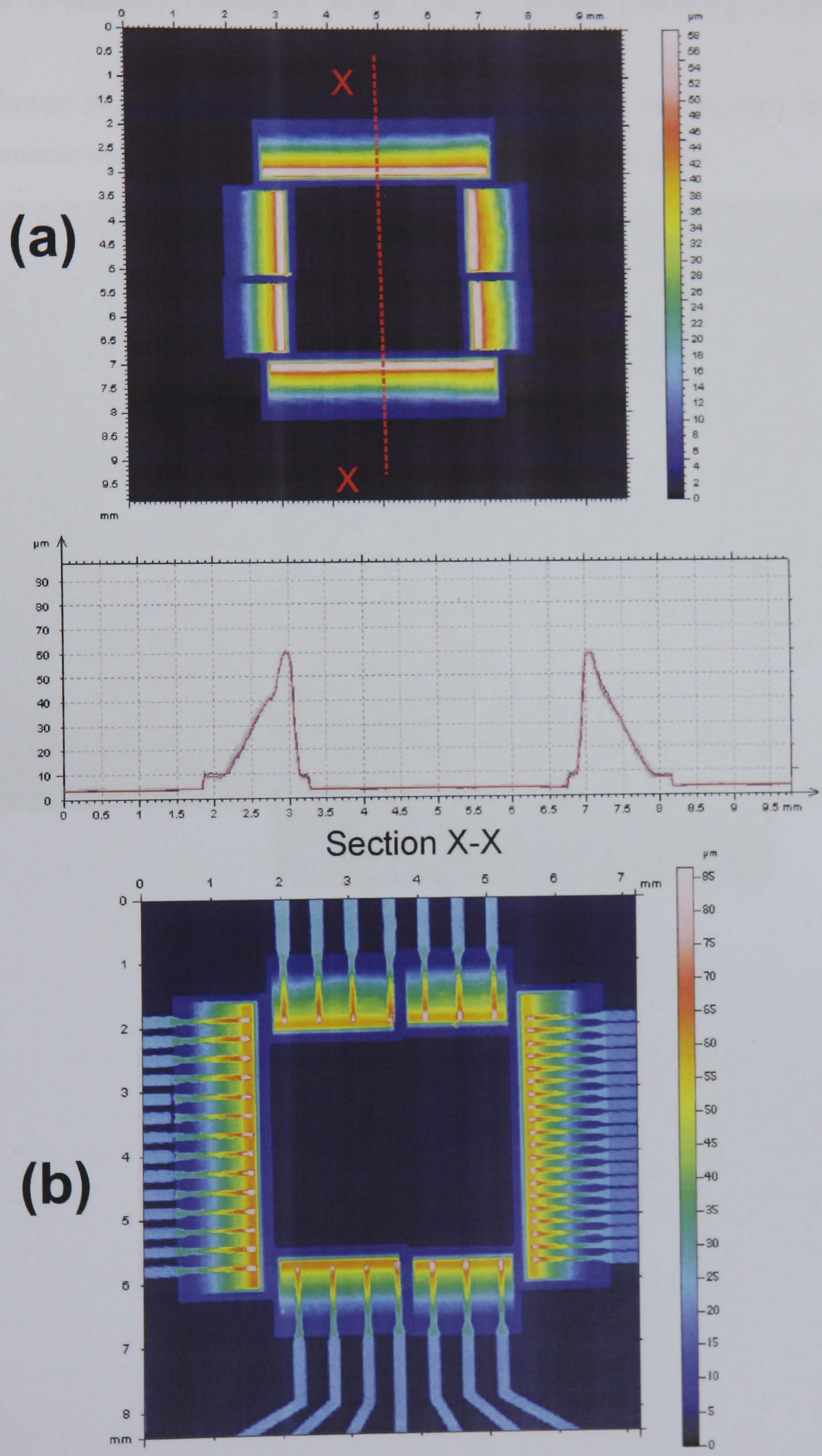

Figure 7.6 (a) 3D profile of the PDMS layer (b) 3D profile of the completed device

From Figure 7.6 (b), it is clear that no deformation of the PDMS layer occurred during the cantilever fabrication stage. This contrasts with the 3D profiles of suspended probe arrays shown in chapter 3 that showed deformation due to warping of the underlying resist. The measured tip co-planarity (measured across a 4 mm section containing 20 probes) was ± 1.5 μm.

An SEM image of *type A* probes is shown in Figure 7.7. It can be seen that the new fabrication process was also capable of producing probes at 23 μm pitch.

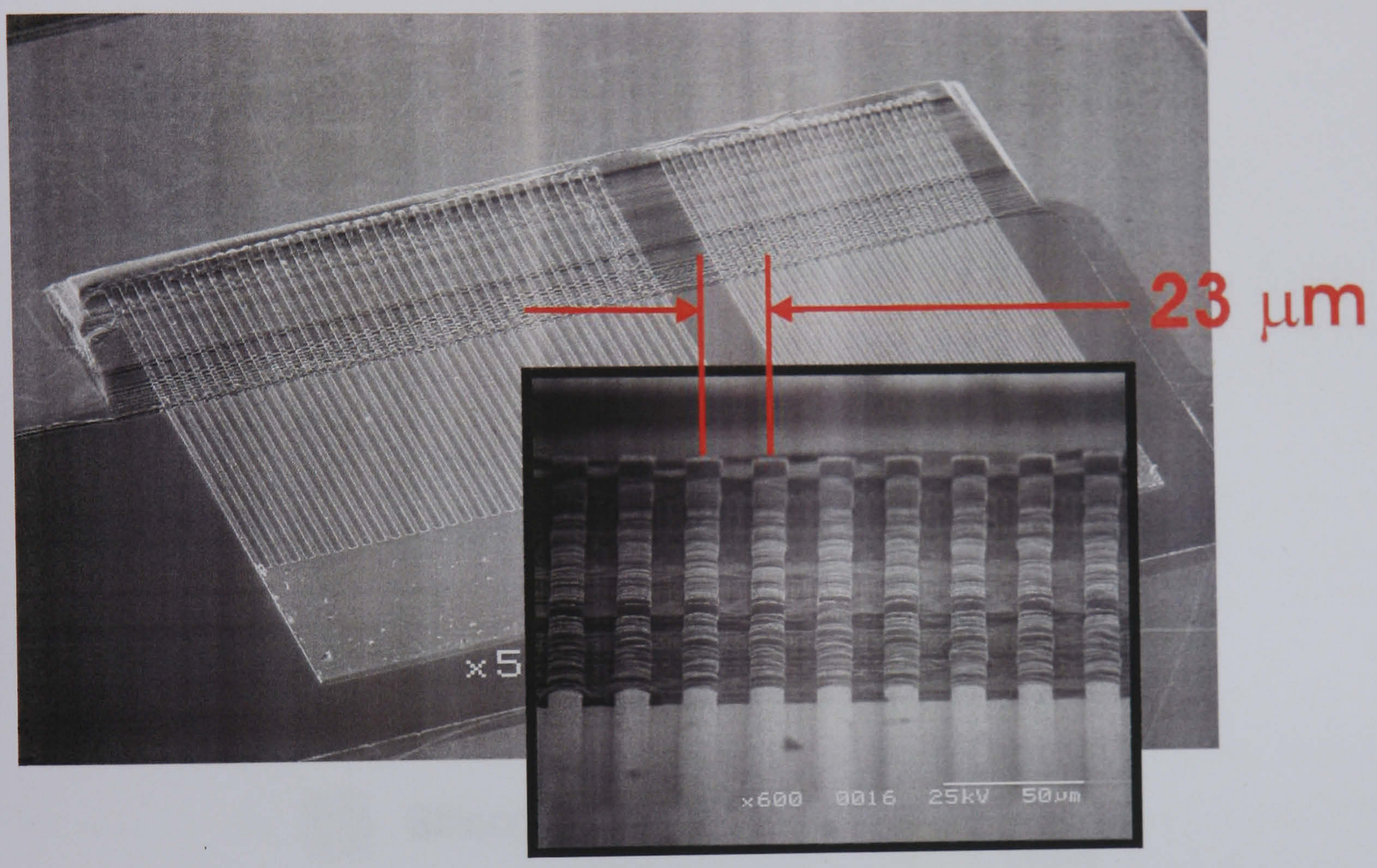

Figure 7.7 Fine pitch cantilevers

7.3.2 Mould fabrication

The geometry of the PDMS mould was defined using the same greyscale lithography techniques described in chapter 3.

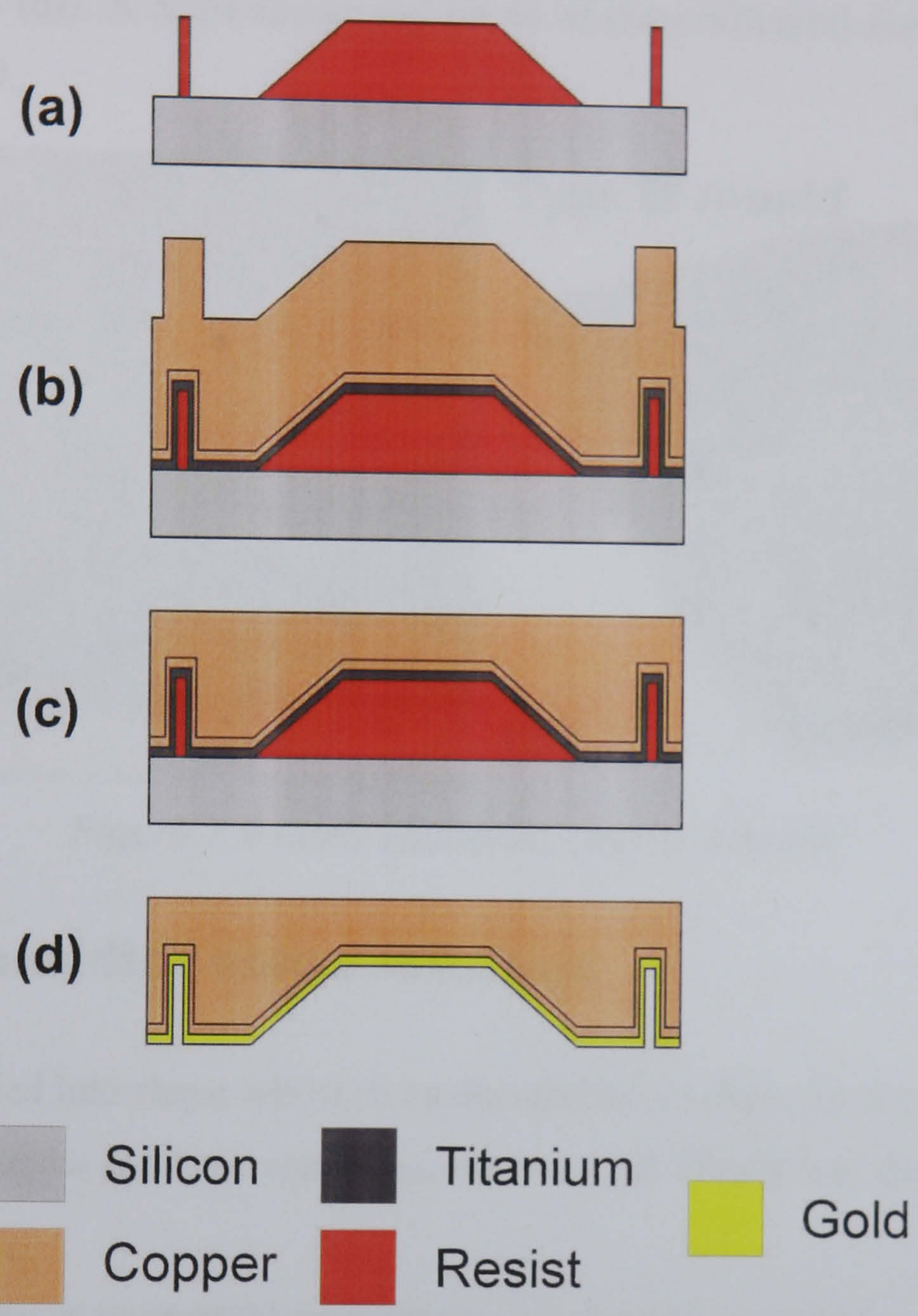

Figure 7.8 Mould fabrication

A cleaned silicon wafer was spun coated with three layers of AZ9260 photoresist to a thickness of 55 μm and baked. The resist was then exposed using a binary halftone mask and developed to produce a resist former of the desired geometry (Figure 7.8 (a)). The wafer was then sputter coated with a 30 nm titanium adhesion layer and 100 nm copper seed layer before electroplating copper to a thickness of approximately 500 μm (Figure 7.8 (b)).

Although nickel is traditionally used in moulding applications copper was chosen as its lower internal stress made it simpler to electroplate to the required thickness. Additionally the lower mechanical strength and wear resistance of copper compared to nickel was not found to be a problem since the PDMS was liquid when being moulded (see section 7.3.3).

After the copper electroplating, the top face of the copper was ground flat to produce a surface parallel with the wafer surface beneath (Figure 7.8 (c)). Finally the silicon wafer, resist and titanium adhesion layer were dissolved in 90 °C KOH (350 g/l) and the surface of the released copper mould was sputter coated with gold to help the PDMS de-moulding process (Figure 7.8 (d)). A SEM image and photo of (two different) completed moulds are shown in Figure 7.9.

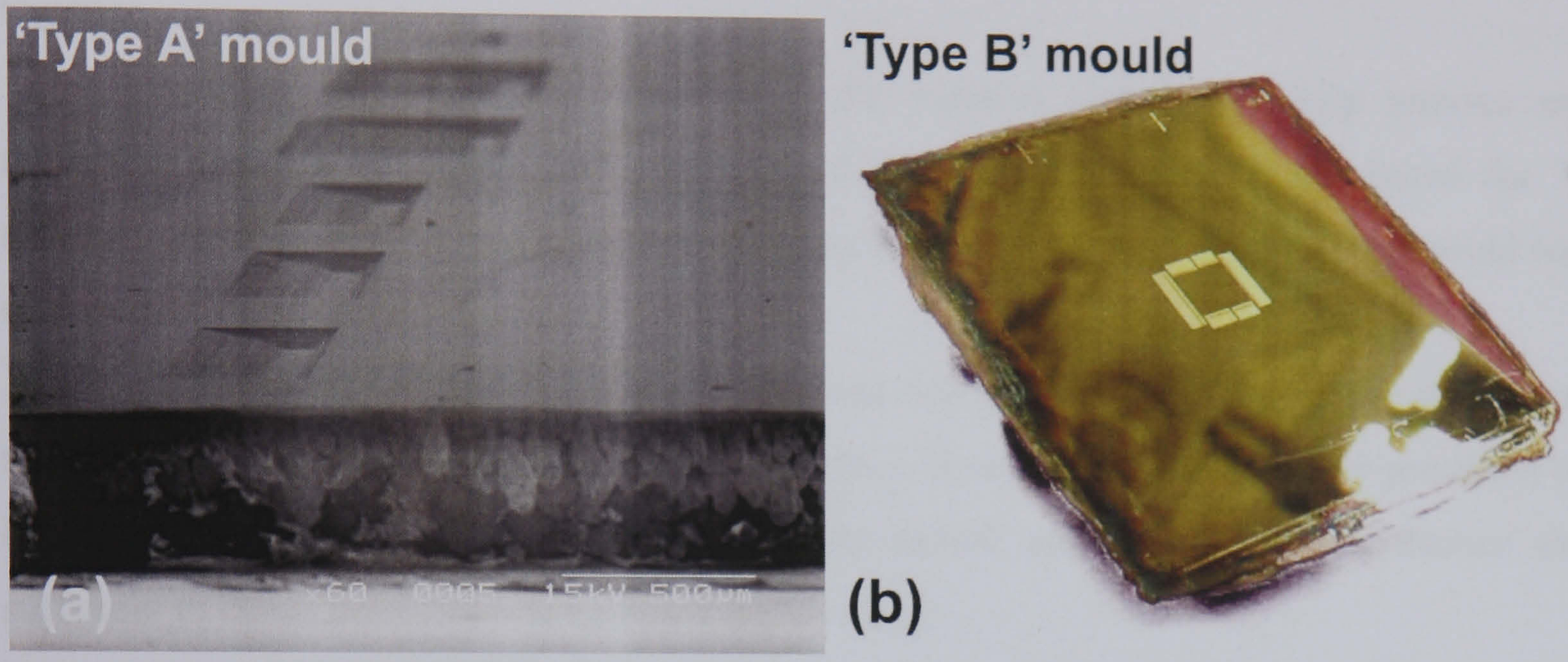

Figure 7.9 Gold sputtered copper moulds

7.3.3 PDMS moulding onto a substrate

PDMS was moulded into shape whilst in its uncured liquid state. To accelerate the reaction between the curing agent and base elastomer, the moulded PDMS was then heated to form a solid rubber.

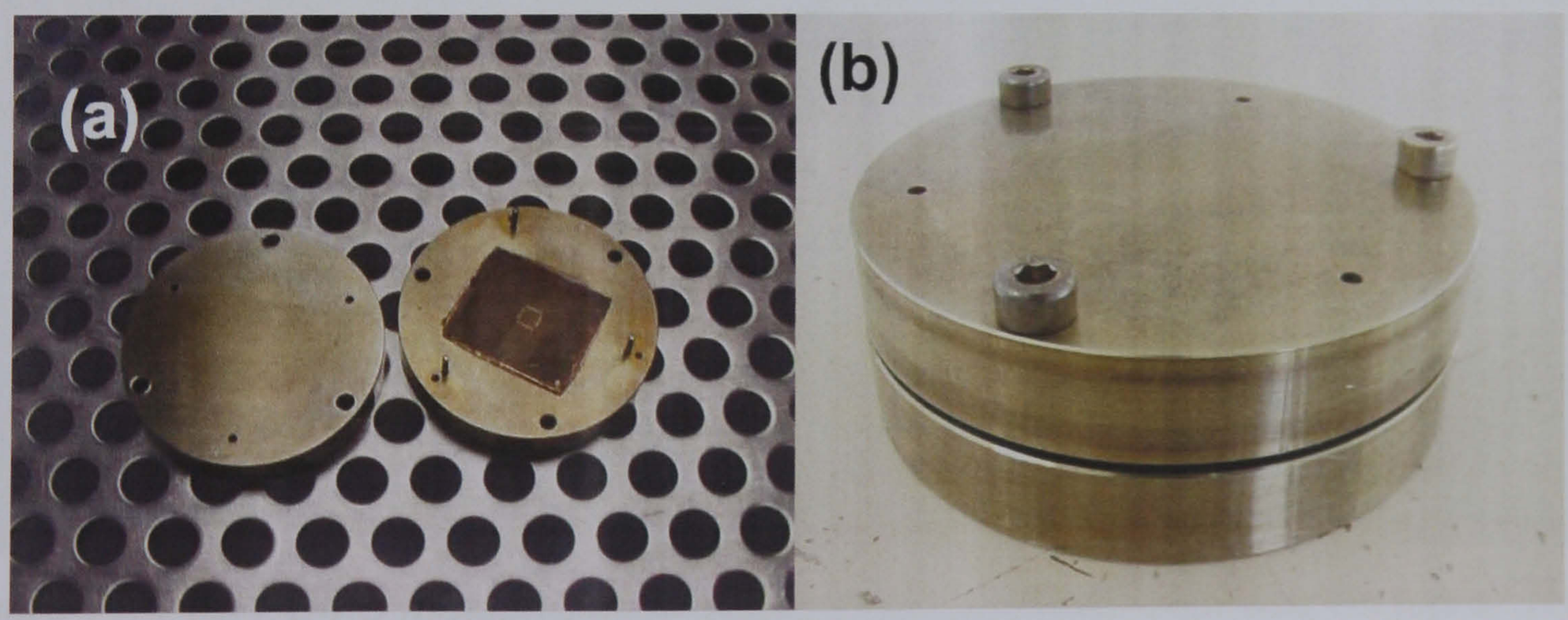

Figure 7.10 The vice used to mould PDMS. (a) Vice in parts (b) Vice assembled

PDMS base silicone elastomer (Sylgard 184, Dow Corning) was mixed with curing agent (184 curing agent, Dow Corning) in a ratio of 10 parts base elastomer to 1 part curing agent.

The mixture was then out-gassed by placing it in a vacuum chamber (pressure 10^{-2} torr) to remove trapped air from the mixture. A small volume of the mixture was then dispensed onto the copper mould and out-gassed for a second time. This was required to remove air trapped between the PDMS and surface of the mould.

A borosilicate glass substrate was then placed on top of the mould and the pair were placed in a mechanical vice (see Figure 7.10) which was used to press the substrate and mould together.

The assembled vice was then placed into the vacuum chamber to help remove any remaining trapped air before being transferred to a 140 °C hot plate and baked for 30 minutes. Once the PDMS was cured, the substrate was allowed to cool before the mould was removed.

Gold on the surface of the copper mould ensured that the PDMS adhered more strongly to the glass substrate than it did to the mould's surface. It was found that the force produced by inserting the tip of a scalpel blade between the mould and substrate at one corner was sufficient to cause delamination between the interfaces.

Images of moulded PDMS layers are shown in Figure 7.11. The left image is of PDMS moulded on a borosilicate glass wafer. The right image shows PDMS moulded on top of an titanium film evaporated on glass. The fringes that can be seen show that a thin but non-uniform layer of PDMS remains over the surface of the substrate. The non-uniform nature of this 'flash' resulted from the basic set up of the moulding process since it was impossible to get a even pressure distribution across the mould.

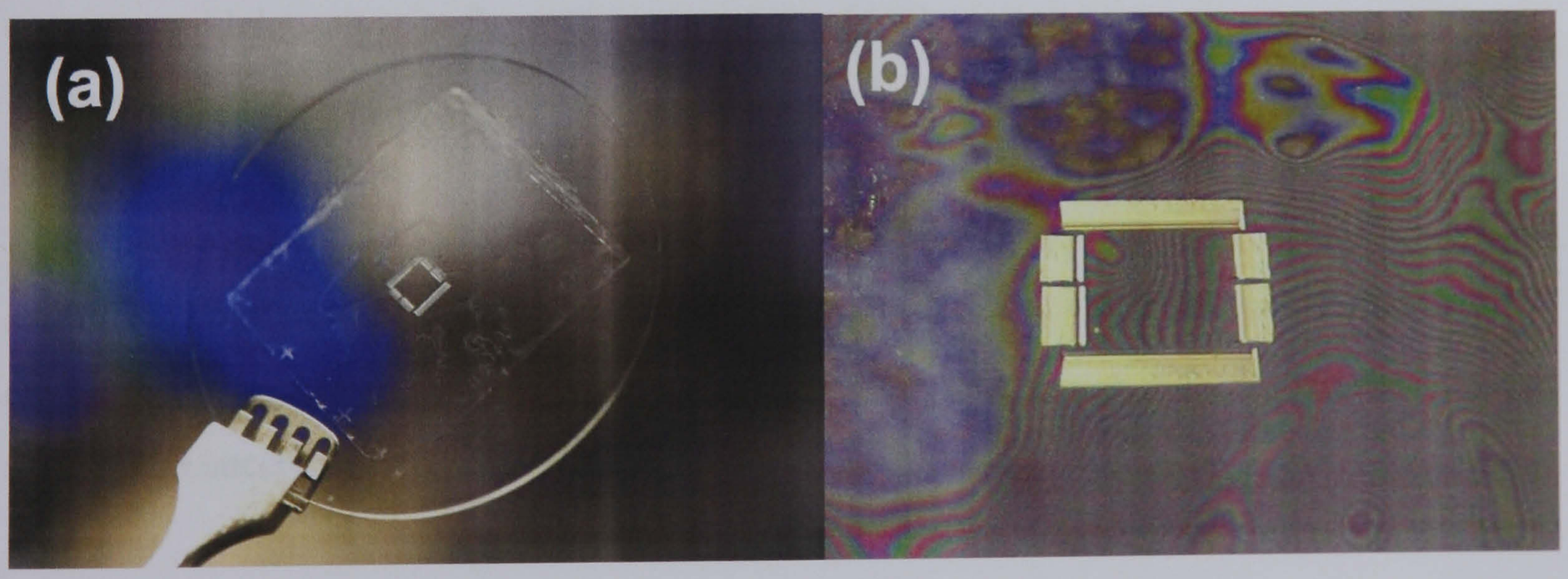

Figure 7.11 (a) PDMS moulded onto glass wafer (b) PDMS moulded on top of Ti film on glass wafer showing PDMS 'flash' remaining

7.3.4 PDMS oxygen treatment

If was found that if metal was sputtered or evaporated directly on top of the PDMS then it tended to crack. This was attributed to the extremely poor adhesion of metal to the PDMS so that even small internal stresses in the film caused delamination.

It is known that PDMS cannot be dry etched in pure oxygen [3] since a silicon rich layer forms at the surface preventing further etching. Therefore dry etching chemistry always utilises a fluorine containing gas such as CF_4 or SF_6.

It was postulated that a silicon rich layer could help improve metal adhesion, and hence reduce or eliminate cracking. Such an effect by oxygen plasma on PDMS has been reported elsewhere [4, 5].

To test the hypothesis, moulded PDMS samples (on glass) were exposed to an oxygen plasma using an Oxford PlasmaLab 80Plus (quartz cover platen at 20 °C, 40 sccm O_2, 200 mT, 200 W) for 15 minutes.

A treated and untreated sample were sputter coated with a 30 nm titanium adhesion layer and 60 nm copper seed layer. The sputter deposition was conducted at optimised pressures to minimise the internal stress of the films (see chapter 3). The samples were examined before electroplating copper from a bath of the formulation described in chapter 3. The electroplating step was intended to identify defects in the sputtered film.

If areas of the sputtered film were electrically isolated prior to electroplating, due to cracking, then the sputtered copper in these areas would be dissolved during the electroplating process due to the low pH of the solution. If however the sputtered films had no isolated areas (i.e. were continuous or had discontinuous cracks) then it was expected that copper would deposit over the entire substrate surface.

Images of an untreated and treated PDMS sample, after sputtering and electroplating are shown in Figure 7.12.

Cracks are clearly visible in the metals sputtered on the sample that was not oxygen treated and this is confirmed by the subsequent electroplating. Conversely there is little evidence of cracks in the sputtered film on the oxygen treated sample and this is supported by the subsequent successful deposition of copper by electroplating.

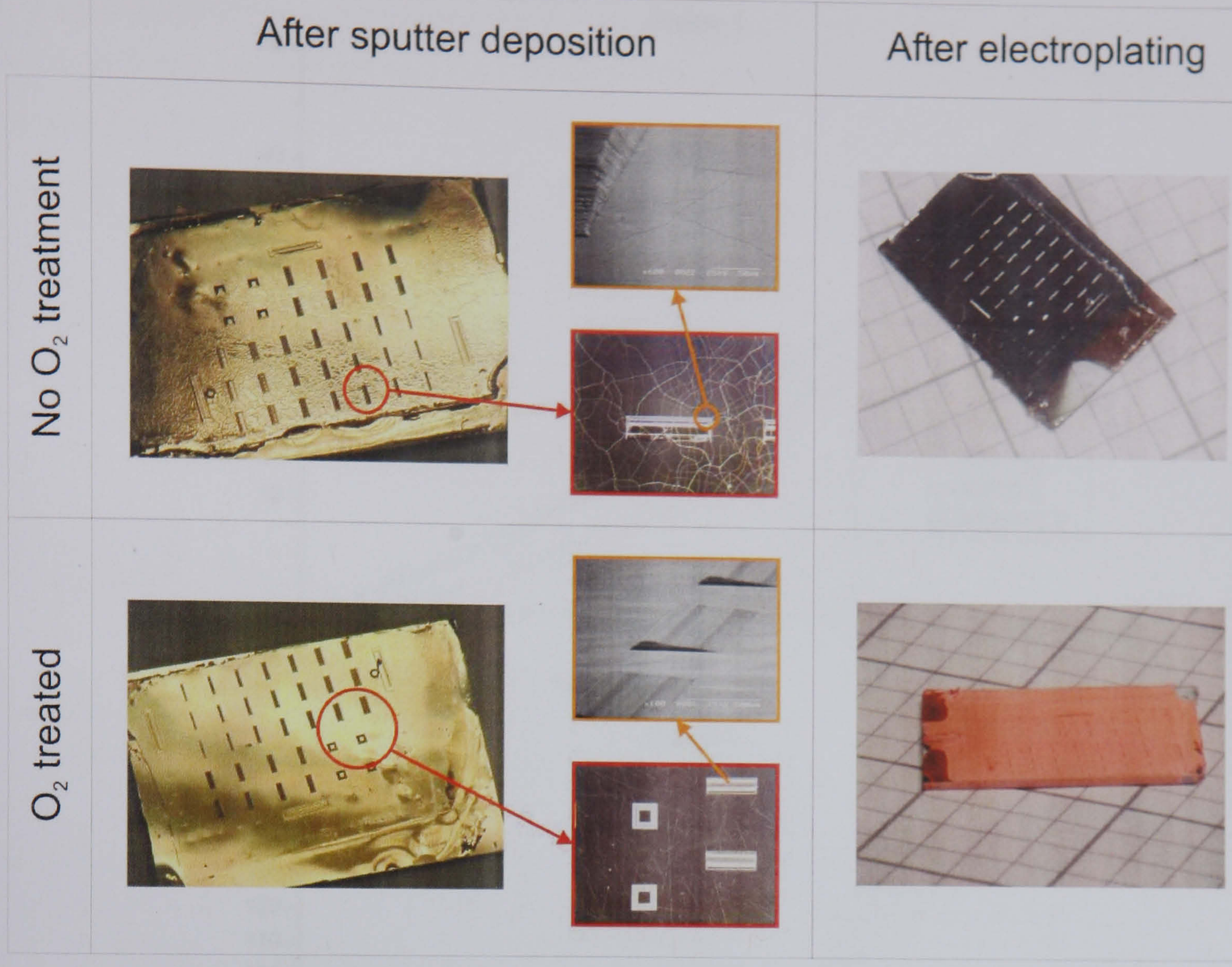

Figure 7.12 Effect of oxygen plasma of metal adhesion to PDMS

7.4 Mechanical testing

Six identical probes were tested to obtain force-deflection data using the method and equipment describe in chapter 4. The tested devices were of *type B* and so had the same dimensions as shown in Figure 7.1 (except that no cantilever tips were fabricated). Typical mechanical results are shown in Figure 7.13. Testing was performed by applying either 0.5 μm (probes 1,2,3) or 1 μm (probes 4,5,6) displacement steps to the nano-positioning stage with a 3 second pause between movements. The 3 second pause allowed the force readings to settle and reduced any effects of strain rate which are known to influence elastomer mechanical properties [6].

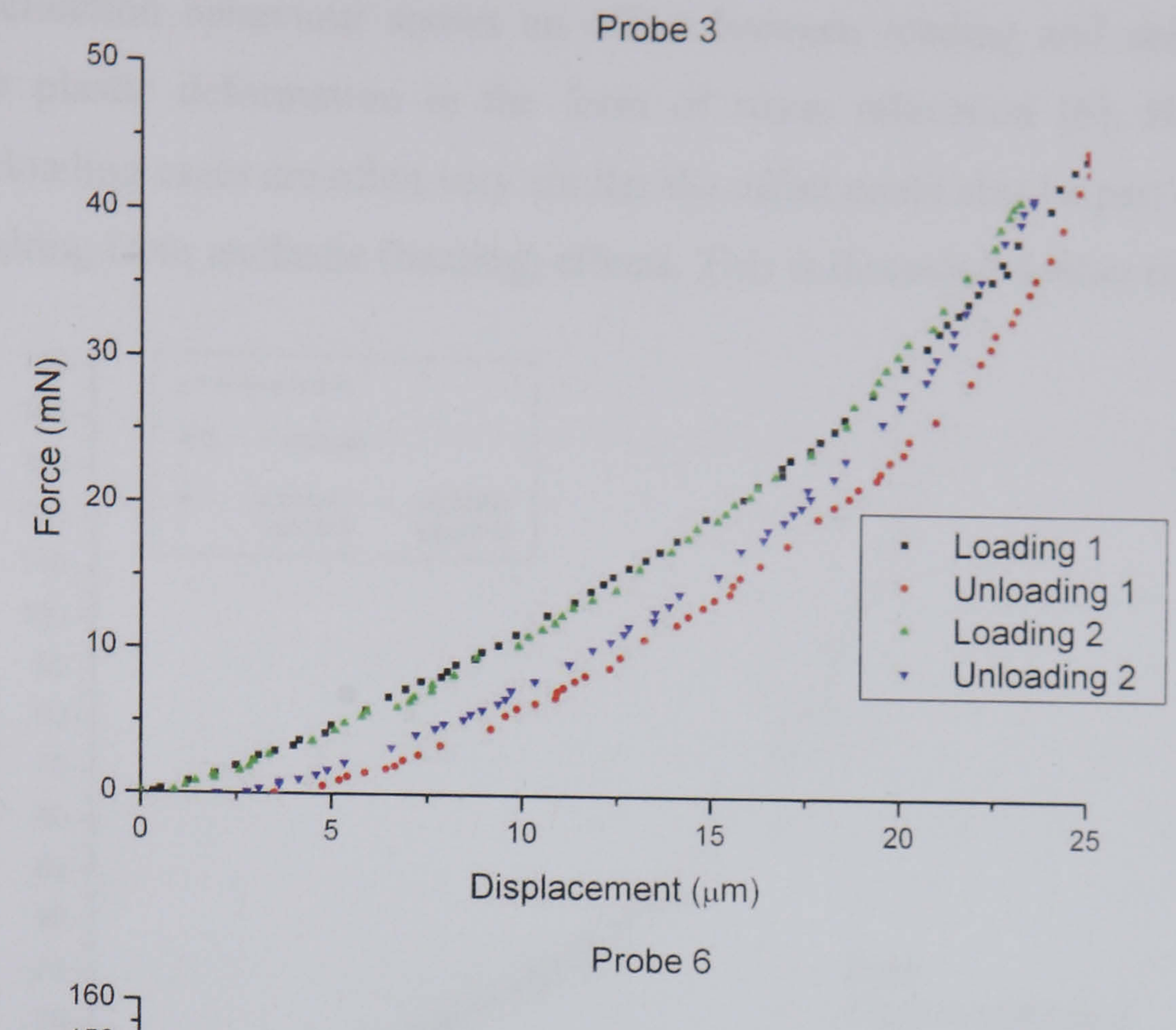

Figure 7.13 Force-deflection behaviour

Comparing the results shown in Figure 7.13 to those discussed in chapter 5 it can be seen that the PDMS probes were much stiffer than the suspended cantilevers. The stiffest suspended cantilever design applied a maximum force of 9 mN compared to approximately 140 mN for the PDMS probe (both measured at 40 μm deflection).

During the testing of the PDMS probes the deflection of the balance was significant and had to be subtracted from the total deflection. The results shown in Figure 7.13 have been corrected assuming that the balance had a linear force-deflection behaviour that could be characterised by a spring constant of 11.7 mN/μm (see chapter 4, Figure 4-14).

The force-deflection behaviour shows an offset between loading and unloading which could indicate plastic deformation in the form of stress relaxation [6]. However, since loading and reloading cases are often very similar the offset could also be part of a clockwise hysteresis resulting from anelastic (heating) effects. This is discussed further in section 7.4.1.

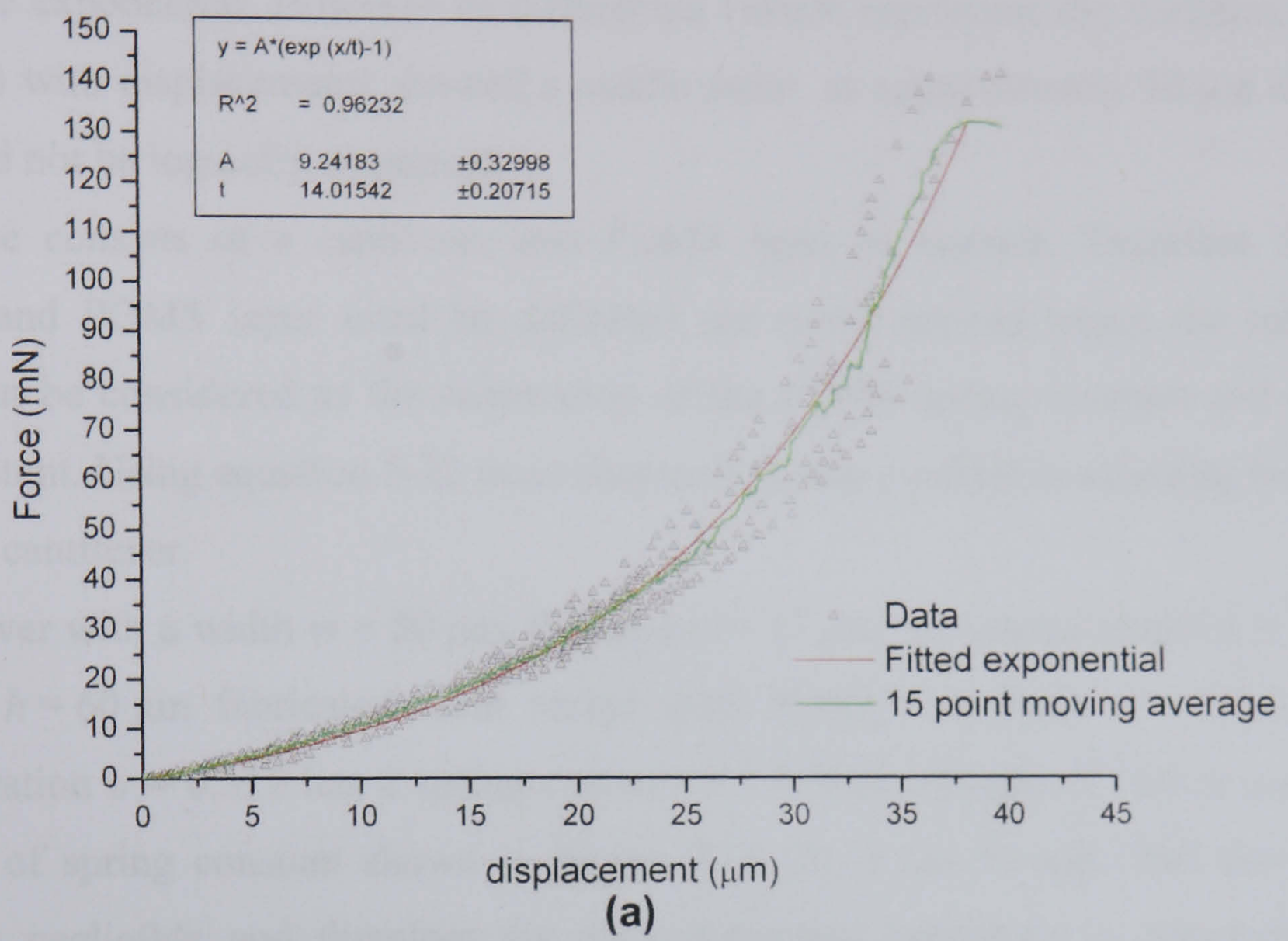

Figure 7.14 (a) Exponentially fitted force-deflection data (b) Calculated derivative (spring constant)

Loading data from the six tested probes was combined and an empirical exponential curve was fitted. An exponential function was chosen since it fitted the data well. Graphs showing

the data with fitted exponential function and its differential can be seen in Figure 7.14 (a) and (b) respectively.

Other functions were investigated however an exponential function was found to fit the data most convincingly. For instance, a quartic equation could be fitted with a similar R^2 factor to the exponential. However its differential (which represents the variation in spring constant (k) with displacement) showed a saddle point, at approximately 10 μm deflection, which could not be logically explained.

The probe consists of a cantilever and PDMS layer in contact. Therefore the nickel cantilever and PDMS layer must be deflected the same amount hence the total spring constant can be considered as the summation of the PDMS spring constant and cantilever spring constant. Using equation 5-22 from chapter 5, it was possible to calculate the stiffness of only the cantilever.

A cantilever with a width $w = 50$ μm, thickness $t = 15$ μm, horizontal length $L = 1000$ μm, tip height $h = 60$ μm fabricated from nickel with Young's modulus $E = 146.2$ GPa and Poisson's ration $\upsilon = 0.312$ has a spring constant $k = 0.0061$ mN/μm. If this is compared to the values of spring constant shown in Figure 7.14 (b) is can be seen that the cantilever stiffness is negligible and therefore the force-deflection behaviour is dominated by the behaviour of the PDMS layer.

The non-linear increase in force with large strain compression is similar to experimental results obtained elsewhere [7] and is well known for rubbers [8]: however it is not well understood. It could either result from non-linear strain fields due to the large percentage strains or from the fundamental behaviour of elastomers.

A generally agreed theory of elasticity in rubbers was developed it the 1940's [9], but continues to evolve. A rubber above its glass transition temperature (-125 °C for PDMS [2]) can be thought of as an amorphous three dimensional molecular network cross-linked at a few points [8]. The portions of the molecules in-between junction points are flexible chains that consist of several freely jointed ridged links [7]. When in the relaxed state, these chains are free to oscillate in a large variety of geometries and so take randomly kinked forms due to thermal energy. Upon the application of a tensile stress, the chains can start to straighten which reduces their freedom of oscillation and the entropy of the rubber. During stretching the kinetic energy of oscillation is released as heat. It is this entropy change that is responsible for the elastic energy stored in the rubber.

If strains are applied below the rubber's plastic limit then the removal of the strain allows the rubber to return to its original shape. The restoring force stems from the fact that the

molecules cannot move past one another during deformation as they are fixed by cross links. When the rubber contracts to its original state it absorbs heat from its surroundings.

The source of non-linearity of stress-strain behaviour is still a hot topic. A recent proposal is that the non-linearity results from a heat-driven movement of the cross linking points [10].

Rubbery materials like PDMS are volume incompressible [7] and so compression in one dimension causes an expansion in others. When a sheet of rubber is indented, tensile forces are set up along the surface of the rubber as well as in the bulging walls of the layer. It is these forces that were responsible for the measured force-deflection behaviour of the probes.

7.4.1 Mechanical durability

The SEM image shown in Figure 7.15 and 3D profile shown in Figure 7.16 are of the probes after mechanical testing.

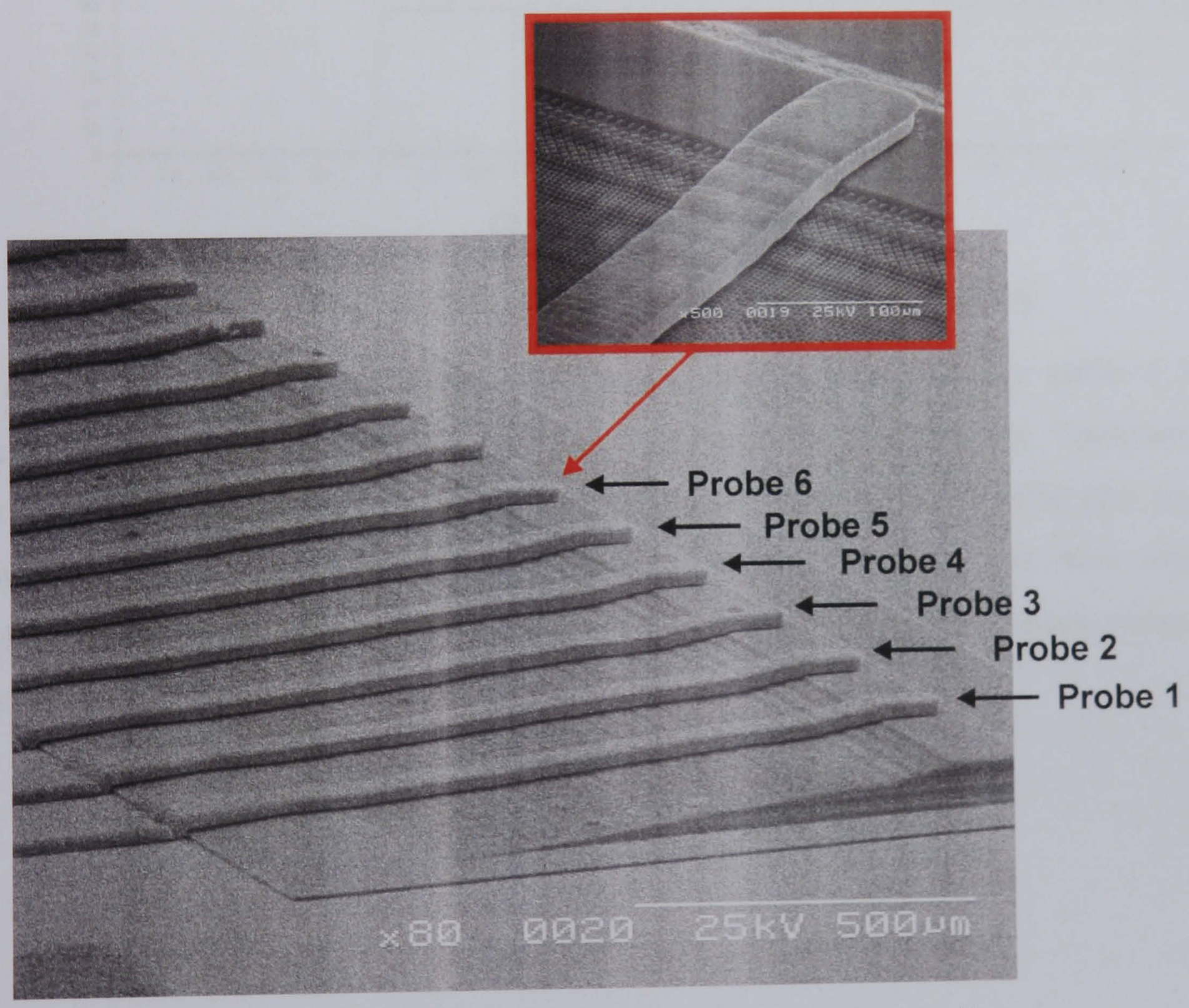

Figure 7.15 SEM of probes after mechanical testing

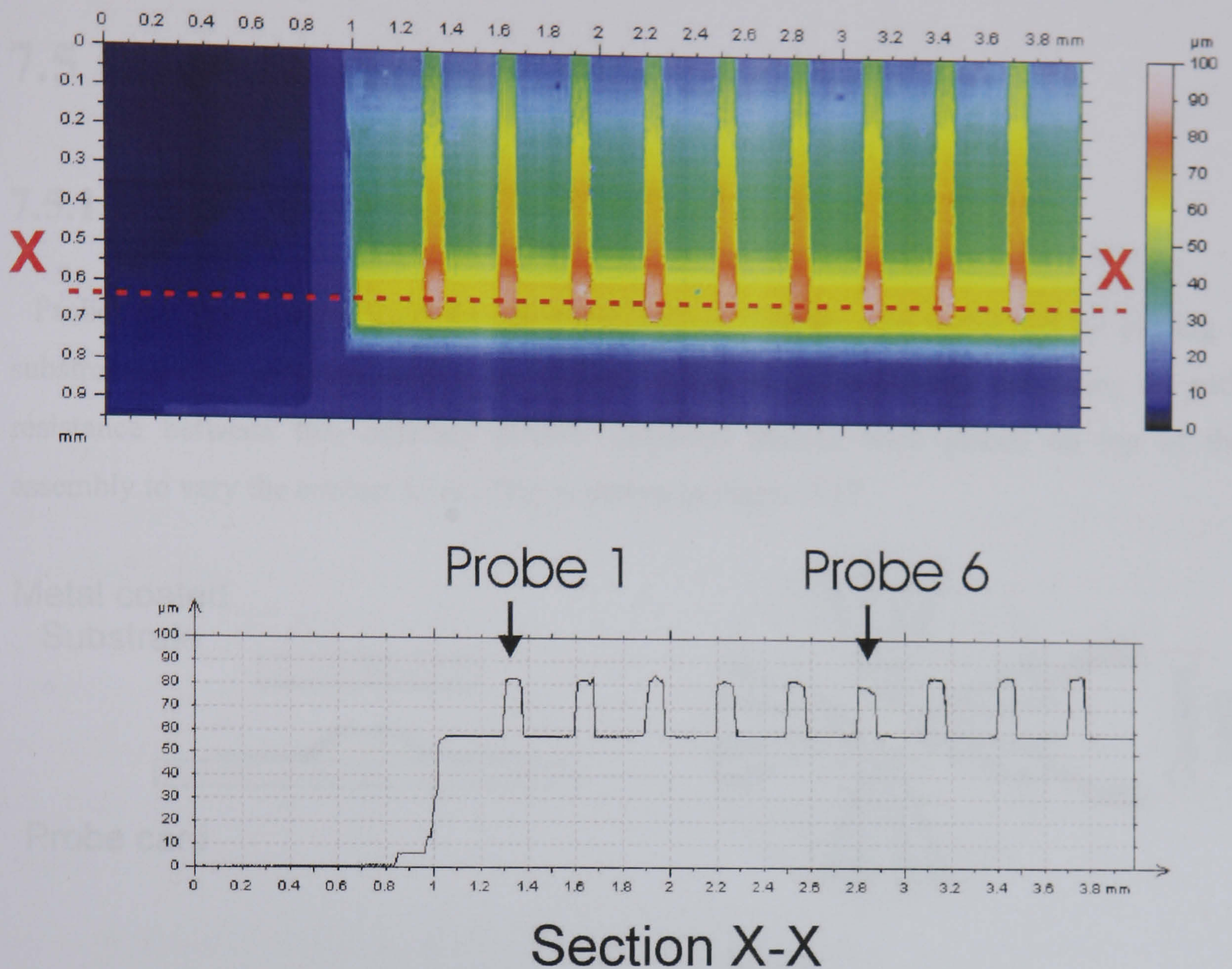

Figure 7.16 3D profile of probes after mechanical testing

As can be seen there is no evidence of damage to the probes despite probe 6 being deflected 40 μm, which is over 70% of the thickness of the PDMS layer. Therefore, the offset seen between the loading and unloading curves must be recoverable (for the test conditions applied). The durability of PDMS to large deformation has been reported elsewhere, for instance Jeong et. al. [11] saw no determination of a PDMS micro pump over 18,000 cycles.

7.5 Electrical testing

7.5.1 Experimental setup

Probes of *type B* were used for electrical testing. Testing was performed by placing a substrate, coated with the desired metal film, on top of the probes and measuring the path resistance between two adjacent probes. Different masses were placed on top of the assembly to vary the contact force. This is shown in Figure 7.17.

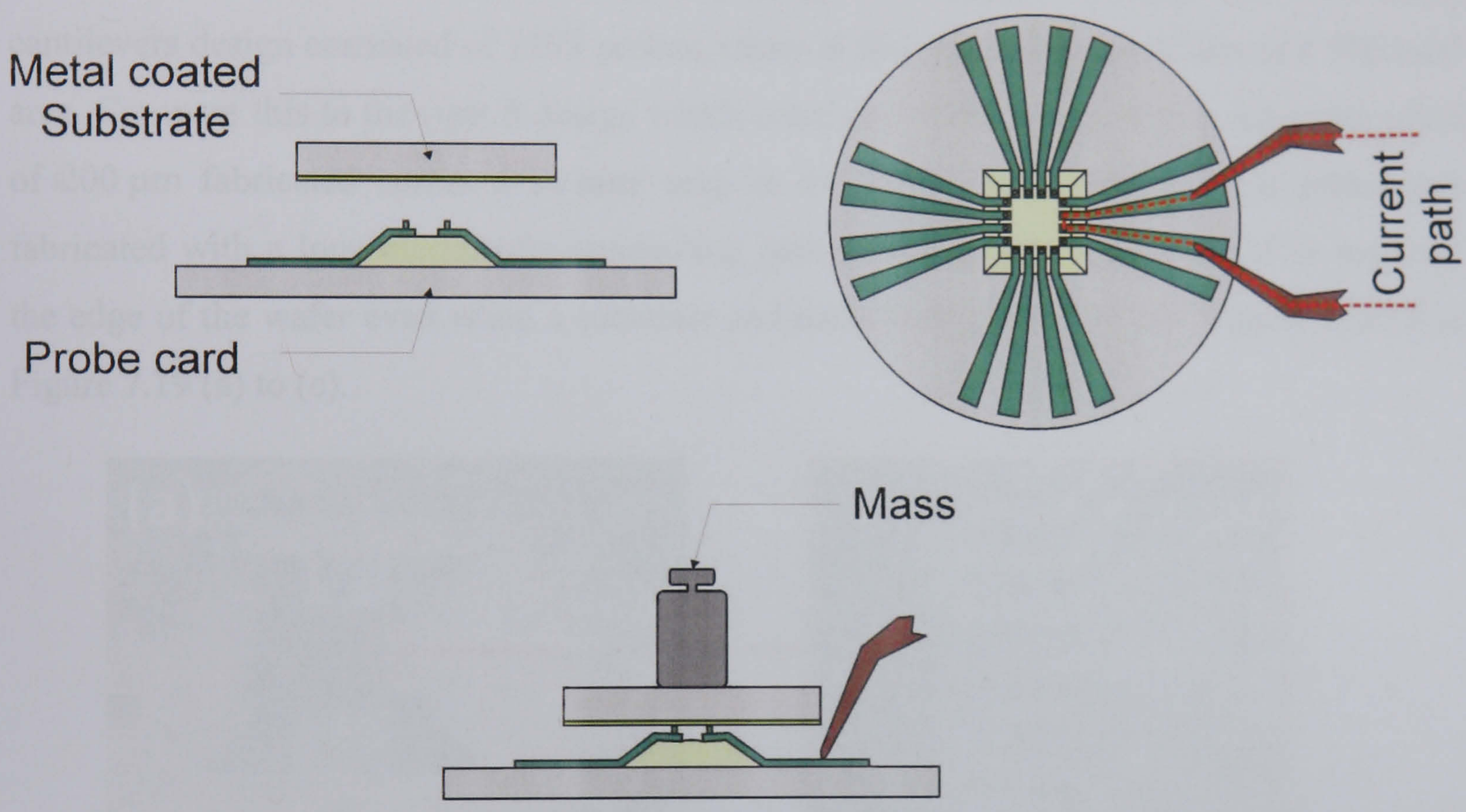

Figure 7.17 Electrical testing setup

This testing method did not require the use of a 'test tip' (see chapter 4) and instead allowed the testing to be performed directly against evaporated metal films on silicon (or other) substrates. This removed the inherent variation introduced by the non-uniform nature of the test tip surface. However, this method also had major limitations since it was not possible to obtain force-resistance data and all probes had to be contacted simultaneously. Additionally, the exact force on any one probe could not be known since it depended on the position of the mass with respect to the probe wafer (see Figure 7.18).

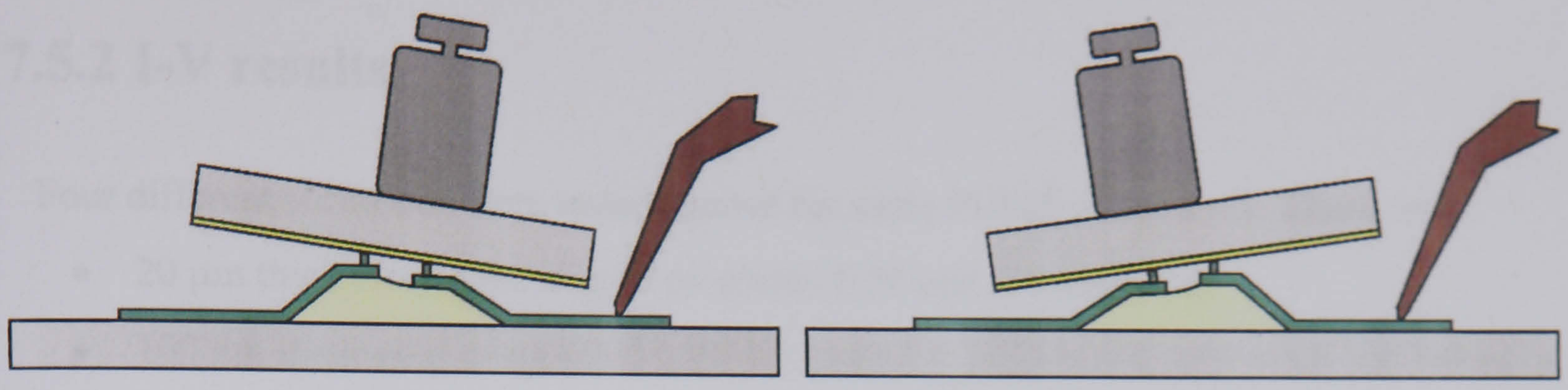

Figure 7.18 Effect of mass position

It should be noted that it would not have been possible to use this method to test the suspended probes. Firstly, the suspended probes were much more delicate than the PDMS probes and so would have been broken during the testing. Secondly, the suspended cantilevers design consisted of 1198 probes, many at fine pitch, fabricated across a 500 mm² area. Compare this to the *type B* design which consisted of 48 probes with a minimum pitch of 200 µm fabricated across a 36 mm² area in the centre of the wafer. Each probe was fabricated with a long electrically conducting path to which connections could be made at the edge of the wafer even when a substrate and mass were placed on top. This is shown in Figure 7.19 (a) to (c).

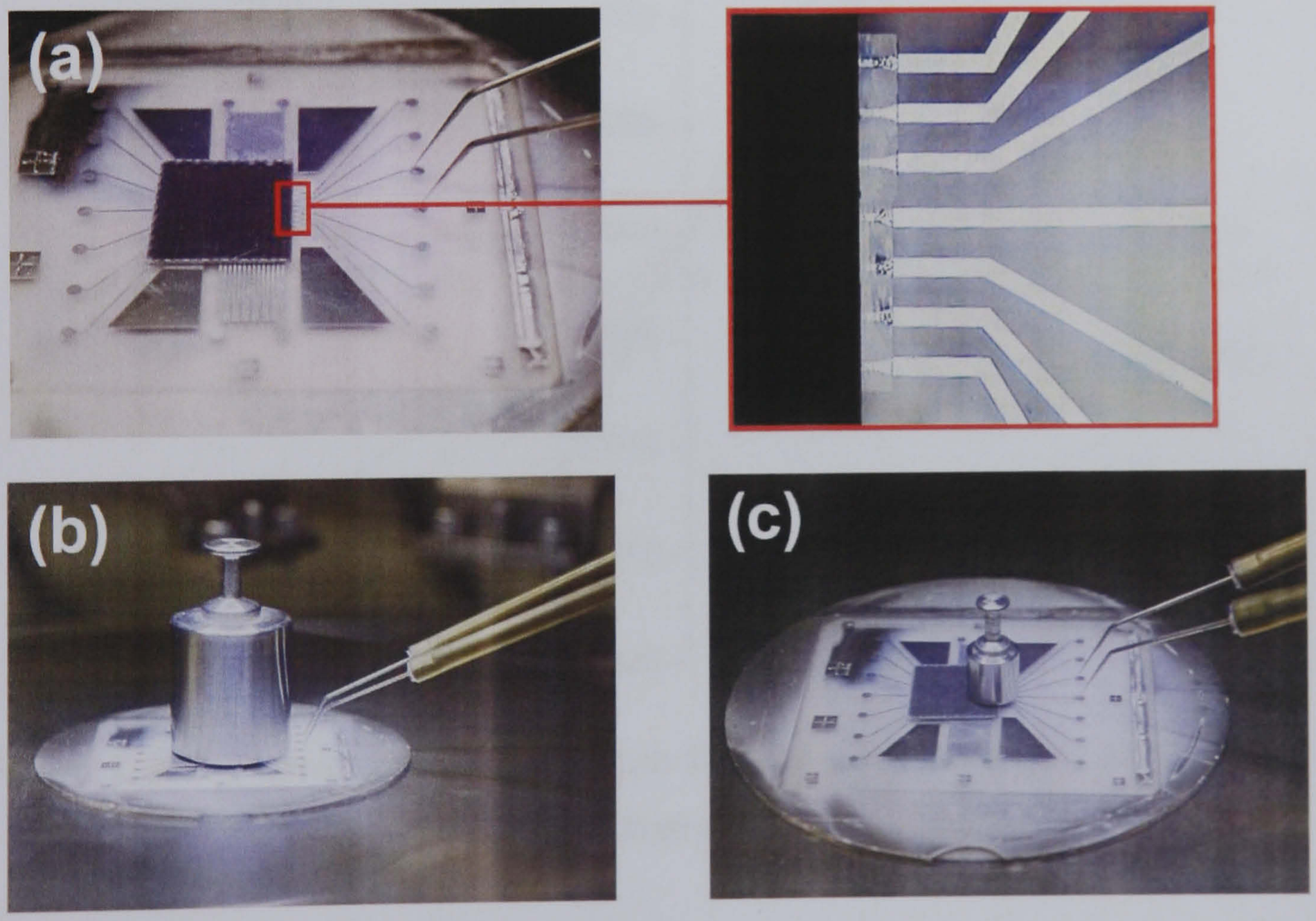

Figure 7.19 Examples of the PDMS probes under test

7.5.2 I-V results

Four different substrates were tested against the same PDMS probe array. These were:

- 20 μm thick electroplated gold on plastic (CiCorel, Switzerland)
- 100 nm thick gold evaporated onto 1.5 μm thick photoresist layer spun and baked on silicon substrate
- 300 nm thick copper evaporated onto borosilicate glass substrate
- 300 nm thick aluminium evaporated onto borosilicate glass substrate

I-V measurements were taken using a HP4145B parameter analyser by sweeping the voltage from -2 V to +2 V in 0.05V steps and measuring the current (the current limit was ± 20 mA). Results for different substrates each measured with different masses are shown in Figures 7.20 to 7.23.

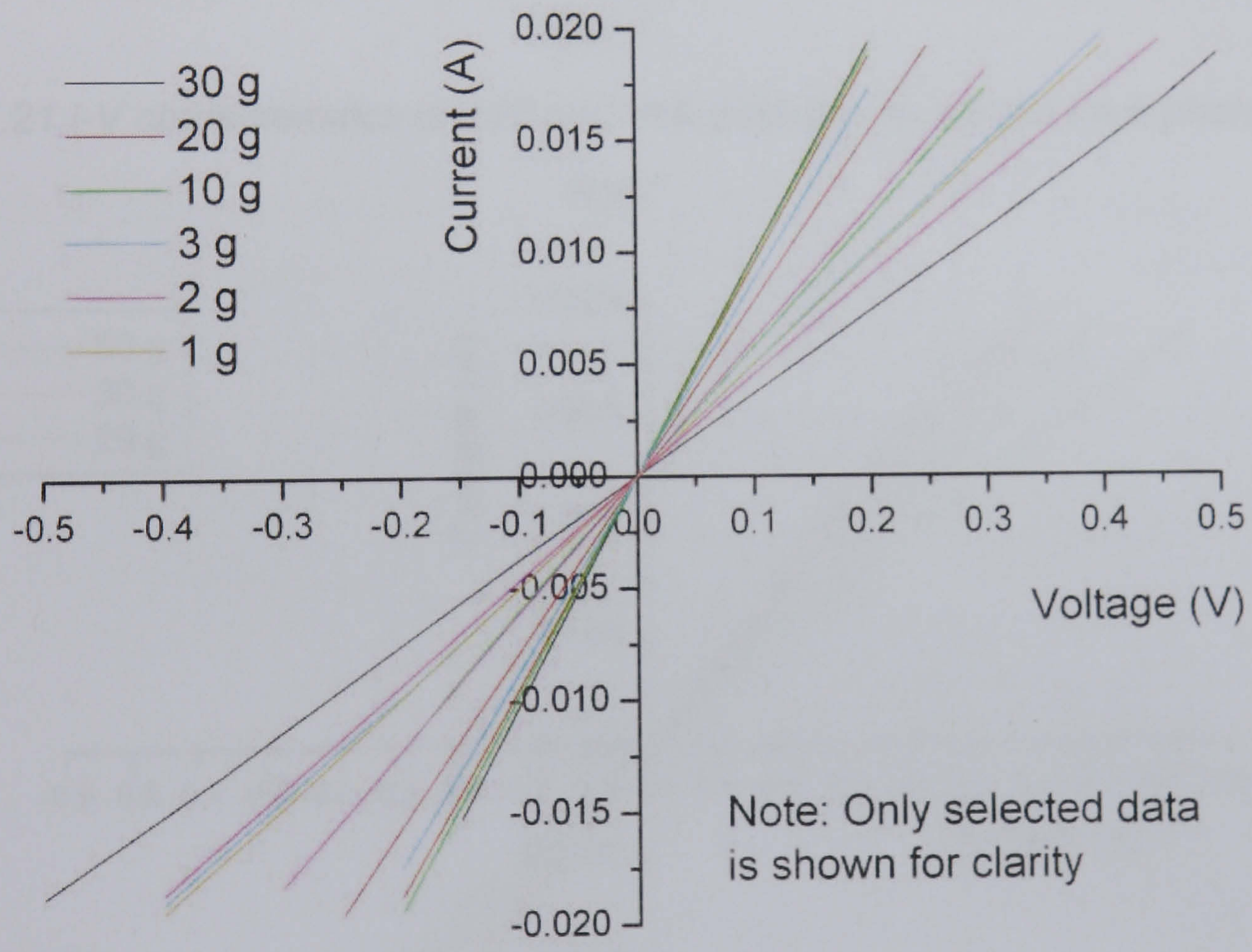

Figure 7.20 I-V measurement of 20 μm thick electroplated gold film on plastic substrate

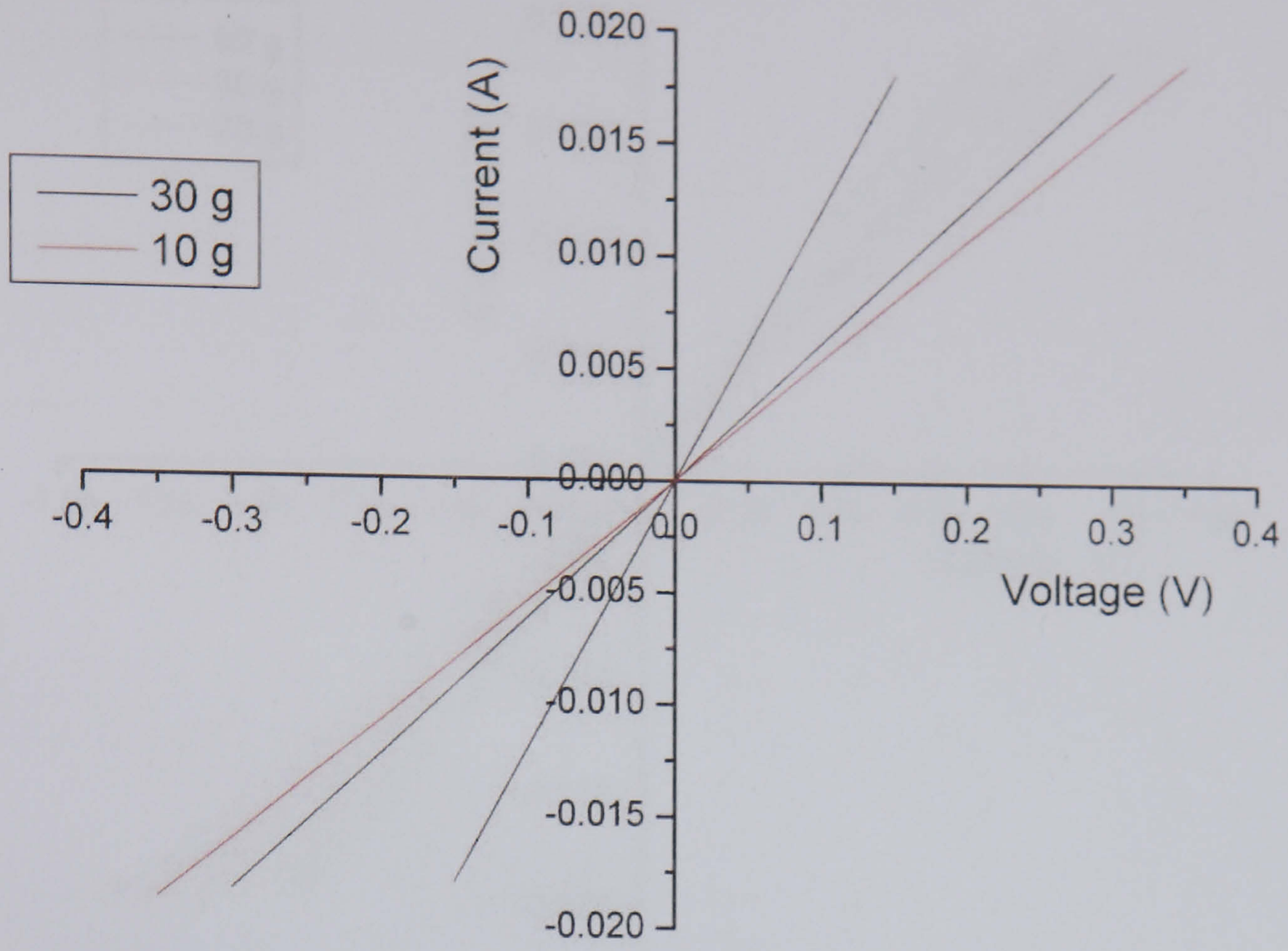

Figure 7.21 I-V characteristics of 100 nm thick gold film on 1.5 μm thick photoresist layer

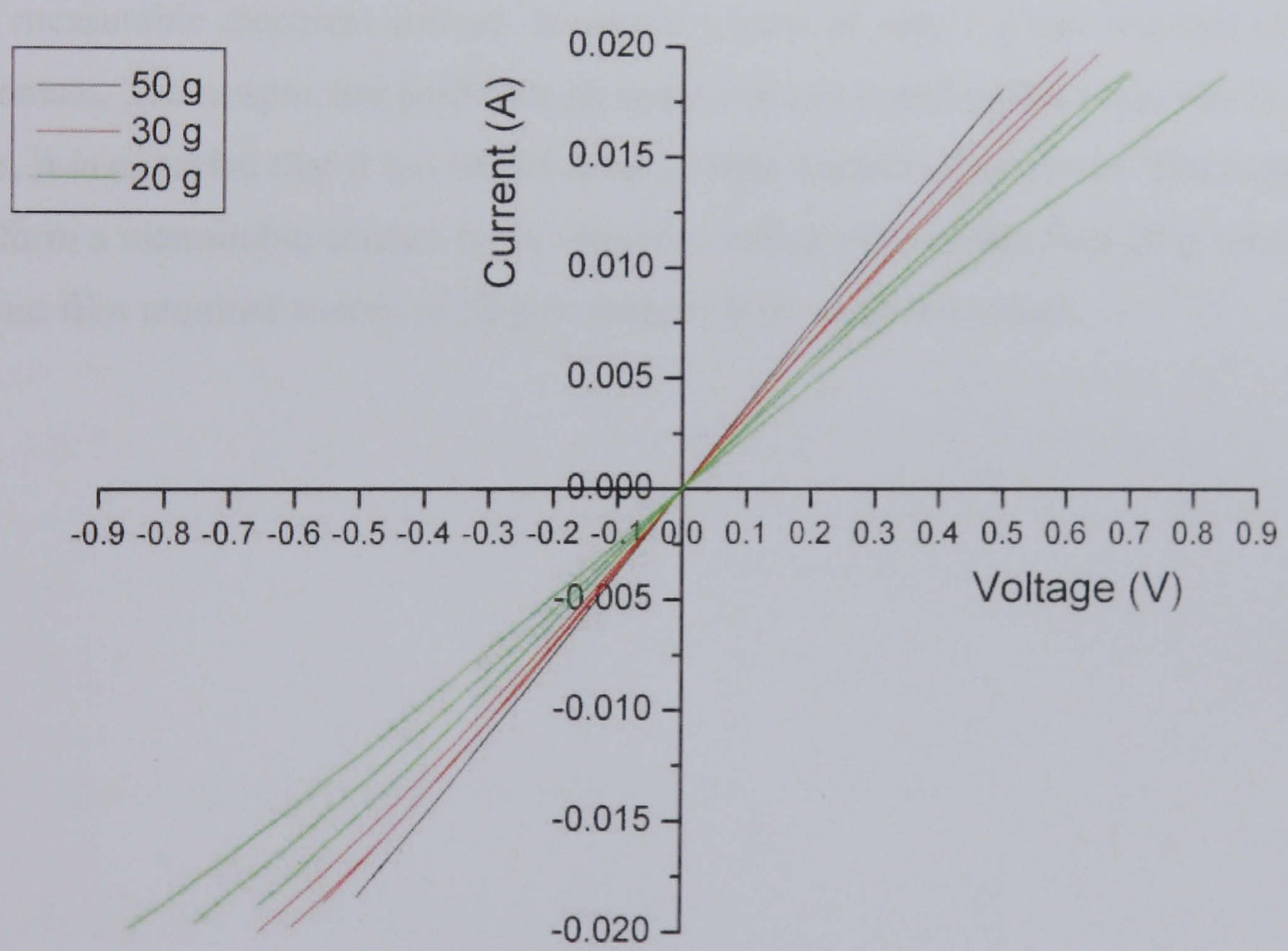

Figure 7.22 I-V characteristics of 300 nm thick copper film on glass substrate

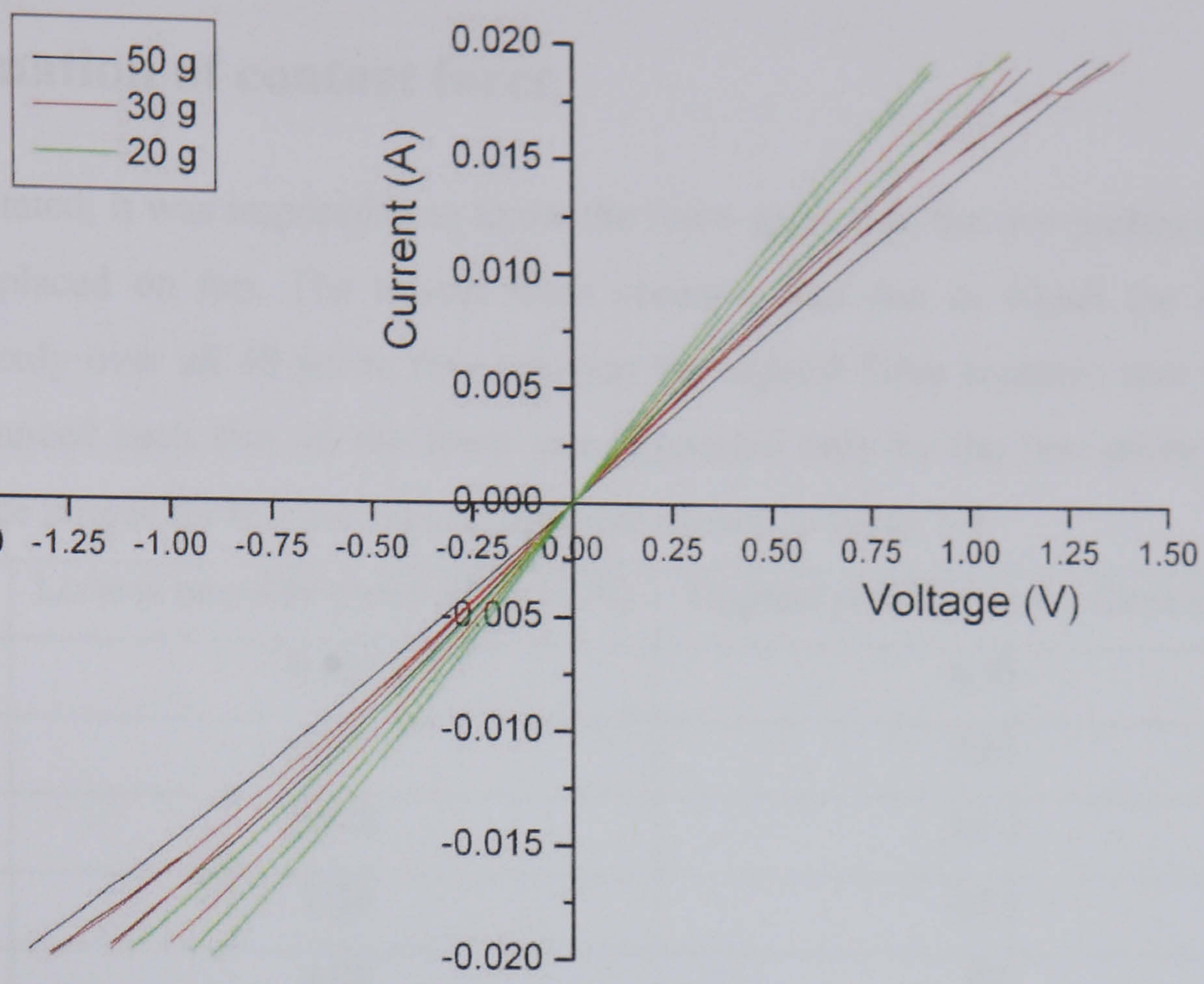

Figure 7.23 I-V characteristics of 300 nm thick aluminium film on glass substrate

The electroplated gold substrate had a mass of 0.064 g which on its own was not sufficient to get a measurable electrical contact. However a mass of only 1 g was required to form a stable contact. The evaporated gold film on resist was not tested with a mass less than 10 g; however, it is expected that it too would form a stable contact at low force. The copper film did not form a measurable contact when weighted with a mass of less than 20 g, whereas the aluminium film required a mass of 30 g or more to form a stable contact.

7.5.3 Estimation of contact force

As already stated, it was impossible to know the force applied to the two probes of interest by the mass placed on top. The lowest force scenario was one in which the mass was distributed evenly over all 48 probe tips, whereas the highest force scenario was where the mass was balanced such that all the force was supported only by the two probe tips. The calculated force ranges for the test masses used are shown in Table 7-1.

Mass (g)	Lowest possible probe force (mN)	Highest possible probe force (mN)
1	0.204	4.91
2	0.408	9.81
3	0.613	14.7
10	2.04	49.1
20	4.08	98
30	6.13	147
50	10.3	246

Table 7-1Probe contact force bounds as a function of applied mass

For comparison, by extrapolating from the mechanical testing results (section 7.4), it takes approximately 460 mN to deflect a probe 55 μm (i.e. until the PDMS layer is completely crushed). It should be noted that it is much more likely that the true probe force was closer to the lower than the upper boundary. This is the case since the lower boundary is fairly insensitive whereas the upper one is very sensitive to altering the number of probe tips the mass is distributed between. E.g. 50 g supported by 40 probes (12.3 mN/probe) is very similar to 50 g supported by 48 probes (10.3 mN/probe) whereas 50 g supported by two probes (246 mN/probe) is a very different force to 50 g supported by 8 probes (61.3 mN/probe).

7.5.4 Estimated contact resistance

It can be seen that all the I-V measurements (section 7.5.2) give approximately linear responses. Therefore it was a simple process to calculate the total path resistance from the reciprocal of the gradient. The fact that the responses were linear, as opposed to noisy, shows that the contact resistances must have been stable.

The total resistance of the tungsten probes, wires, contact between the tungsten probes and nickel surface and electroplated nickel tracks and cantilevers was measured as 6.29 Ω. By subtracting this from the total path resistance and dividing the result by two, the estimated contact resistance, for a single PDMS probe to metal film contact, could be calculated. These calculated values as a function of applied mass and the film material are shown in Figure 7.24.

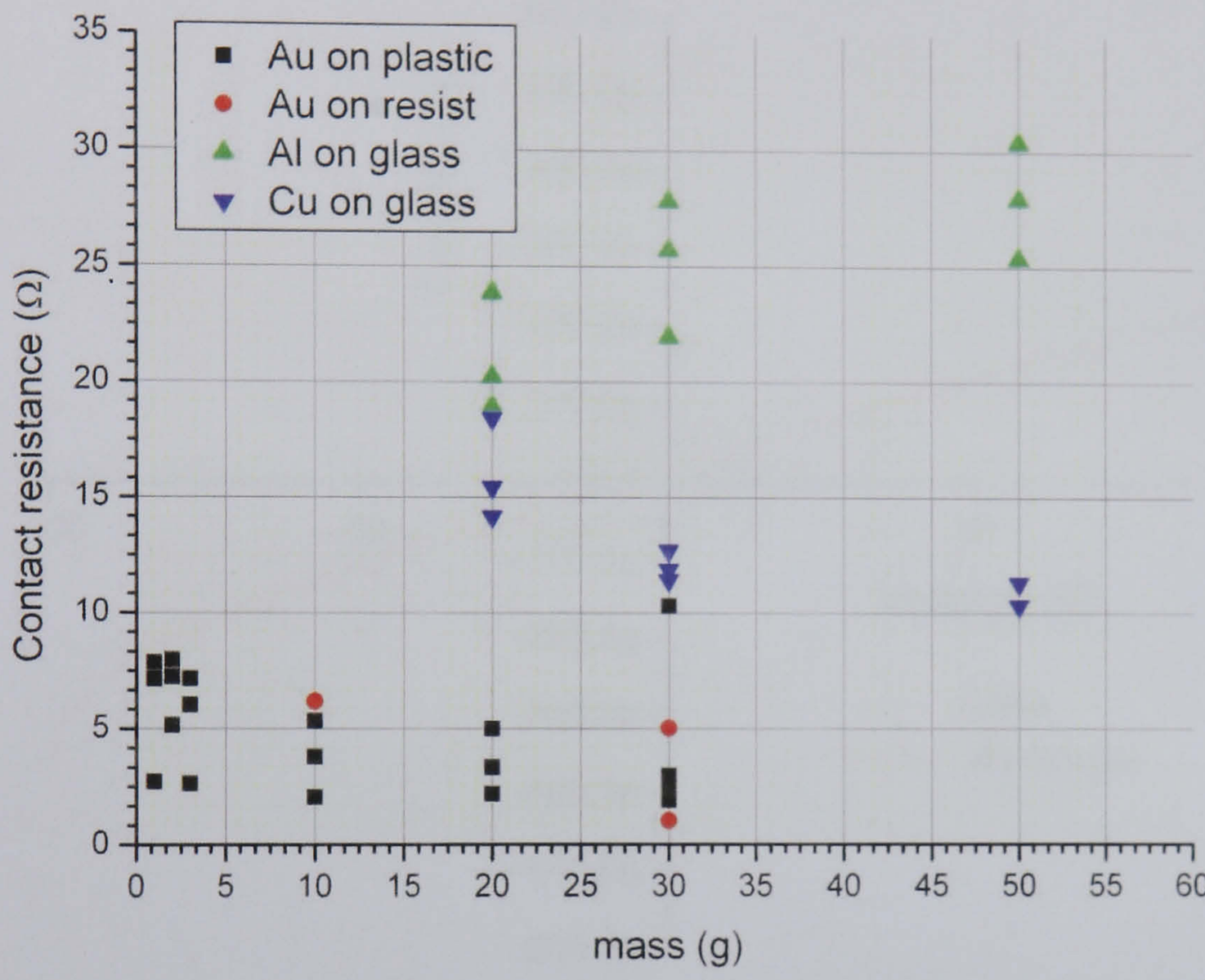

Figure 7.24 Estimated probe contact resistance as a function of metal and mass

The contact resistance to gold, whether measured against the 20 μm thick electroplate or a 100 nm thick evaporated layer on photoresist, was typically below 5 Ω for masses of 10 g or greater. The contact resistance of copper was typically between 15 and 10 Ω for masses between 20 and 50 g, whereas the aluminium contact resistance was between 20 and 30 Ω over the same mass range.

According to the theory in chapter 6, the contact resistance is expected to be proportional to the square root of the reciprocal of contact force. This is clearly not the case for aluminium which actually increases. Therefore this strongly suggests that the force per probe, for the two probes being measured, was not directly proportional to the applied mass. This was, as already stated, due to the position of the mass relative to the probes being measured.

7.5.5 Leakage current

The leakage current between adjacent, unconnected probes was measured using a HP4145B parameter analyser. One probe was grounded whilst a voltage was applied to the other. The voltage was swept from -100 V to +100 V in 2 V steps. The current passing between the probes was measured and is shown in Figure 7.25. As can be seen, the leakage current was less than 0.5 nA.

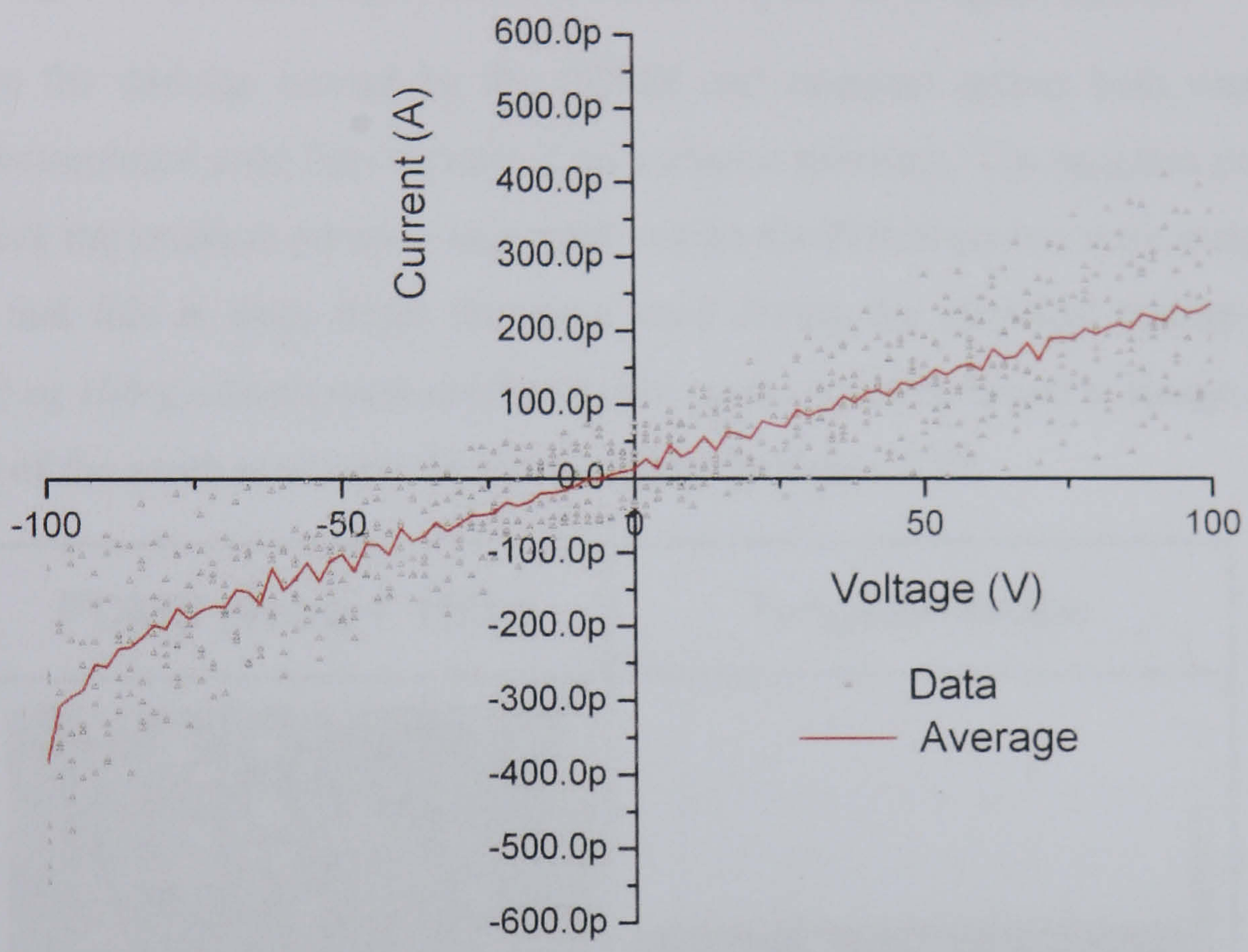

Figure 7.25 Leakage current as a function of voltage

7.6 Scrub mark comparison

It was noticed that it was not possible to make electrical contact to the 100 nm thick evaporated gold film on the photoresist layer using traditional tungsten probes. This was since the probes punched straight through both the gold and resist layers (see Figure 7.26). This was not the case when the PDMS probe card was used which indicates its potential usefulness for plastic electronic testing where the substrate can be similarly soft and gold is a common choice for the electrode material.

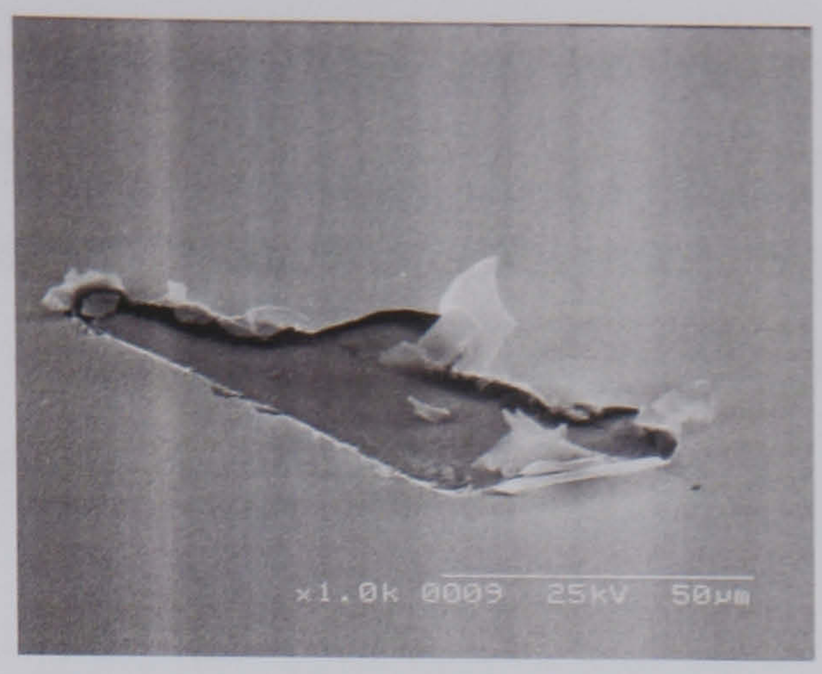

Figure 7.26 Damage made to Au on resist by tungsten probe

To compare the damage caused by the PDMS and tungsten probes both were used to contact an electroplated gold film deposited on a silicon substrate. The tungsten probes were adjusted to give the smallest possible skid mark whilst the PDMS probes were weighted with 150 g. Note that this is three times the mass used during the electrical testing: however, when only 50 or 100 g masses were used no scrub marks could be found to image. AFM and SEM images of the scrub marks produced are shown in Figure 7.27.

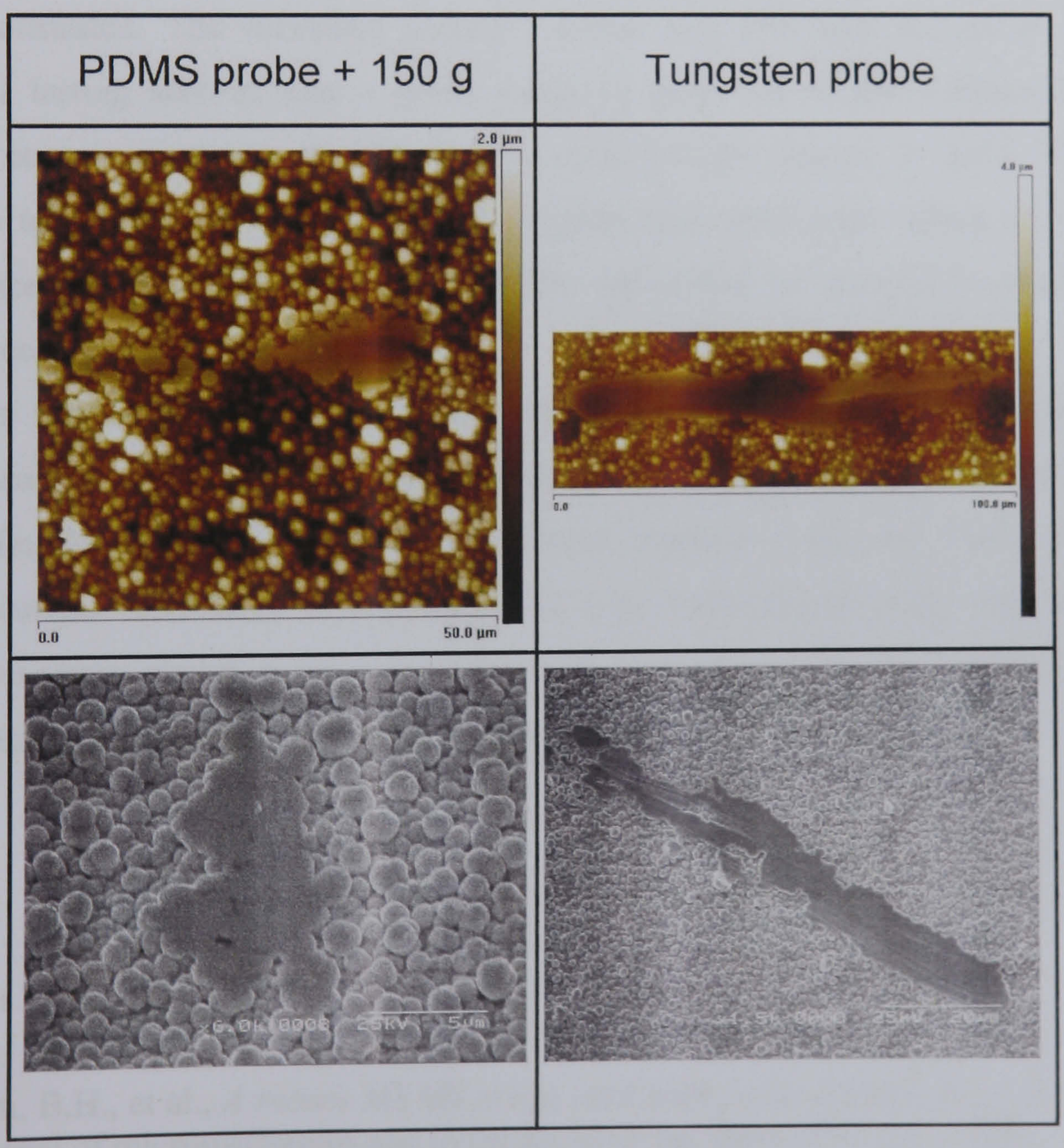

Figure 7.27 Comparison between the effect of a PDMS and tungsten probe on an electroplated gold film

As can be seen, even with a mass of 150 g the PDMS probe scrub mark has caused very little damage and has only flattened the tops of some asperities whereas the tungsten probe has caused a skid mark resulting in significant damage to the gold surface. The tungsten probe caused a scrub mark with a maximum depth of 1.1 μm and a maximum height of 0.9 μm above the (average) surface level.

7.7 Summary

Inclusion of a PDMS layer beneath the nickel cantilever increased the probe force significantly. It was found that the PDMS layer produced an exponential increase in force with deflection. This allowed stable electrical connections to be made to gold, copper and aluminium films. Although the exact contact forces were not known, a comparison of scrub marks suggests that the forces applied during electrical testing were significantly less than those applied by a traditional tungsten probes. A 23 μm pitch and excellent tip co-planarity were demonstrated. The measured leakage current was less than 0.5 nA at 100V and mechanical testing showed that a probe could be deflected 40 μm without damage. A minimum contact resistance of 1.01 Ω was measured for contact to gold. The contact resistances to copper and aluminium were slightly high (minimum values of 10.3 Ω and 18.9 Ω respectively) however they were stable and could be reduced by increasing the contact force

Therefore this new probe design meets the specification for pitch (less than 25 μm), leakage current (less than 1 nA) and deflection (40 μm without damage) given in chapter 2. The specification given in chapter 2 for contact resistance was less than 2 Ω to gold. Although contact resistances of less than 2 Ω were demonstrated they were not typical. Therefore to ensure contact resistances of less than 2 Ω are regularly achieved, a (total) force of more than 30 gf should be applied to the probe card.

References

1. Kim, B.H., et al., *A robust MEMS probe card with vertical guide for a fine pitch test.* Journal of micromechanics and microengineering, 2007. **17**(7): p. 1350.

2. Loetters, J.C., et al., *The mechanical properties of the rubber elastic polymer polydimethylsiloxane for sensor applications.* Journal of Micromechanics and Microengineering, 1997. **7**: p. 145-147.
3. Tserepi, A., et al., *Etching behaviour of Si-containing polymers as resist materials for bilayer lithography: The case of poly-dimethyl siloxane.* Journal of Vacuum Science & Technology B: Microelectronics and Nanometer Structures, 2003. **21**: p. 174.
4. Owen, M.J. and P.J. Smith, *Plasma Treatment of Polydimethylsiloxane.* Polymer Surface Modification: Relevance to Adhesion, 1995: p. 3-15.
5. Chua, D.B.H., H.T. Ng, and S.F.Y. Li, *Spontaneous formation of complex and ordered structures on oxygen-plasma-treated elastomeric polydimethylsiloxane.* Applied Physics Letters, 2000. **76**: p. 721.
6. Vlack, V., *Elements of materials science: An introductory text for engineering students*. second ed. 1964, Japan: Addison-wesley.
7. Huang, R.C. and L. Anand, *Non-linear mechanical behaviour of the elastomer polydimethylsiloxane (PDMS) used in the manufacture of microfluidic devices*, in *Innovation in Manufacturing Systems and Technology (IMST)*. 2005.
8. Ashby, M.F. and D.R.H. Jones, *Engineering materials 1 - An introduction to their properties and applications*. 1996, Butterworth Heinemann.
9. Treloar, L.R.G., *The Physics of Rubber Elasticity, Clarendon*. 1975, Oxford.
10. Xing, X., P.M. Goldbart, and L. Radzihovsky, *Thermal Fluctuations and Rubber Elasticity.* Physical Review Letters, 2007. **98**(7): p. 75502.
11. Jeong, O.C. and S. Konishi, *Fabrication and drive test of pneumatic PDMS micro pump.* Sensors & Actuators: A - Physical, 2007. **135**(2): p. 849-856.

Chapter Eight

OFET probe

In this chapter a probe is described that was designed specifically to meet the need of organic field effect transistor (OFET) testing. The work is distinct from the main focus of the thesis since the probe was designed to allow testing of only single devices which had specific requirements not common to most wafer level scenarios.

8.1 Introduction

The emerging field of plastic electronics has largely not been addressed by the probe card manufacturers since the drivers for probe card innovation are still manly from the silicon industry. This is because many aspects of plastic electronics, such as relaxed pad pitches and low number of I/O's, can be easily accommodated by established epoxy probe card technology. However plastic electronics does generate some unique demands on probe cards. especially devices produced at the research level. One such requirement is the ability to form contacts to thin metal films on top of soft dielectric layers.

This chapter described a probe especially for testing thin film organic field effect transistors (OFETs). The design and fabrication were very different from the devices discussed in the main body of the thesis and so it is contained within a separate chapter. The concept was to build a probe that could be used to test a single OFET at a time. The OFETs were fabricated by an external institution (the PETEC centre) and had the following general structure:

- Patterned titanium / gold films formed the source and drain electrodes on a glass substrate.
- A thin (10s nm) active organic layer was spin coated on top of the source drain electrodes.
- A 500 to 600 nm dielectric layer were deposited on top of the organic layer.
- The gate electrode was formed by evaporating gold through an aligned shadow mask.

To make contact to the source and drain connections it was therefore necessary for the probes to penetrate the organic and dielectric layers. Conversely, to make contact to the gate electrode it was necessary to apply a low force so as not to punch through the soft organic and dielectric layers.

8.1.1 Probe design

The important aspects of the probe design are shown in Figure 8.1.

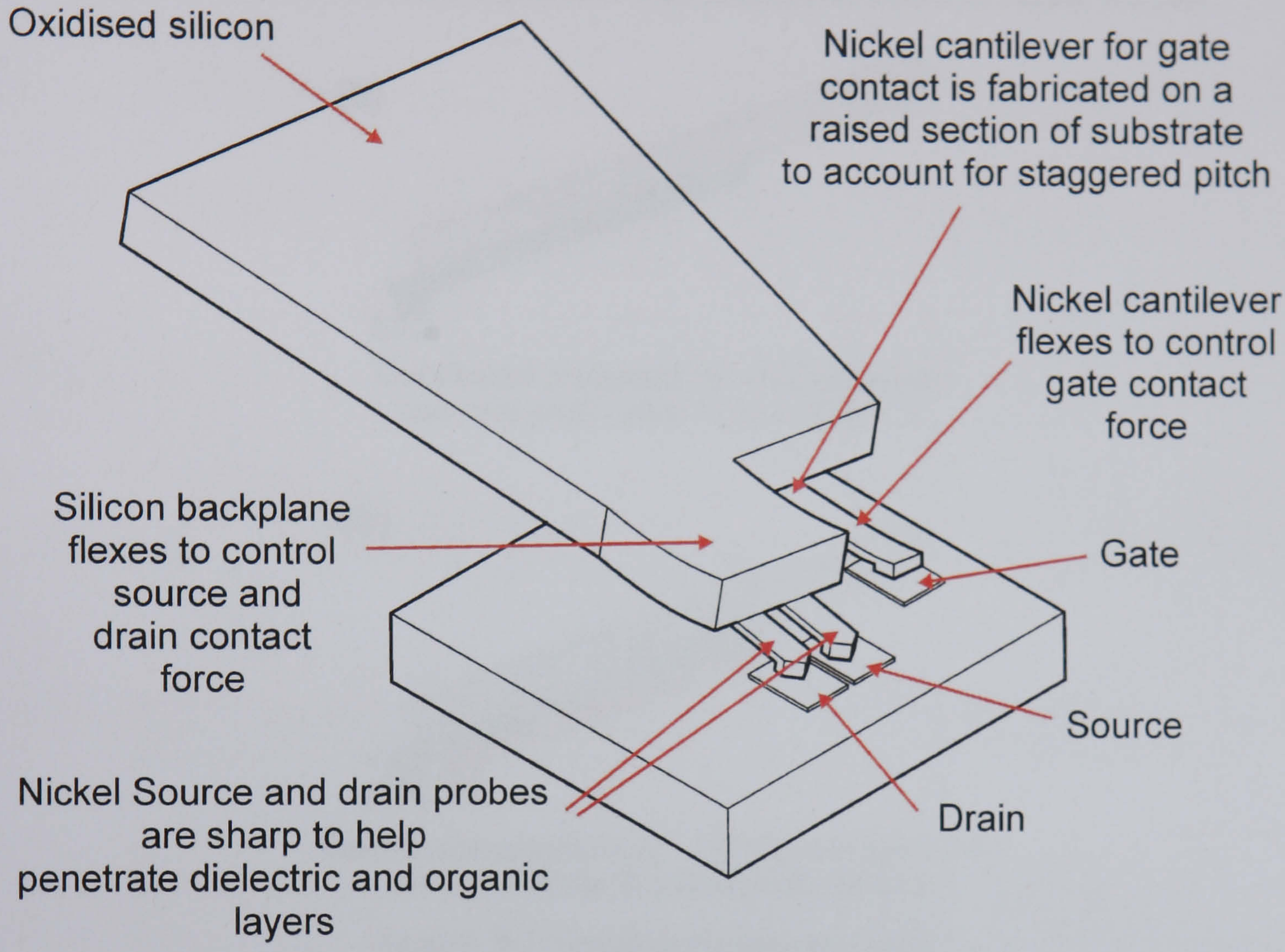

Figure 8.1 Probe design

The design consisted of a structured silicon chip held at an angle (~ 7°) to the OFET substrate. Attached to the underneath of the silicon were nickel probes. The probes for the source and drain were short cantilevers. These were sufficiently stiff that under an applied load it was the silicon substrate and not the cantilevers that flexed. The gate electrode was a long cantilever. When a load was applied to this, the cantilever deflected and so it was its geometry that controlled the contact force.

The gate electrode of the devices being tested was staggered with respect to the source and drain electrodes. To account for this offset the gate cantilever had to be fabricated on a raised section of substrate. This was achieved by structuring the silicon substrate to create two levels before the cantilevers were deposited. This concept is shown in Figure 8.2 (b).

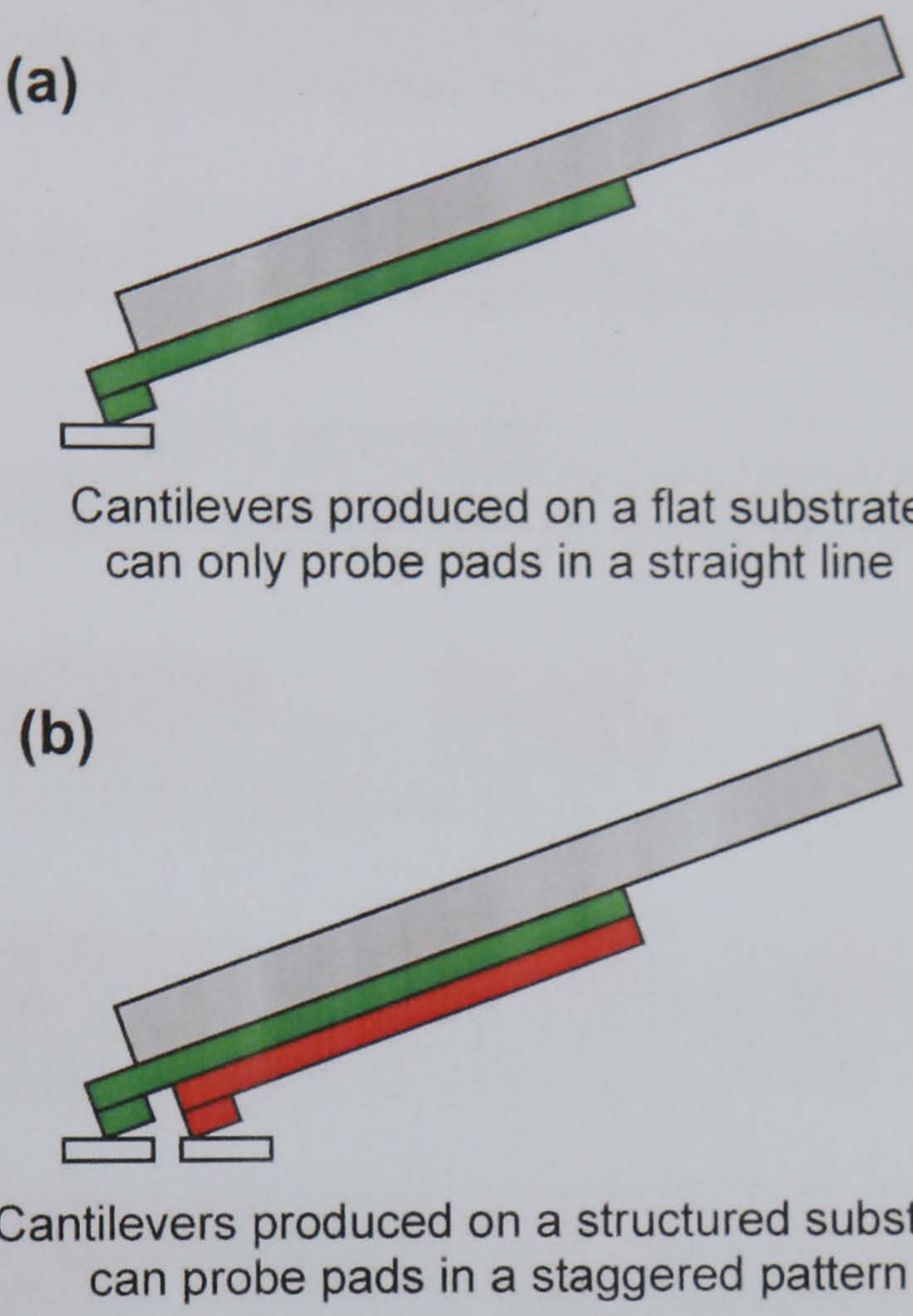

Figure 8.2 Probing staggered pads

8.1.2 Probe fabrication

The probe fabrication sequence is shown in Figure 8.3. The fabrication used RIE to structure the substrate, oxidation to make the substrate electrically insulating and define the release etch windows and finally nickel electroplating to fabricate the probes.

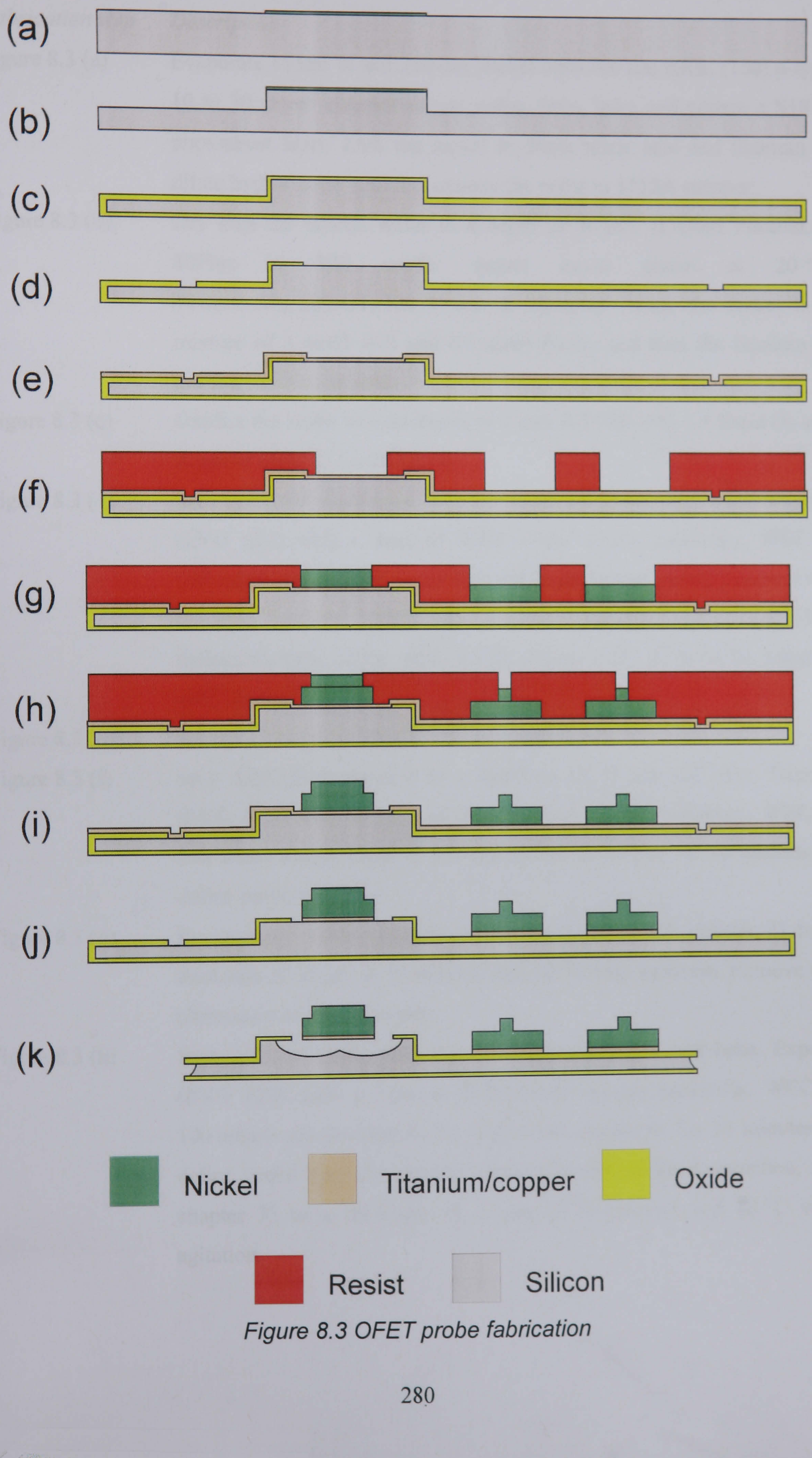

Figure 8.3 OFET probe fabrication

Fabrication step	*Description*
Figure 8.3 (a)	Evaporate 15 nm Ti and 250 nm Nickel onto 300 μm thick, (100) p-type 10 to 30 Ωcm^{-1} cleaned silicon wafer. Spin, bake and pattern a S1813 photoresist layer. Etch the nickel in dilute nitric acid and titanium in dilute hydrofluoric acid and remove the resist in 1112A stripper.
Figure 8.3 (b)	Dry etch the silicon wafer to a depth of 50 μm. (Oxford PlasmaLab 80Plus in RIE mode: quartz cover platen at 20 °C, 40 sccm SF_6, 200 mT, 300 W for 50 minutes) . Etch the nickel in a mixture of 3 mol/l HCl and 0.5 mol/l $FeCl_3$, and then the titanium in dilute hydrofluoric acid.
Figure 8.3 (c)	Oxidise the wafer to a thickness of 2 μm: 0.3 l/min N_2, 1.5 l/min O_2 and steam at 1060 °C for 18 hours.
Figure 8.3 (d)	Spin AZ9260 photoresist to a thickness of 55 μm and bake. Expose (EVG 620) with a dose of 2000 mJ/cm² (2 μm proximity, WEC = 100 mbar) and develop in 2:1 H_2O:400K developer for 10 minutes. Etch oxide in buffered hydrofluoric acid (4:1 NH_4F:HF) until clear (this defines windows in the oxide for the release etch). Remove the resist in 400T stripper.
Figure 8.3 (e)	Sputter 20 nm titanium and 150 nm copper.
Figure 8.3 (f)	Spin AZ9260 photoresist to a thickness of 55 μm and bake. Expose (EVG 620) with a dose of 2000 mJ/cm² (2 μm proximity, WEC = 100 mbar) and develop in 2:1 H_2O:400K developer for 10 minutes to define probe moulds.
Figure 8.3 (g)	Electroplate nickel (smooth nickel formulation, see chapter 3) to a thickness of 35 μm at 10 mA/cm² and 60 °C with agitation. Remove the photoresist in 400T stripper.
Figure 8.3 (h)	Spin AZ9260 photoresist to a thickness of 55 μm and bake. Expose (EVG 620) with a dose of 2000 mJ/cm² (2 μm proximity, WEC = 100 mbar) and develop in 2:1 H_2O:400K developer for 10 minutes to define probe tips. Electroplate nickel (smooth nickel formulation, see chapter 3) to a thickness of 10 μm at 10 mA/cm² and 60 °C with agitation.

Figure 8.3 (i) Remove the photoresist in 400T stripper.

Figure 8.3 (j) Selectively etch the copper seed layer in 1:1:2 H_2O_2:CH_3COOH:H_2O and then etch the titanium adhesion layer in dilute hydrofluoric acid.

Figure 8.3 (k) Release the probe by etching thorough the wafer with XeF_2 (170 x 1 minute cycles with an cycle chamber pressure of 4.0 torr).

After releasing the probe it was bombarded with nitrogen by spraying with a high pressure gun. This helped to shatter the unwanted suspended oxide layers that are a result of the undercutting during XeF_2 etching.

8.1.3 Fabrication results

Images of a fabricated probe are shown in Figure 8.4. Note that the probe shown had a 100 nm gold layer evaporated on top of the nickel in places. This is not shown in the fabrication sequence but was to ensure a good quality electrical connection could be made to the probe by silver paste.

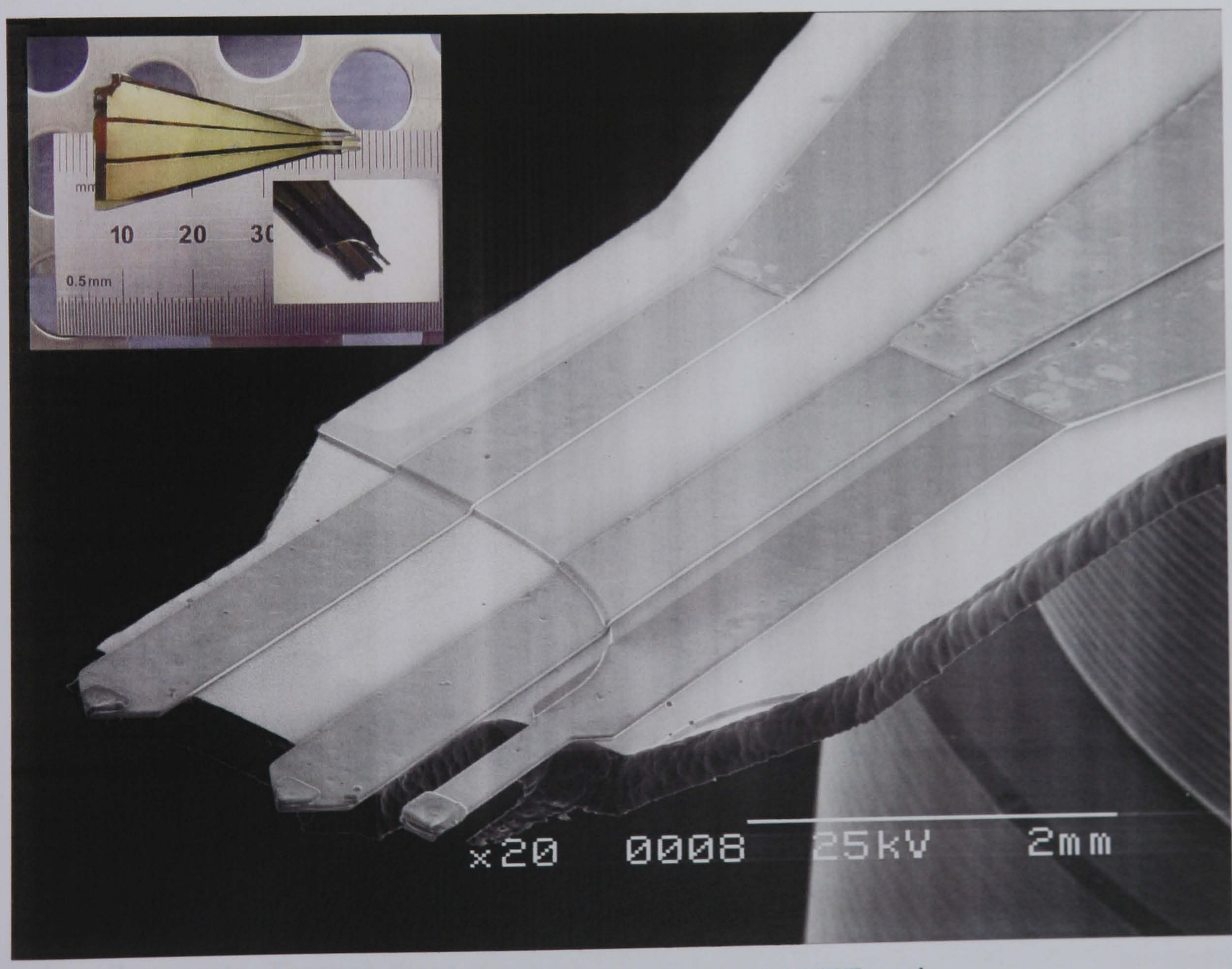

Figure 8.4 Images of fabricated OFET probe

8.1.4 Leakage current

The leakage current between adjacent probes was measured using a HP4145B parameter analyser. One probe was grounded whilst a voltage was applied to the other. The voltage was swept from -90 V to 90 V in 2 V steps. The current passing between the probes was measured and is shown in Figure 8.5.

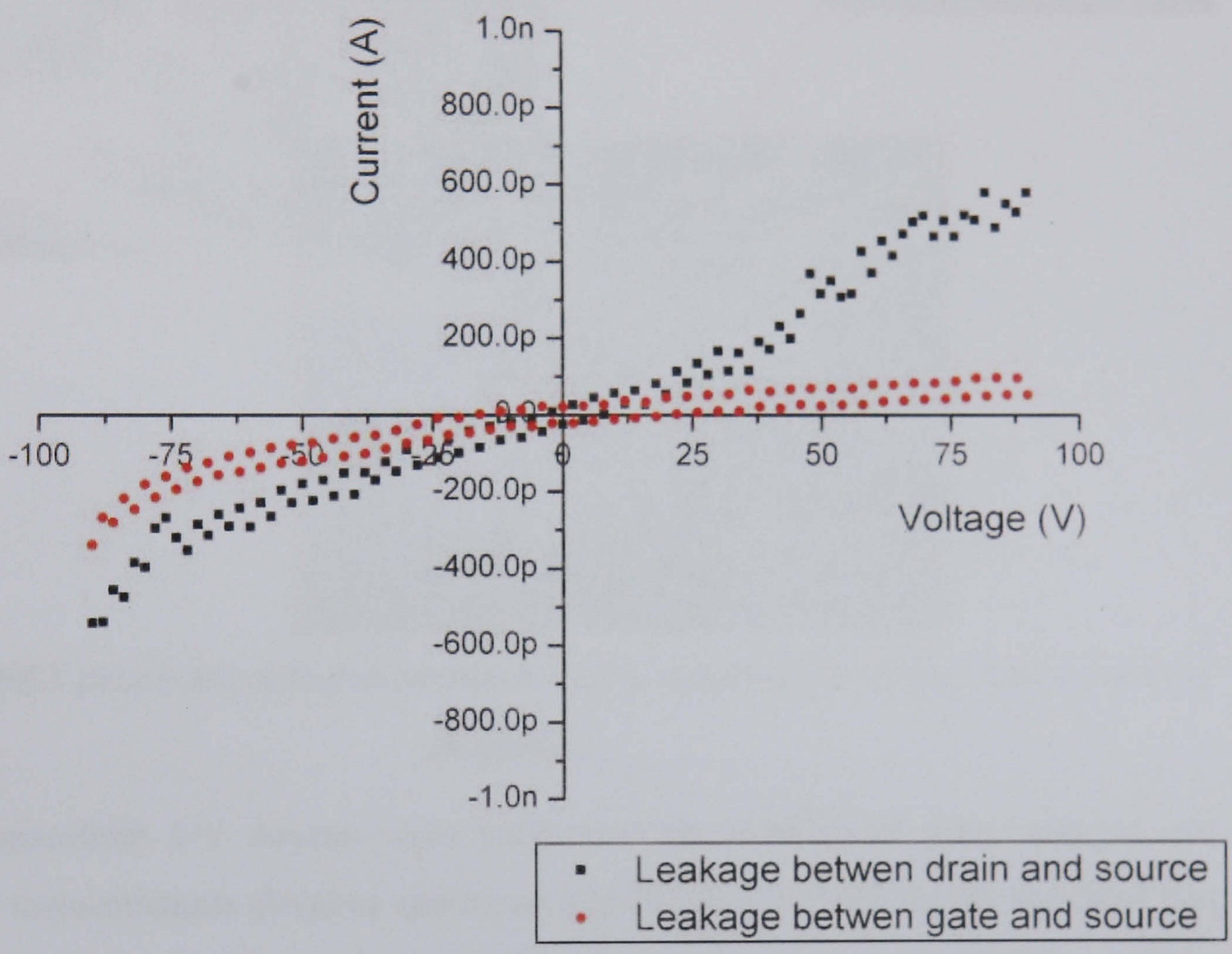

Figure 8.5 Leakage current between probes

As can be seen the leakage current was less than 1 nA at 90 V.

8.1.5 Wafer level device testing

The fabricated probe was mounted onto a specially machined plastic adapter allowed it to connect to a standard ground-signal-ground (GSG) probe manipulator (Cascade Microtech Inc. Beaverton, Oregon USA). This allowed control of x-y-z positioning as well as y-z tilt correction. Electrical connections were made by gluing wires to the gold coated nickel tracks using silver paste. Through these wires the probes were connected to a HP4145B parameter

analyser. Photos showing the probe mounted in a probe station and comparison to traditional tri-axial tungsten probes can be seen in Figure 8.6.

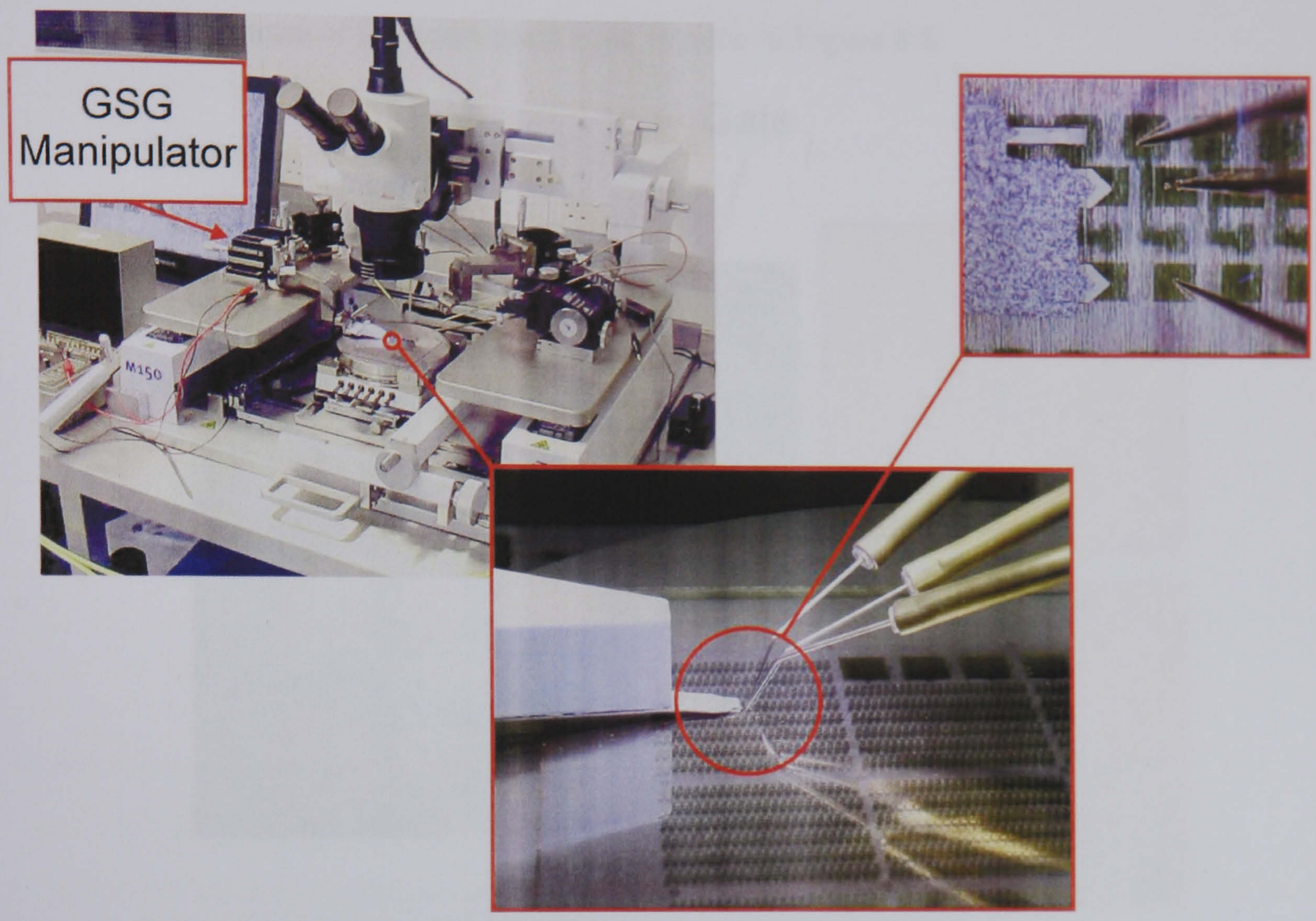

Figure 8.6 OFET probe mounted to standard GSG manipulator being used to probe devices

Standard source-drain I-V sweeps were performed for a series of gate voltages. An example of the measurements obtained can be seen in Figure 8.7. Such results indicated that the probes functioned as expected and compared well to results taken by the OFET supplier.

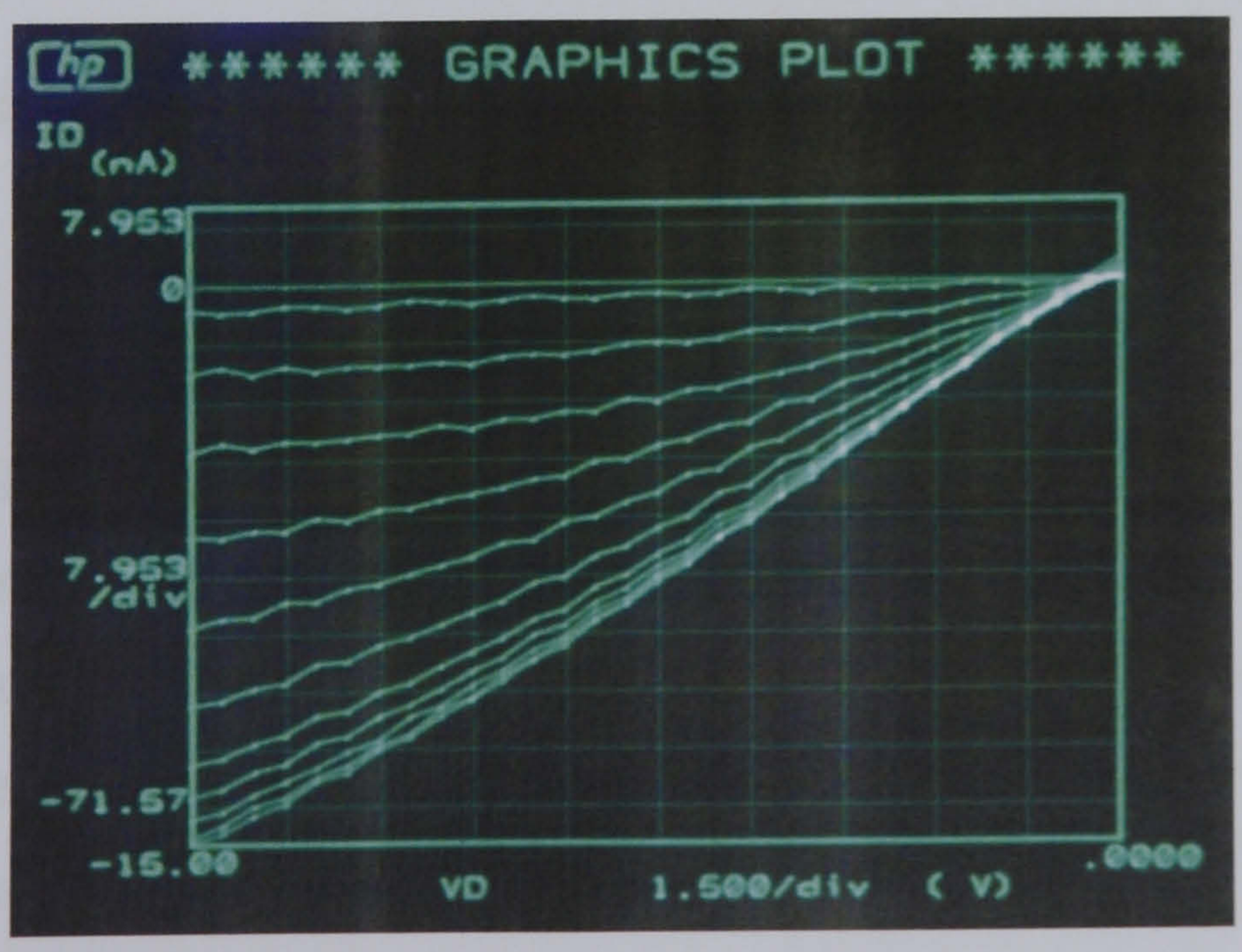

Figure 8.7 Example source- drain I-V traces for different gate voltages

8.1.6 Scrub marks

Microscope images of the scrub marks can be seen in Figure 8.8.

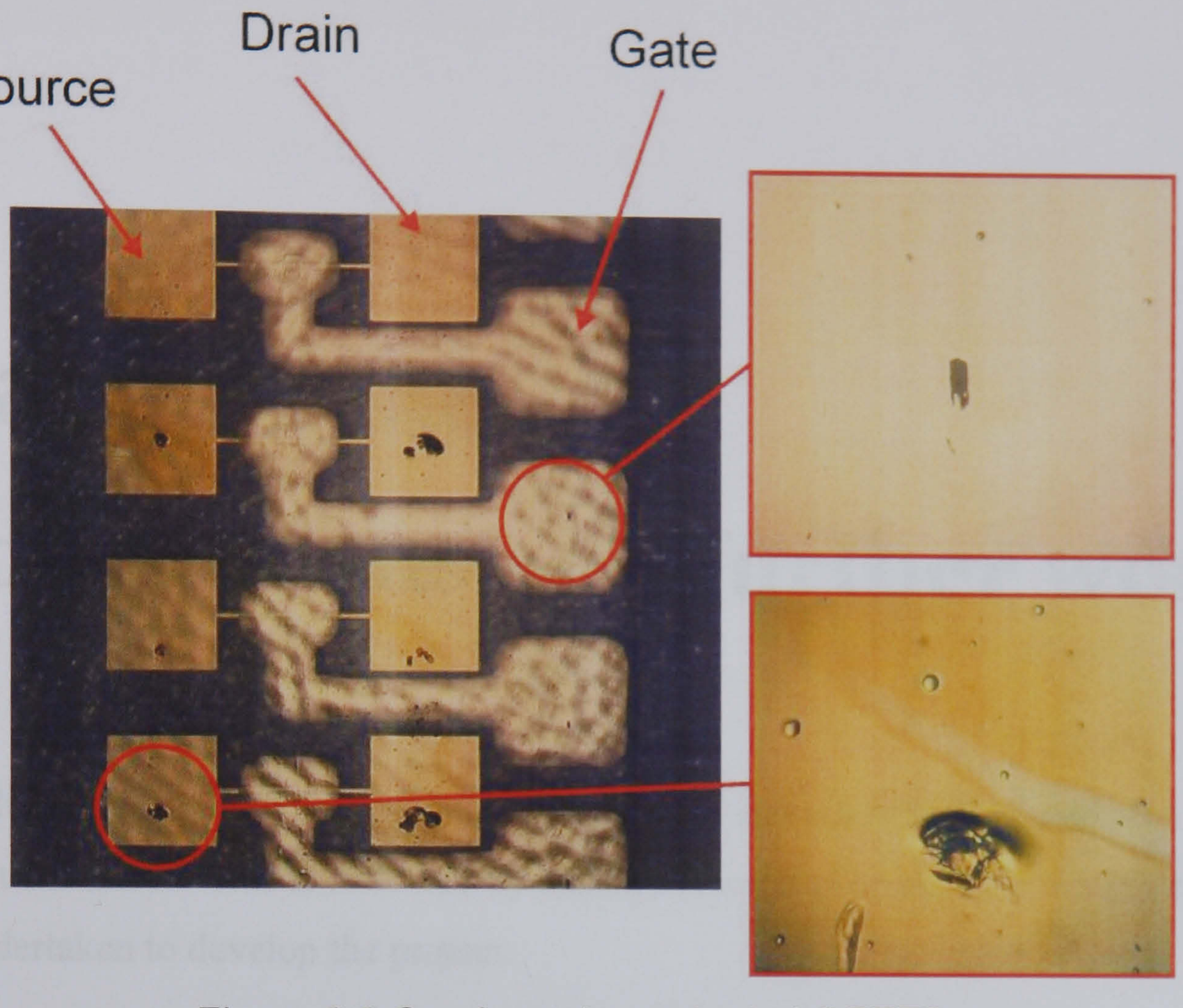

Figure 8.8 Scrub marks on tested OFETS

As can be seen the damage caused by the gate probe is much less than the source or drain probes. However the gate probe still applies sufficient force to scrape the gold from the dielectric. Therefore the geometry of the cantilever should be optimised to further reduce the force applied.

8.1.7 Conclusions

A simple process has been described that allows the fabrication of robust probes that can be mounted on a traditional GSG manipulator. By varying the length of the nickel cantilevers, the probe force can be adjusted such that different probes apply different forces for the same level of overdrive. By structuring the silicon substrate before forming the nickel probes it was possible to align the cantilevers with staggered pad arrangements. No optimisation of the design was performed. However, initial wafer level testing of OFET devices was successful.

Chapter Nine

Conclusions and further work

In this concluding chapter an assessment is made on the success of the body of work and key results are summarised. This is followed by additional areas of research or development that could be undertaken to develop the project.

9.1 Conclusions

9.1.1 Results and specification

The devices described in chapter 7 meet all the required parameters specified in chapter 2. Testing showed the probes provided stable and robust electrical connections with measured minimum contact resistances of 1 Ω against gold, 10 Ω against copper and 19 Ω against aluminium metallisations. The damage produced by the probes was significantly less than traditional tungsten needles. This permitted electrical connections to be made to delicate substrates such as a gold film on a photoresist layer. Such contacts were not possible using traditional probes. The probes were fabricated on a glass substrate with PDMS layer and demonstrated a very low leakage current (less than 0.5 nA at 100 V). Additionally, since both the PDMS and glass were transparent the probes could be easily aligned optically to the device being tested.

A summary of the key parameters demonstrated with respect to the original specification outline in chapter 2 is given in Table 9-1.

Specification	*Comment*
Less than 25 μm pitch	A minimum of 23 μm pitch was demonstrated
Less than 1 nA leakage	A leakage current of less than 10 pA for suspended cantilevers and 500 pA for the PDMS device were measured at 100 V.
Stable contact resistance of less than 2 Ω (to gold)	Contact resistances of typically less than 5 Ω were demonstrated against gold whilst some contacts showed resistances between 2 and 1 Ω.
Low manufacturing time and cost	The fabrication was based on batch, rather than serial, processes. In the lab, manufacturing times were typically less than 2 weeks. Although an analysis of costs was not conducted the fabrication required only standard MEMS fabrication equipment and no manual assembly processes.

Tolerate 30 to 40 μm deflection without damage	With 10 μm thick suspended cantilevers a horizontal length of 600 μm or greater was required to prevent yield at 40 μm deflection. Testing of the 1 mm long PDMS probes showed no damage after 40 μm of deflection.
Minimise contact force whist obtaining a low and stable contact	Detailed contact force-resistance behaviour for forces of 10 μN to 3.5 mN was measured using the suspended cantilevers. It was found that these forces were insufficient to reliably break contaminating films. Conversely the PDMS probes provided stable electrical contacts to gold, copper and aluminium. Because of the testing method used, the contact force and resistance were not measured simultaneously. However it was shown that the PDMS probes applied lower forces than traditional needles. The PDMS probe contact force can be sensibly estimated to be in the 30 to 70 mN range.
Have a substrate independent fabrication	The fabrication was based entirely on surface machining and was independent of the substrate material.
Probes have an inclined cantilever structure	Both the suspended and PDMS probes were inclined cantilevers although other 3D structures were demonstrated in chapter 3.

Table 9-1 Summary of achievements

An alternative probe described in chapter 8 was used for testing OFETs. This probe was much simpler than the others described; however, it was only designed for testing single devices. Only superficial testing was conducted and I-V results obtained with the probe compared well to data taken by the OFET supplier.

9.1.2 Discussion

A great deal of the work in this thesis was dedicated to the development and characterisation of novel three dimensional fabrication processes suitable for the production of probe structures. In particular there was a detailed analysis of the capabilities, in terms of dimensional control, and limitations, in terms of stability, of thick photoresist sacrificial layers. Critical to the performance of such photoresist layers was the remaining coating solvent which reduced the effective glass transition temperature and caused bubbles to form during subsequent bake steps. Despite these limitations, with careful optimisation of film stress and adhesion and etch profiles, suspended cantilever probes with widths as thin as

13 μm at 23 μm pitch with ± 2 μm tip co-planarity were demonstrated. The fabrication method was based entirely on surface machining and was therefore independent of the substrate material, in theory allowing probes to be fabricated directly on top of integrated circuits.

Suspended structures were found not to apply sufficient contact force to provide reliable and robust electrical connections and so the fabrication process was modified to include a PDMS layer beneath the probes. This layer caused the contact force to increase exponentially with displacement. A 55 μm thick layer was capable of applying more than 150 mN when deflected by 40 μm, after which there was no discernible damage to the PDMS or cantilever. Although PDMS is a common material in microfluidics, the integration of PDMS as a structural element within a surface machining fabrication sequence is a new application as far as the author can determine. These new probe structures could still be fabricated with the same fine pitch as the suspended structures, while the stability of the PDMS layer significantly increased the fabrication yield and allowed a ± 1.5 μm tip co-planarity. It must be noted however that the inclusion of a PDMS layer beneath the probes is at the expense of mechanically coupling the deflection of adjacent probes. The degree of inter-probe displacement will also be a function of probe pitch. The implications of this should be assessed in a production testing environment since its impact depends on the planarity and deformation of the wafers being tested.

Suspended nickel cantilever structures were tested both mechanically, to determine the force-deflection and yield behaviour, and electrically, to determine the force-contact resistance behaviour. This testing was conducted using a bespoke system capable of measuring 10 μN forces and 0.1 μm displacements. Measurement errors were dominated by thermal expansion and mechanical settling of the test rig causing a typical drift of 200 nm/min. The development of a specialised 'test tip' allowed simultaneous contact resistance and force measurements critical to understanding the electrical interface.

Mechanical testing showed that the Young's modulus of the electroplated nickel differed between the fabricated suspended cantilevers and tension testing samples and that the yield stress varied considerably between cantilevers. The difference in Young's modulus was attributed to a systematic experimental error in conjunction with either a variation in microstructure with deposition thickness or an uncontrolled dissimilarity in deposition conditions. The high variation in yield stress was attributed to the dominating effect of point defects during plastic deformation. Both the variation between sample's Young's modulus and deviation within a sample's yield stress have repercussions for the design of

electroplated structural elements in MEMS devices. Firstly. the control of electroplating conditions and deposition thickness must be carefully monitored both between and across individual wafers. Such monitoring would require the fabrication of on wafer test structures that could be used to determine the elastic properties of the deposited nickel. Secondly, designs should include a large factor of safety, or else risk plastic deformation during normal operating conditions. Such precautions are less imperative with bulk machined silicon elements since the homogeneity of material properties is high and occurrence of defects very low.

With a knowledge of Young's modulus and Poisson's ratio it was possible to accurately model the stiffness of the suspended cantilevers. It was shown that analytical models were accurate (less than 2% error) for a horizontal length greater than 5 times the cantilever width, and a cantilever width greater than five times the thickness. Further, it was necessary only to consider bending moments since the effects of shear and axial load were insignificant. For cantilevers with lengths comparable to their widths FEA models were required. The stiffness predicted by FEA models were bounded by analytical plane stress and plane strain assumptions which underestimated and overestimated the stiffness respectively. For short cantilevers it was necessary to accurately model their geometry since a small 'plateau' region, which resulted from the fabrication process, had a strain concentrating effect which was significant to their behaviour. In longer cantilevers the stiffness of the 'plateau' region was much greater than the main body of the probe and so could be neglected.

A detailed analysis of contact force-resistance behaviour for nickel and gold coated tips (of smooth or cuspidated texture) against nickel, aluminium or gold coated nickel test tips was undertaken. The results suggested that surface contaminating films largely determined the quality of the contact at low forces. If these films could be fractured then a stable contact could be made even at low force. The likelihood of a stable contact was enhanced by the presence of gold which was attributed to contact adhesion.

If a contact resistance was stable, the estimated area of electrical contact was found to be very small ('a-spot' radius 28 to 136 nm). Conversely the mechanical areas of contact, as identified by surface damage, were of the order of microns. It was taking this fact into account in conjunction with the observed large variation in contact resistances (including during the testing of gold-on-gold contacts) that led to the proposition that there must have been contaminating films.

The effects of the hardness and resistivity of the contacting surfaces was detectable when minimum contact resistance values were analysed. These effects followed the general trend

that lowering either resistivity or hardness decreased the contact resistance for the same contact force. However the analytical expressions for contact resistance proposed by Holm [1] were found not to accurately represent the contact force-resistance behaviour over the 50 μN to 3.5 mN range. Frequently, the lowest value of contact resistance did not correspond to the greatest contact force. There was evidence of plastic deformation of the contact since the unloading contact resistances were typically lower than the loading values.

Key conclusions observed from the fabrication, mechanical and electrical testing of the various probe designs are summarised in Table 9-2.

Thick photoresist sacrificial layers	Thick photoresist layers were found to be thermally unstable as a result of residual casting solvent. This significantly reduced device yield and geometric control.
Young's modulus of electroplated nickel	The Young's modulus of nickel was found to significantly vary between the tension testing samples and suspended cantilever structures. This was attributed to systematic experimental errors in extension measurements in conjunction with a possible variation in microstructure with deposit thickness.
Yield stress of electroplated nickel	Yield stress in the electroplated nickel was found to be dominated by point defects. This led to a large spread in the yield behaviour of the suspended cantilevers.
Analytical modelling of inclined cantilever stiffness	It was found that only bending moments needed to be considered to derive an accurate model. The models were applicable to cantilevers with lengths greater than 5 times their widths and width greater than 5 times their thickness.
Low force electrical contacts (< 3.5 mN)	Electrical contact at low forces was found to be dominated by surface contamination.

Table 9-2 Summary of conclusions

9.2 Further work

Additional work relating to the fabrication process and testing should be undertaken if the work presented in this thesis was to be developed into a commercial product. These areas of work are outline below.

9.2.1 Fabrication

9.2.1.1 PDMS moulding

The current moulding technique is crude and results in a 'flash' with non-uniform thickness. This flash would become increasingly problematic as moulding over larger areas was attempted. Therefore the mechanics of the moulding processing including the use of commercial embossing tools should be investigated.

9.2.1.2 PDMS adhesion promoter

At present, no adhesion promoter is used between the substrate and PDMS and as a result the adhesion is weak and can fail during fabrication. A brief review of literature suggest that compounds such as trimethoxysilylpropyl methacrylate (TMSM) [2] should be investigated as an adhesion promoter between silicon dioxide and PDMS.

9.2.1.3 Dielectric layers or substrates compatible with PDMS etching

The fabrication process described in chapter 7 uses an O_2-SF_6 plasma to etch the PDMS layer. Since the substrate is borosilicate glass, this is also attacked by the plasma. A timed etch was used to reduce the amount of substrate damage. However, due to the non-uniform thickness of the PDMS flash it was necessary to over etch, damaging the substrate. Alternative insulating substrates or barrier layers deposited beneath the PDMS should be investigated to prevent this. A promising material is aluminium oxide. The boiling point of SiF_4, the by product of SiO_2 dry etching, is -95.7 °C whereas AlF_3 sublimes at 1272 °C [3]. Therefore the etch rate of Al_2O_3 in fluorine plasmas should be very low, except that the sputter yield of AlF_3 is quite high and so it would be physically etched [4]. Even so, in optimised etches of low kinetic energy the selectivity between SiO_2 and Al_2O_3 can be ~ 400 [4].

9.2.1.4 PDMS etching optimisation

The current PDMS etching process (see appendix 7.1) was not optimised. The etching had a tendency to leave 'grass' presumably due to micro-masking. Both the copper masking step and plasma etch conditions should be optimised to reduce this allowing clean, anisotropic etching of the PDMS layer.

9.2.1.5 Probe tip material

Different electroplating formulations should be investigated for the deposition of hard wearing alloys such as nickel cobalt. Such alloys would help prolong the probes' life. In parallel the effects of these alloys on contact resistance must also be investigated.

9.2.2 Mechanical testing

9.2.2.1 Tip compliance

A known problem with membrane probe cards is that they cannot accommodate a large difference in tip deflection between adjacent probes. Inclusion of a PDMS layer effectively makes the probe card a cantilever-membrane hybrid and so the limitations of tip compliance should be investigated. This includes the effect of pitch and PDMS layer thickness.

9.2.2.2 High or low temperature effect on PDMS

As stated in chapter 2, wafer level testing is often performed at high or low temperatures for 'burn in' testing. Since the mechanical properties of rubber are intimately connected to temperature and heat transfer their effects on mechanical performance should be investigated.

9.2.2.3 Reliability

Commercial probe cards are designed to be used for millions of touchdowns before they are replaced. Therefore it is necessary to cyclically test the probes to determine their useful life time. This should include effects from the environment, such as temperature.

9.2.3 Electrical testing

9.2.3.1 Contact resistance versus contact force

Due to time constraints, the detailed analysis of contact resistance as a function of probe force was not investigated for the PDMS probes. Such measurements should be taken to allow a better understanding of the interface and allow accurate determination of the probing force required to reliably fracture contaminating films.

9.2.3.2 Steady state and switching current

The magnitude of steady state and switching currents used during wafer level testing is increasing. Therefore the current carrying capabilities of the probes should be determined.

9.2.3.3 High frequency measurements

Testing is often performed at or close to functional speeds. Therefore an assessment of losses and impedances of the probes needs to be performed in order to determine their bandwidth. This should be succeeded by design refinements for the inclusion of strip lines or co-axial structures if necessary.

9.2.4 Other

9.2.4.1 Tip cleaning

During probe use material adheres to probe tips and degrades the quality of electrical contact. For this reason the commercial probe tips are cleaned periodically. The frequency of probe cleaning and damaged caused by such processes should be investigated.

9.2.4.2 Integration with PIB and commercial use

The final stage in a probe card development should be the design of the probe interface board and its integration in the MEMS probe. Only then could commercial trials be undertaken in order to assess the true performance of the probe.

References

1. Holm, R. and E. Holm, *Electrical Contacts Theory and Applications*. 4th ed. 1967. Berlin/Heidelberg/New York: Springer-Verlag.
2. Loetters, J.C., et al., *The mechanical properties of the rubber elastic polymer polydimethylsiloxane for sensor applications.* Journal of Micromechanics and Microengineering, 1997. **7**: p. 145-147.
3. Köhler, J.M., *Etching in Microsystem Technology*. 1999: Wiley-VCH.
4. Hsiao, R., *Fabrication of magnetic recording heads and dry etching of head materials.* IBM journal of research and development, 1999. **43**: p. 89-102.

Appendix 3-1: Fabrication process flow

Method 1

Basic wafer clean

Wash borosilicate wafer by sonicating in IPA then H_2O and dry with N_2

Etch alignment marks into glass substrate (Figure 3.45 (a))

Bake 160 °C on vacuum hotplate for 10 minutes to dehydrate wafer
Puddle dispense HMDS and spin dry at 3000 rpm
Spin Microposit S1813 at 3700 rpm for 30 s (5 s, 500 rpm spreading stage)
Bake at 95 °C on vacuum hotplate for 7 minutes
Expose (EVG 620) 2.3 s (vacuum + hard contact)
Develop (4:1 H_2O:351 Microposit developer) for 1 minute
Hard bake at 120 °C on vacuum hotplate for 5 minutes
Etch marks into substrate using Oxford instruments Plasmalab 80Plus: 25 sccm Ar, 25 sccm CHF_3, 30 mT chamber pressure, 200 W using RIE mode for 40minutes
Remove resist by sonicating in acetone then IPA and then H_2O

Thorough wafer clean

Sonicate wafer in 10:1 H_2O:'Decon' detergent, rinse in several H_2O baths
Immerse in 1:1 H_2SO_4:H_2O_2 for 30 minutes, rinse in several H_2O baths
Sonicate H_2O

Definition 3D resist layer (Figure 3.45 (b))

Bake wafer at 160 °C on vacuum hotplate for 10 minutes to dehydrate wafer
Puddle dispense HMDS and spin dry at 3000 rpm
Spin AZ electronic materials AZ9260 resist at 1000 rpm for 1 minute (300 rpm spreading stage for 15 s)
Wait 2 minutes before baking at 95 °C on vacuum hotplate for 5 minutes. Waiting for 5 minutes allows some coating solvent to evaporate and reduces the risk of bubbles forming in the resist layer as it is baked
Remove wafer and allow to cool for 1 minute
Spin and bake 2 more layers of AZ9260 in identical fashion
Remove the resist edge bead using a jet of acetone directed onto edge of wafer rotating at 6000 rpm
Bake wafer for on a vacuum hotplate using temperature profiles show in Figure 1

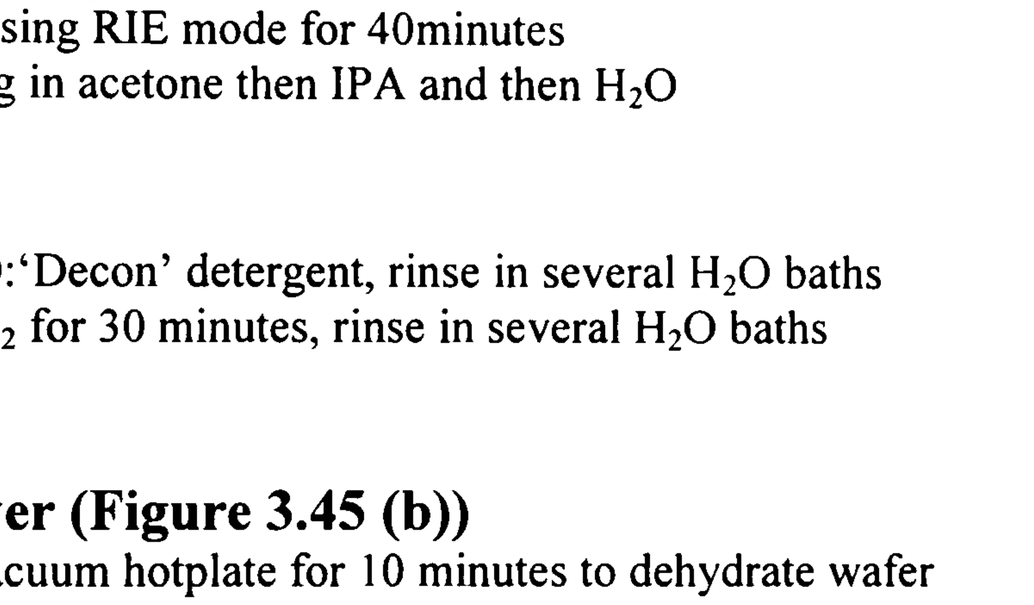

Figure 1: Hot plate temperature ramp

Hydrate in H_2O at 20 °C for 15 minutes (or leave for 12 hours in 40 – 60 % relative humidity atmosphere)
Expose (EVG 620) 1200 mJ/cm^2 (soft contact)
Develop in 2:1 H_2O:AZ 400K developer until clear (8 minutes)
Oxygen clean resist residues using Yield engineering systems R3 plasma cleaner: sample on floating electrode, chamber pressure 2.4 torr, 120 W for 20 minutes

Sputter coat resist using Moorfield Minilab sputter system (Figure 3.45 (c))

Base pressure less than 1.0×10^{-6} mbar
Argon flow rate 5 sccm
Stage rotation 25 rpm, Stage and chamber temperature 10 °C, Stage bias 0 V

Ti deposition (30 nm): RF magnetron (forward power 204 W), chamber pressure 6.5 mT
Cu deposition (60 nm): DC magnetron (magnetron current 0.7 A), chamber pressure 20 mT

Copper electroplate (Figure 3.45 (d))

Cover alignment mark areas with PMMA (use PMMA dissolved in chlorobenzene, 9 % solids)
Electroplate copper to a thickness of 5 µm at a current density of 20 mA/cm^2. Stirrer rotation of 600 rpm, bath temperature 20 °C, electroplating current 125 mA, for 12 minutes (rotate substrate 180° after 6 minutes)
Wash wafer in H_2O
Remove PMMA using acetone, wash wafer in IPA and H_2O

Define anchors (Figure 3.45 (e))

Spin AZ electronic materials AZ9260 resist at 1000 rpm for 1 minute (300 rpm spreading stage for 15 s)
Wait 2 minutes before baking at 95 °C on vacuum hotplate for 5 minutes
Remove wafer and allow to cool for 1 minute
Spin and bake 2 more layers of AZ9260 in identical fashion
Remove the resist edge bead using a jet of acetone directed onto edge of wafer rotating at 6000 rpm
Bake wafer for on a vacuum hotplate using temperature profiles show in Figure 1
Hydrate in H_2O at 20 °C for 15 minutes (or leave for 12 hours in 40 – 60 % relative humidity atmosphere)
Expose (EVG 620) 1530 mJ/cm^2 (hard contact)
Develop in 2:1 H_2O:AZ 400K developer until clear (5 minutes)

Etch anchors (Figure 3.45 (f))

Etch copper in 250 g/l Sodium persulphate until clear, rinse in H_2O
Etch titanium in 10:1 H_2O:HF until clear
Remove resist in AZ 400T resist stripper, rinse in H_2O

Sputter coat using Moorfield Minilab sputter system (Figure 3.45 (g))

Base pressure less than 1.0×10^{-6} mbar
Argon flow rate 5 sccm
Stage rotation 25 rpm, Stage and chamber temperature 10 °C, Stage bias 0 V

Ti deposition (50 nm): RF magnetron (forward power 204 W), chamber pressure 6.5 mT
Ni deposition (10 nm): DC magnetron (high magnet strength, magnetron current 0.57 A), chamber pressure 10 mT

Define cantilevers (Figure 3.45 (h))

Spin AZ electronic materials AZ9260 resist at 1000 rpm for 1 minute (300 rpm spreading stage for 15 s)
Wait 2 minutes before baking at 95 °C on vacuum hotplate for 5 minutes
Remove wafer and allow to cool for 1 minute
Spin and bake 2 more layers of AZ9260 in identical fashion
Remove the resist edge bead using a jet of acetone directed onto edge of wafer rotating at 6000 rpm
Bake wafer for on a vacuum hotplate using temperature profiles show in Figure 1
Hydrate in H_2O at 20 °C for 15 minutes (or leave for 12 hours in 40 – 60 % relative humidity atmosphere)
Expose (EVG 620) 1530 mJ/cm^2 (hard contact)
Develop in 3:1 H_2O:AZ 400K developer until clear (10 minutes)
Cover alignment mark areas with PMMA (use PMMA dissolved in chlorobenzene, 9 % solids)
Oxygen clean resist residues using Yield engineering systems R3 plasma cleaner: sample on floating electrode, chamber pressure 2.4 torr, 120 W for 20 minutes

Electroplate cantilevers (Figure 3.45 (i))

Electroplate nickel (smooth nickel formulation) to a thickness of 10 μm at a current density of 12 mA cm^2.
Stirrer rotation of 600 rpm, bath temperature 60 °C, electroplating current 11.3 mA, for 46 minutes (rotate substrate 180° after 23 minutes)
Remove PMMA and AZ resist using acetone, wash wafer in IPA and H_2O

Define tips (Figure 3.45 (j))

Spin AZ electronic materials AZ9260 resist at 1000 rpm for 1 minute (300 rpm spreading stage for 15 s)
Wait 2 minutes before baking at 95 °C on vacuum hotplate for 5 minutes
Remove wafer and allow to cool for 1 minute
Spin and bake 2 more layers of AZ9260 in identical fashion
Remove the resist edge bead using a jet of acetone directed onto edge of wafer rotating at 6000 rpm
Bake wafer for on a vacuum hotplate using temperature profiles show in Figure 1
Hydrate in H_2O at 20 °C for 15 minutes (or leave for 12 hours in 40 – 60 % relative humidity atmosphere)
Expose (EVG 620) 1530 mJ/cm^2 (hard contact)
Develop in 3:1 H_2O:AZ 400K developer until clear (10 minutes)
Cover half the alignment mark area with PMMA to form a "U shape" (use PMMA dissolved in chlorobenzene, 9 % solids)
Oxygen clean resist residues using Yield Engineering Systems R3 plasma cleaner: sample on floating electrode, chamber pressure 2.4 torr, 120 W for 20 minutes

Electroplate tips (Figure 3.45 (k))

Smooth nickel tips
Electroplate nickel (smooth nickel formulation) to a thickness of 4 μm at a current density of 10 mA/cm^2.
Stirrer rotation of 600 rpm, bath temperature 60 °C, electroplating current 6.6 mA, for 22 minutes (rotate substrate 180° after 11 minutes)

Cuspidated nickel tips
Electroplate nickel (cuspidated nickel formulation) to a thickness of 4 μm at a current density of 12 mA/cm^2.
Stirrer rotation of 600 rpm, bath temperature 88 °C, electroplating current 7.9 mA, for 25 minutes (rotate substrate 180° after 12½ minutes)

Lift off (if tips are to be coated with gold)
E-beam evaporate titanium (10 nm) and then gold (150 nm)
Sonicate in acetone to perform 'lift-off, wash wafer in IPA and H_2O

Remove resists (if not performing lift off)
Remove PMMA and AZ resist using acetone, wash wafer in IPA and H_2O

Release devices

(During release stages the devices must be kept 'wet' until the CPD drying stage is complete)
Etch sputtered titanium (through 10 nm nickel layer) in 10:1 H2O:HF until clear **(Figure 3.45 (l))**
Etch copper by placing in 2:1:1 H_2O:CH_3COOH:H_2O_2 until clear (leave overnight) **(Figure 3.45 (m))**
Etch sputtered titanium in 10:1 H_2O:HF until clear **(Figure 3.45 (n))**
Remove 3D resist in AZ 400T resist stripper, rinse several times in H_2O **(Figure 3.45 (o))**
Soak in 3 successive IPA baths, 10 minutes in each
Release in Autosamdri 815B critical point dryer

Method 2

Basic wafer clean

Wash borosilicate wafer by sonicating in IPA then H_2O and dry with N_2

Etch alignment marks into glass substrate (Figure 3.48 (a))

Bake 160 °C on vacuum hotplate for 10 minutes to dehydrate wafer
Puddle dispense HMDS and spin dry at 3000 rpm
Spin Microposit S1813 at 3700 rpm for 30 s (5 s, 500 rpm spreading stage)
Bake at 95 °C on vacuum hotplate for 7 minutes
Expose (EVG 620) 2.3 s (vacuum + hard contact)
Develop (4:1 H_2O:351 Microposit developer) for 1 minute
Hard bake at 120 °C on vacuum hotplate for 5 minutes
Etch marks into substrate using Oxford instruments Plasmalab 80Plus: 25 sccm Ar, 25 sccm CHF_3, 30 mT chamber pressure, 200 W using RIE mode for 40minutes
Remove resist by sonicating in acetone then IPA and then H_2O

Thorough wafer clean

Sonicate wafer in 10:1 H_2O:'Decon' detergent, rinse in several H_2O baths
Immerse in 1:1 H_2SO_4:H_2O_2 for 30 minutes, rinse in several H_2O baths
Sonicate H_2O

Definition 3D resist layer (Figure 3.48 (b))

Bake wafer at 160 °C on vacuum hotplate for 10 minutes to dehydrate wafer
Puddle dispense HMDS and spin dry at 3000 rpm
Spin AZ electronic materials AZ9260 resist at 1000 rpm for 1 minute (300 rpm spreading stage for 15 s)
Wait 2 minutes before baking at 95 °C on vacuum hotplate for 5 minutes. Waiting for 5 minutes allows some coating solvent to evaporate and reduces the risk of bubbles forming in the resist layer as it is baked
Remove wafer and allow to cool for 1 minute
Spin and bake 2 more layers of AZ9260 in identical fashion
Remove the resist edge bead using a jet of acetone directed onto edge of wafer rotating at 6000 rpm
Bake wafer for on a vacuum hotplate using temperature profiles show in Figure 1
Hydrate in H_2O at 20 °C for 15 minutes (or leave for 12 hours in 40 – 60 % relative humidity atmosphere)
Expose (EVG 620) 1200 mJ/cm^2 (soft contact)
Develop in 2:1 H_2O:AZ 400K developer until clear (8 minutes)
Oxygen clean resist residues using Yield Engineering Systems R3 plasma cleaner: sample on floating electrode, chamber pressure 2.4 torr, 120 W for 20 minutes

Sputter coat resist using Moorfield Minilab sputter system (Figure 3.48 (c))

Base pressure less than 1.0 x 10^{-6} mbar
Argon flow rate 5 sccm
Stage rotation 25 rpm, Stage and chamber temperature 10 °C, Stage bias 0 V

Ti deposition (30 nm): RF magnetron (forward power 204 W), chamber pressure 6.5 mT
Cu deposition (60 nm): DC magnetron (magnetron current 0.7 A), chamber pressure 20 mT

Copper electroplate (Figure 3.48 (d))

Cover alignment mark areas with PMMA (use PMMA dissolved in chlorobenzene, 9 % solids)
Electroplate copper to a thickness of 5 µm at a current density of 20 mA/cm^2. Stirrer rotation of 600 rpm, bath temperature 20 °C, electroplating current 125 mA, for 12 minutes (rotate substrate 180° after 6 minutes)
Wash wafer in H_2O
Remove PMMA using acetone, wash wafer in IPA and H_2O

Define cantilevers (Figure 3.48 (e))

Spin AZ electronic materials AZ9260 resist at 1000 rpm for 1 minute (300 rpm spreading stage for 15 s)
Wait 2 minutes before baking at 95 °C on vacuum hotplate for 5 minutes
Remove wafer and allow to cool for 1 minute
Spin and bake 2 more layers of AZ9260 in identical fashion
Remove the resist edge bead using a jet of acetone directed onto edge of wafer rotating at 6000 rpm
Bake wafer for on a vacuum hotplate using temperature profiles show in Figure 1
Hydrate in H_2O at 20 °C for 15 minutes (or leave for 12 hours in 40 – 60 % relative humidity atmosphere)
Expose (EVG 620) 1530 mJ/cm^2 (hard contact)
Develop in 3:1 H_2O:AZ 400K developer until clear (10 minutes)
Cover alignment mark areas with PMMA (use PMMA dissolved in chlorobenzene, 9 % solids)
Oxygen clean resist residues using Yield Engineering Systems R3 plasma cleaner: sample on floating electrode, chamber pressure 2.4 torr, 120 W for 20 minutes

Electroplate cantilevers (Figure 3.48 (f))

Electroplate nickel (smooth nickel formulation) to a thickness of 10 µm at a current density of 12 mA cm^2.
Stirrer rotation of 600 rpm, bath temperature 60 °C, electroplating current 11.3 mA, for 46 minutes (rotate substrate 180° after 23 minutes)
Remove PMMA and AZ resist using acetone, wash wafer in IPA and H_2O

Define tips and Electroplate tips (Figure 3.48 (g))

Spin AZ electronic materials AZ9260 resist at 1000 rpm for 1 minute (300 rpm spreading stage for 15 s)
Wait 2 minutes before baking at 95 °C on vacuum hotplate for 5 minutes
Remove wafer and allow to cool for 1 minute
Spin and bake 2 more layers of AZ9260 in identical fashion
Remove the resist edge bead using a jet of acetone directed onto edge of wafer rotating at 6000 rpm
Bake wafer for on a vacuum hotplate using temperature profiles show in Figure 1
Hydrate in H_2O at 20 °C for 15 minutes (or leave for 12 hours in 40 – 60 % relative humidity atmosphere)
Expose (EVG 620) 1530 mJ/cm^2 (hard contact)
Develop in 3:1 H_2O:AZ 400K developer until clear (10 minutes)
Cover half the alignment mark area with PMMA to form a "U shape" (use PMMA dissolved in chlorobenzene, 9 % solids)
Oxygen clean resist residues using Yield Engineering Systems R3 plasma cleaner: sample on floating electrode, chamber pressure 2.4 torr, 120 W for 20 minutes

Smooth nickel tips
Electroplate nickel (smooth nickel formulation) to a thickness of 4 µm at a current density of 10 mA/cm^2.
Stirrer rotation of 600 rpm, bath temperature 60 °C, electroplating current 6.6 mA, for 22 minutes (rotate substrate 180° after 11 minutes)

Cuspidated nickel tips
Electroplate nickel (cuspidated nickel formulation) to a thickness of 4 µm at a current density of 12 mA/cm^2.
Stirrer rotation of 600 rpm, bath temperature 88 °C, electroplating current 7.9 mA, for 25 minutes (rotate substrate 180° after 12½ minutes)

Remove plating mould (Figure 3.48 (h))

Lift off (if tips are to be coated with gold)
E-beam evaporate titanium (10 nm) and then gold (150 nm)
Sonicate in acetone to perform 'lift-off, wash wafer in IPA and H_2O

Remove resists (if not performing lift off)
Remove PMMA and AZ resist using acetone, wash wafer in IPA and H_2O

Cover anchor regions with resist (Figure 3.48 (i))

Spin AZ electronic materials AZ9260 resist at 1000 rpm for 1 minute (300 rpm spreading stage for 15 s)
Wait 2 minutes before baking at 95 °C on vacuum hotplate for 5 minutes
Remove wafer and allow to cool for 1 minute
Spin and bake 2 more layers of AZ9260 in identical fashion
Remove the resist edge bead using a jet of acetone directed onto edge of wafer rotating at 6000 rpm

Bake wafer for on a vacuum hotplate using temperature profiles show in Figure 1
Hydrate in H_2O at 20 °C for 15 minutes (or leave for 12 hours in 40 – 60 % relative humidity atmosphere)
Expose (EVG 620) 1530 mJ/cm^2 (hard contact)
Develop in 3:1 H_2O:AZ 400K developer until clear (10 minutes)

(During release stages the devices must be kept 'wet' until the CPD drying stage is complete)

Selectively etch copper and titanium (Figure 3.48 (j))

Etch copper in 1:1 H_2O:CH_3OOH until clear
Etch titanium in 10:1 H_2O:HF until clear

Remove all resist (Figure 3.48 (k))

Remove 3D and anchor protecting resist in AZ 400T resist stripper, rinse several times in H_2O

Etch copper between cantilevers at anchor (Figure 3.48 (l))

Etch copper in 250 g/l Sodium persulphate until clear, rinse in H_2O

Etch titanium to isolate cantilevers (Figure 3.48 (m))

Etch titanium in 10:1 H_2O:HF, rinse in H_2O

Dry devices

Soak in 3 successive IPA baths, 10 minutes in each
Release in Autosamdri 815B critical point dryer

Appendix 5-1: Cantilever dimensions and strain gradient calculations

Cantilever Dimensions

Below is an image explaining what measurements were taken (using optical profiler) before cantilevers were released.

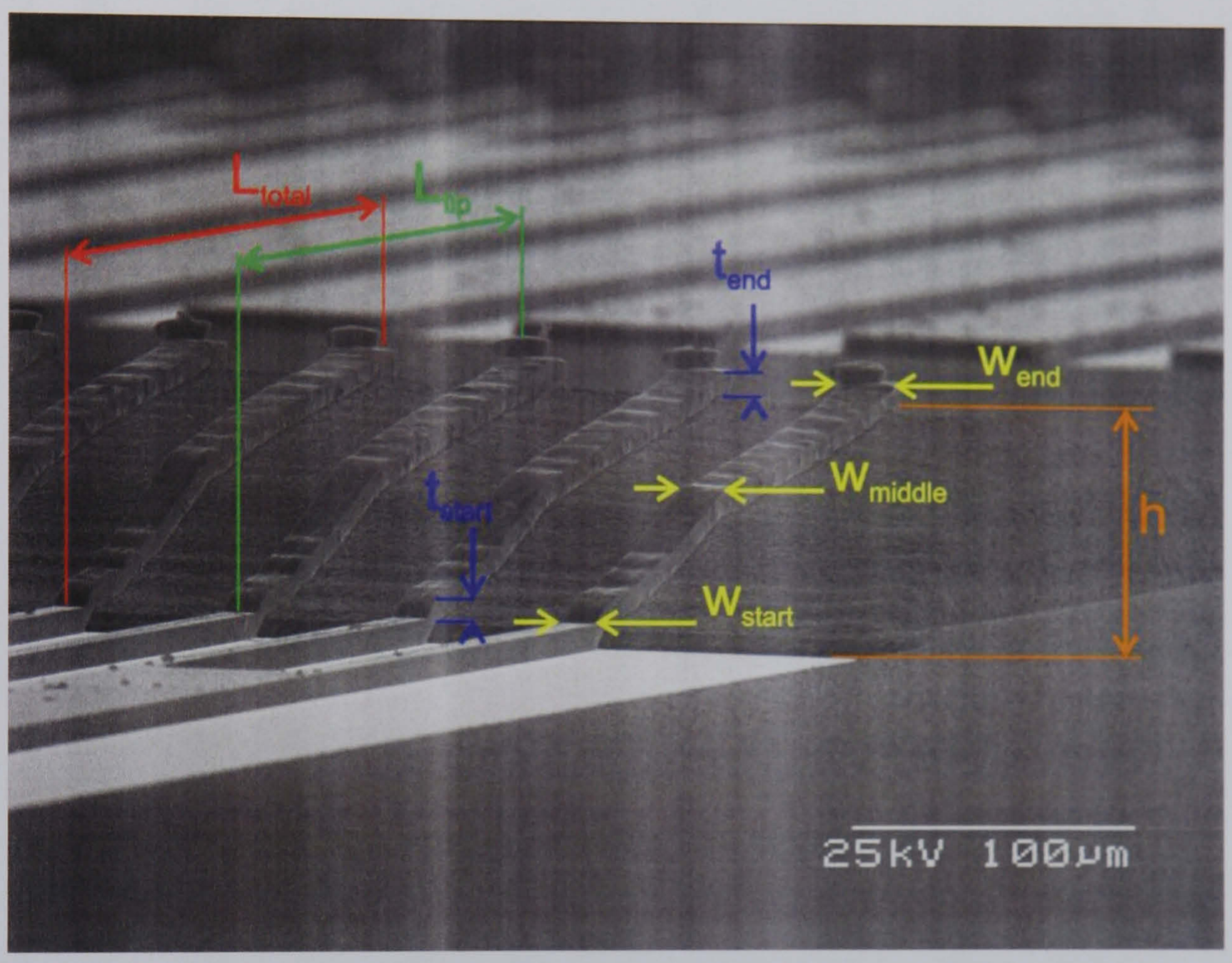

- L_{total} – The horizontal length from the anchor point to the tip of the cantilever
- L_{tip} – The horizontal length from the anchor point to where the probe tip is. Note that during the mechanical testing the force is applied to the probe tip
- t_{start} – The thickness of the cantilever near the anchor point
- t_{end} – The thickness of the cantilever near the cantilever tip
- w_{start} – The width of the cantilever near the anchor point
- w_{start} – The width of the cantilever near the midpoint of the cantilever
- w_{end} – The width of the cantilever near the cantilever tip
- h – The vertical height, from the substrate to the underside of the cantilever. The measurement is taken beneath the centre point of the cantilever tip (tip height).

The following table lists the designed and measured dimensions of the cantilevers. All dimensions given are in microns.

Probe name	designed values		measured values (before release)								measured values (after release)
	w	L	w_{start}	w_{middle}	w_{end}	t_{start}	t_{end}	L_{total}	L_{tip}	h	h
100 x 50	50	100	49.1	55.3	57.7	8.6	10.2	128	109	63.1	59.8
100 x 40	40	100	42.5	47.2	49.5	8	9	128	108	60.8	57
100 x 30	30	100	33.3	37.9	39.9	7.4	8.9	130	112	66.7	62.1
100 x 20	20	100	19.7	24.8	29.4	6.6	8.2	129	110	67.3	60.8
100 x 10	10	100	12	14.7	16.2	6.6	7.3	127	110	67	58.7
200 x 50	50	200	49.7	55.3	57.6	9.1	10.3	228	214	68.5	64.7
200 x 40	40	200	40.7	45.2	47.4	8.4	9.8	229	212	68.2	63.2
200 x 30	30	200	31.6	33.9	36.1	7.8	9.7	227	211	68.7	62.3
200 x 20	20	200	22.6	24.9	26	7.7	9.3	226	210	69.6	64.7
200 x 10	10	200	12.4	13.6	17	7.6	9.5	228	215	70.4	64.5
300 x 50	50	300	48.6	54.3	56.5	9.1	10.7	331	308	72.4	63.3
300 x 40	40	300	40.7	47	47.4	8.2	9.2	326	304	66.5	62.8
300 x 30	30	300	30.5	35	35	8.5	9.6	330	305	70.9	62.4
300 x 20	20	300	20.4	24.9	27.1	8.4	9.2	328	308	70.1	64.8
300 x 10	10	300	11.3	13.5	15.8	8	9.3	326	310	71.5	60.7
400 x 50	50	400	48.6	54.2	55.3	9.66	10.7	426	410	72.5	61.3
400 x 40	40	400	38.4	44	45.2	8.8	9.8	430	410	68.7	60.2
400 x 30	30	400	29.4	33.9	35	8.4	9.4	430	411	68.7	60.6
400 x 20	20	400	20.4	26.1	30.6	7.9	7.35	430	409	62.7	57.65
400 x 10	10	400	10.2	13.6	16.1	8.2	9.9	426	411	67.5	59.1
500 x 50	50	500	46.4	54.1	58.8	9.8	10.9	531	515	71.6	58.1
500 x 40	40	500	37.1	48	48	8.8	10	535	515	65.4	57
500 x 30	30	500	24.8	37.1	37.1	8.6	9.3	527	509	65.7	60.7
500 x 20	20	500	20.1	24.8	24.8	9	9.8	533	507	68.1	55.2
500 x 10	10	500	9.3	15.5	15.5	8.9	10.3	530	515	71.3	58.7
600 x 50	50	600	48	54.1	55.7	9.4	11.3	624	607	69.7	56.7
600 x 40	40	600	37.1	44.9	46.4	9.4	10.8	622	606	68.2	53.2
600 x 30	30	600	26.3	37.1	37.1	9.2	10.2	625	610	68.6	52.8
600 x 20	20	600	17	26.3	27.8	9	10.3	623	610	67.3	51.7
600 x 10	10	600	9.3	15.5	15.5	9.8	11.1	620	609	69.3	57.9
700 x 50	50	700	48	54.1	57	10.3	10.9	725	714	72	55.1
700 x 40	40	700	37	45	48	9.9	11.5	730	709	68.9	53.5
700 x 30	30	700	28	36.5	37	9.4	10.4	725	710	69.2	53.6
700 x 20	20	700	20.5	26	28	9.4	11.6	725	705	68.3	63.4
700 x 10	10	700	9.7	15	15	10	11.1	730	710	69.3	56.9

Calculation of strain gradient

Theory

A stress gradient can exist in electroplated nickel such that when a cantilever is released from its sacrificial layer the stress causes the cantilever to deflect. If the cantilever is fabricated from a single material then this act of deflection relieves this residual stress. This phenomenon was observed in the cantilevers (tested in chapter 5) since the pre-release and post-release tip heights were not the same. In the following section calculations are detailed that allow the magnitude of the stress/strain gradient (assumed to be linear), to be calculated from the resulting tip deflections.

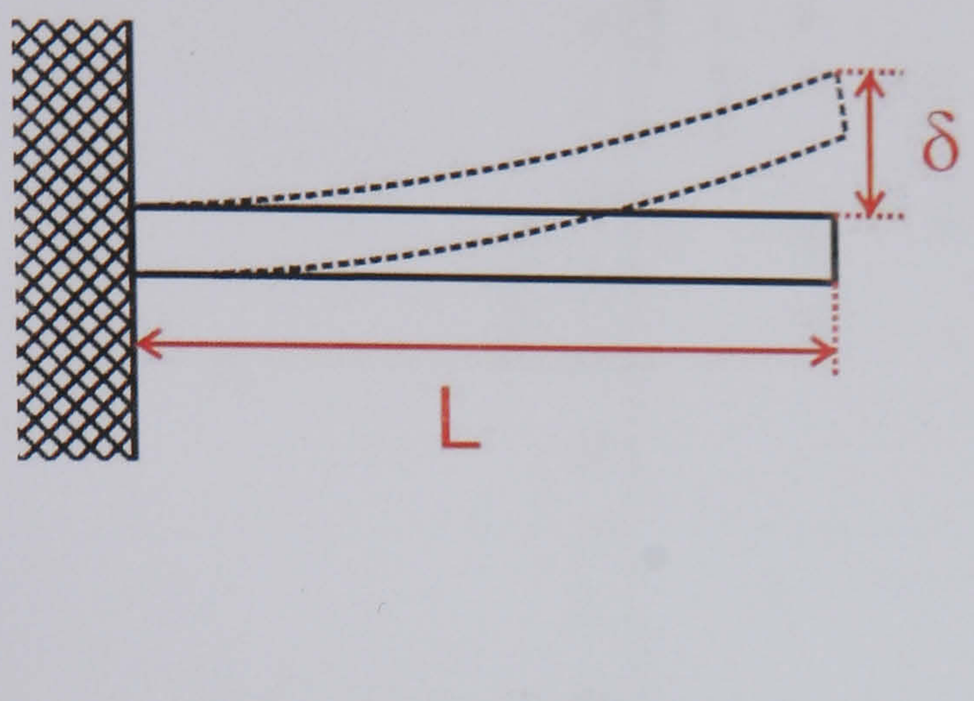

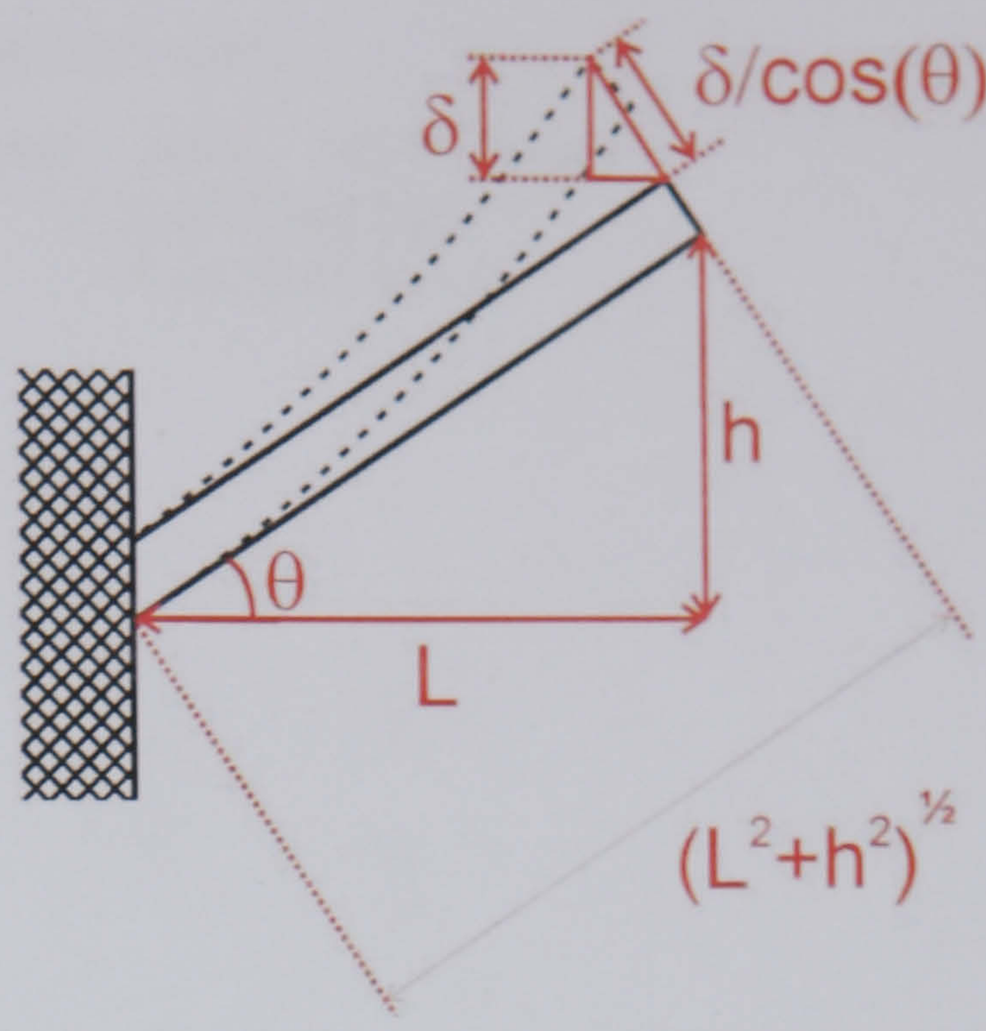

For the horizontal cantilever (shown on the left) the strain gradient, Γ, can be calculated as:

$$\Gamma = \frac{2\delta}{L^2}$$

Therefore, by comparing the inclined cantilever (shown on the right) with the horizontal cantilever (shown on the left) it can be seen that:

$$\Gamma = \frac{2\left(\delta/\cos(\theta)\right)}{\left(\sqrt{L^2+h^2}\right)^2} = \frac{2\delta}{\left(L^2+h^2\right)\cos(\theta)}$$

but $\cos(\theta) = \dfrac{L}{\sqrt{L^2+h^2}}$ and therefore, $\Gamma = \dfrac{2\delta}{L\sqrt{L^2+h^2}}$

rearranging gives:

$$\delta = \frac{L\sqrt{L^2+h^2}}{2}\Gamma$$

Results

By plotting vertical deflection versus the correct function of cantilever length the strain gradient can be determined from the gradient of the graph.

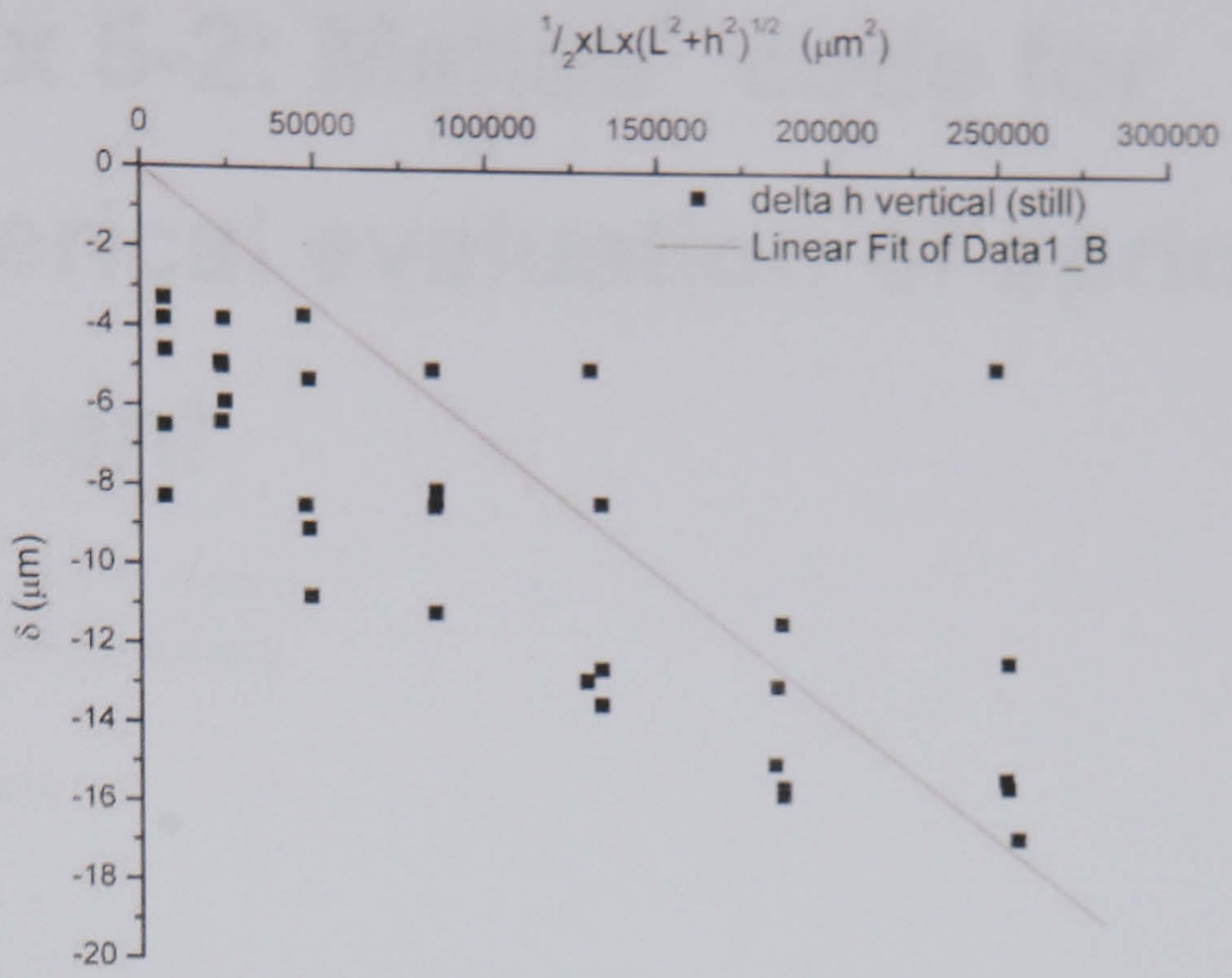

From the proceeding derivation it can be seen that the gradient on the linear fit (through the origin) shown in the above plot gives the pre-release strain gradient, Γ. From the graph it was found that the strain gradient was an average value of -6.8^{-5} μm^{-1}.

It should be noted that the data doesn't form a well correlated data set since there appears to be an offset in the data and that might represent a systematic error. The tip height before release was measured using a white light interferometer where as the height after release was measured using focal plane offset under an optical microscope. The distance between the wafer surface and the top of the cantilever was measured using focal plane offset and the new tip height, *h*, calculated by subtracting the measured thickness of the cantilever from this distance. It is possible that the different measurement techniques are not in perfect calibration with one another.

Strain and stress are related by Young's modulus such that Young's modulus, E, is given by:

$$E = \frac{\sigma}{\varepsilon}$$

where σ it the stress and ε is the strain.

If the Young's modulus is assumed to be 69 GPa (based on tension testing) then the above strain gradient corresponds to a stress gradient of 4.7 MPa/μm.

The thicknesses of the cantilevers varied between different cantilevers however the maximum recorded thickness, *t*, was 12 μm. Since the pre-release stress varied from tensile to compressive (through the thickness of the cantilever), the maximum and minimum stress values correspond to ± t/2. This corresponds to a maximum absolute pre-release stress of 28 Mpa.

Appendix 5-2: Matlab® code for numerical evaluation of spring constant

```
% read in a CSV file containing information
geometry=csvread('c:\geometry_exact.csv');
   caluclate size of array
[row,column]=size(geometry);
 % run script
K=[];
for n=1:1:row
   value=calculate_k_autowide(geometry(n,1),geometry(n,2),geometry(n,3),geometry(n,4),geometry(n,5),geometry(n,6),ge
   ometry(n,7));
   K=[K;value];
end
% output to text file
csvwrite('c:\Spring_constants.txt',K);


function [k]=calculate_k_autowide(w1,w2,w3,L,t1,t2,h)
% define parameters for integration
steps=2000;
% define material constants (Young's in GPa. Poisson's ratio. shear constant)
E=69.1e9;
v=0.312;
C=1.2;
% calculate shear modulus
G=E/(2*(1+v));
%CODE
%set all values into meters
t1=t1/1e6; t2=t2/1e6; w1=w1/1e6; w2=w2/1e6; w3=w3/1e6; L=L/1e6; h=h/1e6;
% calculate the horizontal and vertical load components (assuming a unit load) and diagonal leng
theta=atan(h/L);
Load_vertical=cos(theta);
Load_horizontal=sin(theta);
%diagonal effective thickness
t1=t1*cos(theta);
t2=t2*cos(theta);
%diagonal length
S=((L^2)+(h^2))^0.5;
   integration step
step=S/steps;
```

```
% calculate first order polynomial through thickness and second order through width
x_thickness=[0,S];
thickness=[t1,t2];
x_width=[0,(S/2),S];
width=[w1,w2,w3];
thickness_poly=polyfit(x_thickness,thickness,1);
width_poly=polyfit(x_width,width,2);
% calculate vectors. X (along diagonal) Moment. width and thickness (for each X value)
X=[]; M=[]; W=[]; T=[];
for i=0:step:S
    X=[X,i];
    M=[M,(Load_vertical*S)-(Load_vertical*i)];
    W=[W,((i^2)*width_poly(1,1)+i*width_poly(1,2)+width_poly(1,3))];
    T=[T,(i*thickness_poly(1,1)+thickness_poly(1,2))];
end
% calculate values for numerical integration
wmax=max(W);  % find maxium value of width along cantilever length
count=1;
total_energy=[];
for i=0:step:S
    I=(W(1,count)*(T(1,count)^3))/12;  % calculate second moment
    area=W(1,count)*T(1,count);        % calculate area
% Terms relating to bending to integrate
% determine if need to treat bending component as plane stress or as plane strain. Use E for w/L<0.1 and E/(1-v^2) for
% w/L>0.1
if(wmax/((L^2+h^2)^0.5)>0.1)
   bending_energy=((M(1,count)^2)*(1-v^2))/(2*E*I);
else
   bending_energy=(M(1,count)^2)/(2*E*I);
end
% Terms relating to shear to integrate
shear_energy=(C*(Load_vertical^2))/(2*G*area);
% Terms relating to aixial load to integrate
axial_load_energy=(Load_horizontal^2)/(2*area*E);
% total vector to integrate
total_energy=[total_energy,(bending_energy+shear_energy+axial_load_energy)];
% increment count
    count=count+1;
end
%operform integration
U=trapz(X,total_energy);
% calculate spring constant  by equating to 1/2xloadxdeflection. Load is unity
k=1/(2*U);
% convert into mN um
k=k/1000;
```

Appendix 7-1: Fabrication process flow

Clean wafer

Sonicate wafer in 10:1 H_2O:'Decon' detergent, rinse in several H_2O baths
Immerse in 1:1 H_2SO_4:H_2O_2 for 30 minutes, rinse in several H_2O baths
Sonicate H_2O

Mould PDMS layer onto wafer

Thoroughly mix 1:10 'Sylgard silicone elastomer curing agent': 'Sylgard 184 silicone elastomer base' (Dow Corning corporation)
Remove trapped air bubbles by outgassing the mixture in a vacuum chamber (at 10^{-2} torr) for 30 minutes
Dispense a small volume of the outgassed PDMS onto the gold coated copper mould.
Outgas for a further 10 minutes (as above)
Lay the cleaned borosilicate substrate on top of the mould (covered with PDMS) then place in the vice and tighten.
Outgas the assembly for further 30 minutes (as above)
Remove the assembled vice and bake on a hot plate at 140 °C for 30 minutes then allow to cool to room temperature.
Disassemble vice and peal copper mould away from the substrate

Oxygen treatment to improve metal adhesion to the PDMS

Oxford instruments Plasmalab 80Plus (quartz platen cover): 40 sccm O_2, 200 mT chamber pressure, 200 W using RIE mode for 15 minutes

Sputter titanium – copper seed layer and electroplate copper

Moorfield Minilab sputter system (Base pressure less than 1.0×10^{-6} mbar , argon flow rate 5 sccm, stage rotation 25 rpm, stage bias 0 V)

Ti deposition (30 nm): RF magnetron (forward power 204 W), chamber pressure 6.5 mT
Cu deposition (60 nm): DC magnetron (magnetron current 0.7 A), chamber pressure 20 mT

Paint S1813 photoresist (Shipley corporation) over moulded alignment mark structures (placed near the edge if the wafer)
Electroplate copper to a thickness of 5 µm at a current density of 20 mA/cm^2. Stirrer rotation of 600 rpm, bath temperature 20 °C, for 12 minutes (rotate substrate 180° after 6 minutes)
Remove S1813 photoresist by washing in acetone, IPA and then H_2O
Wash wafer in H_2O

Define anchor areas

Spin AZ electronic materials AZ9260 resist at 1000 rpm for 1 minute (300 rpm spreading stage for 15 s)
Wait 2 minutes before baking at 95 °C on vacuum hotplate for 5 minutes
Remove wafer and allow to cool for 1 minute
Spin and bake 2 more layers of AZ9260 in identical fashion
Remove the resist edge bead using a jet of acetone directed onto edge of wafer rotating at 6000 rpm
Bake wafer for on a vacuum hotplate using temperature profiles shown in Figure 1

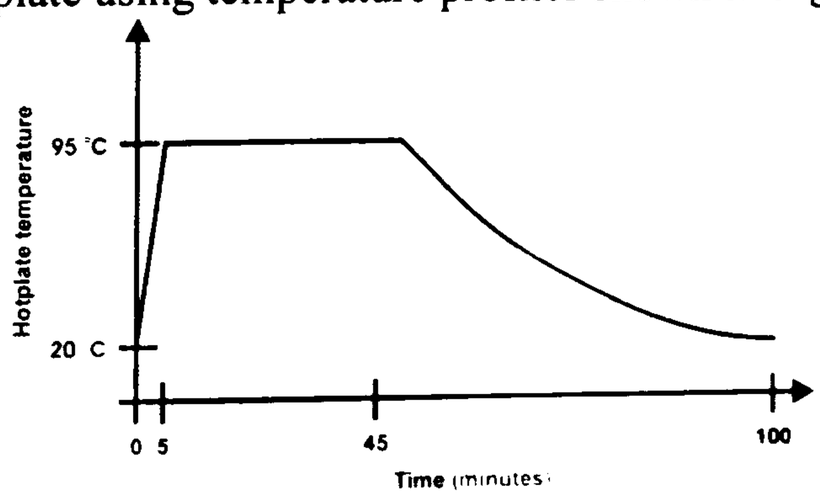

Figure 1: Hot plate temperature ramp

Hydrate in H_2O at 20 °C for 15 minutes (or leave for 12 hours in 40 – 60 % relative humidity atmosphere)
Expose (EVG 620) 1530 mJ/cm^2 (hard contact)
Develop in 2:1 H_2O:AZ 400K developer until clear (8 minutes)

Etch exposed copper, titanium and PDMS

Etch electroplated and sputtered copper in 250 g/l sodium persulphate (10 minutes)
Remove photoresist by washing in acetone, IPA and then H_2O
Etch titanium and PDMS: Oxford instruments Plasmalab 80Plus (quartz platen cover): 20 sccm O_2, 60 sccm SF_6, 100 mT chamber pressure, 300 W using RIE until PDMS clear. This process was found to etch PDMS at approximately 500 nm/min whilst the borosilicate was etched at approximately 5 nm/min.
(note: If 'grass' formed during PDMS etching due to micro-masking it could be removed by washing the wafer in H_2O. The surface tension caused the 'grass' to collapse and it could then be removed by further dry etching)

Sputter titanium – copper seed layer

Moorfield Minilab sputter system (Base pressure less than 1.0×10^{-6} mbar , argon flow rate 5 sccm, stage rotation 25 rpm, stage bias 0 V)
Ti deposition (30 nm): RF magnetron (forward power 204 W), chamber pressure 6.5 mT
Cu deposition (60 nm): DC magnetron (magnetron current 0.7 A), chamber pressure 20 mT

Define cantilevers

Spin AZ electronic materials AZ9260 resist at 1000 rpm for 1 minute (300 rpm spreading stage for 15 s)
Wait 2 minutes before baking at 95 °C on vacuum hotplate for 5 minutes
Remove wafer and allow to cool for 1 minute
Spin and bake 2 more layers of AZ9260 in identical fashion
Remove the resist edge bead using a jet of acetone directed onto edge of wafer rotating at 6000 rpm
Bake wafer for on a vacuum hotplate using temperature profiles shown in Figure 1
Hydrate in H_2O at 20 °C for 15 minutes (or leave for 12 hours in 40 – 60 % relative humidity atmosphere)
Expose (EVG 620) 1530 mJ/cm^2 (soft contact)
Develop in 2:1 H_2O:AZ 400K developer until clear (8 minutes)

Electroplate cantilevers

Electroplate nickel (smooth nickel formulation) to a thickness of 15 µm at a current density of 12 mA/cm^2. Stirrer rotation of 600 rpm, bath temperature 60 °C, electroplating current 11.3 mA, for 70 minutes (rotate substrate 180° after 35 minutes)
Remove AZ resist using acetone, wash wafer in IPA and H_2O

Define tips

Spin AZ electronic materials AZ9260 resist at 1000 rpm for 1 minute (300 rpm spreading stage for 15 s)
Wait 2 minutes before baking at 95 °C on vacuum hotplate for 5 minutes
Remove wafer and allow to cool for 1 minute
Spin and bake 2 more layers of AZ9260 in identical fashion
Remove the resist edge bead using a jet of acetone directed onto edge of wafer rotating at 6000 rpm
Bake wafer for on a vacuum hotplate using temperature profiles shown in Figure 1
Hydrate in H_2O at 20 °C for 15 minutes (or leave for 12 hours in 40 – 60 % relative humidity atmosphere)
Expose (EVG 620) 1530 mJ/cm^2 (soft contact)
Develop in 2:1 H_2O:AZ 400K developer until clear (8 minutes)
Oxygen clean resist residues using Yield Engineering Systems R3 plasma cleaner: sample on floating electrode, chamber pressure 2.4 torr, 120 W for 20 minutes

Electroplate tips

Electroplate nickel (smooth nickel formulation) to a thickness of 15 µm at a current density of 12 mA/cm^2. Stirrer rotation of 600 rpm, bath temperature 60 °C, electroplating current 11.3 mA, for 70 minutes (rotate substrate 180° after 35 minutes)
Remove AZ resist using acetone, wash wafer in IPA and H_2O

Isolate probes

Etch copper seed in 2:1:1 H_2O:CH_3COOH:H_2O_2
Etch Ti layer in 10:1 H_2O:HF
Etch copper electoplate in 2:1:1 H_2O:CH_3COOH:H_2O_2
Etch Ti layer in 10:1 H_2O:HF

Publications

Conferences

Rosamond, M., Gallant, A.J. and Wood, D., 'A robust, fine pitch probe card'. Eurosensors XXIII, 6-9 Sept. 2009 – accepted

Rosamond, M., & Wood, D., 'Substrate independent fabrication of a non-planar probe card', Micro-and Nano-Engineering 32 international conference, Barcelona, Spain 17-20 Sept. pp. 353-354. 2006.

Rosamond, M.C., Cooke, M.D., Kent, B., Zeze, D.A. & Wood, D., 'Testing and Reliability of a Microsystems Probe Card', Micro and Nanotechnology International Conference, London, UK, 12-14 Dec, 2005.

Papers

Rosamond, M. & Wood, D., 'Substrate independent fabrication of a non-planar probe card', Microelectronic Engineering, vol. 84, no. 5-8, pp. 1207 – 1210, 2007.

Aguiar, F.A., Rosamond, M.C., Wood, D., & Kataky, R., 'Towards multifunctional microelectrode arrays' The Analyst, vol.133, pp. 1060 – 1063, 2008.

Aguiar, F.A., Gallant, A.J., Rosamond, M.C., Rhodes, A., Wood, D. & Kataky, R., 'Conical recessed gold microelectrode arrays produced during photolithographic methods: Characterisation and causes', Electrochemistry Communications, vol. 9, no. 5, pp. 879 -885, 2007.

Chiang, C.J., Rothe, C., Rosamond, M., Gallant, A., Ferain, E., Legras, R., Wood, D. & Monkman, A., 'Organic light-emitting diodes incorporating supported nanotemplates', SPIE- Photonic Materials, Devices, and Applications II, vol. 6593, pp. 65930R, 2007.